

UNIVERSITY OF CALIFORNIA,  
IRVINE

Label-free Cell Sorting using Carbon-electrode Dielectrophoresis  
and Centrifugal Microfluidics

DISSERTATION

submitted in partial satisfaction of the requirements  
for the degree of

DOCTOR OF PHILOSOPHY

in Mechanical and Aerospace Engineering

by

Rodrigo Martínez Duarte

Dissertation Committee:  
Professor Marc J. Madou, Chair  
Professor Manuel Gamero Castaño  
Professor Abraham P. Lee

2010



## DEDICATION

Un grand merci à ma chère épouse Anne-Carole dont l'irremplaçable présence ne cesse d'illuminer tant mes jours joyeux que mes jours plus obscurs. Merci pour ton Amour sans limite ni condition ainsi que pour la joie et l'inaltérable soutien que tu m'offres chaque jour

A mis papás, Roberto y María del Rosario, a Harold y Connie<sup>†</sup>, a Favy y Héctor, Laris y Ricardo, a Rober y mi tía Vieja por su amor, su paciencia y su apoyo a lo largo de todo este camino. Gracias por creer en mí

A los "pequeños" de la familia: Faby, Sofi, Mafer, Laris, Ricky, Tin, Mau, Andrea, Dani, Diego y Alexia por darme tantas alegrías. Estoy muy orgulloso de ustedes

A mis amigos, especialmente Rubén, Kiki, Fer, Horacio y Joe por escucharme y darme alas en mis sueños pero siempre mantenerme en la realidad

And last but not least, to God, for blessing me with such beautiful and exciting people

*The pleasure of success is on maintaining who to share it with*

# TABLE OF CONTENTS

LIST OF FIGURES.....	v
LIST OF TABLES.....	viii
ACKNOWLEDGEMENTS.....	ix
CURRICULUM VITAE.....	x
ABSTRACT OF THE DISSERTATION.....	xii
INTRODUCTION.....	1
CHAPTER 1. Background	
1.1 Dielectrophoresis.....	9
1.2 Glass-like carbon and Carbon MEMS.....	19
1.3 Centrifugal Microfluidics.....	30
CHAPTER 2. Fabrication of carbon-electrode DEP devices	
2.1 Electrodes.....	44
2.2 Fluidic Network.....	92
2.3 Fluidic and electrical interconnects.....	100
2.4 Resume of fabricated devices and discussion.....	105
2.5 Possible improvements to current carbon-DEP devices.....	110
CHAPTER 3. Electromagnetic and Fluidic dynamic characterization of a selected carbon-electrode DEP device	
3.1 Electromagnetic characterization.....	120
3.2 Fluidic dynamic characterization.....	137
3.3 Discussion.....	140
CHAPTER 4. Cell sorting using carbon-electrode DEP	
4.1 Experimental considerations.....	147
4.2 Experimental samples.....	160
4.3 Experimental validation of carbon-DEP.....	167

CHAPTER 5. The integration of DEP and centrifugal microfluidics	
5.1 Platform components and fabrication.....	184
5.2 Electrical and mechanical characterization of the SpinDEP platform.....	189
5.3 Flow characterization for SpinDEP experiments.....	189
5.4 Cell sorting using the SpinDEP platform.....	196
5.5 Advantages and broader impact of the SpinDEP platform.....	211
CONCLUSION.....	214
REFERENCES.....	216

## LIST OF FIGURES

		Page
Figure 1.1	Comparison between the use of 2D and 3D electrodes	16
Figure 2.1	Fabrication flow chart of carbon-DEP devices	43
Figure 2.2	The different processes required for the fabrication of carbon electrodes for DEP applications	46
Figure 2.3	Examples of stiction in a SU-8 cylinder array	47
Figure 2.4	Model used to analyze stiction forces	48
Figure 2.5	Variation of the moment of the inertia when the surface area of the geometry or the characteristic dimension change	54
Figure 2.6	Variation on the moment of inertia when a circle transforms into an ellipse and a square into a rectangle	55
Figure 2.7	The effect of SU-8 post radius, gap between posts and immersion liquid on the maximum post height and aspect ratio that can be fabricated without stiction	56
Figure 2.8	Fabrication flow chart for carbon electrodes	59
Figure 2.9	Typical carbon electrode array used for carbon-DEP and its SU-8 precursor	60
Figure 2.10	Characterization of the post adhesion to the substrate	64
Figure 2.11	Examples of carbon electrodes and their connecting leads	78
Figure 2.12	Examples of high aspect ratio carbon structures	78
Figure 2.13	Characterization of shrinkage during pyrolysis	81
Figure 2.14	Comparison between the aspect ratio of the carbon structures and their SU-8 precursors	82
Figure 2.15	Characterization of structure detachment during pyrolysis	84
Figure 2.16	Schematics of a four point probe station	85
Figure 2.17	Electrical resistance vs. length of carbon electrical leads	89
Figure 2.18	Thin SU-8 layer patterned around the carbon electrodes	90
Figure 2.19	Voltage along a connection lead at different sample conductivities	91
Figure 2.20	Planar and volumetric electrodes contained in a SU-8 channel	96

Figure 2.21	A PDMS channel positioned around an array of carbon electrodes	97
Figure 2.22	Isometric view of microfluidics fabricated using double-sided pressure-sensitive adhesive and polycarbonate	99
Figure 2.23	Selected cross-section of a carbon-DEP devices to exemplify the fluidic and electric interconnects	102
Figure 2.24	Alternative fluidic connector using O-ring and polycarbonate	104
Figure 2.25	Resume of carbon-DEP devices fabricated in this work	107
Figure 2.26	Carbon patterns deposited on a piece of glass	115
Figure 2.27	Preliminary results on the use of chromium leads to connect the carbon electrodes	119
Figure 3.1	Model for electromagnetic and fluid-dynamic simulation	122
Figure 3.2	Experimental validation of the simulation results: Positive and negative-DEP regions	127
Figure 3.3	Experimental validation of simulation results: cell trapping depending on flow rate	129
Figure 3.4	Electromagnetic simulation results: change on electrode height	131
Figure 3.5	Electromagnetic simulation results: change on polarizing voltage	134
Figure 3.6	Electromagnetic simulation results: change on conductivity	136
Figure 3.7	Fluid-dynamic simulation results: flow velocity 3D field	139
Figure 3.8	Fluid-dynamic simulation results: flow pathlines	140
Figure 3.9	Volume distribution of different ranges of electric field magnitude squared depending on electrode height, polarizing voltage and sample conductivity	142
Figure 3.10	Comparison between the flow velocity field and electric field gradient in a carbon electrode array	144
Figure 4.1	Cross-section of a cell membrane	148
Figure 4.2	Membrane potential of a yeast cell as a function of electric field magnitude and frequency	150
Figure 4.3	Volume distribution of different ranges of electric field magnitude depending on electrode height, polarizing voltage and sample conductivity	153

Figure 4.4	Example on the determination of the optimal parameters for DEP experiments	154
Figure 4.5	Real part of the Clausius Mossotti factor depending on frequency For some of the experimental samples	164
Figure 4.6	Real part of the Clausius Mossotti factor depending on frequency and media conductivity for yeast cells and latex particles	166
Figure 4.7	DEP experimental platform using a syringe pump	169
Figure 4.8	Proof-of-concept of yeast manipulation using carbon electrodes	170
Figure 4.9	Performance comparison between 2D and 3D carbon electrodes when trapping yeast cells	172
Figure 4.10	General schematic of a multi-stage filter	173
Figure 4.11	Trapping of viable and non viable yeast using a 2-stage filter	175
Figure 4.12	Theoretical particle mix to demonstrate the full potential of a 2-stage filter	176
Figure 4.13	Focusing of yeast cells using positive-DEP	178
Figure 4.14	Trapping of <i>D. melanogaster</i> using carbon electrodes	181
Figure 5.1	Assembly of a SpinDEP platform	186
Figure 5.2	Example of a carbon-DEP chip used with the SpinDEP platform	188
Figure 5.3	Flow rates established in two different carbon-DEP chips depending on spin speed	190
Figure 5.4	The effect of channel misalignment on the flow rate	193
Figure 5.5	Flow rate characterization of different media depending on spin speed	195
Figure 5.6	Experimental protocol for the use of the SpinDEP platform	198
Figure 5.7	Experimental results on the separation of yeast cells from latex particles using the SpinDEP platform	202
Figure 5.8	Experimental results on the separation of viable yeast cells from non viable yeast cells using the SpinDEP platform	203
Figure 5.9	The effect of particle sedimentation on DEP experiments	206
Figure 5.10	Optimization process to avoid particle sedimentation during DEP experiments	210

## LIST OF TABLES

		Page
Table 1.1	Selected examples of cell manipulation using DEP	11
Table 1.2	Comparison between glass-like carbon electrodes and common electrode materials and configuration used in DEP	16
Table 1.3	Selected properties of different formulations of SU-8 photoresist	26
Table 1.4	Selected SU-8 properties	26
Table 1.5	Processing steps in SU-8 photolithography	28
Table 1.6	Selected examples of biological assays performed using centrifugal microfluidics	33
Table 2.1	Second moment of inertia for selected cross-sections	52
Table 2.2	Surface tension of selected liquids	57
Table 2.3a	Spin programs used in this work and resultant layer thickness	60
Table 2.3b	Fabrication processes of all structures done in this work	61
Table 2.4	Dimensions of all SU-8 and carbon posts fabricated in this work	80
Table 2.5	Characterization of the glass-like carbon resistivity	86
Table 2.6	Resistivity of glass-like carbon compared to other materials	87
Table 2.7	Different techniques used to fabricate microfluidics network	94
Table 2.8	Development of carbon-DEP chips	106
Table 2.9	Selected properties of materials commonly used as substrates	112
Table 2.10	Resume on solutions used to peel off and deposit carbon films	117
Table 2.11	Selected properties of metals commonly used in microfabrication	118
Table 4.1	Parameters used to calculate membrane potential on yeast cells	149
Table 4.2	Conductivity values of selected buffers	156
Table 4.3	Selected examples of experimental media for DEP	159
Table 4.4	Properties of the experimental samples used in this work	162
Table 4.5	Qualitative determination of the optimal frequency to trap <i>E.coli</i>	179
Table 4.6	Qualitative determination of the optimal frequency to trap <i>D. melanogaster</i> S2 cells	181

## ACKNOWLEDGEMENTS

I want to thank my friend and advisor, Prof. Marc Madou, for giving me the opportunity to conduct exciting research and providing me with so many other opportunities for development in my research career. I hardly imagined graduate school would take me to so many exciting places and lead me to live so many cultural and academic experiences.

Thanks to my friend and first advisor, Prof. Sergio O. Martinez at Monterrey, for all his support which allowed me to start my research career.

Thanks to my committee members, Prof. Abe Lee and Prof. Manuel Gamero-Castaño, for their enthusiasm on my research and providing kind directions to the next step.

Most importantly, I want to thank my colleagues and advisors for helping me advance in my scientific pathway and sharing with me the ups and downs of this often frustrating road. There is no price on the support and cheers given after a failed experiment which let us get up and continue with our research. After all, the joy that comes with a result is definitely worth the trouble.

## **CURRICULUM VITAE**

### **Rodrigo Martínez Duarte**

- 2004 B.S. in Electrical Engineering, Tecnológico de Monterrey,  
Campus Monterrey
- 2005 Project Scientist, Detection of Leukemia Relapse, Tecnológico  
de Monterrey, Campus Monterrey
- 2005-10 Research Assistant, BioMEMS Research Group, University  
of California, Irvine
- 2006 Visiting Scholar, California-Catalonia Alliance for Miniaturization  
Science and Engineering, Universitat de Barcelona
- 2007 Visiting Scholar, California-Catalonia Alliance for Miniaturization  
Science and Engineering, Universitat de Barcelona  
Visiting Scholar, INDO-US Centre for Research Excellence in  
Fabronics, Indian Institute of Technology, Kanpur  
Teaching Assistant, Fundamentals of Microfabrication, University  
of California, Irvine
- 2008 Visiting Scholar, Tecnológico de Monterrey, Campus Monterrey
- 2009 M. S. in Mechanical and Aerospace Engineering, University of  
California, Irvine  
Visiting Scholar, Ulsan National Institute of Science and  
Technology, Republic of Korea
- 2010 Ph. D. in Mechanical and Aerospace Engineering, University of  
California, Irvine

#### **FIELD OF STUDY**

Microfluidics and Microfabrication

## PUBLICATIONS

“Fluidodynamic and Electromagnetic Characterization of 3D Carbon Dielectrophoresis with Finite Element Analysis.” *Sensors & Transducers Journal* 3 (2008):, 25-36.

“Perspectives of Micro and Nanofabrication of Carbon for Electrochemical and Microfluidics Applications.” *Microfluidics and Microfabrication*. Ed. S. Chakraborty. New York: Springer, 2009. 181-263.

“The integration of 3D Carbon-electrode Dielectrophoresis on a CD-like Centrifugal Microfluidics Platform.” *Lab-on-a-chip* 10 (2010): 1030-1043.

“On-line separation of bacterial cells by carbon-electrode dielectrophoresis.” *Electrophoresis* in press (2010).

# **ABSTRACT OF THE DISSERTATION**

Label-free Cell Sorting using Carbon Electrode Dielectrophoresis  
and Centrifugal Microfluidics

By

Rodrigo Martinez Duarte

Doctor of Philosophy in Mechanical and Aerospace Engineering

University of California, Irvine, 2010

Professor Marc J. Madou, Chair

The integration of 3D carbon-electrode dielectrophoresis (carbon-DEP) on a Compact Disk (CD)-like centrifugal platform is presented in this work towards developing an automated platform for label-free cell sorting with application in point-of-care diagnostics and cell-based therapies. The use of DEP can eliminate functionalized magnetic beads or fluorophores required by other separation techniques such as magnetophoresis and flow cytometry and reduce assay complexity, time and costs. This can expand the availability of diagnostic tests, such as for HIV, and make therapies for cancer or degenerative diseases available to a broader number of patients.

Glass-like carbon electrodes are used here to enable DEP-assisted cell sorting. These electrodes are obtained after the pyrolysis of organic polymer structures previously fabricated using photolithography following the C-MEMS technique. Carbon-electrode DEP (carbon-DEP) combines the advantages of other more traditional DEP techniques such as metal-based and insulator-based DEP and represents a new alternative for DEP applications. The use of carbon electrodes yields advantages such as 1) wide electrochemical stability to minimize the possibility of sample electrolysis, 2) excellent

biocompatibility and 3) chemical inertness to almost all solvents/electrolytes. The integration of DEP with centrifugal microfluidics significantly reduces the footprint and complexity of traditional DEP platforms which tend to rely on a combination of syringes, tubing, valves, and fluidic ports for fluid manipulation. Key benefits of centrifugal pumping over other forms of propulsion techniques include 1) its insensitivity to most physicochemical properties of the sample being pumped, such as pH, ionic strength or chemical composition, 2) the vented nature of the system and 3) the fact that the system is easy to miniaturize and that it lends itself easily to assay multiplexing.

## INTRODUCTION

The lack of affordable medical infrastructure is one of the main causes of high mortality rate in the world. Many patients still die due to complications of an otherwise simple condition because of the dependence on centralized laboratories and special reagents to accurately diagnose and treat disease. Cell sorting is at the core of many diagnostic tests (for example a complete blood count) and is a cornerstone for cell-based therapies. Basic techniques for cell sorting exploit the fact that different cells may feature different densities. For example, centrifugation is commonly used to separate red blood cells from blood plasma. White blood cells (or blood plasma cells) are heavier than red blood cells and tend to sediment faster. Centrifugation is a common and affordable technique used to separate cells using the differences between the densities of different cells and the suspending media. However, alternative techniques must be used when the targeted cells have a similar density to all others contained in the same sample. In this case, the use of external tags or stains is common to differentiate the targeted cells from their background. Commercial examples of such cell sorting platforms that are currently available rely on cell flow cytometry and magnetically-actuated techniques such as FACS<sup>®</sup> and MACS<sup>®</sup>. These techniques offer high performance but require expensive infrastructure, skilled personnel and special reagents. Many efforts are currently in place to simplify and bring this advanced cell sorting to the point-of-care such that results are obtained within minutes and the need for expensive infrastructure and skilled personnel is eliminated. Unfortunately many of these efforts are miniaturizations of current systems and still rely on the use of expensive antibodies and other special stains to sort targeted

cells. Antibodies require special handling, such as refrigeration and/or distilled water for their reconstitution, which is not always possible. The cost of most antibody-based assays is still high so continuous monitoring; timely diagnosis and novel cell therapies still cannot be offered to the larger number of patients, especially those in under privileged areas. Up to 44% of the world population, approximately 3 billion, is expected to have low income by the year 2015 while those with median income will account for an extra 42%. Only 14% will perceive a high income as estimated by the Human Development Report. The development of affordable medical infrastructure is of extreme importance. For example, there are currently more than 33 million HIV patients in the world whose population of CD4 cells must be continuously monitored to determine the appropriate time to start antiviral therapy and improve their chance of survival. Most of them do not have access to diagnostic tools because they live either in an impoverished country without access to medical infrastructure or in a developed country where they cannot afford the cost of such test. Cell therapy can also benefit from a lower cost cell sorting platform. In current cell therapy protocols, stem cells must first be sorted out from a blood or tissue sample of either a donor or the patient himself/herself and later get transplanted to the patient in specific places. These stem cells can trigger the replenishment of a cell population (blood cells, cardiomyocytes, insulin-producing islet cells, etc.) and have the potential to cure many diseases and conditions such as leukemia (0.22 million deaths per year worldwide), heart disease (7.2 million deaths per year worldwide), spinal cord injury (130,000 patients worldwide), diabetes (285 million patients worldwide) and neurodegenerative diseases such as Alzheimer's (35 million patients worldwide, expected 115 million by 2050) and Parkinson's (6.5 million patients

worldwide). Cell therapy is a very promising clinical technique and significant advances had been made in the field but the cost of cell procurement prohibits such treatment for the majority of eligible patients.

This dissertation presents the integration of carbon-electrode dielectrophoresis (carbon-DEP) on a Compact Disk (CD)-like centrifugal platform towards developing an automated platform for label-free cell sorting with application in point-of-care diagnostics and cell-based therapies. The ultimate goal is to implement an affordable sample-to-answer system where human intervention is only needed to load a sample from a patient, *e.g.*, blood, saliva or urine, choose the assay to be performed and retrieve either a numeric result, for example the number of CD4 T-cells present in HIV patients, or an enriched cell population to be used in cell therapy.

Dielectrophoresis (DEP) is advantageous over other current cell sorting techniques such as FACS<sup>®</sup> (Fluorescence-activated cell sorting) and MACS<sup>®</sup> (Magnetic-activated cell sorting) because discrimination between different cells is based solely on their intrinsic physical properties, *i. e.*, membrane morphology and internal compartmentalization and not on usually expensive external tags such as antibodies. These physical properties determine the cell's dielectric properties and give it a characteristic dielectric phenotype. Therefore, the use of DEP eliminates functionalized magnetic beads or fluorophores required by other separation techniques such as magnetophoresis and flow cytometry. The elimination of these often expensive labels reduces assay complexity, time and costs which can expand the availability of diagnostic tests, such as for HIV, and make therapies for cancer or degenerative diseases available to a broader number of patients.

Cell sorting using DEP relies on the varying magnitude and direction of the dielectrophoretic force acting on different particles contained in the sample. Given fixed experimental conditions, the DEP force may act stronger on some particles than on others. The direction of the force acting on different particles may also vary. The magnitude of the dielectrophoretic force on a given particle mainly depends on the size of the particle and the magnitude of the electric field gradient that surrounds it. The direction depends directly on the difference between the complex permittivity of the particle and that of the suspending media. Different sorting techniques exist. Some of the most common ones include sequential trap and release, Field-Flow Fractionation (FFF) and deflection of a focused stream of cells into different outlets. Sequential trap and release is explored in this work.

Most of the work in DEP relies on the use of metal microelectrodes contained in a flow channel to induce the required electric field gradient for the DEP manipulation of particles in the sample. However, the use of metal microelectrodes in direct contact with the sample severely restricts the magnitude of the applied voltages as one must prevent sample electrolysis. An alternative to the use of metal microelectrodes is to use arrays of insulator structures, usually fabricated from polymers or glass, to locally distort the electrical field. In this technique, known as insulator-based dielectrophoresis or iDEP, metal electrodes (for example extruded wire rods or machined metal plates) positioned outside the flow channel are used to set up the field over the insulator structures. A voltage as high as thousands of volts is applied to the metal electrodes to generate a uniform electric field that is rendered non uniform in the vicinity of the insulator structures. When using this technique, the sample is usually contained in the insulator

array and the possibility of electrolyzing the sample is minimized. However, iDEP requires very high voltages (electric field magnitude is inversely proportional to the gap between electrodes and in iDEP the separation between metal electrodes can be in the order of centimeters) to create a suitable electric field for dielectrophoresis.

Carbon micro electrodes are used here to create the electric field gradient in a sample and induce a DEP force on targeted particles. Carbon-electrode DEP (carbon-DEP) combines the advantages of metal-based and insulator-based DEP. For example, the possibility of sample electrolysis is reduced with the use of carbon electrodes, an advantage shared with iDEP, while low voltages are enough to polarize the carbon electrodes and create an electrical field suitable for DEP, an advantage shared with metal-electrode DEP. The possibility of sample electrolysis is minimized when using carbon electrodes because carbon has a much wider electrochemical stability window than metals commonly used in thin film electrode fabrication such as gold and platinum and affords higher applied voltages in a given solution without electrolyzing it. Even though the electrical conductivity of glass-like carbon is lower than that of metals, suitable electric fields for DEP can be generated by polarizing carbon electrodes with voltages in the range of tens of volts instead of the hundreds or thousands of volts between metal plates required in iDEP. The use of carbon electrodes yields other advantages: 1) excellent biocompatibility, 2) chemically very inert in almost all solvents/electrolytes and 3) excellent mechanical properties.

The carbon electrodes presented here are fabricated using the Carbon MEMS (C-MEMS) technique in a very simple high yield process. C-MEMS refers to a fabrication technique where glass-like carbon is obtained through the pyrolysis of organic polymers that have

been patterned using photolithography, molding, embossing or any other suitable technique. Photolithography is used here to pattern SU-8, a negative photoresist, and obtain the carbon precursor structures.

A further advantage on the use of carbon electrodes in DEP stems from the relatively easy fabrication process of 3D carbon structures using the C-MEMS technique. The use of 3D electrodes that cover most of the height of a flow channel greatly improves filter throughput by reducing the mean distance of any particle to the closest electrode surface. This is in contrast to the filter throughput achieved when using 2D (planar) electrodes positioned at the bottom of a flow channel where many targeted particles immersed in the bulk volume of the channel do not come close to the electrical field gradient surrounding the planar electrodes and cannot get trapped. The use of 3D electrodes reduces or eliminates the number of re-flow cycles that are required to improve filter throughput when using 2D electrodes.

Although the costs of a diagnostics assay can be reduced with the elimination of labels by using DEP and the performance of traditional DEP devices can be improved using carbon-DEP, a millimeter-sized DEP chip must still be interfaced to large and often expensive precision apparatus for fluid dispensing. Traditional DEP experimental platforms rely on a combination of syringes, tubing, valves, and fluidic ports for fluid manipulation that significantly increases their complexity and has prevented the practical implementation of DEP-based platforms in settings other than research. The use of a CD platform significantly reduces the footprint and cost of a DEP system and makes it amenable for assay automation. The entire fluid network is contained in a single DEP chip to eliminate the use of syringes, external valves, tubing and any other supporting

fluidic elements. This work differs from DEP platforms where electroosmosis is used as pumping force in that centrifugal pumping does not depend on the electric nor physicochemical properties of the sample.

Microfluidic CD technology has been developed as a unique alternative for handling biological analysis. CD microfluidics rely on forces and pressure gradients induced on a spinning CD platform to move sample liquids. Centrifugal pumping compares advantageously to other standard propulsion techniques such as syringe pumps, ultrasonic, or electrokinetic pumping. Key benefits of centrifugal pumping over other forms of propulsion techniques include its insensitivity to most physicochemical properties of the sample being pumped, such as pH, ionic strength or chemical composition, and the fact that the system is easy to miniaturize and that it lends itself easily to assay multiplexing. A wide variety of fluidic functions including valving, decanting, mixing, etc. have been utilized to enable a variety of biological assays on “Lab-on-a-CD” setups. Examples of commercial applications of Lab-on-a-CD technology include the Piccolo<sup>®</sup> xpress (from Abaxis, Inc.) for a blood electrolyte analysis and Gyrolab<sup>®</sup> (from Gyros AB) for the automation of immunoassay processing.

The work presented here is organized as follows. Chapter 1 presents a general background on the three main topics integrated in this work: dielectrophoresis, glass-like carbon and centrifugal microfluidics. Chapter 2 resumes the fabrication of carbon-DEP devices and possible further improvements to it. Chapter 3 details the modeling and analysis of the electric and flow velocity fields in a carbon electrode array. Chapter 4 details the experimental validation of using carbon-DEP devices for cell sorting. Chapter

5 presents the integration of carbon-DEP devices and centrifugal microfluidics and the validation on the use of the resultant platform in DEP applications.

## CHAPTER 1. Background

### 1.1 Dielectrophoresis

Dielectrophoresis (DEP) enables the selective manipulation of a targeted particle, or population of particles, using the interaction of a non uniform electric field with the induced effective dipole moment of the particle(s)<sup>9</sup>. DEP is advantageous over other particle separation techniques such as FACS (Fluorescence-activated cell sorting) and MACS<sup>®</sup> (Magnetic-activated cell sorting) because discrimination between different particles is based solely on their intrinsic physical properties, *i. e.*, membrane morphology and internal compartmentalization in the case of cells, and not on external tags. These physical properties determine the particle's dielectric properties and give it a characteristic dielectric phenotype. Therefore, the use of DEP eliminates functionalized magnetic beads or fluorophores required by other separation techniques such as magnetophoresis and flow cytometry. The elimination of the often expensive labels reduces assay complexity, time and costs which can expand the availability of diagnostic tests, such as for HIV, and make therapies for cancer or degenerative diseases available to a broader number of patients.

#### 1.1.1 Historical overview

Dielectrophoresis was first described by Pohl back in 1951<sup>1</sup>. His work is described in his 1978 book “Dielectrophoresis”<sup>2</sup>. However, significant work on DEP only came with the advent of microfabrication techniques. The know-how and the wider availability of tools to fabricate closely-spaced microelectrodes allowed for the generation of electric field gradient magnitudes that could be used for DEP using only tens of volts. Pethig,

Gascoyne and collaborators generated an explosion on DEP-related journal articles throughout the 1990s. Selected examples include the separation of latex particles<sup>3</sup>, the separation of viable and non viable yeast cells<sup>4,5</sup>, the characterization of microorganisms<sup>6,7</sup> and virus<sup>8</sup>, the purification of blood and bone marrow from cancer cells<sup>9,10</sup> and the enrichment of stem cell populations<sup>11,12</sup>. Other pioneers include Morgan and Green<sup>13</sup>, Fuhr<sup>14,15</sup>, Zimmermann<sup>16</sup> and Jones<sup>17</sup>. DEP became mainstream in the 2000s and separation of many different particles including virus<sup>18</sup>, DNA<sup>19</sup> and many other different cells was reported<sup>20</sup>. Alternatives to traditional planar metal electrodes also emerged in the 2000s and include 3D electroplated-metal electrodes<sup>21,22</sup>, insulator-based DEP<sup>23,24</sup>, the use of “liquid electrodes”<sup>25</sup>, the use of doped-silicon electrodes<sup>26</sup> and of course the use of glass-like carbon as it will be detailed in this work. Table 1.1 resumes the capability to manipulate a wide variety of cells using DEP. A given cell type may have been manipulated by authors other than those presented here, especially in the cases of yeast cells, *e.coli* and latex particles. An excellent review on DEP fundamentals and the use of DEP in diagnostics is by Gascoyne and Vykoukal<sup>19</sup>. Excellent book references include those by Jones<sup>17</sup>, Morgan and Green<sup>13</sup> and Hughes<sup>27</sup>.

**Table 1.1** Selected examples of cell manipulation using DEP

Year	Particles	Electrodes		Reference
		Material	Type	
1992	Cellulose spheres, pollen interior, pollen membrane and sporoderm, Cellulose spheres, pollen of <i>Pinus sylvestris</i>	Cr/Au	planar	28
1992	Friend murine erythroleukaemia (DS19)	Au	planar	29
1994	HL-60 leukaemia cells, human blood cells	-	-	30
1995	CD34+	Au	planar	31
1995	<i>Festuca arundinacea</i> , <i>micrococcus luteus</i>	Au	planar	32
1997	Red Blood Cells (RBC), T-lymphocyte, Hepatocyte, DS19, HL-60, MDA-231, MDA-435, MDA-468	-		33
1998	Protoplast	Cr/Au, ITO (Indium Tin Oxide)	planar	34
1999	Carboxyl modified latex spheres (216, 282 and 557 nm diameter), Tobacco mosaic virus, Herpes simplex virus	Ti/Pd/Au	planar	35
2000	Trophoblast cells and mixed peripheral blood mononuclear cells	Ti/Pd/Au	planar	36
2001	Cortical neurons from rat fetuses	Au	planar	37
2002	Normal and <i>Babesia bovis</i> infected erythrocytes	Pt	planar	38
2002	Polystyrene beads, HL-60 cells	Au	3D	21
2003	<i>Escherichia coli</i> strain K12,	Cr	planar	39
2004	Bovine pulmonary arterial endothelial cells, NIH/3T3 fibroblasts	Au (fibronectin covered)	planar	40
2004	Neurons, Glial cells	Pt	planar	41
2004	Normal and Parasitized (Malaria) erythrocytes	Cu	planar	42
2005	B-lymphocytes, T-lymphocytes, CD34+, Granulocytes, Monocytes	Au	planar	43
2005	Yeast cells	p-type heavily doped Si	3D	44
2006	U-937 human lymphoma cells	Au	planar	45
2006	Polystyrene microbeads and HEK293 cells	Au	3D	46
2008	Mouse fetal-derived NSPCs (neurons and astrocytes) Mouse neuroblastoma cells (N115) Human embryonic kidney cells (293 cells)	Au	planar	47
2008	Insulinoma cells (BETA-TC-6 and INS-1)	ITO	planar	48
2008	Small cell lung cancer cells (NCI-H69)	Au	planar	49
2009	Human breast cancer epithelial cells (MCF 7), healthy breast cells (MCF 10A)	Cr/Au	planar	50
2009	Leucocytes (neutrophils, eosinophils)	Pt	planar	51
2009	MDA-MB-435, MDA-MB-468 and MDA-MB-231	Cu/Au	planar	52
2009	RBC, <i>staphylococcus Aureus</i>	Cr/Au	planar	53
2009	DS19 erythroleukemia cells	Cu/Au	planar	54
2010	Mouse hybridoma 3-2H3 cells, MDCK cells of Dog Kidney	W	planar	55

2010	Endothelial progenitor cells (EPCs), white blood cells (Jurkat Cells)	Au	planar	56
2010	HCT116 colorectal cancer cells, Human Embryonic Kidney 293 cells (HEK 293) and Escherichia coli (E. coli)	ITO	planar	57
2010	Alpha-fetoprotein (AFP) carcinoembryonic antigen (CEA)	ITO	planar	58
2010	B16F10 cells (Mouse melanoma lung cells)	Ti/Cu	planar	59
2010	THP-1 human leukemia cells	PDMS (iDEP)	3D	60
2010	Polystyrene beads (8 and 25 $\mu\text{m}$ ) and HepG2 (Human Liver Cells)	Ti	planar	61

### 1.1.2 Theory

The dielectrophoresis force  $F_{DEP}$  on a spherical particle of radius  $r$  in a medium  $m$  is given by:

$$F_{DEP} = 2\pi\epsilon_m r^3 \text{Re}[f_{CM}] \nabla |E_{rms}^2| \quad (1.1)$$

with

$$\text{Re}[f_{CM}] = \frac{\epsilon_p^* - \epsilon_m^*}{\epsilon_p^* + 2\epsilon_m^*} \quad (1.2)$$

where  $r$  denotes the radius of the particle,  $\nabla E$  the magnitude of the electric field gradient,  $\epsilon_p^*$  the complex permittivity of the particle and  $\epsilon_m^*$  of the media. Complex permittivity  $\epsilon^*$  is given by:

$$\epsilon^* = \epsilon - \frac{j\sigma}{2\pi f} \quad (1.3)$$

and depends on the permittivity  $\epsilon$  and conductivity  $\sigma$  of the particle or the media and the frequency  $f$  of the applied electric field. The imaginary number  $\sqrt{-1}$  is represented by  $j$ . A non uniform electric field is necessary to induce a DEP force as stated in equation 1.1 (otherwise  $\nabla E = 0$ ). The magnitude of the induced DEP force on a particle with fixed radius  $r$  is proportional to the absolute value of  $\text{Re}[f_{CM}]$  and the magnitude of the electric

field gradient squared. Positive values of  $Re[f_{CM}]$ , see equation 1.2, for a given particle denote the induction of a DEP force that causes it to migrate towards regions with an electric field gradient magnitude (positive DEP) while negative values of  $Re[f_{CM}]$  denote the opposite behavior with particles moving towards regions of no electric field gradient (negative DEP). The polarity of  $Re[f_{CM}]$  is given by the difference between the complex permittivity of the media and that of the cell. The use of a suspending media with high conductivity usually leads to a complex permittivity that is significantly higher than that of the cell and negative DEP is always induced on the cells when using a frequency within the range from DC up to several tens of MHz. Positive DEP is only obtained when the complex permittivity of the cell is higher than that of the media. The complex permittivity of the cell is determined by its dielectric phenotype. Such phenotype is determined by the cell membrane properties (surface area, thickness), volume, endoplasmic reticulum (if well developed), nuclear size (if reasonably large in proportion to the total cell size), cytoplasmic ion content and ion mobility in the cytoplasm. A shell model is used to model such complex dielectric properties of cells<sup>4</sup>. The number of shells depends on the physical properties of the real cell and may include one or several shells. For example, mammalian cells are usually modeled as one-shell model to account for a cell membrane containing a cytoplasm. Plant cells and certain microorganisms are modeled using a two-shell model to account for the presence of a cell wall enclosing the membrane and the cytoplasm. A double shell model may also be used when the nucleus size is more than 50% of the space inside the cell<sup>62</sup>. For molecules and very small particles in low conductivity media, the volume of the conductive double layer created at the interface of the particle boundary and the conductive media is comparable to or larger

than the particle itself, and the properties of this region are used to determine the AC electrokinetic response of the particle. In fact, the DEP responses of molecules are so completely dominated by the charge double layer that discrimination between subtly different molecules is near impossible. DEP forces exerted over molecular size particles are always positive and are far more dependent on the solution conditions than on structural aspects of the biomolecules<sup>63</sup>.

### **1.1.3 Electrode types and materials commonly used in DEP**

The implementation of a dielectrophoresis force on a sample requires a non uniform electric field across the sample (equation 1.1). This non uniform field creates volumes of different electric field magnitudes across the sample where particles can be selectively positioned according to their dielectric phenotype and different experimental parameters. Most of the work in DEP relies on the use of metal microelectrodes contained in a flow channel to induce such non uniform electric field in the sample. However, the use of metal microelectrodes in direct contact with the sample severely restricts the magnitude of the applied voltages as one must prevent sample electrolysis. Moreover, the fabrication of metal electrodes, especially when dealing with 3D electrodes rather than planar (2D) electrodes, quickly turns relatively complicated and expensive. For example, the use of 3D metal electrodes (e.g., a set of high-aspect ratio posts) requires the use of metal electroplating that often restricts high yields and may result in more expensive devices. Examples of DEP work with electroplated gold structures are the works by Wang et al.<sup>64</sup>, who incorporates the 3D electrodes in the side-walls of a microfluidic channel and uses DEP to focus a stream of particles, and by Voldman et al.<sup>21</sup>, who implements a cell interrogation site for flow cytometry applications by using DEP to trap cells in between

3D electrodes. An alternative to the use of metal microelectrodes as detailed above is to use arrays of insulator structures, usually fabricated from polymers or glass, to locally distort the electrical field. In this technique, known as insulator-based dielectrophoresis or iDEP<sup>23,65-67</sup>, metal electrodes (for example extruded wire rods or machined metal plates) positioned outside the flow channel are used to set up the field over the insulator structures. A voltage as high as thousands of volts is applied to the metal electrodes to generate a uniform electric field that is rendered non uniform in the vicinity of the insulator structures. When using this technique, the sample is usually contained in the insulator array and the possibility of electrolyzing the sample is minimized. However, iDEP requires very high voltages (electric field magnitude is inversely proportional to the gap between electrodes and in iDEP the separation between metal electrodes can be in the order of centimeters) to create a suitable electric field for dielectrophoresis.

The use of 3D structures that cover most of the height of a flow channel greatly improves filter throughput by reducing the mean distance of any particle to the closest electrode surface. This is in contrast to the filter throughput achieved when using 2D (planar) electrodes positioned at the bottom of a flow channel where many targeted particles immersed in the bulk volume of the channel do not come close to the electrical field gradient surrounding the planar electrodes and cannot get trapped as illustrated in Fig. 1.1. The use of 3D electrodes reduces or eliminates the number of re-flow cycles that are required to improve filter throughput when using 2D electrodes. The advantage of using 3D over 2D electrodes is experimentally proven in this work (chapter 4). Previous work on 3D electrodes includes that by Wang et al.<sup>22,64</sup> and Voldman et al.<sup>21</sup> who used electroplated gold structures to induce DEP on cells; that by Iliescu et al.<sup>44,68,69</sup> who used

doped-silicon structures to trap cells using DEP and most of the work in iDEP done by Cummings, Lapizco-Encinas, Davalos and collaborators to sort a variety of cells, proteins and microorganisms<sup>66,67,70,71</sup>. Table 1.2 resumes the advantages and disadvantages of common electrodes used to create a DEP force. The comparison of these electrodes to the use of glass-like carbon electrodes is also presented.

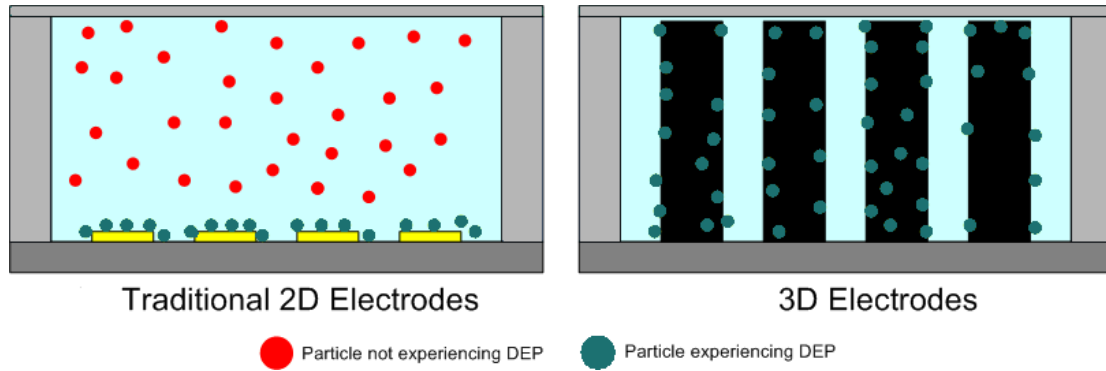


**Fig. 1.1** Comparison between the use of 2D and 3D electrodes

**Table 1.2** Common electrodes used in DEP compared to glass-like carbon electrodes in terms of their advantages and disadvantages

Material	Type	Advantages	Disadvantages
Evaporated metal	2D	easy fabrication, uses low voltage	low throughput, sample electrolysis
Electroplated gold	3D	high throughput, uses low voltage	expensive, fabrication yield, sample electrolysis
Insulator-based (glass, plastics)	2D, 3D	high throughput, eliminates sample electrolysis, amenable for injection molding	need for high voltage
Glass-like carbon	2D, 3D	relatively easy fabrication, high throughput, minimizes sample electrolysis, requires tens of volts only	currently opaque substrate (silicon), carbon is not ideal conductor

### 1.1.5 Glass-like carbon as an alternative electrode material for DEP

Several allotropes of carbon exist including diamond, graphite, lonsdaleite, buckminsterfullerene, graphene and glass-like carbon to name a few (for a complete overview of carbon allotropes the reader is referred to Martinez-Duarte et al.<sup>72</sup>). The physical properties of carbon vary widely with the allotropic form. For example, diamond is highly transparent while graphite is opaque and black. Here the focus is on the patterning of glass-like carbon for the fabrication of micro electrodes. Glass-like carbons are amorphous materials derived through the carbonization, or pyrolysis, of organic polymers in inert atmospheres. The resultant carbon has a glass-like appearance in the sense that is smooth, shiny and exhibits a conchoidal fracture<sup>1</sup> [30]. Because of its appearance, glass-like carbon has also been referred as “vitreous carbon” or “glassy carbon”<sup>2</sup>. The use of glass-like carbon electrodes in dielectrophoresis combines the advantages of metal-based DEP and insulator-based DEP (iDEP) and yields some other key benefits that make carbon-DEP an alternative to current DEP techniques. For example, the possibility of sample electrolysis is reduced with the use of carbon electrodes, an advantage shared with iDEP, while low voltages are enough to polarize the

---

<sup>1</sup> Some crystals do not usually break in any particular direction, reflecting roughly equal bond strengths throughout the crystal structure. Breakage in such materials is known as fracture. The term conchoidal is used to describe fracture with smooth, curved surfaces that resemble the interior of a seashell; it is commonly observed in quartz and glass. Conchoidal fracture. (2009). In Encyclopaedia Britannica. Retrieved April 08, 2009, from Encyclopaedia Britannica Online: <http://www.britannica.com>

<sup>2</sup> Although glass-like carbon is similar to vitreous carbon and glassy carbon, the IUPAC (International Union of Pure and Applied Chemistry) suggested the use of the term glass-like carbon over glassy or vitreous carbon as the latter ones have been previously introduced as trademarks<sup>73</sup>. Fitzer, E., Kochling, K. H., Boehm, H. P., and Marsh, H., Recommended Terminology for the Description of Carbon as a Solid, *Pure and applied chemistry* 67 (3), 473-506, 1995.

carbon electrodes and create an electrical field suitable for DEP, an advantage shared with metal-electrode DEP. The possibility of sample electrolysis is minimized when using carbon electrodes because carbon has a much wider electrochemical stability window than metals commonly used in thin film electrode fabrication such as gold and platinum and affords higher applied voltages in a given solution without electrolyzing it<sup>74</sup>. Even though the electrical conductivity of glass-like carbon is lower than that of metals (more details under electrical characterization in chapter 2), suitable electric fields for DEP can be generated by polarizing carbon electrodes with voltages in the range of tens of volts instead of the hundreds or thousands of volts between metal plates required in iDEP. The use of carbon electrodes yields other benefits as well. Glass-like carbon is chemically very inert in almost all solvents/electrolytes. Remarkably, it withstands attack from strong acids such as nitric, sulfuric, hydrofluoric or chromic and other corrosive agents such as bromine. Even though it reacts with oxygen it only does so at high temperatures and with an oxidation rate that is lower than those of any other carbon form<sup>75</sup>. Glass-like carbon has good mechanical properties: a hardness of 6 to 7 on Mohs' scale, a value comparable to that of quartz and a Young's Modulus in the range from 10 to 40 GPa (compare to 200 GPa of stainless steel)<sup>76</sup>. Thermally, it features a coefficient of thermal expansion of  $2.2\text{-}3.2 \times 10^{-6} \text{ K}^{-1}$ , similar to that of some borosilicate glasses, and thermal conductivity less than  $1 \text{ W mK}^{-1}$ . Carbon is the building block of nature and thus glass-like carbon has excellent biocompatibility that enables its use in a variety of implants<sup>77-79</sup> and as a preferred substrate for cells to grow<sup>80</sup>. Glass-like carbon has a density that ranges from 1.4 to about  $1.5 \text{ g/cm}^{-3}$ , compared to  $2.3 \text{ g/cm}^{-3}$  for graphite,

which suggests a significant degree of porosity. X-ray diffraction studies show that glass-like carbon presents a closed pore nature with size  $<1 \text{ nm}$ <sup>81,82 83,84</sup>.

## **1.2 Glass-like carbon and Carbon MEMS**

### **1.2.1 Historical overview**

Glass-like carbon appears to be first derived in 1915 by Weintraub and Miller<sup>85</sup>. However, a sustained flow of publications did not begin until the early 1960s when independent groups from Japan and England first disclosed the properties and methods of derivation of the novel carbon allotrope<sup>86,87</sup>. Its unique properties have been beneficial to various applications along the years. Initially, its extreme chemical inertness and gas impermeability were exploited to fabricate laboratory equipment such as beakers, basins and boats<sup>75</sup>. Since glass-like carbon is not wetted by a wide range of molten metals, it is an ideal material for the fabrication of crucibles with applications in metallurgical and chemical engineering<sup>88</sup>. Its resistance to erosion and high melting point makes it an ideal material for mandrels, steam, fuel and rocket nozzles and other equipment in mechanical and electrical applications. Moreover, glass-like carbon has been used in heart valve implants and other biomedical devices thanks to its biocompatibility<sup>79,89-91</sup>. “Glassy” carbon electrodes have become so popular that they represent a significant fraction of the multi-billion electrochemistry market.

From the microfabrication standpoint, glass-like carbon microstructures were not reported until the late 1990s by Schueller and co-workers at Harvard University. In their process, polydimethylsiloxane (PDMS) molds were fabricated using soft lithography and then used to pattern furfuryl alcohol-modified phenolic resins and phenol-formaldehyde

resins, which were subsequently carbonized<sup>92-94</sup>. This fabrication technique allowed them to work with flat or curved surfaces and derive different structures (including free-standing lateral comb drives, diffraction gratings and grids) with dimensions as small as a few micrometers and featuring high aspect ratios if desired. Microelectromechanical functions were also demonstrated<sup>95</sup>. During the same decade, initial work on the derivation of carbon from photoresists emerged in the quest for alternatives to carbon films produced by physical deposition techniques. The interest was driven by the use of pyrolyzed photoresists in batteries, electrochemical sensors, capacitors and MicroElectroMechanical Systems (MEMS). Electrochemical studies of carbon films derived from positive photoresists were conducted in 1998 by Kim et al. in Berkeley, CA<sup>96</sup> and later by Ranganathan et al.<sup>97</sup> at Ohio State University (OSU). By 2000, Kostecki and co-workers patterned these carbon films as microelectrodes and studied the influence of the geometry in their electrochemical response<sup>98</sup>. Pyrolyzed Photoresist Films still derived from positive resists were surface-characterized in 2001 and determined to have a near-atomic flatness<sup>99</sup>. The resultant carbon showed an electrochemical behavior similar to glass-like carbon although with decreased surface roughness. In 2002 the derivation of carbon from negative photoresists was reported by Singh et al. at OSU<sup>100</sup>. They used SU-8, a relatively new epoxy-based photoresist at that time<sup>101</sup>, and polyimide to fabricate circular patterns. The carbon obtained with this precursor showed higher resistivity and vertical shrinkage than the one synthesized from positive resists. Furthermore, the carbon derived from SU-8 showed higher vertical shrinkage and poorer substrate adhesion than that from polyimide. Nevertheless, resistivity from SU-8 carbon was slightly lower than polyimide's<sup>100</sup>. In 2005, structures with aspect ratios higher than 10 were reported by

Wang et al. at the University of California, Irvine (UCI)<sup>74</sup>. A variety of complex high-aspect ratio structures, such as posts, suspended carbon wires, bridges, plates, self organized bunched posts and networks, were built this way. Continuous work on carbon micro and nanostructures has been conducted since 2004 by the same group at UCI and collaborators in a variety of applications including Lithium-ion batteries<sup>102-104</sup>, fuel cells<sup>105,106</sup>, electrochemical sensors<sup>107</sup>, cell culturing substrates<sup>80</sup>, dielectrophoresis<sup>108-110</sup>, micromolding<sup>111,112</sup> and fractal electrodes<sup>113,114</sup>. Other groups have also recently integrated carbon structures for their use in gas sensors<sup>115</sup>.

### **1.2.2 Carbon MEMS**

Carbon-MEMS (or C-MEMS) can be defined as the set of methods that can be used to derive glass-like carbon structures from patterned organic polymers, featuring dimensions ranging from hundreds of micrometers down to tens of nanometers. C-MEMS combines different polymer micro and nanofabrication techniques with pyrolysis to derive glass-like carbon features. These polymer fabrication techniques include stamping, casting, machining and photolithography. The choice of each technique is dictated by the quality, complexity and final dimensions of the desired carbon part. In this regard, the incorporation of photolithography to the C-MEMS toolbox enabled a more precise control on the dimensions and complexity of the precursor polymer structures. The existence of commercial high-quality precursors and standardized photolithography tools make the fabrication process and the dimensional control highly reproducible. The advent of Next-Generation Lithography (NGL) techniques, such as electron beam lithography

(EBL), nanoimprint lithography (NIL) and focused-ion beam (FIB), will further reduce the dimensions and greatly increase the intricacy of the resulting carbon structures.

### **1.2.3 Carbon derivation**

Carbonization is the process by which solid residues with a high content of carbon are obtained from organic materials, usually by pyrolysis in an inert atmosphere<sup>73</sup>. Different precursors to obtain glass-like carbon may be used, including phenolic resins, polyfurfuryl alcohols, cellulose, polyvinyl chloride and polyimides<sup>76,116-122</sup>. Different degrees of shrinkage and carbon yield (the ratio of the weight of carbon to the weight of the original polymer sample) are obtained during carbonization depending on the precursor used. Phenol-formaldehyde, polyfurfuryl alcohol and polyvinyl alcohol have the highest yields, with an approximate 50% carbon<sup>117</sup>. Novolac resins, or acid-catalyzed phenol formaldehyde resins, are commonly used as photoresists and have recently become the material of choice to derive carbon structures featuring micro and nano dimensions. Their volume shrinkage varies from 50 to 90%<sup>74,97,100,123</sup>. As with all pyrolytic reactions, carbonization is a complex process with many reactions taking place concurrently, including dehydrogenation, condensation, hydrogen transfer and isomerization<sup>124-130</sup>. The pyrolysis process of organic compounds can be divided into three major steps: pre-carbonization, carbonization and annealing. During pre-carbonization ( $T < 573$  K) molecules of solvent and unreacted monomer are eliminated from the polymeric precursor. The carbonization step can be further divided into two stages. From 573 to 773 K (300 to 500 °C), heteroatoms such as oxygen and halogens are eliminated causing a rapid loss of mass while a network of conjugated carbon systems is formed. Hydrogen atoms start being eliminated towards the end of this stage. The second

stage of carbonization, from 773 to 1473 K (500 to 1200 °C), completely eliminates hydrogen, oxygen and nitrogen atoms and forces the aromatic network to become interconnected. At this point, permeability decreases and density, hardness, Young's modulus and electrical conductivity increase. Sulfur does not evolve until even higher temperatures (> 1800 K), and certain metallic impurities, e. g. iron, may even require a leaching process to be eliminated. The final step, annealing, is carried out at temperatures above 1473 K , allowing to gradually eliminate any structural defects and evolve further impurities. The final pyrolysis temperature determines the degree of carbonization and the residual content of foreign elements. For instance, at T ~ 1200 K the carbon content of the residue exceeds a mass fraction of 90% in weight , whereas at T ~ 1600 K more than 99% carbon is found<sup>128,131</sup>. Glass-like carbon is characterized as a type of char<sup>3</sup> and is classified as a non-graphitizable, or non-graphitizing, carbon. It is important to mention that glass-like carbon is usually derived from thermosetting resins which do not melt during the carbonization process but rather maintain their shape along the process. Glass-like carbon does not graphitize even when heat treated at 3273 K (3000 °C). The inability of the graphitic planes to grow and stack parallel to each other even at high temperatures is due to the entangled nature of glass-like carbon structure. The most widely known and accepted model is the one that considers this type of carbon as made up of tangled and wrinkled aromatic ribbon molecules that are randomly cross-linked by carbon-carbon covalent bonds. The ribbon molecules form a networked structure, the unit of which is a

---

<sup>3</sup> Char is a solid decomposition product of a natural or synthetic organic material. If the precursor has not passed through a fluid stage, char will retain the characteristic shape of the precursor (although becoming of smaller size). For such materials the term "pseudomorphous" has been used. In contrast, coke is produced by pyrolysis of organic materials that have passed, at least in part, through a liquid or liquid-crystalline state during the carbonization process.

stack of high strained aromatic ribbon molecules. Such structure of crystallites reflects the features of thermosetting resins structure which are commonly used as precursors for glass-like carbons. This model explains the most experimental results obtained so far on glass-like carbons including its impermeability, brittleness and conductivity<sup>81,82</sup>.

#### **1.2.4 Carbon MEMS using SU-8 Photolithography**

The carbon electrodes presented in this work were fabricated using the Carbon MEMS (C-MEMS) technique with SU-8 as the organic precursor. Photolithography was used to pattern the electrodes. Photolithography refers to the use of light to pattern a substrate. Due in part to its heavy use by the Integrated Circuits (IC) industry, UV photolithography is the most widely used form of lithography. SU-8 is an acid-catalyzed negative photoresist<sup>4</sup>, made by dissolving EPON<sup>®</sup>-SU-8 resin (a registered trademark of Shell Chemical Company) in an organic solvent such as propylene glycol methyl ether acetate (PGMEA), cyclopentanone or gamma-butyrolactone (GBL) and adding up to 10 wt% of triarylsulfonium hexafluoroantimonate salt as a photoinitiator. Commercial formulations also include 1-5% propylene carbonate. In a chemically amplified resist like SU-8, one photon produces a photoproduct that in turn causes hundreds of reactions to change the solubility of the film. Since each photolytic reaction results in a “amplification” via catalysis, this concept is dubbed “chemical amplification”<sup>132</sup>. The viscosity of the photoresist, and hence the range of thicknesses accessible, is determined by the ratio of

---

<sup>4</sup> If the photoresist is of the type called negative (also negative tone), the photochemical reaction strengthens the polymer, by random cross-linkage of main chains or pendant side chains, thus becoming less soluble. If the photoresist is of the type called positive (also positive tone), the photochemical reaction during exposure of a resist weakens the polymer by rupture or scission of the main and side polymer chains, and the exposed resist becomes more soluble in developing solutions. In other words, in negative photoresists light crosslinks while in positive ones light scissions.

solvent to SU-8 resin. The EPON resist is a multifunctional, highly-branched epoxy derivative that consists of bisphenol-A novolac glycidyl ether. On average, a single molecule contains 8 epoxy groups which explain the 8 in the name SU-8. The material has become a major workhorse in miniaturization science because of its low UV absorption (up to thicknesses of 2 mm), high chemical and thermal resistance and good mechanical properties that make it suitable as a structural material. For example, Abgrall et al.<sup>133</sup> fabricated SU-8 microfluidic devices with different techniques including the successive lamination and patterning of SU-8 layers on existent topographies. The use of SU-8 photoresists allows for the coating of thick layers (up to 500  $\mu\text{m}$ ) on a single spin coat, or thicker layers in multiple spin coatings, and high aspect ratio structures with nearly vertical side walls. SU-8 cross-linking starts upon the irradiation of the photoresist. In the exposed areas, the photoinitiator decomposes to form hexafluoroantimonic acid that protonates the epoxides on the oligomer. These protonated oxonium ions are in turn able to react with neutral epoxides in a series of cross-linking reactions after application of heat. In other words, irradiation generates a low concentration of a strong acid that opens the epoxide rings and acts as a catalyst of the chemically amplified cross-linking process that gets further activated by the application of heat.

Based on discoveries in the late 1970s by Crivello and Lam at General Electric<sup>134-136</sup>, scientists at IBM discovered that certain photo-initiators, such as onium salts, polymerize low-cost epoxy resins such as EPON<sup>®</sup>-SU-8. Compositions of SU-8 photoresist were patented by IBM as far back as 1989<sup>137</sup> and 1992<sup>138</sup>. Originally, SU-8 was intended for printed circuit board and e-beam lithography but it is now used in a wide variety of other processes. In view of its many advantages over available UV photoresists, including the

fabrication of high aspect ratio MEMS features, different formulations of SU-8 photoresists began to be commercialized by MicroChem ([www.microchem.com](http://www.microchem.com)) in 1996 (see Table 1.3). Gersteltec has recently entered the market ([www.gersteltec.ch](http://www.gersteltec.ch)) with novel SU-8 compositions that include dyes and silica or silver nanoparticles. Some of the most important SU-8 properties are listed in Table 1.4. Data sources for the SU-8 properties listed here (and many more) can be found in Chollet<sup>139</sup> and Guerin<sup>140</sup>.

**Table 1.3** Viscosity, percentage of solids and density of different SU-8 photoresist formulations available from MicroChem

SU-8 casting solvent: gamma-butyrolactone				SU-8 2000 casting solvent: cyclopentanone				SU-8 3000 casting solvent: cyclopentanone			
	$\mu$ (cSt)	%sol	$\rho$ (g/ml)		$\mu$ (cSt)	%sol	$\rho$ (g/ml)		$\mu$ (cSt)	%sol	$\rho$ (g/ml)
				2000.5	2.49	14.3	1.070				
2	45	39.5	1.123	2002	7.5	29	1.123				
5	290	52	1.164	2005	45	45	1.164	3005	65	50	1.075
				2007	140	52.5	1.175				
10	1050	59	1.187	2010	380	58	1.187	3010	340	60.4	1.106
				2015	1250	63.45	1.2				
25	2500	63	1.200	2025	4500	68.55	1.219	3025	4400	72.3	1.143
				2035	7000	69.95	1.227	3035	7400	74.4	1.147
50	12250	69	1.219	2050	12900	71.65	1.233	3050	12000	75.5	1.153
				2075	22000	73.45	1.236				
100	51500	73.5	1.233	2100	45000	75	1.237				
				2150	80000	76.75	1.238				

Note:  $\mu$  equals viscosity, %sol equals percentage of solids and  $\rho$  equals density

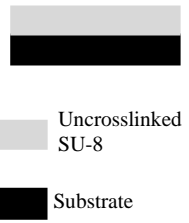
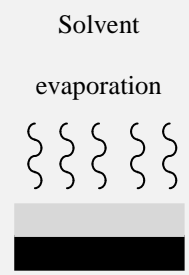
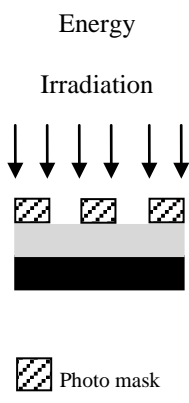
**Table 1.4** Selected SU-8 properties

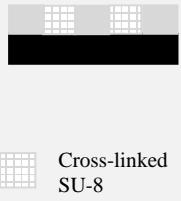
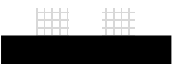
Young's modulus	4.02 - 4.95 GPa
Poisson ratio	0.22
Friction coefficient	0.19
Glass temperature ( $T_g$ )	50 – 55 °C un-cross-linked > 200 °C cross-linked
Degradation temperature ( $T_d$ )	~ 380 °C
Boiling point	204 °C
Coefficient of thermal expansion (CTE)	52 $10^{-6}$ /K
Thermal conductivity	0.2 W/m K
Specific heat	1500 J/kg K
Vapor pressure	0.3 mmHg at 20 °C
Density (of EPON <sup>®</sup> SU-8 resin)	1200 kg/m <sup>3</sup>
Refractive index	1.668 un-cross-linked 1.67 – 1.8 cross-linked
Dielectric constant	4 – 4.5 $\epsilon_0$
Electrical breakdown fields	~ $10^7$ V/m
Resistivity	> $10^8$ $\Omega$ cm

SU-8 photolithography generally involves a set of basic processing steps: photoresist deposition, soft bake, exposure, post-exposure treatment and developing. De-scumming and post-baking might also be part of the process. A detailed resume of all the possible SU-8 photolithography steps is presented in Table 1.5. When patterned at 365 nm, the wavelength at which the photoresist is the most sensitive, total absorption of the incident light in SU-8 is reached at a depth of 2 mm. In principle, resist layers up to 2 mm thick can be structured <sup>141</sup>. Yang and Wang recently confirmed this astounding potential experimentally <sup>142</sup> by fabricating structures with aspect ratios above 190 (for features with a 6  $\mu\text{m}$  thickness and a height of 1150  $\mu\text{m}$ ). Aspect ratios greater than ten are routinely achieved with SU-8. Aspect ratios up to 40 for lines and trenches have been demonstrated in SU-8-based contact lithography <sup>143-145</sup>.

For a more thorough review on the fundamentals of photolithography and its use to pattern other resists the reader is referred to Madou<sup>146</sup>. The reader is also encouraged to consult SU-8 photolithography reviews by del Campo et al. <sup>147</sup> and Abgrall et al.<sup>133</sup>.

**Table 1.5** SU-8 photolithography processing steps

Process Step	Process Description	Processing Parameters	Remarks
<p><b>Photoresist Deposition</b></p>  <p>Uncrosslinked SU-8</p> <p>Substrate</p>	<p>Photoresist is deposited on a clean substrate. Substrate materials include glass, Si, quartz, polymers, etc. Different deposition techniques exist but spin coating is the most common</p>	<p>Spin time, speed and acceleration when using spin coating. Layer thickness is inversely proportional to spin time, speed and acceleration</p>	<p>Layer thicknesses from a few micrometers to hundreds of micrometers (~ 500 μm) are possible in a single coat                      Long spin times at a given speed yield better layer uniformity                      Accumulation of resist on the substrate edges during spin coating causes ridges (known as edge beads) and can be removed with commercial solutions or acetone                      Lamination and casting are alternatives to spin coating to deposit layers thicker than 500 μm</p>
<p><b>Soft Bake or Pre-bake</b></p>  <p>Solvent evaporation</p>	<p>Casting solvent is evaporated from the photoresist. SU-8 does not flow at room temperature after a proper soft bake. The glass transition temperature of SU-8 resist at this point, in the un-cross-linked state, is 55 °C</p>	<p>Temperature and time. Soft bake temperature is usually 95 °C. Times can be as short as a couple of minutes (layers &lt;5 μm-thick) or as long as hours (layers &gt; 200 μm-thick)</p>	<p>The use of a hotplate is recommended to avoid <i>skin effects</i>. Baking the photoresist layer in convection ovens evaporates the solvent present on the top surface of the photoresist first, hardens the surface and hinders the evaporation of solvent from the bulk of the photoresist                      Elevated temperatures (&gt;120 °C) during soft bake can activate resist polymerization and reduce contrast                      A sufficient amount of residual solvent in the soft-baked resist allows the polymer matrix to relax more and thus minimizes the residual stress which otherwise can cause pattern debonding from the substrate at the end of the photolithography process</p>
<p><b>Exposure</b></p>  <p>Energy Irradiation</p> <p>Photo mask</p>	<p>Irradiation from an energy source generates a low concentration of a strong acid that opens the epoxide rings of the resist and acts as a catalyst of the chemically amplified cross-linking reaction</p>	<p>Exposure dose. This value is also known as energy dose and is given by the product of the source power intensity times the exposure time. In practice, the power intensity of the source is usually fixed and the energy dose can be varied by changing the exposure time</p>	<p>Energy sources include extreme, deep and near ultra-violet (UV) lights, x-rays and ion and electron beams                      SU-8 is commonly exposed using light in the near UV range (including the i-line (365 nm) and g-line (435 nm) of a mercury lamp). In this case, the use of a filter to eliminate light wavelengths below 360 nm is recommended to minimize <i>T-topping</i>, or an exaggerated negative slope of the structure walls                      Multi-level topographies can be fabricated in one exposure step using <i>gray tone masks</i> or <i>software masks</i>                      Photoresist can be exposed through the substrate (known as back-side exposure) if the substrate has a low UV-absorption coefficient. This approach yields structure walls with shallow, positive slopes that prove ideal in molding applications</p>

<p><b>Post Exposure Bake</b></p>  <p>Cross-linked SU-8</p>	<p>The cross-linking process activated during exposure gets further activated by the application of heat. SU-8 is fully polymerized after a proper post exposure bake. The glass transition temperature of cross-linked SU-8 is above 200 °C</p>	<p>Temperature and time. More than time, PEB temperature is of crucial importance. A two-step post-exposure bake (at 65 °C and 95 °C for different times) is recommended by MicroChem but temperatures between 55 and 75 °C and extended baking times have been suggested to minimize internal stresses in the pattern</p>	<p>The precise control of PEB times and temperatures critically determines the quality of the final features  Insufficient PEB times and/or temperatures that are too low yield structures that are not completely cross-linked and can be attacked by the developer  Temperatures below 55 °C do not polymerize the matrix completely regardless of the bake time  Thermal stresses increase with resist thickness and can cause cracking of the pattern's surface, structure bending or complete peeling from the substrate in the worst cases  The use of a substrate material with a coefficient of thermal expansion similar to that of SU-8 can minimize thermal stresses in the pattern</p>
<p><b>Develop</b></p> 	<p>Un-polymerized SU-8 dissolves upon immersion in a developer agent such as Propylene Glycol Methyl Ether Acetate (PGMEA)</p>	<p>Time and agitation rate. Development times range from few minutes (for layers thinner than 10 µm) to hours (for layers more than 400 µm-thick). Agitation is usually done manually. In this case, an approximate value for agitation rate is 60 Hz.</p>	<p>Constant agitation during development is recommended to constantly feed fresh developer to the resist pattern and decrease developing times  Care must be taken when developing high aspect ratio structures, as excessive agitation can cause mechanical breakage  Layers thinner than 2 µm are recommended to be developed by rinsing with PGMEA instead of batch immersion in the developer  Megasonic cleaning systems can be useful to develop densely packed high aspect ratio structures.</p>
<p><b>Drying</b></p>	<p>This step removes the developer. Drying methods include nitrogen blowing, spinning, freeze-drying and supercritical drying</p>	<p>Surface tension of the liquid where the SU-8 pattern is immersed in prior to drying. The replacement of PGMEA by a liquid with lower surface tension is recommended for the prevention of structure collapse during the resist drying process</p>	<p>Iso-propyl alcohol (IPA) is the most commonly used liquid to replace the developer  Stiction forces developed in narrow gaps can be strong enough to bend and join SU-8 patterns together during drying, even when using IPA  As the gap between high aspect ratio structure decreases below a few micrometers, freeze-drying and supercritical drying methods must be employed</p>

## **1.3 Centrifugal Microfluidics**

### **1.3.1 Historical overview**

The field of centrifugal microfluidics began in the late 1960s with the development of the centrifugal analyzer. The inventor, N. Anderson from Oak Ridge National Labs (ORNL), developed a clinical chemistry analyzer which incorporated a rotating disc with a multi-cuvette assembly, and a stationary optical detector designed for use with a computer. In a short time other optical technologies were incorporated to measure light transmittance, fluorescence, chemiluminescence, and light-scattering properties of several simultaneously initiated reaction mixtures. The implementation of these analysis systems helped to create new tools to develop new methods for clinical laboratory applications, including chemistry, toxicology, immunology, and hematology.

By the time Anderson published his landmark paper in 1969<sup>148</sup>, multiple companies were offering prototype versions of the centrifugal analyzer. The first commercial system was introduced by Electro-Nucleonics, Inc. in 1970. By 1981, the commercial field had grown to five companies that were offering related products: Electro-Nucleonics, Inc. offered the GEMSAEC and GEMINI; Centri Union Carbide offered the CentrifChem; American Instruments the Rotochem; Instrumentation Laboratories, Inc. offered the Multistat, and Roche the Cobas-Bio. The next phase in development of centrifugal microfluidics was in 1989 with the formation of Abaxis, Inc. who bought the patents from ORNL for their version of the clinical analyzer and began to develop it as a tool for blood analyte analysis. This represented a shift in the utilization of centrifugal microfluidics from a research-oriented tool to a diagnostic platform. In 1995, Abaxis introduced the Piccolo<sup>®</sup> rotor system which integrated sample processing steps required for analyte analysis and

incorporated self-contained reagents for each step. The Piccolo system would become the flagship for a range of blood panel products encompassing several areas of medicine.

In 1998, Madou and Kellogg from Gamera (a US startup company based on microfluidic centrifugal technology) introduced the next generation of centrifugal microfluidics as described in “The LabCD: A centrifuge-based microfluidic platform for diagnostics.”<sup>149</sup>

The paper outlined basic centrifugal theory of pumping fluids and introduced valving, mixing, sample entry and metering as basic fluidic functions on a CD. Their work represented an expansion of centrifugal technologies into new realms of biological and chemical analysis by introducing microfabrication techniques to create and merge miniaturized fluid networks and microsensors on a single disposable CD platform. This was a departure from previous efforts which relied on larger assemblies made with standard production methods and represented the first example of micro-scale features embedded on a CD. Instead of large rotors, compact discs and CD readers were used for analysis. Madou, Kellogg, and the entire Gamera team were also the first to realize that the CD platform could be used as an advanced sample-to-answer system. Even though clinical analyzers had the advantage of being able to perform high throughput assays in a short time, they often required trained technicians to carry out several steps on different machines. The LabCD offered a unique and attractive platform to overcome limitations of the macro-scale centrifugal systems of that time. It also opened up the possibility for more advanced tools to be created; if other chemistries could be retained on the CD, like antibodies necessary for ELISAs or probes necessary for DNA analysis, then applications for drug development through genomics and proteomics and molecular diagnostics and genetic testing could become possible. Gamera, later acquired by Tecan in July 2000,

would continue to develop the LabCD mainly for assays related to drug development such as ADMET – absorption, distribution, metabolism, excretion and toxicity<sup>150</sup>. Even though Tecan advanced Gamera's system significantly, Tecan discontinued their CD efforts in 2005.

The early 2000s saw a rapid development of academic and commercial endeavors to incorporate new assay designs on a CD. In this context, Kido et al. first introduced disc-based immunoassay microarrays for agriculture and environmental analysis in 2000<sup>151</sup>. In that work, a piezoelectric inkjet applicator mounted on a standard CD drive was used to apply high density microarrays of proteins on a standard CD-sized polycarbonate substrate. Competitive inhibition immunoassays were then performed with an incubation step of a fluorescent tracer on the disc followed by analysis via a fluorescence scanner. In that same year, Gyros AB was founded and would go on to commercialize a CD-based assay system that automated sandwich immunoassay processing. Their products available on the market are used today as a tool for high-throughput immunoassay analysis<sup>152</sup>. Several other companies would later adapt immunoassay technology on the CD platform in various implementations: Quadraspec developed label-free technology for identifying changes in protein arrays, while Burstein Technologies<sup>153</sup> and Advanced Array Technology<sup>154</sup> developed array methods on the disc for analyzing nucleic acids. Table 1.6 resumes selected works on the use of centrifugal microfluidics.

**Table 1.6** Selected examples of biological assays and fluidic functions performed using centrifugal microfluidics

Biological Assay	Fluidic Functions					References
	valving	decanting	mixing	metering	Sample splitting	
Whole blood processing	X	X		X		155-158*
Colormetric detection of biochemical markers	X		X	X	X	155,157*
Sample lysis and homogenization	X	X		X		159
Nucleic acid amplification	X		X			160,161
Immunoassay	X		X	X	X	152,158,162
DNA microarray hybridization	X				X	163-165
Cell culture and manipulation	X					109,166,167
Organism culture	X			X		168,169

**\*Note:** in the Abaxis system<sup>155,157</sup> both whole blood processing and colormetric detection of biochemical markers are integrated in one disk but their fluidic functions are isolated from each other. After blood processing the sample is transferred to a separate set of chambers where is split and mixed with reagents for colormetric detection

### 1.3.2 Centrifugal microfluidics in diagnostics applications

Centrifugal microfluidics has emerged as an advanced technology for biological analysis. The platform has the potential to become a standard tool for mainstream diagnostics. All steps needed to manipulate a fluid in a network, such as mixing, valving and metering of sample fluids, can be automated simply by implementing different spinning profiles. The use of microfabrication allows for the miniaturization of the network and the integration of multiple analysis steps on a single disc towards the development of microfluidic sample-to-answer systems also known as micro total analysis systems ( $\mu$ TAS)<sup>170</sup>. Another benefit of miniaturization is multiplexing; many individual assays can be run simultaneously on the same disc. Furthermore, optical systems can be developed to interface with disc-based assays and allow for the rapid identification of biological targets.

Centrifugal microfluidics platforms offer many advantages when compared to other chip-based pumping techniques. Centrifugal pumping involves a minimal amount of instrumentation, requiring only a simple and compact motor to create the forces needed for fluid manipulation. The fluid is propelled at a rate proportional to the rotation speed of the platform. Centrifugal pumping does not require external interconnects to induce fluid movement such as when using a syringe pump. This allows for the complete fluidic network (and indeed the inclusive assay or set of clinical tests) to be contained within a single disc. Since centrifugal microfluidics is usually a vented system, air bubbles are eliminated from the network. The use of centrifugal pumping is advantageous over electrokinetic methods because it does not depend on the physicochemical properties of the fluid, such as its pH or ionic strength. Since CDs can be made from inexpensive materials, like polycarbonate, and are easily mass-produced, they can be manufactured very inexpensive to enable disposable devices.

A variety of fluids have been successfully pumped using the microfluidic CD platform and include solvents, surfactants and biological fluids (*e.g.* blood, mucus, urine, milk). Many fluidic functions other than pumping have been successfully integrated on the CD platform and include valving, decanting, calibration, mixing, metering, sample splitting, and fluid separation. The automation of these functions guarantees a minimal dependence on the skill of the platform operator and reduces time and error of a given assay due to handling.

### **1.3.3 Fluidic functions in centrifugal microfluidics**

This section introduces various microfluidic functions that have been implemented on the CD for biological processing. An explanation of the individual functions serves as an

introduction to give the reader insight into how the integration of such systems enables biological processes on-CD. The complex fluid handling involved in biological assays often requires the combination of several of the functions presented below.

### ***Centrifugal pumping***

Centrifugal pumping remains the primary method of propelling fluids in a CD. As the CD spins, centrifugal forces induced on the fluid drive it outwards from the CD center toward the edge of the disc. Centrifugal flow rates depend on the rotational speed, radial location of the fluid reservoirs/channels, channel geometry, and fluidic properties (*e.g.*, viscosity, density, etc.) of a sample<sup>171,172</sup>. The flow rate  $Q$  in a micro channel featuring laminar, viscous and incompressible flow is given by the general equation:

$$Q = \frac{\Delta P}{R} \quad (1.4)$$

where  $\Delta P$  denotes a pressure gradient and  $R$  the fluidic resistance exhibited by the channel. This resistance depends on the cross section of the channel. For example, in the case of a circular cross section the Hagen-Poiseuille equation applies with  $R = 128\mu L/\pi D^4$  where  $D$  is the diameter of the channel cross-section,  $L$  is the length of the channel and  $\mu$  is the dynamic viscosity (in  $\text{Ns}\cdot\text{m}^{-2}$ ). In the case of a rectangular cross section with an aspect ratio  $\gg 1$ , the fluidic resistance  $R$  is given by<sup>173</sup>:

$$R = \frac{12\mu L}{wh^3} \quad (1.5)$$

where  $L$  is the length of the channel and  $w$  and  $h$  are the width and height of the channel cross-section respectively. The flow rate in a rectangular cross section micro channel is thus obtained as:

$$Q = \frac{\Delta P w h^3}{12 \mu L} \quad (1.6)$$

The centrifugal pressure  $P_c$  depends on the distance  $r$  from the center of rotation as:

$$\frac{\delta P_c}{\delta r} = r \rho \omega^2 \quad (1.7)$$

where  $\rho$  is the density of the fluid and  $\omega$  is the angular velocity of the centrifugal platform. Integration of Equation 1.7 from  $r_1$ , the point of the channel closest to the center of the disc, to  $r_2$ , the point of the channel furthest away from the center, results in:

$$\Delta P_c = \rho \omega^2 \bar{r} \Delta r \quad (1.8)$$

Where  $\bar{r} = (r_2 + r_1) / 2$  and  $\Delta r = r_2 - r_1$ . Plugging equation 1.8 into equation 1.6 thus yields the flow rate induced by the centrifugal force in a channel of rectangular cross section as:

$$Q = \frac{\rho \omega^2 \bar{r} \Delta r w h^3}{12 \mu L} \quad (1.9)$$

Madou and Duffy *et al.* demonstrated that the flow rates predicted by simple centrifuge theory follow well with experimentally measured flow rates<sup>174</sup>. Flow rates ranging from 5 nl·s<sup>-1</sup> to over 0.1 ml·s<sup>-1</sup> have been achieved by various combinations of rotational speed from 400 to 1600 rpm, channel widths from 20 to 500 μm, and channel depths from 16 to 340 μm. The dynamic pumping range of the CD platform extends far beyond these limits, as wider channels and higher rotation speeds are easily achieved<sup>175</sup>. Duffy *et al.*<sup>176</sup> measured flow rates of various kinds of samples including water, plasma, bovine blood, urine and polymerase chain reaction (PCR) products, and reported good agreement between experiment and theory, noting also that the centrifugal flow rates are relatively insensitive to physiochemical properties such as ionic strength, pH, conductivity, and the presence of various analytes. Thus, the microfluidic CD platform provides a unique pumping mechanism that can be controlled with precision and accuracy, providing a very

large dynamic range in terms of fluidic pumping rates and volumes as well as types/properties of fluids being pumped. This is one of the most important aspects of utilizing the CD platform for biological applications, as it allows successful pumping of many different fluids on the same disc where, for example, one may need to pump both viscous and less viscous blood (depending on the patient) as well as standard reagents and buffers.

## ***Valving***

### Capillary valves

Valving is essential to CD microfluidics to precisely control fluid movement throughout assay processing. Capillary valves, in particular have been extensively used in many centrifugal microfluidic systems for biomedical applications<sup>171</sup>. The fundamental principle is based on a balance between capillary pressure (*i.e.*, surface-tension induced pressure,  $P_s$ ) and centrifugally-induced pressure ( $P_\omega$ ): liquid will not pass through a capillary valve as long as the centrifugal pressure is less than or equal to the capillary barrier pressure. Capillary pressure develops from heightened surface tension at the liquid-air interface when the cross section of a hydrophilic capillary expands abruptly. Duffy *et al.* modeled capillary valving by balancing the pressure induced by centrifugal forces with the capillary pressure  $P_s$ <sup>177</sup>. Madou *et al.* have utilized critical burst frequency calculations to achieve sequential operation of multiple, serial capillary valves by simply increasing the spin speed<sup>178-180</sup>. Experimental capillary-valve burst frequencies on a CD have been shown to be in good agreement with calculated burst frequency values<sup>180</sup>.

## Hydrophobic valves

Hydrophobic valves rely on either a sudden narrowing in a hydrophobic channel, or functionalized hydrophobic regions in microchannels to impede fluidic movement.<sup>19, 20</sup> In both cases, fluid can be forced past these valves when the rotational speed exceeds a certain critical value. Hydrophobic valves have been implemented in several ways for biological assays. For example, Gyros AB used hydrophobic patches at the entrances of microchannels as a similar method to control the fluidic movement within a centrifugal device<sup>152</sup>.

## ***Siphoning***

A CD-based siphon structure is often used for both liquid valving and transfer<sup>155,175</sup>. Siphoning relies on the priming of liquid into a siphon channel due to capillary action; therefore the siphon channel surface must be hydrophilic. When the CD is spinning at high speeds, centrifugal forces keep the meniscus front below the crest level of the siphon. When the rotating disc speed is reduced below a critical value, the channel is primed, and the siphon can transfer the liquid as soon as the meniscus passes the crest point. The liquid flow stops as soon as the liquid level is hydrostatically balanced or there is a discontinuity in the liquid column. Siphon valving in centrifugal microfluidics provides a valving solution for CD applications that require higher spin speeds as the first step of the operation (*e.g.* plasma separation from whole blood).

## ***Volume metering***

Liquid volume metering is an essential function in centrifugal fluidics, not only to achieve proper reagent volumes for diagnostic assays, but also to ensure reproducible

valving processes on a CD. For example, excessive or insufficient fluid volumes in a chamber can result in the premature breakage of a capillary valve or failure of a siphon valve. Volume metering in a CD is primarily achieved through the simple use of an overflow channel connected to a fluidic chamber<sup>152,181</sup>. Once the chamber has been filled to the radial level of the overflow channel, any additional fluid is routed to a waste chamber. Steigert et al. discuss the significance of “wicking” that occurs along the edges of CD-based metering chambers, and introduce design principles to reduce its negative effect on metering variation. As part of an integrated colorimetric assay, they reported the metering of 300 nL with a 5% coefficient of variability<sup>156</sup>. Centrifugal devices must be designed to minimize the “wicking” effects since the precision of the metered volume is of utmost importance in the metering process.

### ***Mixing***

Mixing is necessary in biomedical diagnostic applications in order to homogenize samples and to combine various reagents for downstream analysis. However, mixing is difficult to achieve in microfluidic platforms due to constraints of the microscale domain. As with microfluidics in general, the microscale channels in centrifugal platforms feature low Reynolds numbers and thus operate in the laminar flow regime<sup>173</sup>. This means that there is no convection and fluidic mixing is limited to mixing by diffusion which can be a very slow process. A number of approaches to achieve rapid mixing have been demonstrated on centrifugal microfluidic platforms to overcome this problem<sup>159,175,181</sup>. One method uses rapid oscillations of the CD to achieve rapid mixing in low-Reynolds number regimes (*viz.*, oscillations between clockwise and counter clockwise rotation)<sup>182</sup>. The flow inertia and counteracting viscous damping improves the rapid mixing in larger-

scale fluidic chambers. Additionally, by introducing paramagnetic particles in the liquid and by positioning permanent magnets aligned in non-symmetrical positions underneath the mixing chamber, a magnetic stirring effect can further decrease mixing time<sup>159</sup>. Ducree et al. have also shown that the Coriolis pseudo-force is also efficient for continuous-flow mixing in “macroscopic” fluid chambers in centrifugal systems<sup>183</sup>.

### ***Flow switching***

Complex biological assays often require various analytes to be directed to different chambers and/or channels on the CD. Controlling the direction of the flow can be achieved by various methods on a centrifugal microfluidic platform. A common method for flow switching in a centrifugal device is to utilize the Coriolis force within a Y-shaped structure (a single inlet channel splits into two symmetric outlets)<sup>175</sup>. The equation for the Coriolis force is:

$$F_{coriolis} = 2\rho\omega\bar{v} \quad (1.10)$$

where  $v$  is the velocity of flow in the rotating disc, and the remaining terms were defined above. At low spin frequencies,  $\omega$ , the Coriolis force is negligible compared to centrifugal forces and the liquid is evenly distributed between the two outlet channels. However, at higher frequencies, the Coriolis force is large and the flow can be directed fully to one or the other of the outlet channels depending upon the direction of the CD rotation.

In addition, flow switching can also be achieved by exploiting surface property differences of the channel structures on the disc. In a centrifugal device developed by Gyros AB, hydrophobic patches at the channels entrances were utilized to direct flow to downstream chambers. Depending on the centrifugal force, the fluid either breaks past

the capillary valve, or continues past it and flow into the second hydrophilic channel<sup>152</sup>. Flow switching has great potential in rapid biological analysis utilizing, for example, solid-phase extraction. After a protein binding assay and the washing steps, the eluted sample product can be transferred to a different chamber simply by utilizing one of the above mentioned flow switching methods.

## CHAPTER 2. Fabrication of carbon-electrode DEP devices

The use of carbon electrodes for DEP combines advantages offered by traditional techniques such as metal-electrode DEP or insulator-based DEP (iDEP). The benefits of using carbon electrodes in DEP are detailed in chapter 1. Briefly, the possibility of sample electrolysis is reduced with the use of carbon electrodes, an advantage shared with iDEP, while low voltages are enough to polarize the carbon electrodes and create an electrical field suitable for DEP, an advantage shared with metal-electrode DEP. Other important benefits include the excellent biocompatibility of carbon, its remarkable chemical inertness and good mechanical properties. The fabrication of carbon-DEP devices is presented in this chapter. To the best knowledge of this author no previous integration of carbon electrodes and microfluidics has been done for DEP applications. A flow diagram of the fabrication process is shown in Fig 2.1. The process starts with the fabrication of the electrodes. The carbon-DEP chips presented in this work feature glass-like carbon electrodes that are derived through the pyrolysis of patterned SU-8<sup>5</sup>. A microfluidic network is then fabricated or positioned around the electrodes. On-substrate microfluidics are fabricated by patterning SU-8 around the electrodes and covering the fluidic network with drilled glass or polycarbonate. Off-substrate microfluidics refers to the fabrication of the fluidic network using a process that is independent from the fabrication of the carbon electrodes. Casted PDMS or a stack of patterned polycarbonate and double-sided adhesive are fabricated off-substrate and then manually positioned around the electrodes. The fluidic and electrical interconnects permit the connection of the carbon-DEP chip to a syringe pump and a function generator respectively. Each

---

<sup>5</sup> Even though SU-8 is used in this work, carbon can be derived from a variety of organic precursors as detailed in chapter 1

fabrication step in the process is detailed in the first part of this chapter. The characteristics of all the different carbon-DEP devices fabricated here are then resumed to illustrate the development from the initial proof-of-concept to the current state-of-the-art. Such resume is followed by a discussion on the reliability and fabrication cost and time of each generation of carbon-DEP devices. Initial results on possible improvements to current carbon-DEP devices such as the use of transparent substrates and metal interconnecting leads to the base of the carbon electrodes are presented to conclude the chapter.

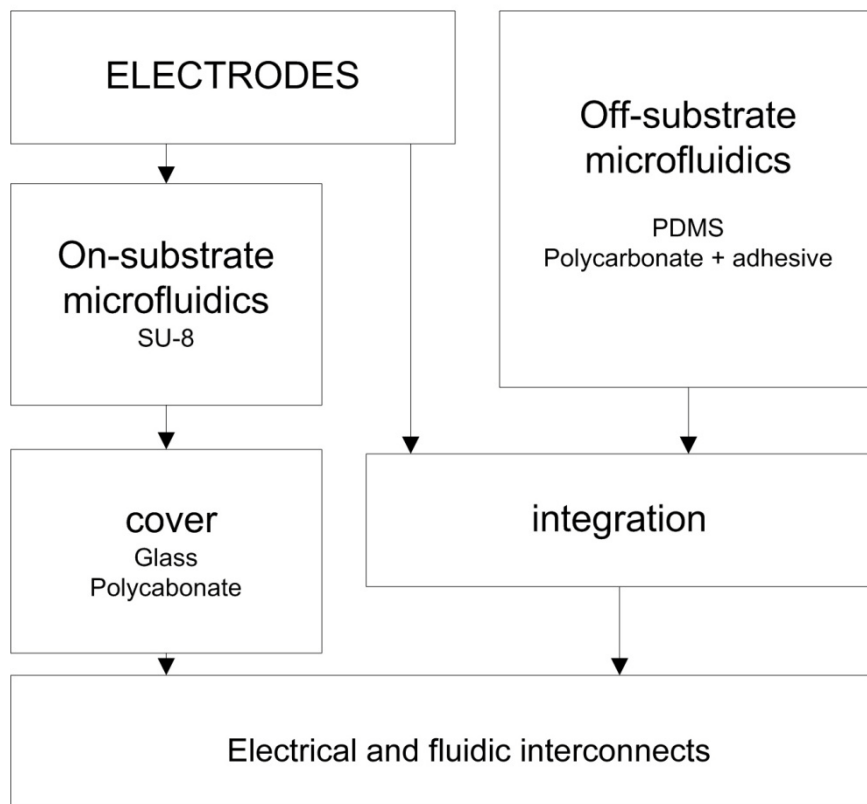


**Fig. 2.1** Fabrication flow chart of carbon-DEP devices

## 2.1 Electrodes

DEP applications require for the electrodes, regardless of their material, to be closely spaced and to provide the biggest trapping volume possible. The DEP force is directly proportional to the squared magnitude of the established electric field gradient between electrodes as stipulated in eqn.1.1. The electric field  $E$  is directly proportional to the voltage  $V$  used to polarize the electrodes and inversely proportional to the gap  $d$  between them ( $E = V \cdot d^{-1}$ ). If the gap between electrodes increases, the applied voltage must increase accordingly to meet the electric field requirements. Since electric fields up to  $10^5 \text{ V} \cdot \text{m}^{-1}$  <sup>63</sup> are necessary to create a suitable DEP force, electrode gaps narrower than  $100 \text{ } \mu\text{m}$  must be fabricated to keep the voltage levels below  $10 \text{ V}$ . In the case of carbon-DEP, the precursor SU-8 structures can shrink up to  $50\%$  during pyrolysis and thus the gaps in the SU-8 pattern must be fabricated significantly smaller than those desired between carbon electrodes. The electrodes used in DEP are also required to provide with the biggest trapping volume possible to increase the throughput during DEP-assisted cell sorting. The trapping volume is directly proportional to the contact area between an electrode and the solution containing the targeted cells. For example, a  $100 \text{ } \mu\text{m}$ -diameter carbon cylinder will provide more trapping volume than a  $50 \text{ } \mu\text{m}$ -diameter electrode of the same height. A tall cylinder will provide more trapping volume than a shorter one of the same diameter. Furthermore, a square prism with a cross-section featuring  $50 \text{ } \mu\text{m}$ -sides will provide more trapping volume than a  $50 \text{ } \mu\text{m}$ -diameter cylinder but less than a  $100 \text{ } \mu\text{m}$ -one if the three structures have the same height. Obviously, the trapping volume can be increased by adding more electrodes to the array. Electrodes that are as tall as the micro-channel containing them are also desired. Tall channels are desired because the

flow rate inside them is bigger than that inside shorter channels of the same width. Yet, the flow velocity in both channels is the same. The continuity equation establishes that the mass flow rate  $Q$  in a micro-channel equals the product of the flow velocity  $v$  and the cross-section area  $A$  of the channel ( $Q = v \cdot A$ ). The cross-section area of the channel can be increased by fabricating taller or wider channels. Taller, rather than wider, channels are desired to maintain a small footprint of the DEP chips. The flow rate in the channel is thus increased to process a given sample volume in a shorter period of time. But the flow velocity is kept constant following the continuity equation. The hydrodynamic drag force acting upon cells flowing in a micro-channel depends directly on the flow velocity. If the hydrodynamic drag force is stronger than the DEP trapping force created on the positive-DEP regions around the electrodes, the targeted cells will never be trapped. Therefore, low flow velocity translates into a hydrodynamic force that can be easily overcome by a DEP force created using practical voltages and electrode gaps. In resume, carbon-DEP, and DEP in general, benefits from the use of dense arrays of tall electrodes.

The fabrication of carbon electrodes is illustrated in Fig. 2.2: SU-8 photolithography is first used to pattern the precursor resist (Fig. 2.2a); followed by pyrolysis to carbonize such pattern (Fig. 2.2b) and then de-scumming to physically isolate each carbon electrode. SU-8 photolithography is also used after de-scumming to pattern a thin SU-8 layer around the carbon electrodes (Fig. 2.2c). This thin layer serves both as an electrical insulator and a protective barrier to the carbon connecting leads located underneath. The transition from Fig. 2.2a to 2.2b illustrates how the structures shrink during pyrolysis. The quality and dimensions of the carbon electrodes depend mainly on those of the SU-8 precursors and thus the SU-8 photolithography process must be optimized accordingly.

Several references exist on the fabrication of tall high aspect ratio SU-8 structures<sup>142,184,185</sup> but those structures are usually fabricated hundreds of micrometers apart. Few authors discuss the fabrication of dense arrays of tall (>100 μm), high aspect ratio (> 1:1) SU-8 structures, for example<sup>186</sup>. In this case a compromise between the aspect ratios of the gap (between structures) and the structures must be established to prevent structure bending and stiction during pattern drying after development in an aqueous solution. This section starts with the modeling of stiction in different array geometries. The fabrication of carbon electrodes as illustrated in Fig. 2.2 is then detailed.

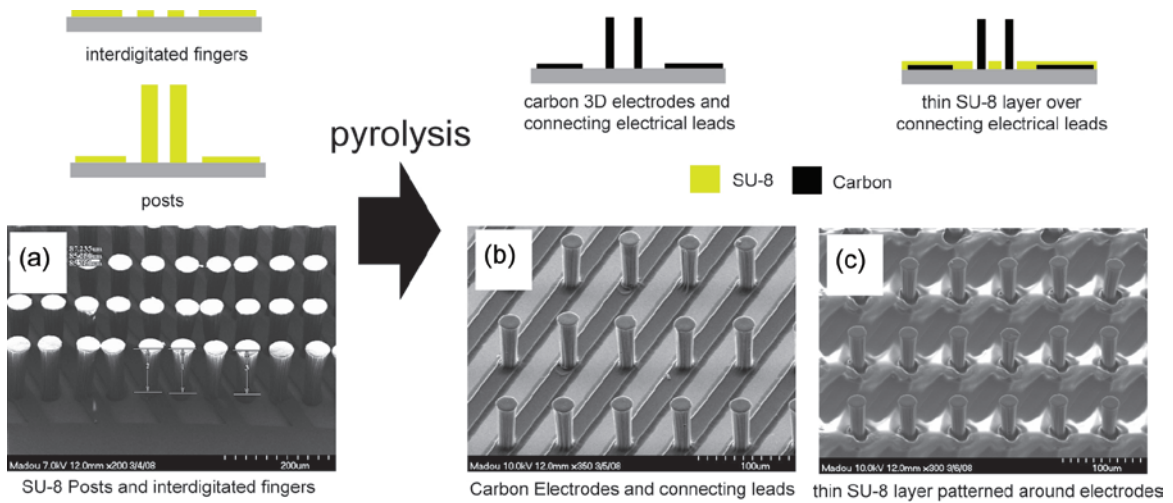


**Fig. 2.2** The different processes required for the fabrication of carbon electrodes for DEP applications

### 2.1.1 Modeling of stiction between high aspect ratio structures

Stiction is an important problem in the micro-world. The surface tension forces that develop in a narrow gap during the drying of patterns from developer fluid can be capable of pulling structures together as shown in Fig. 2.3. Stiction can be minimized by increasing the stiffness of the individual structures, increasing the gap between them or

by using a developer with low surface tension. The replacement of developer with a liquid with even lower surface tension, *i.e.*, acetone or 2-propanol, before drying can also prove beneficial. Here we focus on alternatives to reduce stiction between SU-8 structures. In general, the stiffness of a structure mainly depends on the Young modulus of the material. However if the structure must be fabricated out of a specific material, such as SU-8 in this case, the geometry, dimensions and aspect ratio of the structure must be optimized to prevent stiction. The effect of structure dimensions and geometry on preventing stiction is detailed in this section. The impact of varying the gap between structures and the fluid used to immerse the pattern before drying is also detailed but a theoretical model is first developed.

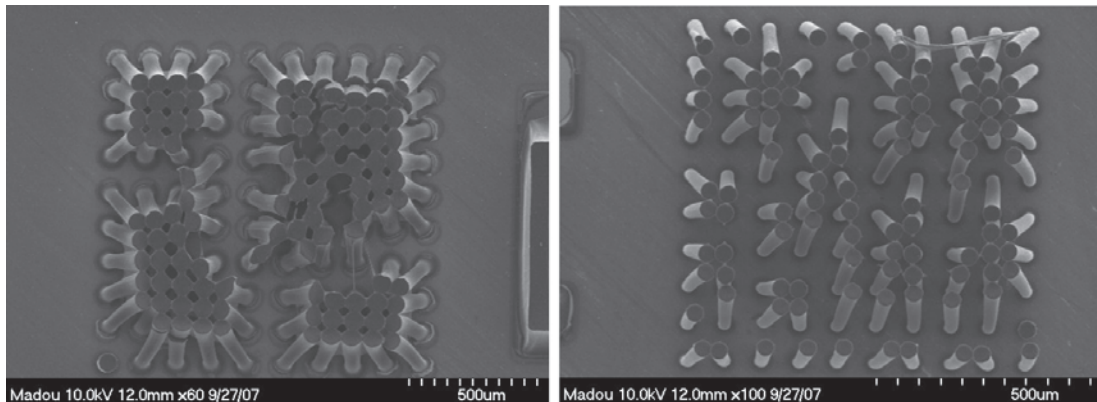


**Fig. 2.3** Examples of stiction in a SU-8 cylinder array

The force  $F$  acting on the two structures shown in Fig. 2.4 can be calculated by

$$F = \Delta P * D \quad (2.1)$$

where  $D$  is the contact length of the structure with the air-fluid interface. The capillary pressure difference  $\Delta P$  across the surface of the air-fluid interface can be calculated using the Young-Laplace equation

$$\Delta P = \gamma \left( \frac{1}{R_1} + \frac{1}{R_2} \right) \quad (2.2)$$

where  $\gamma$  is the surface tension of the liquid.  $R_1$  and  $R_2$  denote the principal radii of curvature<sup>6</sup> of the air-fluid interface and are given by

$$R = \frac{g}{2 \cos \theta} \quad (2.3)$$

where  $g$  is the gap between structures and  $\theta$  is the contact angle of the fluid with the structure.

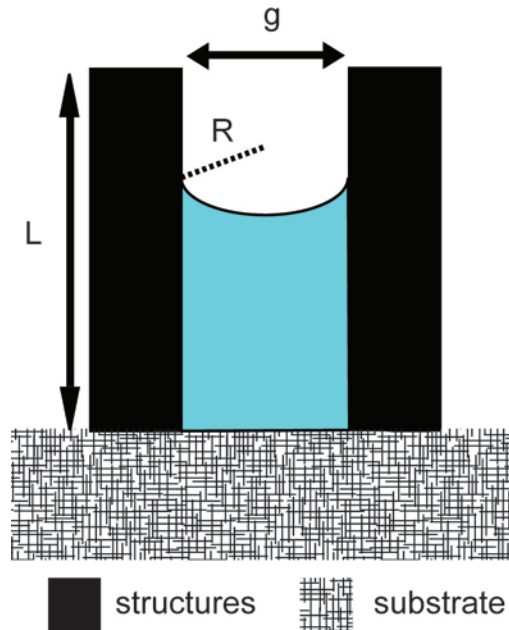


**Fig. 2.4** Model used to analyze stiction forces developed when drying the liquid between two structures

<sup>6</sup> The principal curvatures at a given point of a surface are the eigenvalues of the shape operator at the point. They measure how the surface bends by different amounts in different directions at that point

Here the capillary in between two structures is modeled as two infinite parallel plates and  $R_2$  is considered to be infinite. Other authors have considered the case of a 2 X 2 array of square columns and modeled the capillary as a tube <sup>187</sup> or considered a variation on the radii of curvature as the deflection of the structure increases <sup>188</sup>. The case of only two structures is detailed here since the electrode arrays presented below are asymmetric. The gap between the electrodes in one axis is approximately half of that between electrodes in the other axis. It is assumed stiction is eliminated at the wider gap as long as it is prevented from happening in the narrower gap. In an ideal situation equal capillary forces act on both sides of a column contained in the array, counteract each other and stiction is not expected to happen (except for the structures at the outer edge of the array). However, in a real device stiction results from the interaction of many factors that frequently are hard to control such as contaminants. The radii of curvature  $R$  is maintained constant in this model since the beam deflection is calculated only at its tip. The tips of the beams are typically the first regions to make contact since it is here where the effect of the pulling force from the fluid is most severe. In this simplified model there is no need to account for changes in  $R$  as the bending increases. The structures presented here are modeled as beams with one end fixed on the substrate and the other end free (fixed-free). A uniformly distributed load along the length of the beam is given by the pulling action of the fluid contained between the beams. In this case the deflection of the tip of the beam  $\delta$  is given by

$$\delta = \frac{FL^4}{8EI} \tag{2.4}$$

where  $F$  is the force (capillary force in this case) acting along the height  $L$  of the structure and  $E$  and  $I$  are the Young modulus and the second moment of inertia of the structure respectively. Solving for  $\delta$  using equations 2.1 through 2.4 gives

$$\delta = \frac{2\gamma\cos\theta DL^4}{8gEI} \quad (2.5)$$

In simplified terms, stiction happens when the deflection of the beams is more than half the gap between them so  $\delta_{\max} = \frac{g}{2}$ . Solving for  $L$  in equation 2.5 to obtain the upper limit on the height of the structures to prevent stiction gives

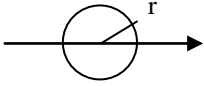
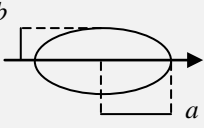
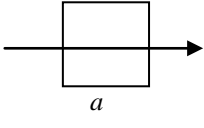
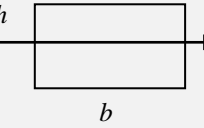
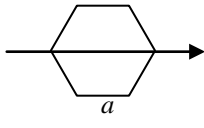
$$L^4 = \frac{2EIg^2}{D\gamma\cos\theta} \quad (2.5)$$

Therefore the maximum height of the structures depends directly on the Young modulus  $E$  of the structure material, the gap  $g$  between structures and the moment of inertia  $I$  given by the geometry and dimensions of the structures. The maximum height is inversely proportional to the surface tension  $\gamma$  of the immersion liquid, the contact angle  $\theta$  between such liquid and the structural material and to the contact length  $D$  between the capillary and the structure. The structural material in this work is assumed to be SU-8 and a Young modulus of 4.02 GPa is considered. The Young modulus of SU-8 depends greatly on the processing conditions and different values from 3.5 to 5.88 GPa have been reported<sup>189,190</sup>. The value used here is that of SU-8 baked at 95 °C after exposure but not hard baked<sup>139</sup>. The Young modulus of glass-like carbon is in the range of 23-30 GPa<sup>75,81,191</sup>. The impact of the moment of inertia, gap between structures and the choice of immersion liquid on the maximum structure height is detailed next.

The second moment of inertia of a given structure is determined by the geometry and dimensions of its cross-section at a plane parallel to the substrate. Only structures with a

constant cross-section along their length are considered here. The equations to calculate the area and moment of inertia of typical geometries are presented in Table 2.1. A wider selection can be found in the work by Symonds et al<sup>192</sup>. The stiction force acting on the structures is assumed to be positioned on the axis illustrated by the arrows in the table figures. The cases where the force acts on a different axis are not considered here since the structures fabricated in this work are collinear to each other.

**Table 2.1** Second moment of inertia for different cross-sections with respect to an horizontal axis through the centroid of each shape (denoted by the arrow in selected figures). From <sup>192</sup>

Geometry		Area (m <sup>2</sup> )	Moment of inertia (m <sup>4</sup> )
Circle		$\pi r^2$	$\frac{\pi r^4}{4}$
Ellipse		$\pi ab$	$\frac{\pi ab^3}{4}$
Square		$a^2$	$\frac{a^4}{12}$
Rectangle		$bh$	$\frac{bh^3}{12}$
Hexagon		$2.598a^2$	$0.5413a^4$
Equilateral Polygon $a$ = length of side $n$ = number of sides		$\frac{na^2}{4 \tan\left(\frac{\pi}{n}\right)}$	$\frac{na^4}{96 \tan\left(\frac{\pi}{n}\right)} \left( \frac{3}{2 \left(\sin\left(\frac{\pi}{n}\right)\right)^2} - 1 \right)$
Pentagon $n=5$		$1.7204a^2$	$0.2395a^4$
Heptagon $n=7$		$3.6339a^2$	$1.055a^4$
Octagon $n=8$		$4.8284a^2$	$1.8594a^4$

The moment of inertia depending on the area of the cross-section or the characteristic dimension of the cross-section geometry is plotted in Fig. 2.5 a) and b) respectively. The moment of inertia is independent from the geometry as long as equilateral polygons featuring the same area are used. For example the use of a square, circle or octagon geometry yields the same moment of inertia as long as their area is kept constant. Wider areas yield higher moments of inertia as shown in Fig. 2.5b. In this case the characteristic

dimension of the geometries is maintained equal. The characteristic dimension is either the side length of a polygon (when the number of sides  $n$  is 5, 6, 7 and 8), the radius of a circle or the side length of a square. The use of an octagon geometry yields the highest moment of inertia but only because its area is the widest.

The variation on the moment of inertia as a circle transforms into an ellipse or a square into a rectangle is plotted and illustrated in Fig. 2.6a and b respectively. The moment of inertia increases proportional to the dimensions of the structure. Most importantly, the moment of inertia is more efficiently increased by elongating the circle or the square along an axis perpendicular (instead of parallel) to the force acting on the structure (denoted by the arrows in the figure).

Structures with circular cross-section (posts) are considered in the rest of this work. A post array minimally disturbs the laminar flow established in a micro-channel as detailed in chapter 3, section 3.2. Moreover, the use of post electrodes creates an electric field gradient in the sample that is more gentle to biological cells than the gradient established using an electrode cross-section with sharp corners, *i. e.*, square or hexagon. The moment of inertia of a structure with circular cross-section is the same as that of structures with other equilateral polygon cross-sections (square, pentagon, etc.) as long as their area is equal.

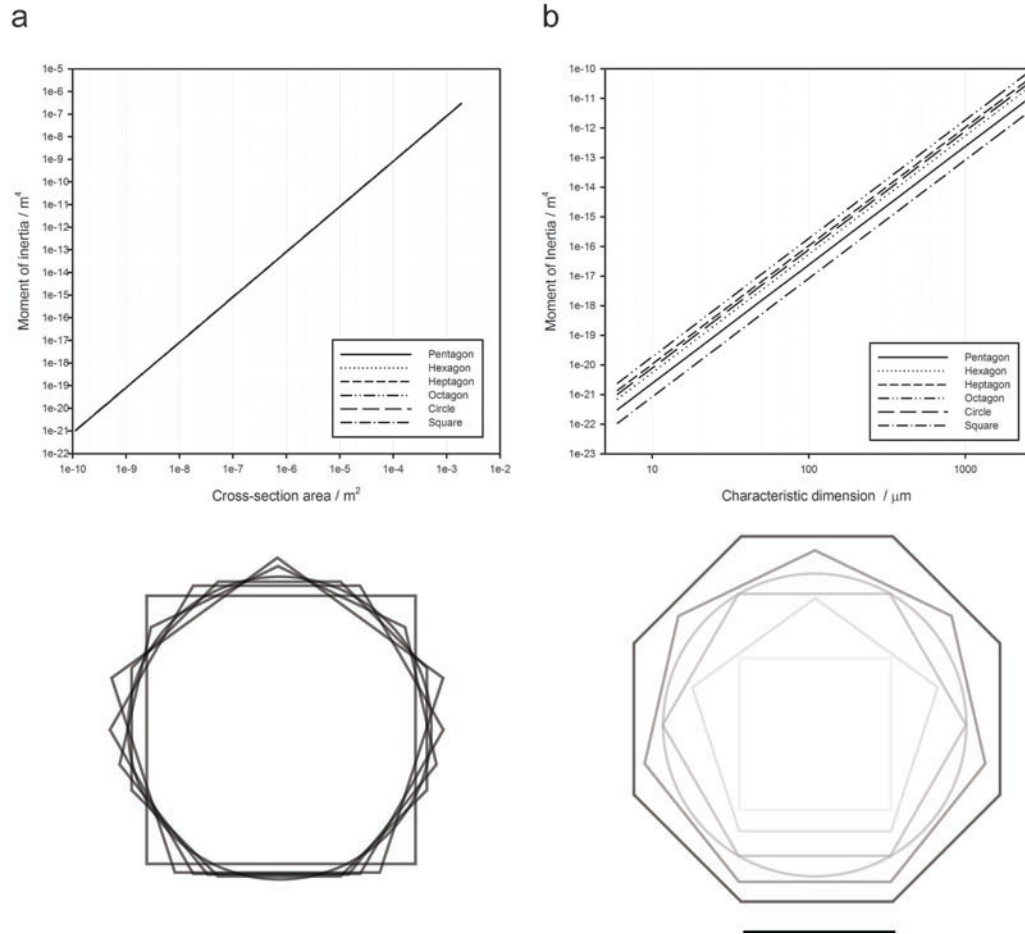


**Fig. 2.5** The variation of the moment of inertia when a) the surface area of the geometry or b) the characteristic dimension of equilateral polygons are maintained constant

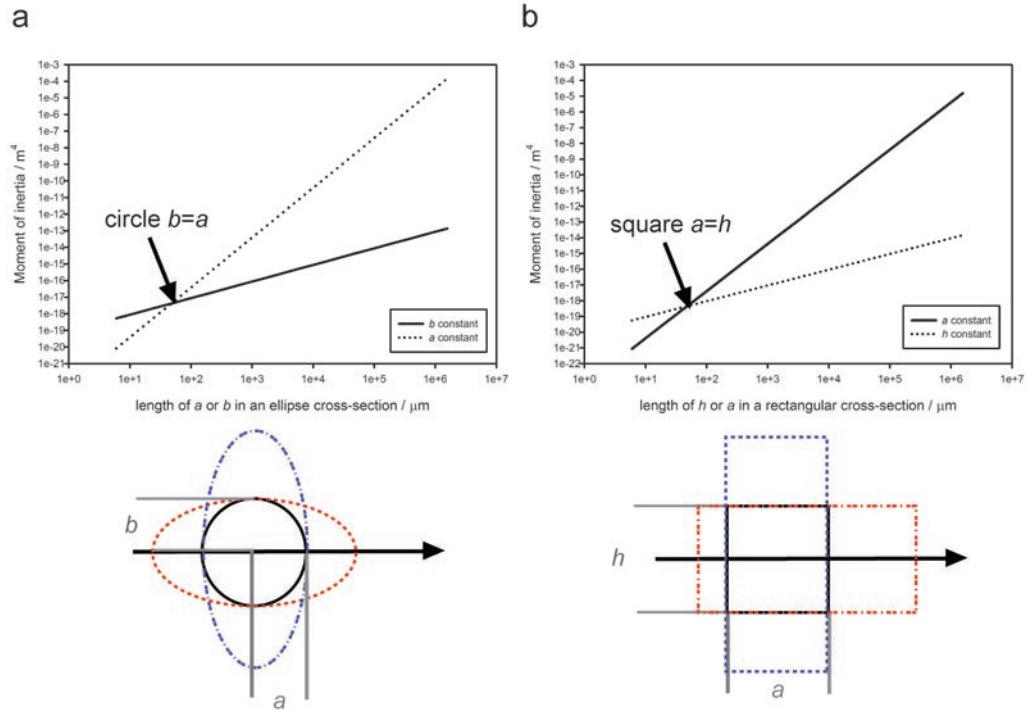


**Fig. 2.6** Variation on the moment inertia when a) a circle transforms into an ellipse and b) a square becomes a rectangle

The effect of the SU-8 post radius and the correspondent moment of inertia on the maximum post height  $L$  and aspect ratio  $AR = \text{height}/\text{width}$  is shown in Fig. 2.7a and b respectively. The plots were obtained using equation 2.5 assuming the immersion liquid to be water ( $\gamma = 72.7 \text{ mN}\cdot\text{m}^{-1}$ ) and the gap between SU-8 structures to remain constant at  $20 \mu\text{m}$ . The height  $L$  is left as a function of  $D$ . The contact angle between water and SU-8 is assumed to be  $80^\circ$ <sup>186</sup>. Although the use of wider posts enables the fabrication of taller posts the aspect ratio of the structure is equal at all dimensions. Equation 2.5 was again used to estimate the effect of the gap between posts on the maximum electrode height and aspect ratio but now assuming a constant post radius of  $50 \mu\text{m}$ . All other parameters are equal to those detailed immediately above. The use of wider gaps between structures allows for the fabrication of taller posts given a post radius which increases the aspect ratio of the structure.

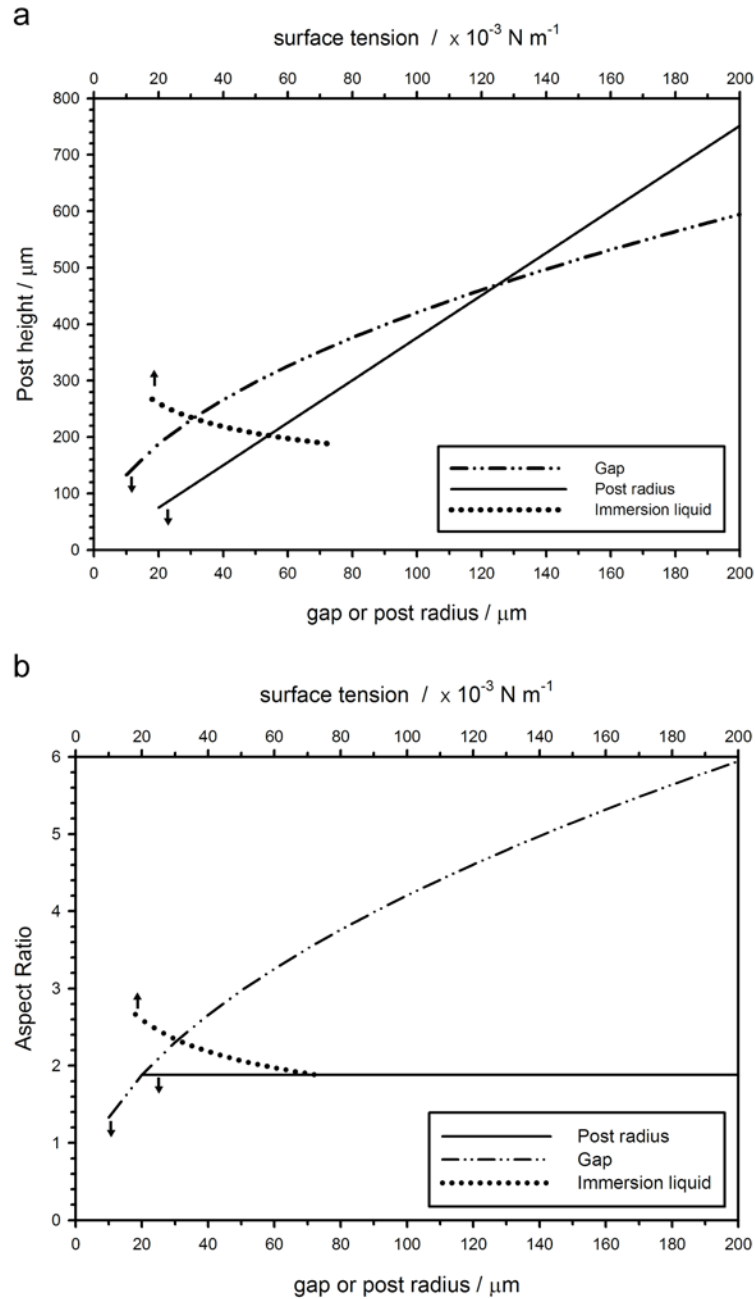


**Fig. 2.7** The effect of SU-8 post radius, gap between posts and immersion liquid on the maximum a) post height and b) aspect ratio that can be fabricated without stiction

The effect of the choice of immersion liquid is also illustrated in Fig. 2.7. A liquid with low surface tension enables the fabrication of taller posts with higher aspect ratio. However, the change on post height depending on the immersion liquid is not as

significant as that obtained when increasing the gap. For example, the surface tension of water is  $72.7 \text{ mN}\cdot\text{m}^{-1}$  while that of isopropyl alcohol (IPA) is only  $23 \text{ mN}\cdot\text{m}^{-1}$ . Even though the surface tension of water is 3.16 times more than that of IPA, the maximum post height using IPA ( $248 \mu\text{m}$ ) is only 1.31 times higher than when using water ( $188 \mu\text{m}$ ). Although the contact angle between water and SU-8 is around  $80^\circ$ , this angle changes depending on the liquid employed. Here the contact angle is kept constant regardless of the immersion liquid. This is not completely accurate and the contact angle between SU-8 and the liquid of choice must be used to obtain a more realistic result. Table 2.2 resumes the surface tension of different liquids. Immersion of the sample in liquids with very low surface tension such as perfluorohexane prior drying has been suggested to reduce stiction<sup>193</sup>. The use of critical point drying (CPD) also proves beneficial. More details on CPD are given in the section “Development, Drying and Hard bake” below.

**Table 2.2** Surface tension of selected liquids. For a wider selection visit [www.surface-tension.de](http://www.surface-tension.de)

name	$\gamma$ ( $\text{mN}\cdot\text{m}^{-1}$ )
Water	72.7
SU-8 developer (PGMEA - propylene glycol monomethyl ether acetate)	26.90
Acetone	25.20
Cyclohexane	24.95
1-Chlorobutane	23.10
Isopropyl alcohol	23.00
Methanol	22.60
Ethanol	22.9
n-Octane (OCT)	21.62
Tert-Butylchloride	19.60
n-Hexane (HEX)	18.43
Perfluorooctane	14.00
Perfluorohexane	11.91

## 2.1.2 SU-8 Photolithography

The use of photolithography allows for highly precise patterning of thick (up to hundreds of micrometers) SU-8 layers to obtain tall high aspect ratio structures with near-vertical side-walls. The basic SU-8 photolithography process includes substrate cleaning, spin coating, soft bake, exposure, post exposure bake and development. A comprehensive overview on SU-8 photolithography and the pyrolysis process is given in Chapter 1. In the work presented here a two-step photolithography process is implemented as shown in Fig. 2.8. The first step is to fabricate what will become after pyrolysis the carbon connection pads to the function generator, and the electrical connection leads from these pads to the bottom of the electrodes. The second step is used to fabricate the 3D carbon electrodes and may not be needed when fabricating 2D electrodes since the electrodes and the connection pads can be patterned out of the same layer (a finished SU-8 device and the corresponding carbon structures are shown in Fig. 2.9 to illustrate the connection pads, leads and electrode posts). The first and second steps include all the basic photolithography process with the exception of substrate cleaning which is not needed in the second step. Fiducials are fabricated in the first layer and are used to align the second mask. These alignment marks are covered using adhesive polyimide tape before the coating of the second SU-8 layer. The SU-8 fiducials may otherwise not be resolved during mask aligning since they would be surrounded by SU-8. The tape, and the resist deposited on it, is removed after soft baking and prior exposure of the second layer. Table 2.3a and b resume the different recipes followed to fabricate various thicknesses of both the first layer (denoted by Leads) and the posts.

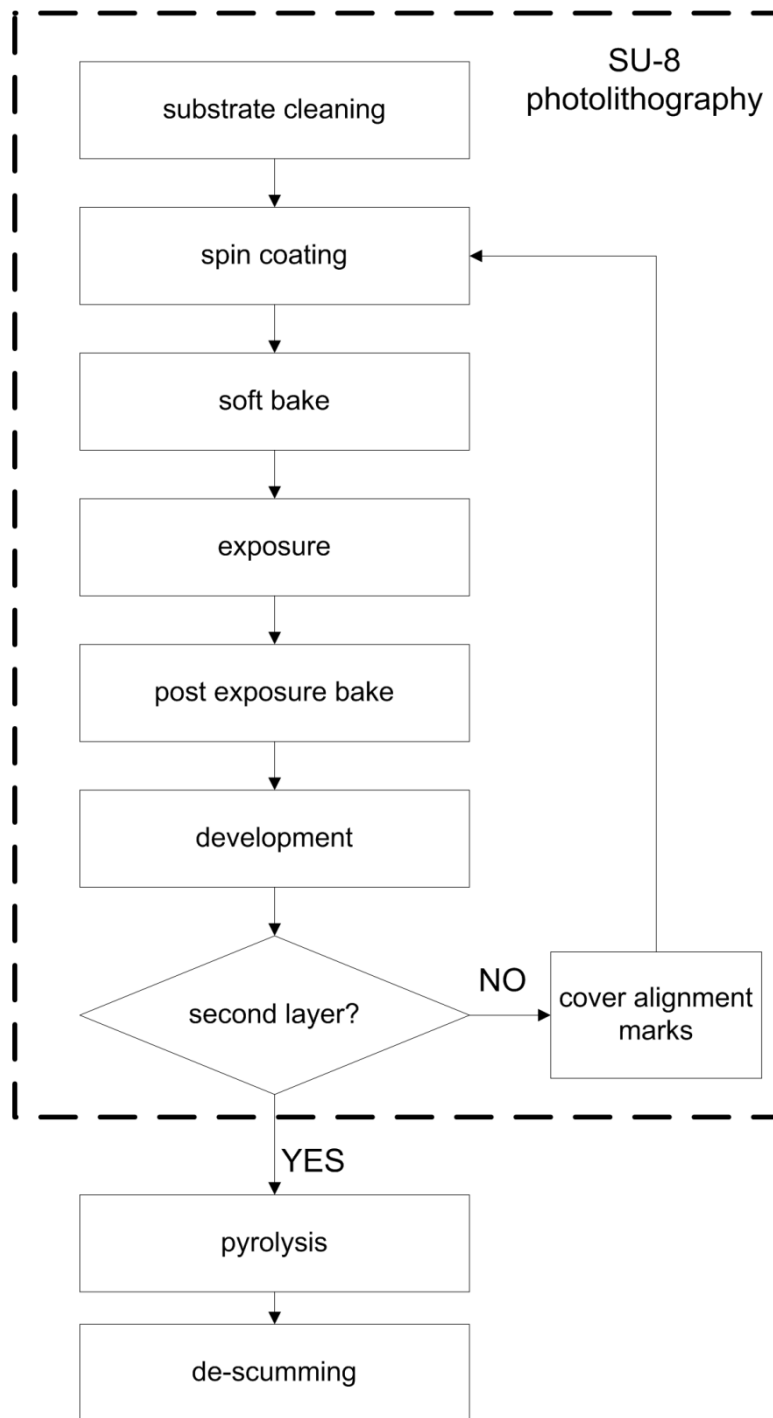


**Fig. 2.8** Fabrication flow chart for carbon electrodes

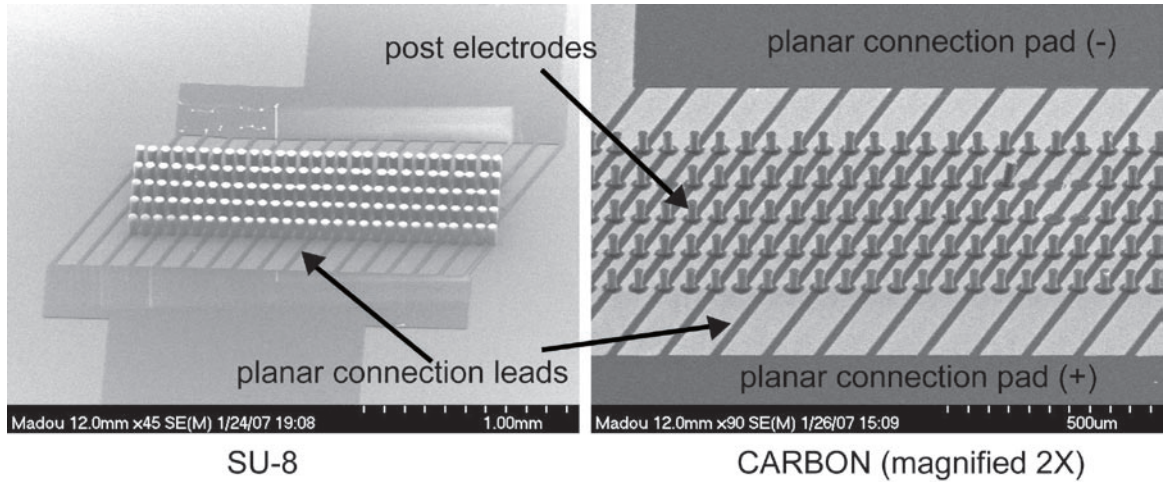


**Fig. 2.9** A typical carbon electrode array used for carbon-DEP and its SU-8 precursor

**Table 2.3a** Spin programs used in this work and resultant layer thicknesses

ID tag	SU-8	First step - spread			Second step – thickness definition			$T_{\text{SU-8}}$ ( $\mu\text{m}$ )	Substrate	
		$a$ (rpm/s)	$s$ (rpm)	$t$ (s)	$a$ (rpm/s)	$s$ (rpm)	$t$ (s)		Size	Type
FILTER 1 (F1)	50	80	500	10	255	2000	40	-	2" square	glass
FILTER 2 (F2)	25	170	500	10	255	700	40	-	5" square	glass
PLANAR INTERDIGITATED FINGERS THAT WILL BECOME ELECTRICAL LEADS										
Leads 1	10	255	500	10	310	3000	40	8.95	4" circle	SiO <sub>2</sub>
Leads 2	10	255	500	10	340	3000	40	9.67	4" circle	SiO <sub>2</sub>
Leads 3	2010	255	500	10	340	3000	40	11.2	4" circle	SiO <sub>2</sub>
Leads 4	25	170	500	10	255	2800	40	16.67	4" circle	SiO <sub>2</sub>
Leads 5	25	170	500	10	255	2500	40	19.1	4" circle	SiO <sub>2</sub>
POSTS THAT WILL BECOME ELECTRODES										
Posts 1	25	170	500	10	255	2250	40	22.52	4" circle	SiO <sub>2</sub>
Posts 2	50	170	500	10	255	1300	40	98	¼ 4" circle	SiO <sub>2</sub>
Posts 3	2150	340	500	15	340	4500	60	100	4" circle	SiO <sub>2</sub>
Posts 4	50	170	500	10	255	1100	40	130	4" circle	SiO <sub>2</sub>
Posts 5	2150	340	500	15	340	2000	60	144	4" circle	SiO <sub>2</sub>
Posts 6	2150	340	500	15	340	2000	60	173	¼ 4" circle	SiO <sub>2</sub>
Posts 7	2150	340	500	15	340	1200	60	333	¼ 4" circle	SiO <sub>2</sub>
Posts 8	2150	170	500	10	340	1000	40	444	¼ 4" circle	SiO <sub>2</sub>
INSULATION LAYER										
Insulation 1	2	425	1000	10	510	3000	60	1.38	4" circle	SiO <sub>2</sub>
Insulation 2	2	425	1000	10	425	2200	60	1.49	4" circle	SiO <sub>2</sub>
Insulation 3	2	425	1000	10	425	1800	60	1.68	4" circle	SiO <sub>2</sub>
ON- SUBSTRATE CHANNEL AND PDMS MOLD										
Channel 1	50	170	500	5	255	3000	30	50	¼ 4" circle	SiO <sub>2</sub>
Channel 2	50	170	500	10	255	1800	40	66.38	½ 4" circle	SiO <sub>2</sub>

Notes:  $a$  = acceleration,  $s$  = speed,  $t$  = time,  $T_{\text{SU-8}}$  = thickness of the SU-8 layer. All circular substrates are 500-550  $\mu\text{m}$  thick <100> wafers. The ¼ 4" circle substrate size is obtained by breaking the wafer in 4 identical pieces. Similarly ½ 4" circle substrate size is obtained by breaking the wafer in 2 identical parts. SiO<sub>2</sub> substrates denote a 5  $\text{\AA}$  layer of SiO<sub>2</sub> on silicon

**Table 2.3b** The fabrication process of all structures done in this work

ID tag	Soft Bake (minutes)	Exposure		PEB (minutes)	Development Type	T <sub>carbon</sub> (μm)	Remarks
		D (mJ·cm <sup>-2</sup> )	Filter used				
Filter 1 (F1)	25	140	none	6	N/A – flood exposure	N/A	65.8% absorban ce
Filter 2 (F2)	50	600	none	9	N/A – flood exposure	N/A	85% absorban ce
<b>PLANAR INTERDIGITATED FINGERS THAT WILL BECOME ELECTRICAL LEADS</b>							
Leads 1	8	160	none	3.5	Immersion	1.38	
Leads 2	7	120	none	2.5	Immersion	1.49	
Leads 3	6	120	none	2.5	Immersion	1.51	
Leads 4	9	140	none	3	Immersion	2.38	
Leads 5	16	200	none	6	Immersion	2.55	
<b>POSTS THAT WILL BECOME ELECTRODES</b>							
Posts 1	10	300	F1	5	Immersion	5.6	
Posts 2	65	800	F1	20	Immersion	52	
Posts 3	75	520	F2	15	Immersion	40	
Posts 4	45	520	F1	15	Immersion	60	
Posts 5	75	480	F2	30	Immersion	73	
Posts 6	75	850	F1	25	Immersion	85	
Posts 7	75	1135	F1	25	Immersion	207	
Posts 8	180	1500	F1	40	Immersion	273	CPD dried
<b>INSULATION LAYER</b>							
Insulation 1	5	120	none	3	Rinsing	N/A	
Insulation 2	5	120	none	2.5	Rinsing	N/A	
Insulation 3	5	120	none	2.5	Rinsing	N/A	
<b>CHANNEL AND PDMS MOLDS</b>							
Channel 1	23	350	none	6	Immersion	N/A	
Channel 2	37	370	none	8	Immersion	N/A	

**Note:** CPD = critical point drying

### ***Substrate cleaning and adhesion***

SU-8 can be patterned on a variety of substrates including glass, silicon and plastics. However, glass and plastics melt at the temperature required for pyrolysis (> 900 °C). Although the melting point of quartz is above 1000 °C the carbon patterns tend to peel off from quartz substrates during pyrolysis due to the difference in the coefficients of thermal expansion of the materials (more details below under Pyrolysis). Silicon wafers

of 4" diameter, 500-550  $\mu\text{m}$ -thickness and crystal orientation  $\langle 100 \rangle$  were purchased from Noel Technologies (Campbell, CA) and are used here for SU-8 photolithography. The wafers feature a thermally-grown 5  $\text{k}\text{\AA}$  layer of  $\text{SiO}_2$ . The oxide layer acts as an electrical insulator between the carbon electrodes.

Prior to spin coating, a wafer (as supplied) was rinsed under a jet of de-ionized (DI) water for 1 minute, rinsed with acetone and iso-propyl alcohol (in that order) and blown-dried using nitrogen. It was then dehydrated in a convection oven set at 120  $^{\circ}\text{C}$ . This basic cleaning procedure is to remove any particles from the wafer surface. If wafer recycling was necessary, the wafer was first stripped out of SU-8 by immersion in a piranha solution (3:1 parts of  $\text{H}_2\text{SO}_4\text{:H}_2\text{O}_2$ ) and then cleaned using the basic procedure just detailed (DI water, acetone, iso-propyl alcohol and dehydration).

Adhesion between SU-8 and silicon oxide depends on both the contact area between them and the aspect ratio (height divided by contact area) of the SU-8 pattern. A structure with small contact area is more likely to detach from the substrate than a structure with a larger contact area and the same aspect ratio. A structure with smaller aspect ratio is more likely to remain on the substrate than a structure with higher aspect ratio and the same contact area. The adhesion of the first layer, that to become the connection pads and the connecting leads to the electrodes, to the silicon oxide was acceptable when the substrate was cleaned as detailed above. However, this layer is short and wide-spread while the posts are thin and tall. Hydrodynamic drag forces introduced in the fluid by agitation during developing are strong enough to detach small posts from the substrate. Stiction forces during drying can be strong enough to cause the detachment of structures with low mechanical strength. Mechanical strength is highly dependent on the Young's module of

the material and the dimensions of the structure. Since in this work all structures are made out of SU-8, the dimensions of the structure become the predominant factors. A basic study was carried on to quantify the detachment of SU-8 posts from a silicon oxide layer depending on the diameter and aspect ratio of the posts. The substrates were first cleaned as detailed above and no adhesion promoters were used. Each substrate was then coated with a single layer of specific thickness. The spin protocols detailed in Table 2.3b for Posts 2, 6, 7 and 8 were used to obtain 98, 173, 333 and 444  $\mu\text{m}$ -thick layers respectively. The mask used for exposure features multiple 10 by 10 circle arrays. All circles in a given array have the same diameter which ranges from 10 to 100  $\mu\text{m}$  depending on the array. The gap between circles equals 40  $\mu\text{m}$  in all the arrays. The complete fabrication procedure is detailed in Table 2.3a and b. The SU-8 posts were characterized qualitatively using an optical microscope. Their thickness was measured using a surface profiler (Dektak3, Veeco Instruments). The results are shown in Fig. 2.10. After characterization, the SU-8 posts were pyrolyzed and the resultant carbon electrodes were characterized using a scanning electron microscope. Some images of the carbon posts as well as their shrinkage characterization are presented below under Pyrolysis (Fig. 2.11). The dependence of adhesion on the diameter of the SU-8 posts and their aspect ratios is detailed next. The curves in Fig. 2.10a correspond to the different layer thicknesses that were coated. Post diameters less than 20  $\mu\text{m}$  do not provide enough adhesion area and are always detached during development. Adhesion to the substrate increases with contact area and posts with a diameter from 20 to 25  $\mu\text{m}$  showed an improvement on adhesion but still detached in 75% of the cases. The detachment of these posts was observed during development or during drying when the stiction force overcomes the post adhesion to the

substrate. Posts featuring a diameter greater than 50  $\mu\text{m}$  never detached. The gray gradient shown in Fig. 2.10a reflects the direct dependence of adhesion on the diameter of the posts.

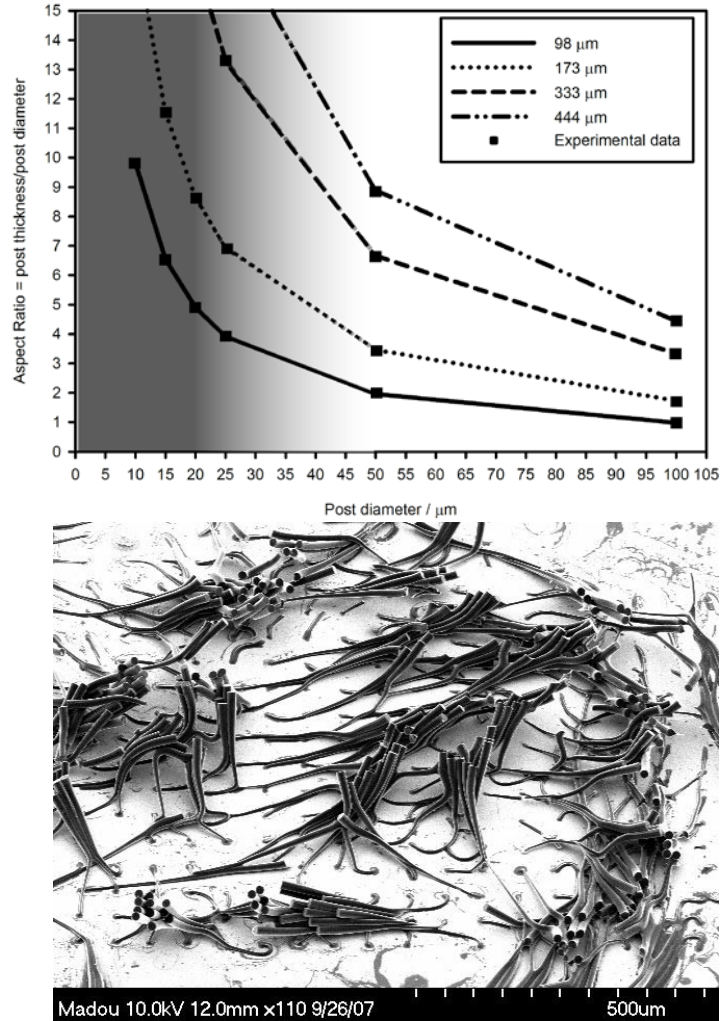


**Fig. 2.10** a) The dependence of adhesion on post diameter and aspect ratio. The gradient reflects the possibility of pattern detachment depending on the post diameter. The white area denotes no detachment. b) Mechanical failure of 25  $\mu\text{m}$  due to stiction forces. Note however how the majority of them remain attached to the substrate

The white area contains those post diameters that never detached from the substrate while the dark gray contains those that did. The probability of detachment varies for the post dimensions contained in the gradient between white and dark gray, the lighter the shade

the less likely a post is to detach from the substrate. Aspect ratios up to 6.5:1 were achieved on posts with a diameter 50 and 100  $\mu\text{m}$ . The aspect ratio of the 100  $\mu\text{m}$  diameter posts was only 4.4:1 due to the thickness of the thickest layer coated in this work. The patterning of thicker layers than 444  $\mu\text{m}$  was not attempted. However, aspect ratios up to 6.5 are expected to be achievable on 100  $\mu\text{m}$ -diameter posts as well if using a gap of 40  $\mu\text{m}$  in between them. Higher aspect ratios were not achieved due to the fact that the mechanical strength of the post is overwhelmed by stiction forces developed during blow-drying using a nitrogen gun. This is clear by the fact that 25  $\mu\text{m}$  diameter posts which are expected to be 333  $\mu\text{m}$  tall (and aspect ratio equal to 13:1) show catastrophic mechanical failure but remain attached to the substrate (Fig. 2.10b). Improvements to basic photolithography must be made to achieve higher aspect ratios and smaller structures. The use of critical point drying (more details below under drying) minimizes stiction forces<sup>7</sup> and allows aspect ratios up to 8.8:1 when patterning a 444  $\mu\text{m}$ -thick layer as 50  $\mu\text{m}$ -diameter posts (top curve on Fig. 2.10a). The use of adhesion promoters such as MicroChem Omnicoat could enable the fabrication of thin posts (diameter < 20  $\mu\text{m}$ ) with high aspect ratios. The fabrication of such posts on top of an existent SU-8 layer, thinner and wider than the post, can also prove beneficial. Since the interest here is on posts of diameter greater than 40  $\mu\text{m}$ <sup>8</sup> the fabrication process is optimized accordingly. No

---

<sup>7</sup> Increasing the gap between the posts also reduces stiction forces. However, DEP applications require small gaps as detailed in the beginning of section 2.2.1 Electrodes

<sup>8</sup> thick posts translate to more surface area and thus provide with more trapping volume, and higher throughput, for DEP applications. Tall channels containing tall posts enable the use of high flow rates, and shorter processing times, while maintaining the particle hydrodynamic drag force at a strength that is below a given DEP trapping force

adhesion promoters are used in this work but the SU-8 posts that will become carbon electrodes for DEP applications are fabricated on top of an existent SU-8 layer. After pyrolysis, this SU-8 layer becomes carbon and acts as electrical connection from the function generator to the base of the electrodes.

### ***Spin Coating***

Different SU-8 photoresist compositions were acquired from MicroChem (Newton, MA) and used to fabricate various geometries of different thicknesses (Table 1.3 in chapter 1 resumes the physical properties of all commercially available SU-8 photoresists). SU-8 10, 25 and 2010 were used to fabricate the precursor polymer structure for 2D carbon electrodes or for the layer that will become the electrical connection pads and leads to the base of 3D carbon electrodes. SU-8 25, 50 and 2150 were used to fabricate the precursor posts for 3D carbon electrodes. Table 2.3a resumes all spin programs used in this work and the resultant layer thickness.

A photoresist can be deposited on a substrate using different techniques such as spray, electrodeposition, casting and lamination (for a detailed review on deposition techniques the reader is referred to Madou et al). Spin coating is used in this work because the thickness of the deposited layer can be precisely controlled by optimizing the spin parameters. All substrates were coated using a programmable spinner (Laurell Technologies Corporation, North Wales, PA model WS-400B-6NPP/LITE). The photoresist is poured directly from the bottle to the substrate right above the substrate axis of rotation. As the photoresist flows onto the substrate it first takes the shape of a cone but later becomes an expanded, or coin-shaped, cylinder. Upon rotation at low speed (500 – 1000 rpm) this cylinder gradually expands side-ways until the centrifugal force

that causes the photoresist to flow towards the edges is in equilibrium with the surface energy of the substrate. Depending on the substrate size, the photoresist may not coat the complete substrate during this spreading step. The rotation speed is then increased (usually to a speed between 1000 and 4000 rpm) to completely coat the substrate, if it hasn't been already, and thin down the photoresist layer to a desired thickness. Speed, acceleration and time of rotation together with the size of the substrate play an important role on the definition of the layer thickness. The influence of the substrate size is first addressed. Other than the speed of rotation the centrifugal force acting on a photoresist fluid element depends on the distance of that element to the spin axis. Large distance translates to a strong force. The use of small substrates over bigger ones leads to a centrifugal force that is less effective on thinning down the photoresist layer given all other parameters are the same (compare Posts 5 and 6 in Table 2.3b where a reduction on substrate size yields an increase of 30  $\mu\text{m}$  in thickness). The layer thickness can also increase due to back-flow of the photoresist that got accumulated at the edge of the substrate during spin coating. This edge bead can be eliminated by rotating at even higher speeds than the layer thinning step or by rinsing the edges of the substrate with a SU-8 dissolver (MicroChem's Edge Bead Removal, SU-8 developer or acetone). If no action is taken to eliminate the edge bead, as in the case of this work, the photoresist will likely flow back towards the substrate center during soft-bake in an attempt to minimize its surface area. This effect is more pronounced when coating thick layers ( $> 50 \mu\text{m}$ ) since the photoresist composition is usually more viscous than those used to coat thin layers. High viscosity and the use of small substrates promote the formation of thicker edge beads and thus there is more resist that flows back during baking, when the viscosity

decreases. Given a substrate size, the layer thickness is inversely proportional to spin speed. Low spin speeds yield thinner layers than high spin speeds. For example, a decrease of 800 rpm in the rotation speed yields an increase of 160  $\mu\text{m}$  in the layer thickness (compare Posts 6 and 7 in Table 2.3b). Variations on the time of rotation may be used to fine tune the thickness of the layer or to improve layer uniformity. Long rotation times translate to thinner and more uniform layers.

### ***Soft bake***

After spin coating, the photoresist must be soft-baked (also known as pre-baking or pre-exposure baking) to evaporate the casting solvent. The rate of solvent loss is determined by the solvent diffusion coefficient. This number increases with temperature and has been suggested to decrease exponentially with the amount of solvent present in the polymer-solvent system<sup>194,195</sup>. Experimental data suggest that the bulk of solvent contained in the photoresist evaporates within the first five minutes of the bake<sup>196</sup>. Since the amount of solvent in the resist exponentially decreases with baking time, the solvent evaporation rate also reduces exponentially as soft bake time increases. All samples in this work were baked on a leveled hotplate (Dataplate®) set at 95 °C for different times. Hot plating the resist is faster, more controllable, and does not trap solvent like convection oven baking does. In convection ovens the solvent at the top surface of the resist is evaporated first, and this can cause an impermeable resist skin, trapping the remaining solvent inside. Baking times range from 5 to 180 minutes depending on the layer thickness and the type of SU-8 used. The baking times used in this work are an approximate 20% longer than those suggested in the MicroChem SU-8 processing datasheet. They are used to guarantee the complete evaporation of the casting solvent and to prevent line broadening

during exposure caused by traces of solvent in the matrix. The casting solvent in the original SU-8 is gamma-butyrolactone while the solvent in the SU-8 2000 series is cyclopentanone. Since the latter is a more volatile compound the soft-baking times of a given layer thickness can be shortened. However, the difference in the evaporation rates tends to disappear as the thickness of the layer increases<sup>196</sup>. In general, thick resists may benefit from a longer bake time to completely remove the solvent. Table 2.3b resumes the soft bake times used in this work depending on the layer thickness and type of SU-8 photoresist.

### ***Exposure and Post Exposure Bake (PEB)***

After soft baking, the coated substrate is transferred to an illumination or exposure system where it is aligned to the features on a photo mask. The photo masks used in this work were Mylar<sup>®</sup> films printed using a high resolution plotter. The masks were acquired from CAD/Art Services Inc. (Bandon, OR). A Karl SUSS MicroTec MA/BA6 Mask Aligner in soft contact mode<sup>9</sup> and equipped with a broadband mercury lamp is used for exposure. The intensity of the light created by the lamp is fixed at  $10 \text{ mW}\cdot\text{cm}^{-2}$ . Exposure time is used here to control the energy dose,  $D$ , used to create a strong acid that initiates cross-linking in the SU-8 layer (the dose, in  $\text{J}\cdot\text{cm}^{-2}$ , is the product of incident light intensity, in  $\text{W}\cdot\text{cm}^{-2}$ , and exposure time, in seconds). SU-8 photoresists feature a high absorption of energy of wavelengths that are less than 350 nm. One of the main reasons for this is that triarylsulfonium hexafluoroantimonate salt, used as photo acid generator in

---

<sup>9</sup> Contact mode can be classified as soft contact and hard contact depending on the amount of contact pressure between the resist and the mask, with higher pressures being applied in hard contact mode. Exposure in a contact setup results in a 1:1 image of the entire mask onto the photoresist

the SU-8 photoresist formulations used here, has absorption bands at 231.5 nm, 268.5 nm and 276 nm, as measured in methanol solution (Crivello et al. 1979). When SU-8 is exposed using a broadband mercury lamp, UV light shorter than 350 nm is strongly absorbed at the photoresist top surface. This causes the creation of more acid that diffuses sideways and polymerizes a thin layer along the top surface of the resist film that can establish mechanical contact between neighboring structures. This effect is commonly known as *T-topping* and selective filtration of the light from the light source is required to eliminate it. Mechanical contact between SU-8 posts translates to electrical contact between carbon electrodes which prevents the creation of the electric field gradient required in DEP applications. Although commercial bandpass filters for 365 nm wavelengths are commercially available, for example the Hoya UV-34 filter used by Lee et al <sup>197</sup> or those sold by Asahi Spectra and Omega Optica Labs, two filters were fabricated in-house following the work by Reznikova et al <sup>198</sup>. Glass plates (2" or 5" square) were first cleaned by immersion in piranha solution (3 parts H<sub>2</sub>SO<sub>4</sub> per one part of H<sub>2</sub>O<sub>2</sub>). The glass substrates were then rinsed with water, acetone and IPA, blown dry and dehydrated in an oven set at 120 °C. The fabrication procedure for each of the filters is detailed in Table 2.3a and b as Filter 1 and 2. The amount of transmitted light of 365 nm wavelength for each of the filters was measured using an UV-meter. Filter 1 features a transmission coefficient of .342 while Filter 2 has a coefficient equal to .15. A coefficient of 1 means perfect transmission. The filters were introduced in the optical pathway between the light source and the mask positioned above the SU-8 layer to be patterned. Filters were only used when fabricating SU-8 posts. Equation 2.6 must be used

to account for the light attenuation factor and deliver a proper radiation dose to the photoresist.

$$\textit{Experimental dose} = \frac{\textit{Recommended dose}}{\textit{Transmission percentage}} \quad (2.6)$$

The recommended dose is that suggested in the SU-8 processing datasheets, while the experimental dose is the one implemented in practice. Underexposure of the photoresist causes the intended pattern to dissolve or to lift off during developing because the cross-linking acid concentration was not enough to start polymerizing the resist all the way down to the underlying substrate. Overexposure leads to extreme T-topping and pattern broadening.

In the case of a chemically amplified resist, such as SU-8, the post-exposure bake (PEB) is critical to complete the cross-linking of the polymer matrix. Thermal energy complements the radiation energy delivered during exposure to finalize cross-linking. The amounts of radiation and thermal energy can be optimized depending on the pattern being fabricated. Large-area patterns that are far apart benefit from increased radiation but reduced thermal energy. In contrast, small-area features with small gaps in between them benefit from high thermal but low radiation energy. High radiation doses are likely to create T-topping on the structures. High thermal energies can create a significant amount of stress in the structure that can cause them to bend and detach from the substrate. More than time, PEB temperature is of crucial importance; longer times at lower temperatures are recommended. High PEB temperatures have been shown to induce a high amount of internal stress in the structure when using traditional substrates such as silicon and glass. The reason behind this is the significant difference between the coefficients of thermal expansion (CTE) of SU-8 and the substrate. Thermal stresses

increase with resist thickness and can cause cracking of the pattern's surface, structure bending or complete peeling from the substrate in the worst cases. These defects are most likely to be present in extended, large surface area features and those with sharp angles but can be minimized by optimizing the time and temperature of the bake. On the other hand, insufficient PEB times and/or temperatures which are too low yield structures that are not completely cross-linked and can be attacked by the developer. This causes extremely high surface roughness or even complete dissolution of the photoresist. MicroChem's processing datasheets recommend post-exposure bake to be carried out at 95 °C but temperatures between 55 and 75 °C and extended baking times have been suggested to minimize internal stresses in the pattern. Temperatures below 55 °C do not polymerize the matrix completely regardless of the bake time<sup>184</sup>. Rapid heating and cooling of the resist should be avoided as swift temperature changes induce a significant amount of stress.

Table 2.3b shows the exposure dose and post-exposure bake parameters used for the patterning of different layer thickness. Layers which are thinner than 100 µm can be easily fabricated following the parameters recommended in MicroChem's datasheet. Variations of up to 20% in the values recommended there do not significantly change the quality of the pattern. As the layer thickness is increased above 100 µm and the gap between the patterns decrease, more significant variations on the exposure dose must be introduced to prevent T-topping. The post-exposure bake must then be adjusted accordingly. For example, a dose between 320 and 550 mJ·cm<sup>-2</sup> and PEB times of 10 minutes at 95 °C are recommended in the datasheet for layer thickness of 100 µm. In this work a combination of net exposure dose (given by the product of the exposure time,

light intensity and transmission coefficient of the filter used) of  $78 \text{ mJ}\cdot\text{cm}^{-2}$  and a 15 minute PEB bake is used to fabricate a similar layer (Posts 3 in Table 2.3).

### ***Development, Drying and Hard bake***

Development is the dissolution of un-polymerized SU-8 that transforms the latent resist image, formed during exposure, into a relief topography. In general, two main technologies are available for resist development: wet development and dry development. The latter is starting to replace wet development for some of the ultimate line-width resolution applications but wet development is still widely used in a variety of applications, including SU-8 photolithography. The development of SU-8 patterns exploits the variation in molecular weight of the cross-linked polymer. During the development of SU-8, those areas that were not cross-linked dissolve upon immersion in Propylene Glycol Methyl Ether Acetate, or PGMEA (sold by MicroChem as SU-8 developer). Constant agitation during development is recommended to constantly feed fresh developer to the resist pattern and decrease developing times but care must be taken when developing high aspect ratio structures, as excessive agitation can cause mechanical breakage. Agitation can be conducted manually, as in this work, or with a rotator. An alternative to mechanical agitation is the use of a sonicator bath. The use of megasonic frequencies instead of ultrasonic ones proves beneficial in the development of high aspect ratio structures. An important distinction between the two sonication methods is that the higher megasonic frequencies (800 – 2000 kHz) do not cause the violent cavitation effects found with ultrasonic frequencies (15-400 kHz). This significantly reduces or eliminates cavitation erosion that can lead to pattern fracture and structure debonding from the substrate<sup>185</sup>.

The development step implemented in this work was done using a glass or propylene beaker in case of immersion and a normal rinse bottle in the case of rinsing. Table 2.3b shows the type of development done for different layers. Thin layers ( $<5 \mu\text{m}$ ) benefit from rinsing developer on the substrate instead of immersing them in it. The use of a developer bath may lead to detachment of the cross-linked thin layer from the substrate. Layers with a thickness in the range from 5 to 20  $\mu\text{m}$  were developed by immersion and using a constant, vigorous manual agitation. Thicker layers patterned as posts were developed by immersion in PGMEA for different times. The bath was sporadically agitated by slowly and manually rotating the beaker one or two revolutions.

Post stiction may be obtained during the drying of dense arrays of high aspect ratio posts. Stiction forces developed in narrow gaps are strong enough to bend and join SU-8 patterns together during drying as shown in Fig. 2.3. The replacement of PGMEA by a liquid with lower surface tension is recommended for the prevention of structure collapse during the resist drying process. In this work the SU-8 pattern resulting after development is rinsed with IPA using a rinse bottle. The pattern is then blown-dried using a nitrogen gun. This approach led to posts with aspect ratio up to 3 and gaps in between them down to 20  $\mu\text{m}$ . If higher aspect ratios are desired alternative drying methods must be implemented. The use of liquids with lower surface tension than IPA such as perfluorohexane rinse has been suggested<sup>193</sup> as well as freeze-drying<sup>199</sup> and supercritical drying<sup>200,201</sup>. In a supercritical liquid, the surface tension becomes negligible and the capillary force that causes pattern stiction is nonexistent. A commercial supercritical drying system (Tousimis Samdri® [www.tousimis.com](http://www.tousimis.com)) is used in this work to achieve posts with aspect ratio up to 9:1 when the gap in between them is 40  $\mu\text{m}$ . The substrate

containing the pattern is first transferred from the developer bath to a beaker containing IPA. The substrate is then transferred from IPA to the machine chamber which was previously filled with high purity (>99%) IPA (Sigma Aldrich). After sealing the chamber the machine starts an automatic process that replaces the IPA with carbon dioxide and brings it to its supercritical point. The bulk of the work presented here did not include the use of critical point drying. The height of the posts obtained by just replacing PGMEA by IPA and then blowing the samples dry was sufficient for this work. Acetone may be used for a final cleaning of the structure. An acetone rinse is more efficient than PGMEA and IPA on rinsing SU-8 residues. However, such rinse must be quick since prolonged contact of the cross-linked SU-8 with acetone at this point may cause pattern swelling and degradation. The cause for this acetone attack is that after development and before hard bake the SU-8 matrix still contains residual solvent that provide entry points for acetone to attack. After hard bake and once all residual solvent has been released, SU-8 is immune to acetone attack. This cleaning step using acetone was not implemented when using critical point drying.

All samples were hard baked for 10-15 minutes at 95 °C using a hot plate to evaporate all residual solvent, improve adhesion to the substrate and anneal the polymer matrix.

### 2.1.3 Pyrolysis and de-scumming

Pyrolysis of SU-8 structures was conducted on a Thermco Mini-Brute MB-71 diffusion furnace featuring a quartz tube. Nitrogen (Praxair) gas was flowed at 2000 sccm (standard cubic centimeters per minute). Details on the pyrolysis process are given in chapter 1. All pyrolysis processes used in this work featured a final temperature of 900 °C. Samples were brought to this temperature using either a one- or two-step heating ramp. A one-step ramp featured a rate of 10 °C/min to heat the samples directly from 25 to 900 °C. A two-step ramp was used to first heat the sample from 25 to 300°C at 25 °C/min and then from 300 to 900 °C at 10 °C/min. A dwell time of 30 minutes was used at 300 °C following previous studies suggesting that SU-8 may liberate oxygen during heating <sup>74</sup>. The dwell allows for enough time for the oxygen to be evacuated from the furnace before ramping it up to 900 °C and prevents SU-8 from burning. However, the results obtained with both pyrolysis protocols do not show a significant difference and the shorter protocol was adopted to reduce the processing time. Furnace was held at 900 °C for 1 hour when using either protocol to complete pyrolysis. The furnace was then turned off and allowed to cool down naturally. The furnace reaches a temperature of 200 °C after 5-6 hours and a room temperature after 8 hours. Samples may be taken out once the furnace temperature is below 200 °C. Examples of carbon electrodes and their connecting leads are shown in Fig. 2.11. Different electrode heights were obtained depending on the height of the precursor posts as detailed in Table 2.4. The SU-8 precursor structures shrink during pyrolysis as it can be observed by comparing the resultant carbon structures and the footprint left by the original polymer structures (dashed circles and lines in the figure). The carbon posts with highest aspect ratio

fabricated in this work (7.9:1) are shown in Fig. 2.12a. These carbon structures, and those in Fig. 2.12b with aspect ratio 4.2:1, resulted from the pyrolysis of the SU-8 structures obtained using critical point drying as detailed above. Such structures were not used for DEP experiments since their fabrication in arrays featuring gaps less than 40  $\mu\text{m}$  in between individual posts proved to be challenging. The highest aspect ratio carbon posts used as electrodes for DEP experiments were those obtained after the pyrolysis of SU-8 structures fabricated following the procedure of Posts 5 in Table 2.3. These carbon electrodes featured an aspect ratio of 2.7:1 given their 26  $\mu\text{m}$ -diameter and 73  $\mu\text{m}$ -height in Table 2.4. In this case, gaps down to 20  $\mu\text{m}$  were achieved without the need for critical point drying.

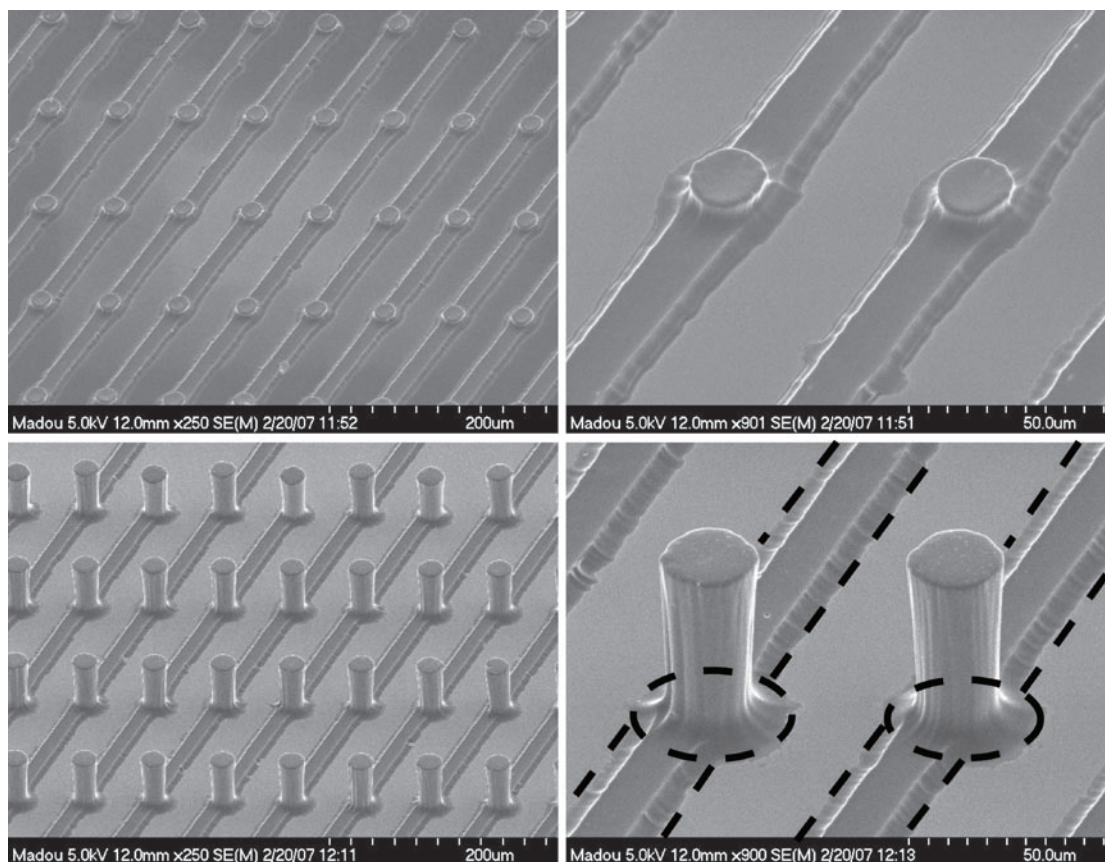


**Fig. 2.11** Examples of carbon electrodes and their connecting electrical leads. The dashed lines represent the footprint of the precursor SU-8 structures and serve as reference point to determine shrinkage during pyrolysis

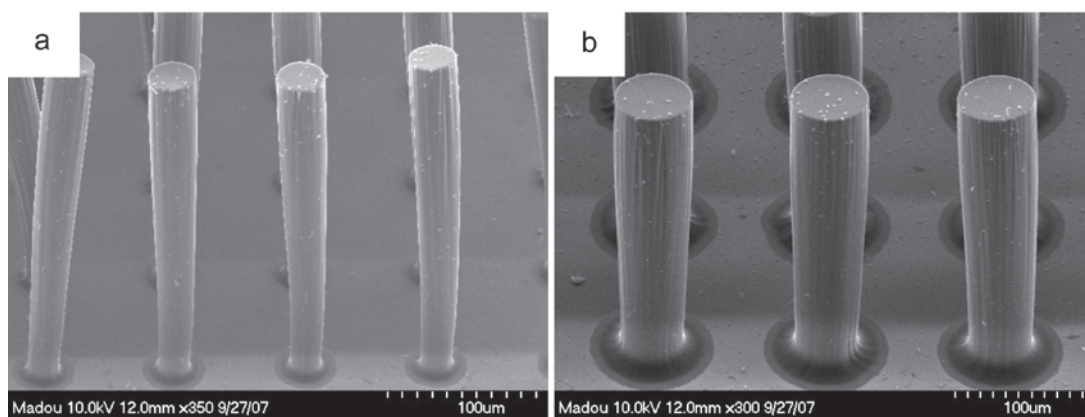


**Fig. 2.12** Carbon structures of aspect ratio a) 7.9:1 and b) 4.2:1 resulting from the pyrolysis of SU-8 posts dried using critical point drying

Table 2.4 resumes the dimensions of all SU-8 posts and the resulting carbon structures fabricated in this work. The measurements were obtained using a Hitachi S-4700-2 FESEM. The table also shows the height reduction of the planar SU-8 interdigitated fingers and connection pads. The height of the SU-8 and carbon layers was measured using a Dektak3 surface profiler. The fabrication process of all SU-8 posts leading to the carbon posts detailed in Table 2.4 can be found in Table 2.3 by correlating the ID tags (first column) of both tables.

The amount of shrinkage depends on the dimensions of the precursor. Shrinkage up to 86% is present when pyrolyzing structures as thin as 1.3  $\mu\text{m}$ . Shrinkage decreases as the dimensions of the precursor increase. SU-8 structures with height greater than 333  $\mu\text{m}$  feature a shrinkage of just 38%. Figure 2.13 illustrate this trend. The shrinkage percentage depending on the height of the SU-8 structure is plotted as a dashed line fitted to experimental points (circles). The solid line represents the height of the carbon structures depending on the height of the SU-8 precursor. The line is fitted to experimental points (triangles).

**Table 2.4** Dimensions of all SU-8 and carbon posts fabricated in this work

ID tag	SU-8			Carbon			Shrinkage		AR <sub>carbon</sub> AR <sub>SU-8</sub>	Remarks
	<i>h</i>	∅	AR	<i>h</i>	∅	AR	<i>h</i>	∅		
PLANAR INTERDIGITATED FINGERS THAT WILL BECOME ELECTRICAL LEADS										
Leads 1	8.95	-	-	1.38	-	-	0.84	-	-	
Leads 2	9.67	-	-	1.49	-	-	0.84	-	-	
Leads 3	11.2	-	-	1.51	-	-	0.86	-	-	
Leads 4	16.67	-	-	2.38	-	-	0.85	-	-	
Leads 5	19.1	-	-	2.55	-	-	0.86	-	-	
POSTS THAT WILL BECOME ELECTRODES										
Posts 1	22.52	50	0.45	5.6	22.5	0.24	0.75	0.54	0.54	used for DEP
Posts 2	98	20	4.9	50.911	12.5	4.07	0.48	0.37	0.83	
	98	25	3.92	56.56	17	3.32	0.42	0.32	0.84	
	98	50	1.96	48.64	33	1.47	0.50	0.34	0.75	
	98	100	0.98	53.59	62	0.86	0.45	0.38	0.88	
Posts 3	100	50	2	40.19	21.5	1.86	0.59	0.57	0.93	used for DEP
Posts 4	130	50	2.5	60	25	2.4	0.53	0.5	0.92	used for DEP
Posts 5	144	50	2.78	73	26	2.70	0.49	0.48	0.97	used for DEP
Posts 6	173	50	3.46	86.16	34.5	2.49	0.50	0.31	0.72	
	173	100	1.73	84.59	67.1	1.26	0.51	0.32	0.72	
Posts 7	333	50	6.66	206.3	32.5	6.34	0.38	0.35	0.95	
	333	100	3.33	210.23	64	3.28	0.36	0.36	0.98	
Posts 8	444	50	8.88	273.15	34.5	7.91	0.38	0.31	0.89	highest AR
	444	100	4.44	273.93	64.73	4.23	0.38	0.35	0.95	

**Notes:** *h* denotes height, ∅ diameter and AR aspect ratio. Shrinkage = 1 - (carbon dimension / SU-8 dimension)

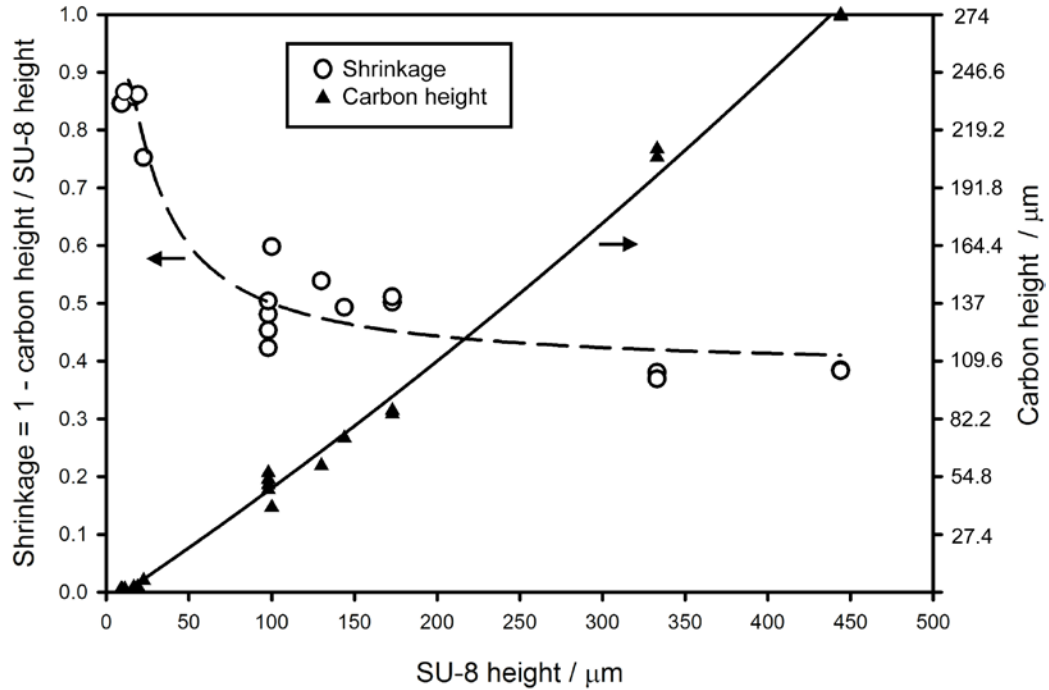


**Fig. 2.13** Experimental results depicting the rate of change on shrinkage (left axis) and carbon height (right axis) as the height of the precursor SU-8 structure varies

The shrinkage obtained at all dimensions is slightly less than isometric. Fig. 2.14 shows the comparison between the aspect ratios of the SU-8 and carbon structures. The diamonds in the graph represent experimental points (column  $AR_{\text{carbon}}/AR_{\text{SU-8}}$  in Table 2.4). The straight lines denote different degrees of shrinkage symmetry. The shrinkage is isometric, 100% symmetric, when the height and diameter of the post shrink in the same proportion (solid line). Shrinkage percentages higher than 100 translate to a bigger shrinkage in diameter than in height while percentages lower than 100 denote the contrary (bigger shrinkage in height than in diameter). The dotted and dashed lines represent shrinkage symmetry percentages of 90 and 80 respectively. The dotted line (90% shrinkage symmetry) is well centered among the experimental data points which supports the fact that post shrinkage is slightly less in diameter than in height. This result

is suspected to be due to the adhesion force that competes with the shrinkage force at the interface between the substrate and the SU-8 pattern and prevents further shrinkage of the post diameter. Free-standing SU-8 structures are expected to shrink isometrically.

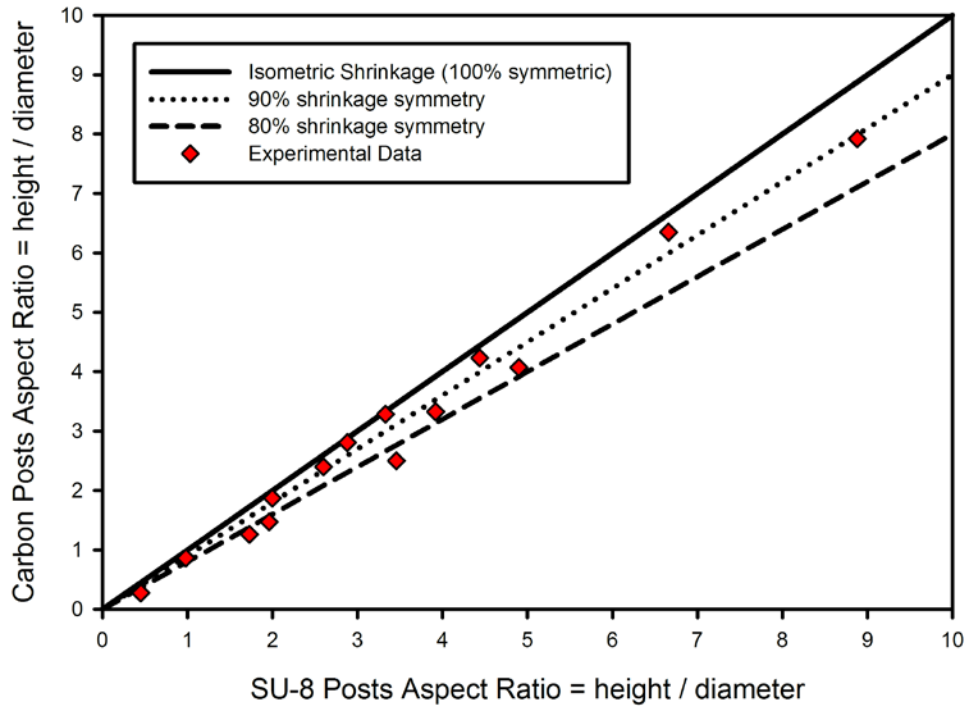


**Fig. 2.14** Comparison between the aspect ratio of the carbon structures and their precursor SU-8 posts

The competition between adhesion and shrinkage forces is also responsible for the characteristic curved wall profile at the base of the carbon posts (Figs. 2.11 and 2.12). If the shrinkage force generated during the pyrolysis of a given precursor structure is stronger than the adhesion force, the pattern will detach from the substrate. The trend was first demonstrated by Turon-Teixidor and resumed in Fig. 2.15 under his permission. A SU-8 layer of thickness equal to 25, 35 and 45  $\mu\text{m}$  (Fig. 2.15 a, b and c respectively) was patterned as discs or cylinders of different diameters on a silicon dioxide substrate and pyrolyzed following a similar protocol as the one described above. The cut-off diameter

to prevent detachment of the carbon structures depends on the initial SU-8 thickness. The patterning of a 25  $\mu\text{m}$ -thick SU-8 layer allows for the fabrication of discs as wide as 1450  $\mu\text{m}$  (possibly wider but results are not available) as shown in Fig. 2.15a. Increasing the thickness to 35  $\mu\text{m}$  limits the cut-off diameter to 400  $\mu\text{m}$  (Fig. 2.15b). A further increase of thickness to 45  $\mu\text{m}$  makes the cut-off diameter decrease to 100  $\mu\text{m}$  (Fig. 2.15c). Therefore the diameter of the pattern is inversely proportional to the layer thickness. SU-8 posts as tall as 444  $\mu\text{m}$  and featuring a 100  $\mu\text{m}$ -diameter were successfully pyrolyzed as demonstrated above and suggest that tall posts benefit from the use of diameters equal or less than 100  $\mu\text{m}$ . Based on the practical experience of this author patterns that require surface areas larger than 5 millimeters square (such as the connection pads described above) benefit from the use of layers thinner than 20  $\mu\text{m}$ . The possibility of detachment greatly increases if the precursor layer thickness is above this value.

The carbon electrodes must be treated with oxygen plasma for de-scumming after pyrolysis. This treatment eliminates any electrical connections between them. These imperceptible connections are likely due to the carbonization of SU-8 residues left during development. Oxygen plasma generated at a pressure of 200 mTorr and power 250 W is used for 1 min to eliminate them. If no connections are present, the resistance value between electrodes must be in the order of tens of  $\text{M}\Omega$ . Thicker connections than those made by carbon derived from SU-8 residues require the use of other measurements to eliminate them, such as mechanical breakage using a point probe. The use of longer or more powerful plasma treatments is not recommended since the electrical conductivity of the thin ( $\sim 1.5$   $\mu\text{m}$ ) connection pads may be severely compromised due to significant

thickness reduction. Carbon resulting from T-topping between SU-8 structures must be broken by mechanical means instead of using oxygen plasma.

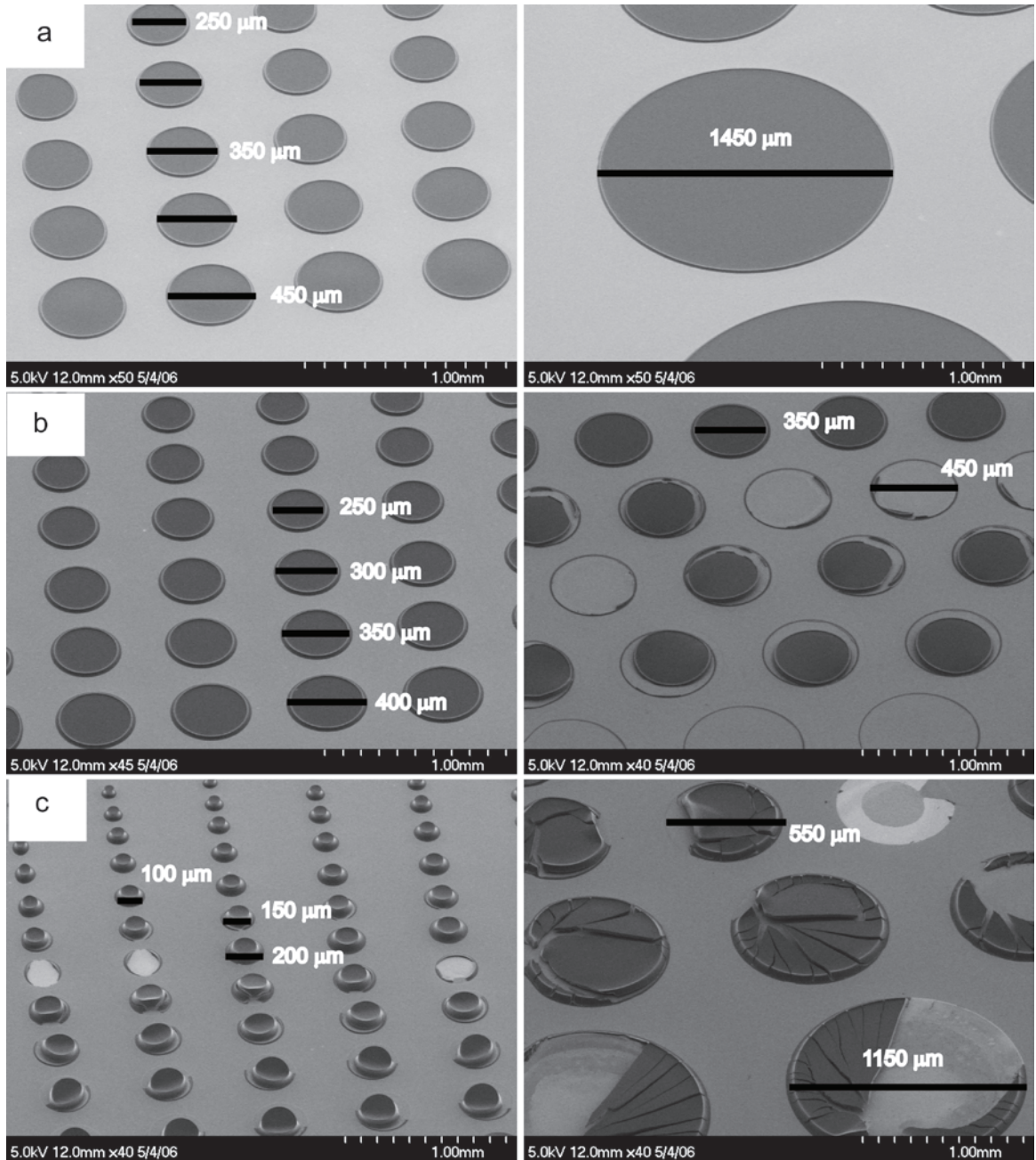


**Fig. 2.15** The carbon structures can detach from the substrate during pyrolysis. Detachment depends on the thickness of the precursor SU-8 layer. a) A layer thickness of 25 μm allows for discs up to 1450 μm. b) The cut-off diameter decreases to 400 μm as the layer thickness increases to 35 μm. c) The use of 45 μm-thick layers does not allow for cylinders wider than 100 μm.

### 2.1.4 Electrical characterization of carbon electrodes

The electrical conductivity of glass-like carbon after de-scumming was determined using a four point probe setup illustrated in Fig. 2.16. The two outer probes establish an electrical circuit for the DC current generated by the current source (Keithley Instruments 225) to flow through the sample. The DC current is constant throughout the experiment and is measured using an amperometer A (Fluke 8060A True RMS Multimeter). The inner probes are connected to a voltmeter V (Fluke 87 V True RMS Multimeter) used to measure the voltage drop between them. The distance between probes is approximately 200  $\mu\text{m}$ . The probes, mounted on micromanipulators, are positioned manually with the aid of a microscope. The resistance of all connecting cables was measured to be negligible ( $< 1 \Omega$ ).

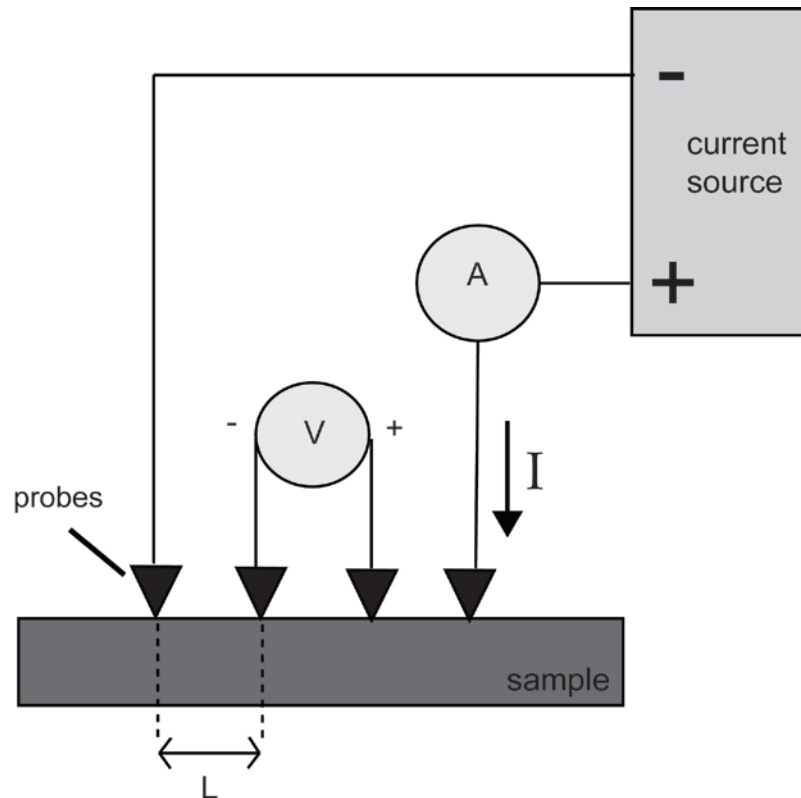


**Fig. 2.16** A four point probe station

In the case of a semi-infinite thin sheet of material (thickness  $\ll$  surface area) the resistivity of the material can be calculated as

$$\rho = \textit{thickness} * R_s = \frac{\pi t V}{I \ln 2} \quad (2.7)$$

where  $t$  equals thickness,  $V$  voltage and  $I$  current. The sheet resistance  $R_s$  is given by

$$R_s = \frac{kV}{I} \quad (2.8)$$

where  $k$  equals  $\pi/\ln 2$  in the case of semi-infinite thin sheets. Multiple current and voltage measurements were conducted on carbon films of different thickness as detailed in Table 2.5. The thin carbon films were fabricated on silicon/silicon oxide substrates following the pyrolysis of a SU-8 film fabricated using the protocol Leads 2 in Table 2.3 and using flood exposure. The thick carbon films resulted from the pyrolysis of free-standing SU-8 films fabricated following the methodology detailed previous work of this same author<sup>112</sup>. Briefly, an SU-8 layer is deposited on polyester films and photo-patterned; the resultant SU-8 patterns are then peeled off from the polyester substrate and pyrolyzed. The thick carbon films were positioned on top of a glass substrate prior to resistance measurements. The sheet resistance is dependent on sheet thickness and thinner sheets have higher resistance than thicker ones. The resistivity of the carbon is independent from sheet thickness and the average value obtained in this work ( $0.982164 \times 10^{-4} \Omega \cdot \text{m}$ ) agrees with that obtained previously ( $1.04 \times 10^{-4} \Omega \cdot \text{m}$ )<sup>202</sup>. The resistivity of glass-like carbon is compared to that of different materials in Table 2.6. Carbon is four orders of magnitude more resistive than silver.

**Table 2.5** Resistivity characterization of glass-like carbon obtained in this work

Measurement	Current $I$ ( $\mu\text{A}$ )	Voltage $V$ (mV)	Sheet Resistance $R_s$ ( $\Omega \cdot \square$ )	Resistivity $\rho$ $\times 10^{-4} (\Omega \cdot \text{m})$
sheet thickness = 1.5 $\mu\text{m}$				
1	456.5	6	59.57152	0.893573
2	456.5	6.3	62.5501	0.938251
3	456.5	5.7	56.59295	0.848894
4	456.5	6.7	66.52153	0.997823
5	456.5	6.5	64.53582	0.968037
6	456.5	6.5	64.53582	0.968037
7	456.5	6.1	60.56438	0.908466
8	456.5	5.8	57.58581	0.863787
sheet thickness = 170 $\mu\text{m}$				
1	11560	1.83	0.717499	1.21975
2	11560	1.79	0.701816	1.19309
3	11560	1.58	0.61948	1.05312
4	11560	1.4	0.548907	0.933141

**Table 2.6** Resistivity of different materials compared to glass-like carbon

Material	Resistivity ( $\Omega \cdot \text{m}$ )
Silver	$1.59 \times 10^{-8}$
Copper	$1.72 \times 10^{-8}$
Platinum	$1.06 \times 10^{-7}$
Graphite	$\sim 1 \times 10^{-5}$
Glass-like carbon from SU-8 pyrolyzed @ 900 $^{\circ}\text{C}$	$0.982164 \times 10^{-4}$
Glass	$10^{10}$

The resistivity value obtained above is used next to estimate the resistance of the connection pads, the electrical connecting leads from the pad to the base of the electrodes and the electrodes used in carbon-DEP devices. The ohmic resistance  $R$  of a conductor is calculated as

$$R = \rho \frac{l}{A} \quad (2.9)$$

where  $\rho$  is the resistivity of the material and  $l$  and  $A$  are the length and cross-sectional area of the conductor respectively. The cross-sectional area of the connection pads and leads was assumed to be rectangular. The dimensions are 1.5  $\mu\text{m}$ -thickness and 20 mm-width for connection pads and 1.5  $\mu\text{m}$ -thickness by 25  $\mu\text{m}$ -width for connecting leads. The cross-sectional area of the electrodes is that of a circle with diameter equal to 25  $\mu\text{m}$ .

Equation 2.9 was used to calculate the resistance of the different structures used in this work: connection pads, connection leads and electrodes. A resistance change of  $78 \Omega$  over a distance of 24 mm was obtained for the connecting pads and thus the voltage drop across the pad can be considered negligible. The voltage drop on the electrodes is also negligible since the resistance of a  $70 \mu\text{m}$ -tall electrode is merely  $14 \Omega$  (the resistance is only  $48 \Omega$  for a  $240 \mu\text{m}$ -tall post electrode). However, the resistance of the connecting leads increases significantly over its length as illustrated in Fig. 2.17. The electrode posts are positioned along the length of a given connecting lead and spaced  $143.2654 \mu\text{m}$  apart. Therefore, the closest an electrode is to the connection pad the less ohmic resistance is subjected to. For example, the resistance difference between a post positioned at a length of  $100 \mu\text{m}$  on the connecting lead and one positioned at  $243.2654 \mu\text{m}$  is  $375 \Omega$  assuming a lead cross-section area of  $1.5 \times 25 \mu\text{m}$ . The maximum length of the connecting leads used in this work averages  $950 \mu\text{m}$ . A maximum resistance close to  $2.4 \text{ k}\Omega$  is obtained at this length. The ohmic loss at the connection leads can be reduced by increasing their cross-section area. For example, Fig. 2.17 compares the resistance variation across the length of a  $1.5 \mu\text{m}$ -thick lead, as the ones used in this work, and a  $5 \mu\text{m}$ -thick one. The use of  $5 \mu\text{m}$ -thick leads decreases the resistance in 70%. However, the cross-section area of the leads must be balanced to prevent their detachment from the substrate as detailed in the Shrinkage section. Wide structures benefit from the use of low thicknesses. The fabrication of connecting leads out of metal instead of carbon proves beneficial to minimize the ohmic losses on the lead. More details are discussed in section 2.5.2.

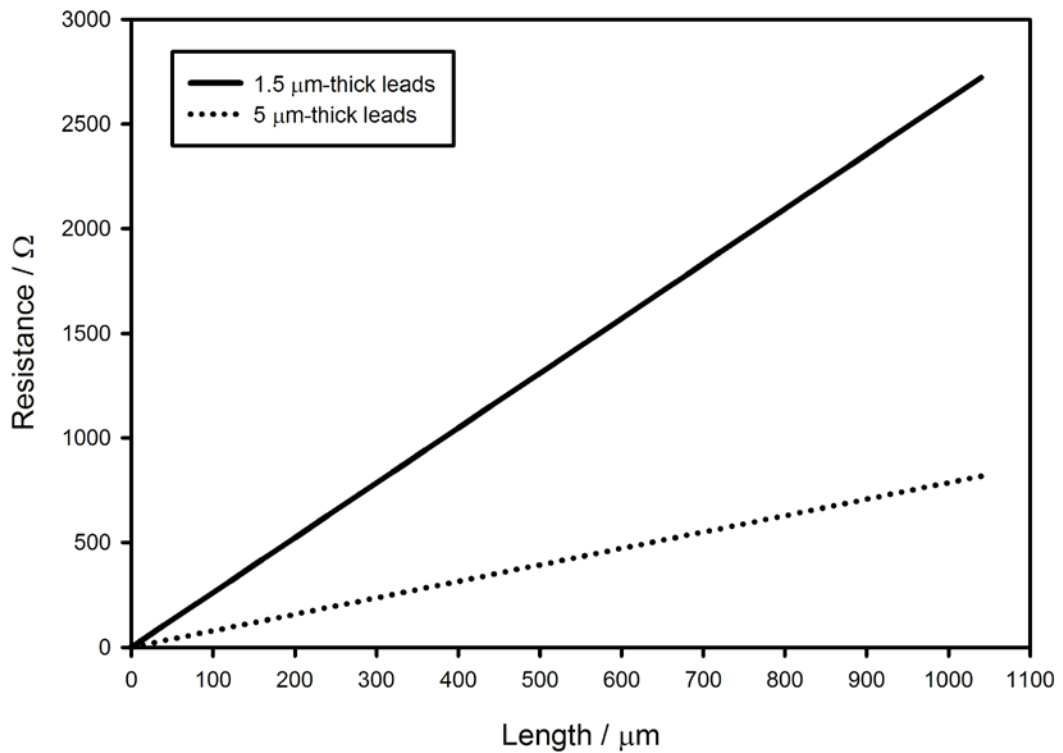


**Fig. 2.17** Resistance vs. length of leads with rectangular cross-sectional area given by either 1.5 or 5  $\mu\text{m}$ -thickness and 25  $\mu\text{m}$ -width

### 2.1.5 SU-8 cover layer

After de-scumming, the substrate containing the different carbon elements (pads, leads and electrodes) was rinsed with IPA and blown dry. A SU-8 layer is then patterned around the carbon electrodes as shown in Fig. 2.18 following the fabrication process of either Insulation 1, 2 and 3 in Table 2.3.

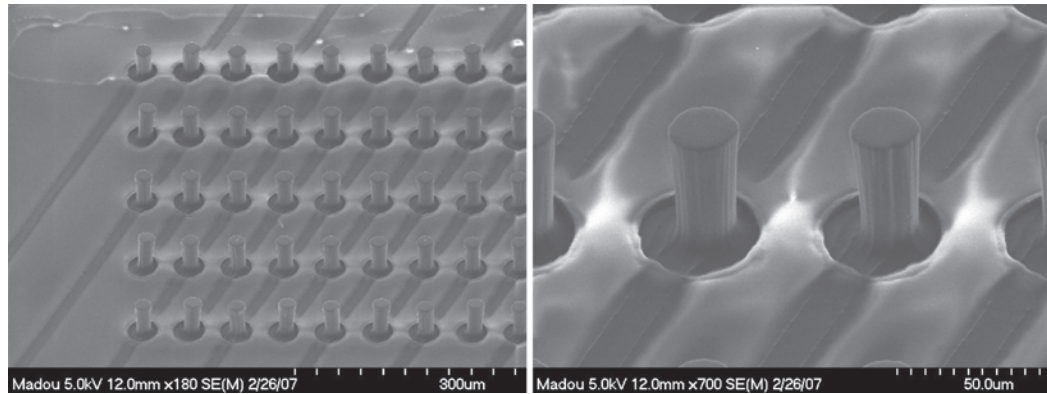


**Fig. 2.18** A thin SU-8 layer patterned around the electrodes

This layer has important implications. First, the SU-8 layer secures the thin connecting leads to the substrate and protects the carbon-substrate interface from attack of different solutions to be flowed through the carbon-DEP device including IPA, sodium dodecyl sulfate (SDS) and NaOH. Lead detachment during experiments was observed if a cover layer was not fabricated over the leads. Second, the thin layer planarizes the bottom of the fluidic channel and eliminates crevices that may otherwise act as physical traps for cells and other particles contained in the sample. A flat surface also allows for the eventual adherence of off-substrate microfluidics to this SU-8 layer (details in the next section). Lastly, the SU-8 cover layer acts as electrical insulator for the connecting leads and reduces the ohmic loss in them. The connection lead makes contact with the sample, when is not covered. Although covering the leads diminishes the electric field, and the trapping volume, created in the sample, the trapping volume created by the leads is insignificant to that created by the posts. The voltage along an SU-8 covered and not covered connection lead is plotted in Fig. 2.19 for different sample conductivities. These results were obtained using finite element analysis running on software (COMSOL Multi-physics). More details on the specifics of the simulation are given in chapter 3, section 3.1. The voltage applied at the connection pad is 5 V. The voltage decreases

proportional to the length of the lead at all sample conductivities but the loss is always less when the cover layer is used than when it is not. The difference on voltage loss between the two cases becomes more significant as the length of the lead and the conductivity of the sample are increased. At sample conductivities of  $10 \mu\text{S}\cdot\text{cm}^{-1}$  the use of the cover layer only yields a maximal improvement of  $0.0062 \text{ V}$  ( $\sim 0.1\%$ ) in the voltage loss but this value increases to  $0.2987 \text{ V}$  when the sample conductivity is  $1000 \mu\text{S}\cdot\text{cm}^{-1}$ . The use of the SU-8 layer in this last case reduces the voltage drop in the lead by 7%. The voltage drop is only reduced a maximum of 0.8% at sample conductivities of  $100 \mu\text{S}\cdot\text{cm}^{-1}$ . Therefore the impact of the cover layer on the reduction of the voltage loss in the connecting leads becomes significant at sample conductivities values higher than  $100 \mu\text{S}\cdot\text{cm}^{-1}$ .

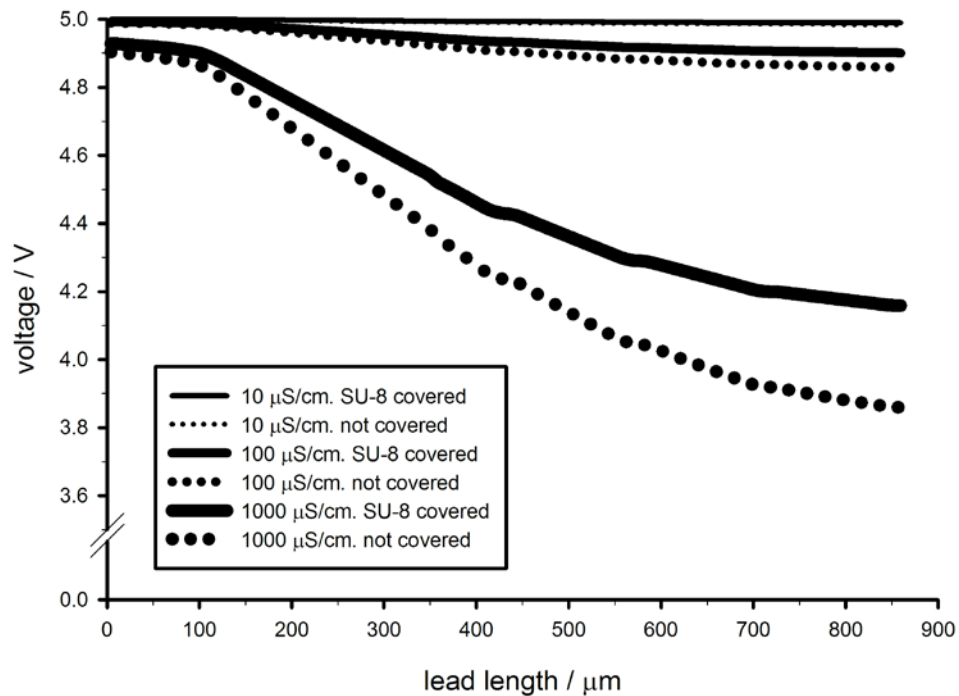


**Fig. 2.19** The voltage along a connection lead (covered or not covered by the SU-8 layer) at different sample conductivities

After patterning the cover layer, the 4" wafer holding the carbon electrode arrays may be cleaved along its crystalline planes into identical pieces if off-substrate microfluidics will be used. The wafers used in this work feature a crystal orientation of  $\langle 100 \rangle$  and thus can be cleaved into four identical pieces. This allows better manageability during the interface of off-substrate microfluidics to individual electrode arrays. The wafer is maintained in one-piece if on-substrate microfluidics will be fabricated.

## **2.2 Fluidic network**

The fluidic networks used in this work are classified as on-substrate where the network was fabricated around the electrodes or as off-substrate where the network was positioned around the carbon electrodes but fabricated in a process independent to the substrate containing the electrodes. The details of all fluidic networks used in this work are resumed in Table 2.6.

### **2.2.1 On-substrate**

A SU-8 layer was patterned as a channel around the carbon electrodes following the process detailed in the rows Channel 1 and 2 in Table 2.3. Channel 1 was used to pattern a 50  $\mu\text{m}$ -high channel around a single quadrupolar DEP trap using 4 planar electrodes (more details on specific designs under Results) as shown in Fig. 2.20a. The Channel 2 fabrication process was used to contain electrode arrays of different heights in different 66  $\mu\text{m}$ -high SU-8 channels as illustrated in Fig. 2.20b. The use of photolithography to pattern the channel allows for automatic alignment of the channel walls to any part of the electrode array. For example, Fig. 2.20 shows how the channel wall exactly covers half of the posts on the outer edge of the array. This prevents the cells in the channel from

flowing through volumes where there is no DEP force as it may be the case with off-substrate microfluidics (details below). Furthermore, the optimization of spin coating enables tailoring the height of the channel to the height of the posts. Since the microfluidics can be exactly tailored to the dimensions of the electrode array, the trapping efficiency may be higher when using this type of microfluidics. The SU-8 channels presented above were closed with a glass piece using SU-8 as adhesive. The glass piece was previously drilled with two holes which became the fluid inlet and outlet. Drilling was done using a DREMEL<sup>®</sup> tool and a diamond drill bit (The Gordon Glass Company, US). Water was used as coolant during drilling.

After drilling, the piece of glass was first cleaned using piranha and then coated with a ~1.5  $\mu\text{m}$ -thick layer of SU-8 using the spin parameters of Insulation 2 in Table 2.3a. The layer was soft baked for 1.5 min on a hotplate at 95 °C. Both the SU-8-coated glass and the substrate containing the SU-8 channel are then heated to 125 °C at which temperature the two are brought together. Mechanical pressure was applied manually to facilitate the bonding. The arrangement was then flood-exposed using an exposure dose of 180  $\text{mJ}\cdot\text{cm}^{-2}$ . The bonding obtained using this procedure was not uniform and cavities on the interface between the glass and the SU-8 channel allowed for the cells to flow through them instead that through the carbon electrode array. The heating of the obtained devices above room temperature is not recommended since miniature fractures introduced in the glass during drilling may expand and crack the glass open.

**Table 2.7** Resume of the different techniques used to fabricate the microfluidics around the carbon electrodes

ID tag	Fabrication	Channel	Cover	Adhesive	Remarks
SU-8	On-substrate	SU-8	Glass	SU-8	<ul style="list-style-type: none"> <li>▪ The microfluidic network is automatically aligned to the electrode array during SU-8 photolithography</li> <li>▪ Fluid network can be easily fitted to the dimensions of the electrode array to prevent cells from flowing through volumes that are not under a DEP force</li> <li>▪ Bonding is not uniform and not repeatable</li> </ul>
PDMS	Off-substrate	PDMS	N/A	Mechanical pressure	<ul style="list-style-type: none"> <li>▪ Photolithography is still used to fabricate the master mold for PDMS casting which increases process cost and time</li> <li>▪ The channel is manually aligned to the electrode array which may introduce wide spacing between the electrode array and the channel wall</li> <li>▪ The interface PDMS-SU-8 contains stationary liquids but leaks upon liquid flow</li> <li>▪ Oxygen plasma was not attempted for bonding</li> <li>▪ PDMS channel can be removed and re-positioned several times</li> <li>▪ Recommended for rapid prototyping and basic proof of different microfluidic designs</li> </ul>
Adhesive	Off-substrate	Adhesive	PC	N/A	<ul style="list-style-type: none"> <li>▪ Network is perfectly sealed. No leaks are present up to <math>6 \text{ ml} \cdot \text{min}^{-1}</math> flows</li> <li>▪ SU-8 photolithography is not needed</li> <li>▪ Fabrication time and costs are greatly reduced</li> <li>▪ The channel is manually aligned to the electrode array which may introduce wide spacing between the electrode array and the channel wall</li> <li>▪ Acetone and NaOH may not be used for cleaning</li> </ul>

### 2.2.2 Off-substrate

Soft lithography was used to obtain PDMS (polydimethylsiloxane) channels. A master mold was fabricated by patterning a SU-8 layer on top of a silicon oxide wafer following the recipe of Channel 2 in Table 2.3. PDMS was then casted on the mold and cured at 95 °C on a hotplate for 10 min, after which the PDMS channel was manually peeled off the mold. The fluid inlets and outlets were created by poking through the PDMS piece using a syringe. The fact that SU-8 photolithography was still used to fabricate the master mold increases the cost and processing time of this kind of microfluidics compared to the SU-8 on-substrate approach detailed above.

The PDMS channel was manually positioned around the electrodes with the aid of a magnification lens. Obviously, the PDMS channel must be wider than the width of the electrode array. Manual positioning of the channel yields large margins of error and wide spaces may exist between the outer edges of the array and the channel walls as shown in Fig. 2.21. Cells may flow through these spaces without being influenced by the DEP force and cause a decrease on the trapping efficiency of carbon-DEP devices. Another downside of the use of PDMS microfluidics is the weak adherence of PDMS to SU-8. This adhesion is enough to contain stationary liquids but is not enough to prevent leaks through the interface once a flow is established in the channel. The use of mechanical clips was required to apply pressure on the PDMS-SU-8 interface and eliminate leaks. However the use of flow rates above  $100 \mu\text{l}\cdot\text{min}^{-1}$  in a channel  $575 \mu\text{m}$ -wide and  $66 \mu\text{m}$ -high still led to leaks in the system regardless of the use of mechanical clips. On the positive side, the capability to remove and re-position the PDMS channel allows for more efficient cleaning of the electrode array. Furthermore, several different microfluidic

designs may be interfaced to the same electrode array. The PDMS approach was found to be better suited for rapid and relatively inexpensive prototyping and basic proof of different designs. The use of oxygen plasma for bonding was not attempted due to the availability of a better technique to fabricate the microfluidics for carbon-DEP devices which is detailed next.

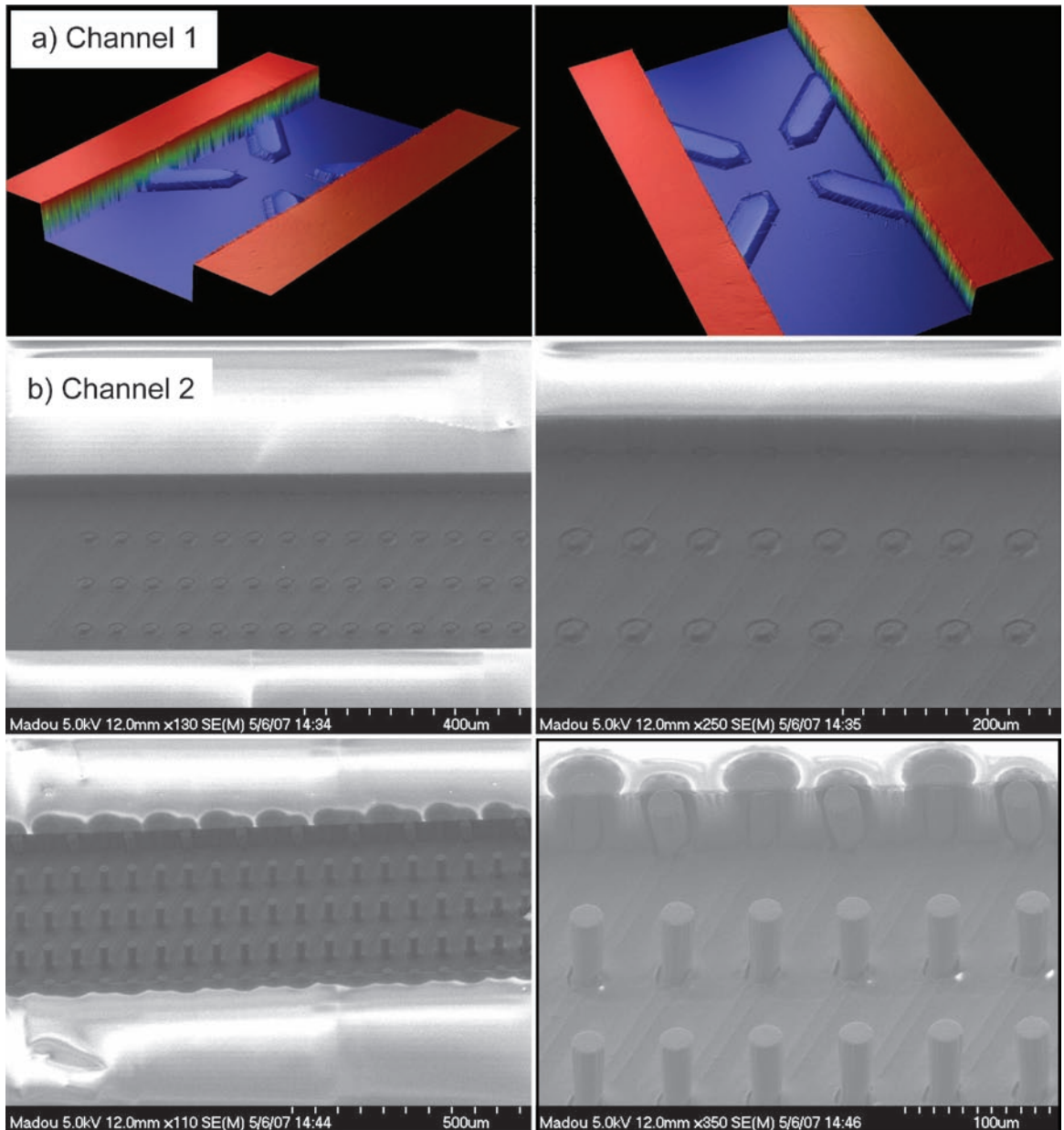


**Fig. 2.20** Planar and volumetric electrodes contained in a SU-8 channel

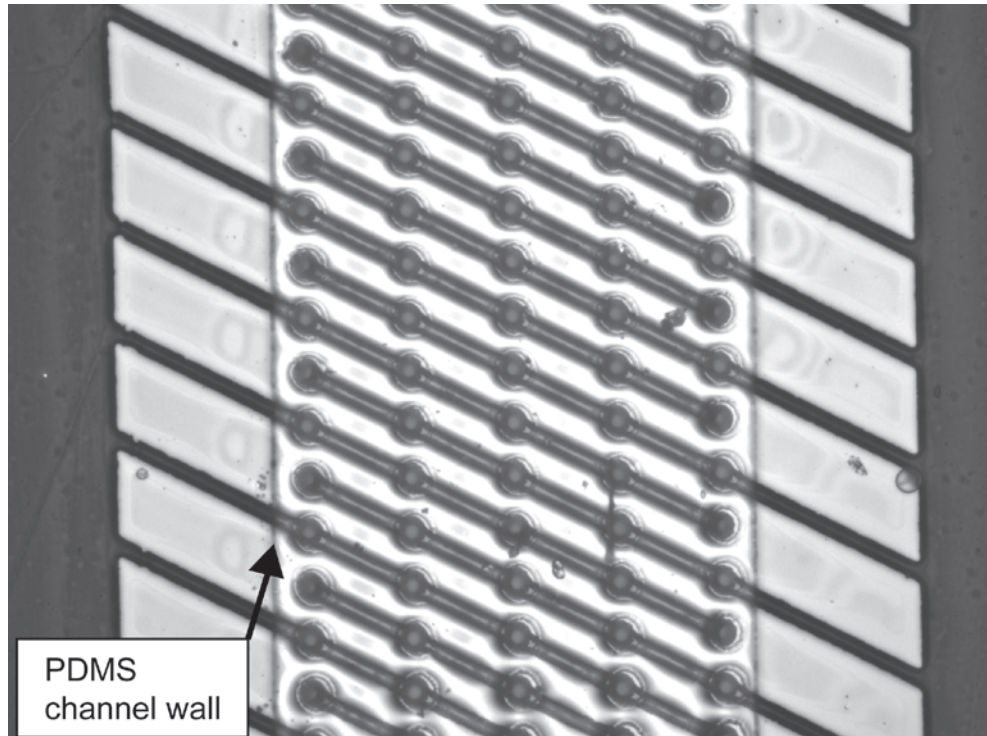


**Fig. 2.21** A PDMS channel (straight lines) positioned around an array of carbon electrodes

A third technique to fabricate the microfluidic network is detailed next. The network was fabricated from polycarbonate (PC) and double-sided pressure-sensitive adhesive (FLEXmount DFM 200 Clear V-95 150 POLY H-9 V-95 4 FLEXcon, MA, USA). In the most basic process, the channels and chambers of the network are cut out from a 100  $\mu\text{m}$  thick adhesive using a cutter plotter machine (Graphtec, Japan-Graphtec CE-2000) while the fluid inlets and outlets are drilled on a piece of polycarbonate using a computer-controlled milling machine (Quick Circuit Series, T-Tech, Norcross, GA). The adhesive and the polycarbonate piece are then aligned (using a two-point alignment device fabricated in-house) and adhered together using a rolling press/laminator (Model Sidewinder, Desert Laminators, Palm Springs, CA). The thickness of the polycarbonate layer and the adhesive may vary depending on commercial availability and this fact must be taken into account in the design process. Channels and chambers may also be milled

on the polycarbonate layer. Therefore, complex fluidic networks can be fabricated by stacking several layers of patterned adhesive and polycarbonate (PC) layers. The microfluidics presented here featured either 2 or 4 layers. All adhesive layers used here featured a thickness of 100  $\mu\text{m}$ . The 2-layer design featured an adhesive layer patterned with a 600  $\mu\text{m}$ -wide channel connecting two 1 mm-diameter chambers. The adhesive is aligned and adhered to a piece of 0.6 mm-thick polycarbonate (McMaster-Carr, CA, USA) previously drilled with two 1 mm holes. This 2-layer stack is then manually aligned to the carbon electrodes and the arrangement is sealed using the rolling press at speeds down to 1  $\text{mm}\cdot\text{s}^{-1}$ . This 2-layer design was used for carbon-DEP devices that were tested using a syringe pump (details chapter 4). The 4-layer microfluidic network was used for carbon-DEP devices tested using centrifugal pumping (details in chapter 5). For example, in the case of the chips used in the SpinDEP platform two different channels are cut in the first adhesive layer: 1) a 600  $\mu\text{m}$ -wide channel to contain the carbon electrode array and 2) a 1 mm channel for sample retrieval. 8 mm diameter circles are then milled from a 1 mm-thick PC sheet to fabricate chambers with volume equal to 50  $\mu\text{l}$ . These chambers are used to load and retrieve the sample from the carbon-DEP chip. A second adhesive layer was patterned with 8 mm-diameter circles to interface the second PC layer with the top cover. A channel is also patterned in this adhesive layer to provide venting to the retrieval chamber. The top PC cover features loading, retrieval and venting holes which were drilled on a 0.6 mm PC sheet. PC and adhesive layers were mechanically aligned and sealed together using the rolling press. An isometric exploded view and a top view are detailed in Fig. 2.22. The first adhesive layer is used to adhere the network to the substrate containing the carbon electrodes.

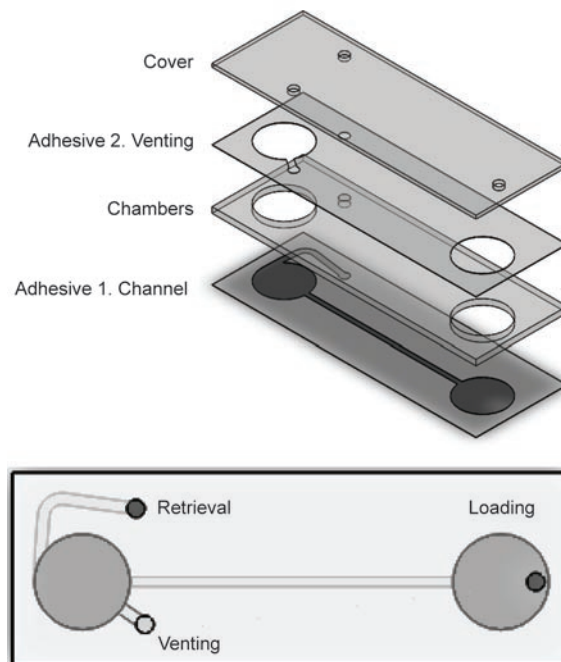


**Fig. 2.22** Isometric exploded view and top view of a 4-layer microfluidic network fabricated using double-sided pressure-sensitive adhesive and polycarbonate

The fluid network was then manually aligned around the carbon electrodes and adhered to the planarized SU-8 surface around the electrodes detailed on the SU-8 cover layer section. The rolling press was again used to seal the arrangement.

This approach offers various advantages over the other two detailed above. The use of adhesive effectively seals the microfluidic chamber and allows flow rates up to  $6 \text{ ml}\cdot\text{min}^{-1}$  without leaking. The replacement of glass with polycarbonate in the fabrication process makes drilling significantly more manageable, reduces weight and cost of the device and most importantly increases the robustness of the experimental chips. Since SU-8 photolithography is no further needed both fabrication time and cost of the microfluidics is greatly reduced. A drawback is that alignment to the carbon electrodes is still conducted manually and wide spacing from the array to the channel wall may still be

obtained. Acetone and NaOH may not be used to clean this type of microfluidics since it attacks polycarbonate. IPA and sodium dodecyl sulfate may be used instead.

### **2.3 Fluidic and electrical interconnects**

Further processing after interfacing the fluid network to the carbon electrodes includes the 1) electrical connection between the carbon electrodes and the function generator and 2) the fluidic connections of the syringe pump and exit reservoirs to the channel inlet and outlet respectively. Fluidic connections are not needed when the carbon-DEP device is intended to be used in an experimental platform using centrifugal pumping. Electrical connections were made by first depositing (using the brush provided) silver conductive paint (SPI Supplies<sup>®</sup>, West Chester, PA) on the carbon pads. Metal wires of caliber AWG18 were then soldered to the silver. Resistance of the carbon-silver interface averages 120  $\Omega$  while the resistance of metal wire to solder is negligible. A cross-section of a typical carbon-DEP chip at the connection pads is illustrated in Fig. 2.23a. The fluidic connections to the inlet and outlet of the channel contained in the chip depend on the type of microfluidics used. In the cases of on-substrate SU-8 and off-substrate adhesive-PC microfluidics the connections were made using commercial components from Upchurch Scientific (now part of IDEX<sup>®</sup> Health and Science, Oak Harbor, WA). Only NanoPort<sup>™</sup> assemblies that allowed for the use of 1/16" OD (outside diameter) tubing were used in this work (catalog number N-333) since a wide variety of commercially available flow control elements such as valves and adapters are optimized to make use of 1/16" OD tubing. The N-333 assembly features a threaded (10-32) plastic reservoir that is attached to the chip (illustrated in Fig. 2.23b) and a correspondent

threaded fitting to secure the tubing to the reservoir as illustrated in Fig. 2.23b and c. Teflon<sup>®</sup> tape was used in the threads to prevent leakage. The cross-section at the channel outlet of a carbon-DEP device featuring adhesive-PC microfluidics is shown in Fig. 2.23b. In the case of PDMS microfluidics, the connections are done by simply inserting 1/16" OD tubing in the holes previously made by poking through the PDMS using a needle. The elasticity of PDMS and the fact that the hole made by the needle is smaller than the tubing diameter allows for a tight connection at low pressures.

A significant problem arising from the use of fluidic connectors such as the NanoPort assemblies is the physical interface to certain objective lenses of a microscope. The fluidic connectors are perpendicular to the carbon-DEP chip and act as two protruding posts that may be close to each other. This separating distance between connectors determines the maximum diameter of an objective lens that may be used to visualize the DEP experiment. Objective lenses with diameter greater than the separating distance cannot be positioned on top of the carbon electrode array. While 5X and 10X objective lenses usually feature working distances of several millimeters, the working distance of 20X and 50X objectives is no more than few millimeters. The use of an objective lens with long working distance (as shown in Fig. 2.23c) greatly benefits DEP experiments when using connectors positioned perpendicular to the chip. Unfortunately, long working distance objectives can be quite expensive.

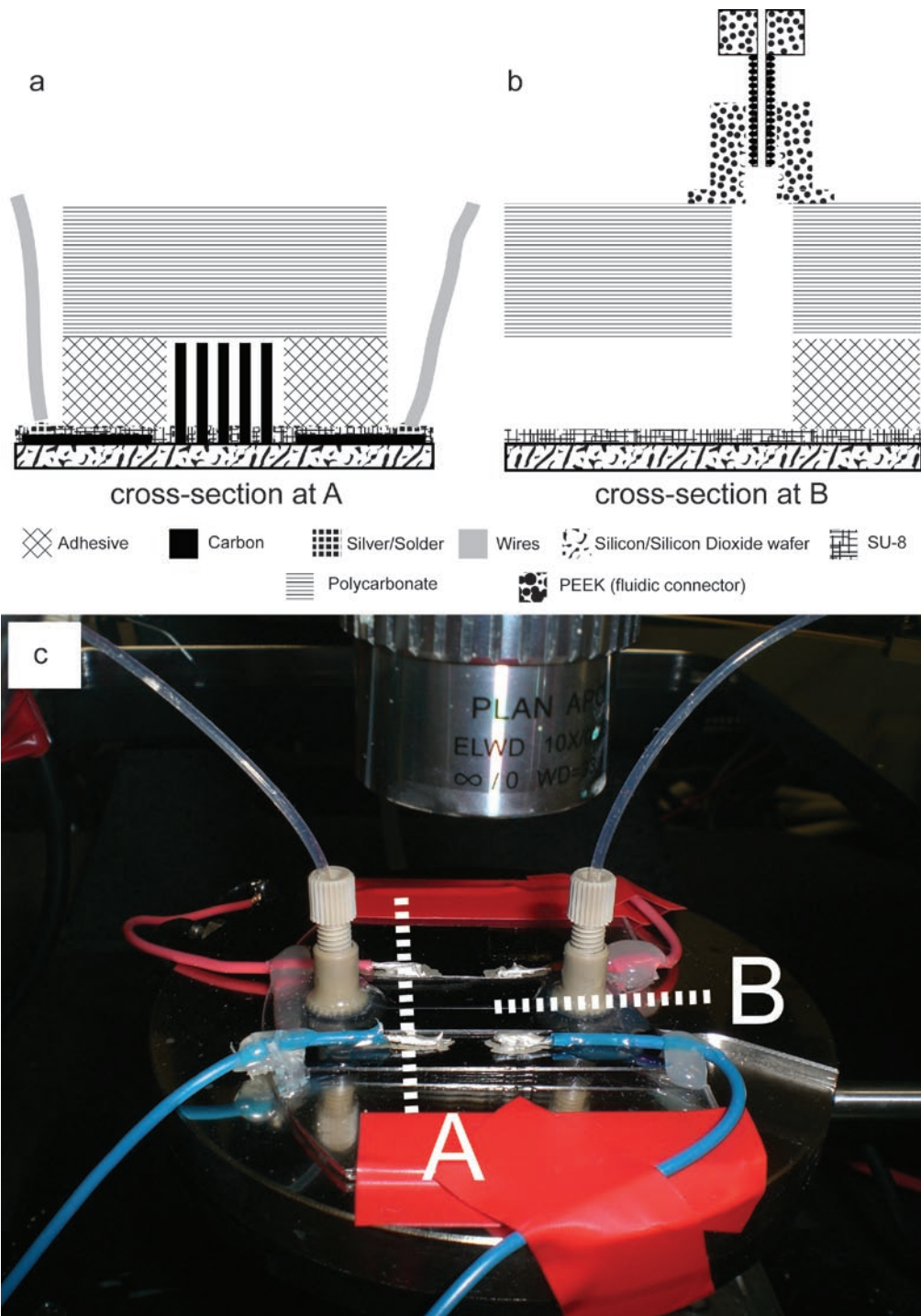


**Fig. 2.23** Cross-sections at different points of a typical carbon-DEP device. Cross-section A exemplifies the electrical connections, Cross-section B exemplifies the fluidic connections

An alternative fluidic connector with low profile was fabricated in this work to allow the physical interface of carbon-DEP chips to wide objective lenses with short working distance. Buna-N O-rings with inside diameter of 5/64" (1.98 mm) were first glued (Loctite<sup>®</sup> All-Plastics Super Glue) to a 0.6 mm-thick piece of polycarbonate. The glue was allowed to fully cure at room temperature for 24 hours. The use of epoxies is not recommended in this case since based on this author's experience the epoxy does not react with Buna-N and the connector leaks. The viscosity of the epoxy also prevents it from flowing into tight spaces which can compromise the seal. After 24 hours, the O-ring glued to the polycarbonate was manually aligned to the channel inlet and glued to the polycarbonate surface of the carbon-DEP chip. The fluidic connection to the channel is done by using a needle to poke through the Buna-N O-ring. The needle is then secured in place using the same glue. A male-luer to female 10-32 adapter (Upchurch Scientific, catalog number P-656) was used to interface the needle to 1/16" OD tubing. This connector allows for a fluidic connection that is parallel to the surface of the chip rather than perpendicular to it as is the case when using traditional connectors. Leaks could not be discerned when flowing water through the connector at rates up to 6 ml·min<sup>-1</sup>. Furthermore, the connector itself is only 3 millimeters high and allows the use of a wider variety of objective lenses. Different views of this alternative connector are shown in Fig. 2.24. An ideal connector would be a transparent hollow dome-shaped rubber piece that can be glued around the channel inlet. The fluidic connection could then be done at any angle depending on the experimental setup. The use of a solid piece of rubber on top of the inlet prevents from connection at an angle of zero degrees or parallel to the channel.

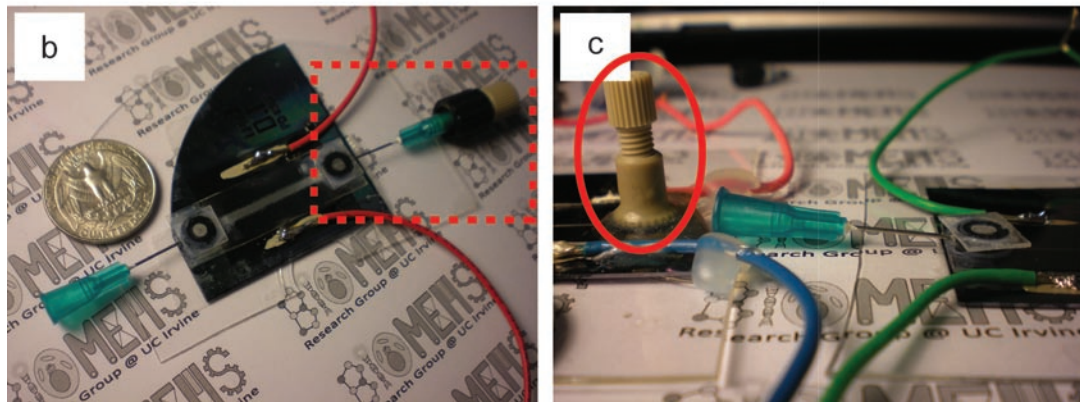
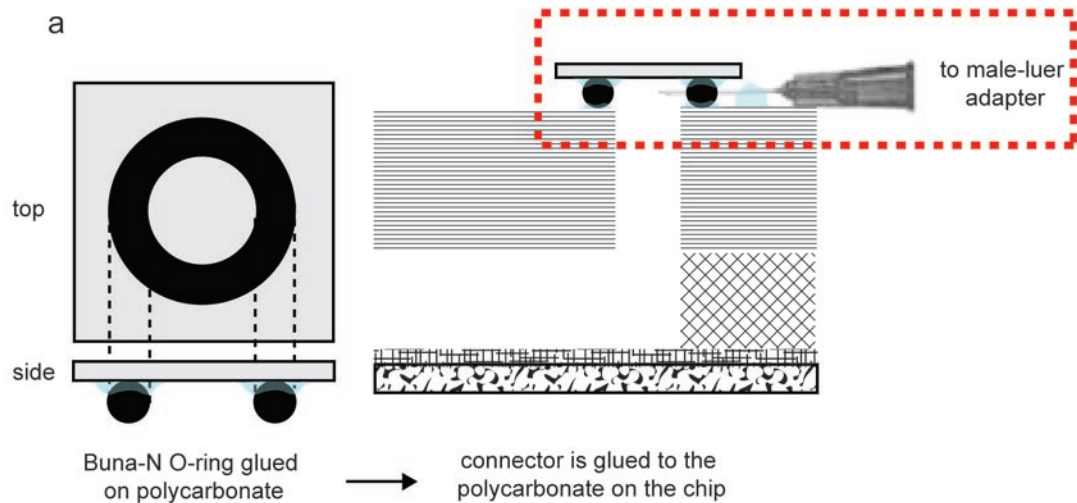


**Fig. 2.24** An alternative connector using buna-N o-ring and polycarbonate. The interface to 1/16" tubing is done by poking with a syringe and using a male-luer adapter. The dashed red squares represent the cross-section of the connection in a) and the view on an experimental device in b). c) A significant reduction on the height of the experimental device is achieved when using the O-ring connector instead of commercial connectors (red solid ellipse)

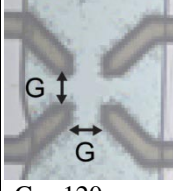
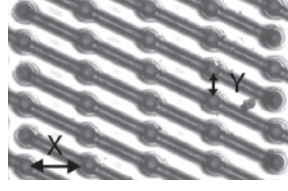
The final carbon-DEP chips may be sealed using epoxy. This is particularly needed when using SU-8 microfluidics since the bonding of the glass cover is not always ideal. Fluidic connections are not needed when the carbon-DEP device is intended to be used in an experimental platform using centrifugal pumping. In this case the sample is manually introduced in the carbon-DEP using a pipette (loading hole in Fig. 2.22).

## 2.4 Resume of fabricated devices and discussion

Several iterations of carbon-DEP devices were fabricated following the methodology just detailed. Table 2.7 resumes the development of carbon-DEP from the initial proof-of-concept to the current state-of-the-art. The different devices are shown in Fig. 2.25. The discussion in this section is about the cost and time of each fabrication process used in this work and the cost and reliability of the different carbon-DEP devices obtained as a result.

Each column in Table 2.8 details the fabrication process for various carbon-DEP devices. The ID tags of the columns reflect the application the chips were used for. Each application is detailed in the next chapter. Briefly, proof-of-concept refers to the use of carbon electrodes to prove the capability to induce negative and positive DEP on yeast cells. Devices fabricated following the 2D and 3D columns were used to quantify the filter efficiency when using 3D and 2D electrodes. 3D + PDMS is essentially the same process as 3D but using PDMS instead of SU-8 to fabricate the microfluidics. 2-stage describes those chips used for the demonstration of a 2-stage filter, *i.e.*, two different electrode arrays polarized with different signals. The SpinDEP column details those devices used with a centrifugal microfluidics platform. Screening devices were used to qualitatively characterize the behavior of *E. coli* and *Drosophila* cells when under the influence of different DEP forces. The most significant changes between the different chips are the height of the carbon electrodes and the type of microfluidics.

**Table 2.8** Development of carbon-DEP chips

Parameter \ ID tag	Proof of concept	2D	3D	3D + PDMS	2-stage	SpinDEP	screening
<b>CARBON ELECTRODES</b>							
Connection leads <sup>¶</sup>	-	Leads 1	Leads 1	Leads 2	Leads 3	Leads 3	Leads 3
Electrodes <sup>¶</sup>	Posts 1	Posts 1	Posts 4	Posts 4	Posts 4	Posts 3 & 5	Posts 3
shape	wedge	cylinder					
height (µm)	5.6	5.6	60	60	60	40 & 73	40
SU-8 cover	none	yes					
Array Configuration	 G = 120 µm	 distance between electrodes: X = 100 µm Y = 45 µm post diameter = 21.5 – 26 µm <sup>±</sup>					
Kind of DEP trap	single quadrupolar	multiple quadrupolar					
<b>MICROFLUIDICS</b>							
Channel material	SU-8			PDMS	Adhesive		
SU-8 photolithography <sup>¶</sup>	YES Channel 1	YES Channel 2	YES Channel 2 used to fabricate mold	not required			
Channel cover	glass			-	polycarbonate		
Channel cross-section							
height (µm)	50	66.38	66.38	100			
width (µm)	500	500	575	600			
Max. flow rate implemented with no leaks (µl·min <sup>-1</sup> )	not tested <sup>§</sup>	500	100	6000			
<b>INTERCONNECTS</b>							
Fluidic	Upchurch N-333			tubing inserts (Upchurch 1522)	N-333	not required	PC + Buna-N O-ring
Electrical	silver conductive paint + solder + AWG18 wires						
<b>COMPARISON</b>							
Cost (material + fabrication)	\$\$\$ <sup>¼</sup>	\$\$\$ (highest)		\$\$ <sup>¼</sup>	\$\$ <sup>¼</sup>	\$ <sup>¼</sup>	\$ <sup>½</sup>
Reliability	++			+	+++ (most reliable)		
Fabrication time	● <sup>¾</sup> (shortest)	●● <sup>¾</sup>	●●● <sup>¼</sup>	●●● <sup>¼</sup>	●● <sup>¾</sup>	●● <sup>½</sup>	●● <sup>¾</sup>

**Notes:** <sup>¶</sup> refer to Tables XX and XX for full fabrication details. ID tags (Leads 1, Posts 4, etc.) must be correlated

<sup>±</sup> refer to Table XX for full details on carbon posts dimensions

<sup>§</sup> max. flow rate during experiments was 10 µl/min

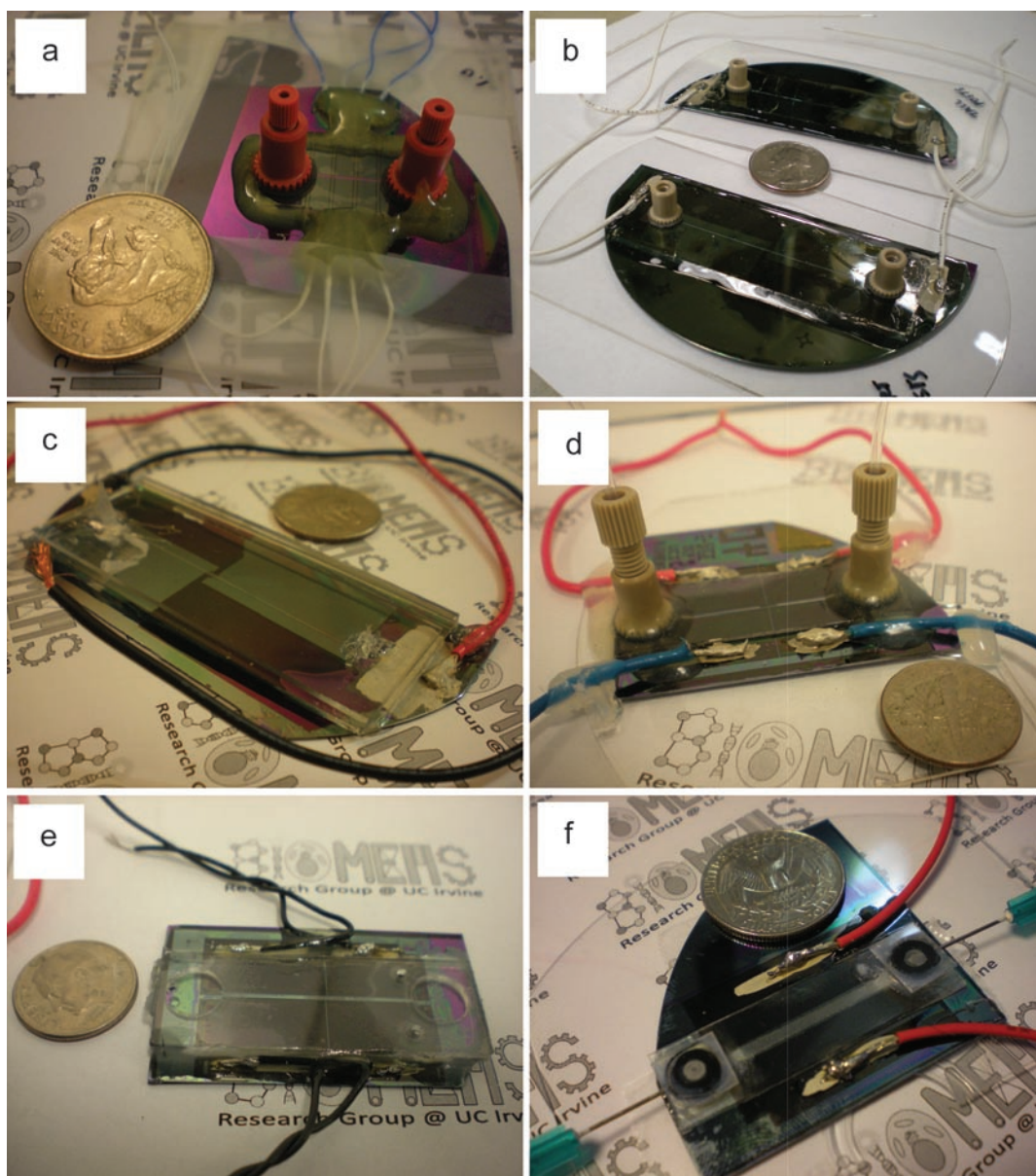


**Fig. 2.25** Different devices fabricated in this work: a) Proof of concept, b) 2D and 3D, c) 3D + PDMS, d) 2-stage, e) SpinDEP and f) screening

Tall electrodes (3D, 2-stage, SpinDEP) were used to improve the trapping efficiency. Electrodes with lower heights (2D, Screening) were used to characterize the DEP behavior of different cells since the fabrication of electrodes of low to medium height (<50  $\mu\text{m}$ ) is less challenging and time demanding than the fabrication of tall ones. The cost to fabricate the different electrodes (in terms of used material and independently from cleanroom usage fees) is basically the same regardless of the electrode height. However, tall electrodes require longer fabrication times than short ones due to longer baking times during the photolithography of SU-8. The fabrication time and cost is significantly less in the case of Proof-of-Concept since only one, relatively thin, SU-8 layer is required to fabricate the electrodes and the SU-8 cover layer is not needed. The biggest difference in reliability and fabrication cost and time between different devices came from the type of microfluidics and back-processing used in each case rather than from the fabrication of carbon electrodes. The rationale behind the comparison made in Table 2.8 is detailed next.

Fabrication costs are determined by the cost of the materials and processing tools involved in the process. One full money (\$) symbol was given for the fabrication of carbon electrodes and connecting leads because this process requires SU-8 photolithography and mask alignment. Three quarters of a symbol was given to the fabrication of planar electrodes because mask alignment is not needed but flood exposure systems still average \$30 000 USD. The type of microfluidics used adds either  $\frac{1}{4}$  or one full symbol. A quarter of a symbol was given for the use of adhesive + polycarbonate since the materials are very low cost (polycarbonate < \$0.32 USD per  $\text{cm}^2$  for thicknesses up to 5 mm, adhesive) and the machines employed to pattern them are relatively

inexpensive (CNC mill, cutter). A full symbol was given when SU-8 photolithography is used, to fabricate the microfluidics or the PDMS mold, since SU-8 is expensive (averages \$1 USD per ml as on 2010) and the equipment used to deposit and pattern it are also expensive (spinner >\$1 000 USD, mask aligner > \$100 000 USD). An extra ¼ was added in the case of PDMS microfluidics to account for the cost of PDMS (Sylgard<sup>®</sup> 184 averages \$0.1 USD per ml) and related casting equipment. Regarding back-end processing, the use of NanoPort assemblies as fluidic connectors adds a full symbol (\$20 USD for each assembly, a chip usually needs two assemblies) while the use of in-house fabricated polycarbonate + O- only adds a quarter of a symbol. The less expensive devices are those fabricated following the process in the SpinDEP column since adhesive+polycarbonate fluidics were used and no back-processing was required.

A device is most reliable when it does not present leaks regardless of the rate used to flow the sample through the channel and when it offers high repeatability. The use of adhesive + polycarbonate microfluidics yields the most reliable devices followed by SU-8 microfluidics. The use of PDMS led to poor results. However, the bonding of PDMS to SU-8 using oxygen plasma is expected to significantly improve reliability.

The fabrication time mainly depends on the height of the carbon electrodes and whether or not SU-8 photolithography is required to fabricate the microfluidics. The symbol (●) is used here to denote the relative fabrication time. The longest process is that with the most (●) symbols. A full (●) symbol is added if tall electrodes are required. Half (½) a symbol is added if medium-height electrodes are fabricated. One half of a symbol is given to the fabrication of connection leads, planar electrodes and the SU-8 cover layer. The use of photolithography to fabricate SU-8 microfluidics or the mold for PDMS adds one full

symbol. PDMS casting adds a quarter of a symbol only when fabricating more than one device with the same mold since the fabrication time of further PDMS pieces decreases. A full symbol must be added if only one device is made since a complete photolithography process would be needed to fabricate this one-time mold. The use of adhesive + polycarbonate microfluidics only adds half a symbol since both the cutter and the CNC mill can pattern a substrate at speeds as fast as 3 mm per second. The positioning of the fluidic connectors adds one quarter of a symbol. The basic device used for the proof-of-concept is the shortest one to fabricate since it only requires one photolithography step and does not require the cover layer. The use of adhesive + polycarbonate microfluidics also decreases fabrication time since no photolithography is required.

## **2.5 Possible improvements to current carbon-DEP devices**

### *2.5.1 Transparent Substrate*

A significant restriction on the type of substrate that can be used for pyrolysis stems from the low number of materials capable of withstanding very high temperatures. The use of substrates other than silicon or silicon/silicon dioxide wafers for pyrolysis of SU-8 structures has not yet been achieved. Unfortunately, silicon and silicon dioxide are opaque and restrict the visualization that can be conducted during experiments to the use of illumination sources positioned on top of the wafer. While this may not represent a challenge when using a microscope featuring top illumination, it does when using an inverted microscope as those featured in many experimental settings (including many

used for cell biology). For example, the interface of carbon-DEP devices to inverted microscopes is challenging and requires the use of special optics (long working distances are required) or drilling/etching of the silicon wafer to fabricate the fluidic inlets and outlets. The fabrication of carbon structures on a transparent substrate allows for far more versatile devices than those being fabricated now. Certain imaging techniques such as confocal microscopy and fluorescence may benefit from the capability to illuminate the sample contained in the device from the top or the bottom (or from both sides). Furthermore, the use of transparent substrates during SU-8 photolithography enables back-side exposure and the fabrication of structures with walls featuring an angle greater than 90° such as micro-needles<sup>112,203</sup>. Selected thermal properties of transparent substrates commonly used in microfabrication are shown in Table 2.9. B270 Superwite<sup>®</sup> and Pyrex<sup>®</sup> are used to exemplify soda-lime and borosilicate glasses respectively. Other borosilicate glasses include Borofloat<sup>®</sup>, 1737F, Eagle 2000<sup>TM</sup>, Duran<sup>®</sup> 8330, Wheaton 180, Wheaton 200, Kimax<sup>®</sup> and Borex<sup>®</sup>. Both soda-lime and borosilicate glasses soften at temperatures below 820 °C and cannot be used for pyrolysis. Some fused Quartz / Silica glasses (GE124 and Dynasyl 1100 for example) soften at temperatures above 900 °C and may be used for pyrolysis using the protocol used here (some pyrolysis protocols require the sample to be heated up to 1700 °C<sup>121</sup>). However, previous work with quartz wafers performed by other members of the research lab of this author showed detachment of the carbon structures from the quartz substrate. The fact that quartz features a coefficient of thermal expansion (CTE) similar to that of silicon oxide ( $0.55 \times 10^{-6} \cdot \text{K}^{-1}$ ) and the SU-8 adhesion to quartz is reported to be better than that to Si [reference microchem] should lead to the conclusion that SU-8 can be pyrolyzed on quartz substrates. However, the

thickness of the silicon dioxide layer on the substrates used for pyrolysis is only 0.5  $\mu\text{m}$  which is 1000 times less than the thickness of the underlying silicon wafer (500-550  $\mu\text{m}$ ) and the net expansion may be considered to be just that of the silicon wafer. The CTE of silicon ( $2.5$  to  $4.442 \times 10^{-6} \cdot \text{K}^{-1}$ ) is in the same order of magnitude than that of glass-like carbon ( $2$  to  $3.7 \times 10^{-6} \cdot \text{K}^{-1}$ ). This may explain why the carbon structures remain on a silicon-based wafer and they do not on a quartz substrate. The use of transparent synthetic sapphire (CTE =  $4.5$  to  $5.3 \times 10^{-6} \cdot \text{K}^{-1}$  and softening point above  $2040 \text{ }^\circ\text{C}$ ) for photolithography and pyrolysis may lead to the fabrication of carbon structures on transparent substrates. An alternative may be the use of aluminium oxynitride, a transparent ceramic. This material is commercialized as ALON<sup>TM</sup> and has a coefficient of thermal expansion of  $7.5$  in the range from  $20^\circ\text{C}$  to  $900 \text{ }^\circ\text{C}$ . Its melting point is  $2150 \text{ }^\circ\text{C}$ . The exact softening and strain point could not be found in the public domain.

**Table 2.9** Selected properties of materials commonly used as substrates for microfabrication

Material	Coefficient of Thermal Expansion ( $10^{-6} \cdot \text{K}^{-1}$ )	Strain Point ( $^\circ\text{C}$ )*	Softening Point ( $^\circ\text{C}$ )	Avg. cost per 4" wafer (US dollars)
Silicon (Hull 1999)	2.5 – 4.442	-	1414	20-25
Silicon Oxide Film (MEMS Exchange 2009)	0.55	-	1700	25-30
Soda-lime (B270 Superwite <sup>®</sup> )	8.9	511	724	<20
Borosilicate (Pyrex <sup>®</sup> 7740)	3.25	510	821	26-40
Synthetic sapphire	4.5-5.3	-	2040	425
<b>FUSED QUARTZ / SILICA</b>				
GE124	0.55	1122	1683	85-95
Corning 7980	0.55	893	1585	
Dynasil 1100	0.55	1000	1600	
Vycor 7913	0.75	890	1530	
NSG OZ Quartz	0.65	1090	1720	

\***Note:** a glass may be heated to its strain point but only intermittently

The cost of the substrate materials just detailed tends to be on the high end as shown in the last column of Table 2.9. Such high cost may be justified in some applications but the use of low cost substrates is desired for carbon-DEP since the devices are likely to be disposable. A disposable device eliminates cross-contamination and cleaning costs. Furthermore, the use of a low cost device derives in inexpensive assays that can be offered to a broad number of patients. Low cost substrates include soda-lime glass and polymers such as polycarbonate, polyester and cyclic olefin. While these materials do not survive the temperatures used in pyrolysis, a desired pattern can be carbonized using a silicon wafer and then transferred to a low cost substrate. The wafer used during pyrolysis can then be re-used. A procedure for pattern transfer is detailed next. The general experiment is described first with details following shortly.

An 11.2  $\mu\text{m}$ -thick SU-8 layer was patterned on either silicon or silicon/silicon dioxide 4" wafers following the fabrication process described in Leads 3 in Table 2.3. The pattern consists of squares and rectangles of different sizes. Some of these patterns also feature arrays of fingers protruding from their side edges. The SU-8 pattern was then carbonized using a one-step pyrolysis protocol as detailed above. After pyrolysis, the resulting 1.5  $\mu\text{m}$ -thick carbon structures were immersed in a solution to induce their detachment from the wafer. Once the structure detaches and gets suspended in solution, it is retrieved using fine tweezers and manually positioned on a glass or polycarbonate (PC) substrate. Remarkably, the carbon structure could be moved freely (by exerting pressure on it using the tweezers) on the glass or PC substrate as long as there was a hydration layer. This layer is eliminated once the carbon pattern is positioned on its final location. This basic

procedure is illustrated in Fig. 2.26 together with the resulting carbon patterns deposited on low cost transparent substrates such as soda-lime glass.

The process was optimized in terms of the solution and temperature used to induce detachment and the media used to deposit the carbon on the glass or polymer substrate. The optimization process is resumed in Table 2.10. The use of piranha solution gives the better results. It has previously been shown that glass-like carbon is chemically inert to piranha <sup>112</sup>. The use of piranha solution at 125 °C led to a rapid detachment from both silicon and silicon dioxide substrates. However, significant bubbling of the solution at this temperature introduces strong hydrodynamic forces that quickly break the carbon patterns once these have been detached. Eliminating the heating of the piranha led to better results. In this case the carbon patterns are not observed to detach from the substrate while immersed in piranha but they readily detached upon immersion in a DI water bath used immediately after the piranha one. No carbon breakage was observed in this case. The different results obtained by just varying the temperature of the piranha batch can be explained by the combination of chemical and physical factors. The rate of chemical attack of piranha to the interface between the silicon-based wafer and the carbon pattern depends on temperature. While at high temperatures the attack is severe enough to rapidly detach the carbon patterns, at room temperature is only strong enough to weaken the interface. Another factor to account for is the degree of bubbling in the solution. The convection forces originated by strong bubbling may be enough to overcome the already weakened adhesion forces holding the carbon on the substrate.

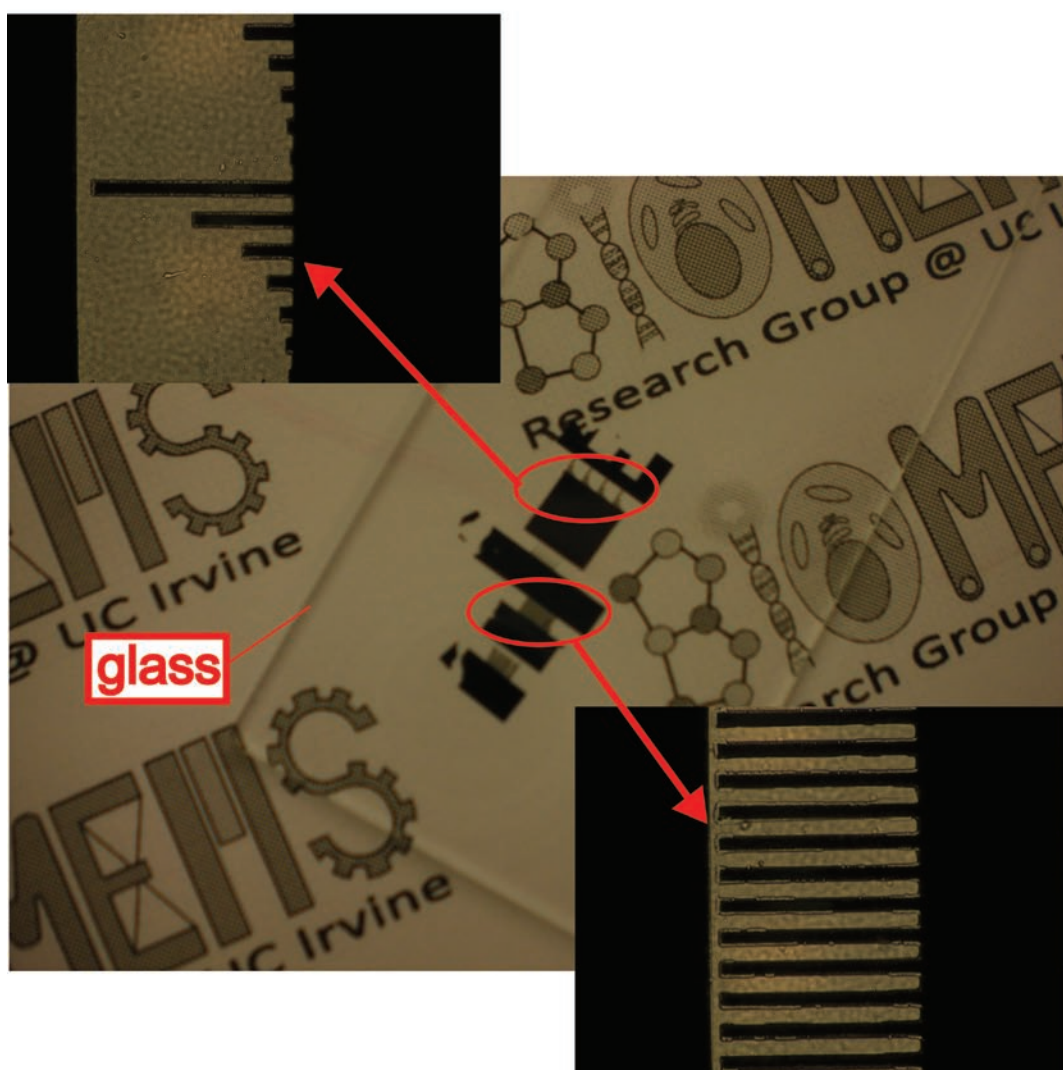
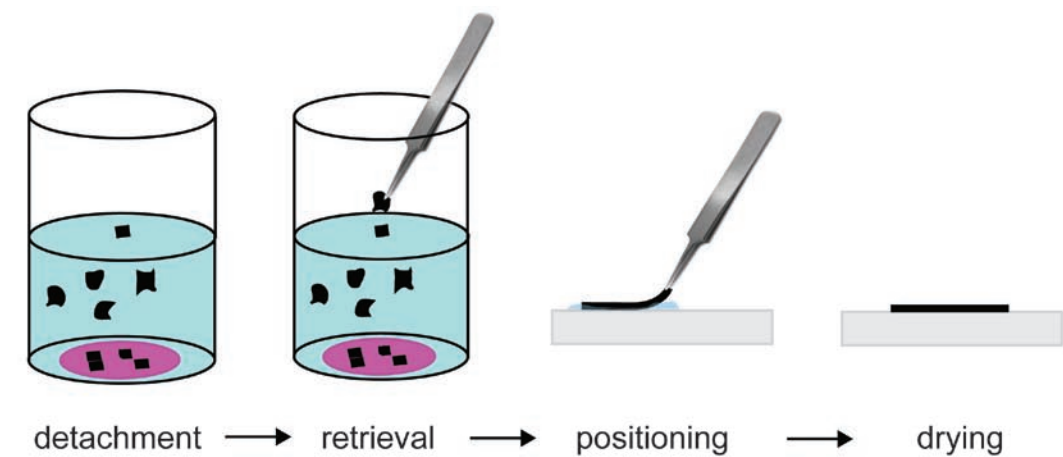


**Fig. 2.26** Carbon patterns deposited on a piece of glass

The degree of bubbling greatly diminishes at room temperatures and the convection forces are not strong enough to overcome the less weakened adherence of carbon to the wafer. Stronger physical forces are induced during the submersion in the DI water bath and thus the carbon film can only be detached then. It is important to mention that detachment in piranha solution was only achieved when the SU-8 structure was not hard baked. Similar experiments were performed on a carbon film resulting from a hard baked (10 min at 95 °C on a hotplate) SU-8 layer and the film could never be detached even after 20 min in piranha solution. In conclusion the use of a piranha bath at room temperature for 5 to 6 minutes is enough to weaken the adhesion between carbon and silicon. A DI-water bath can then be used to remove the carbon patterns from the substrate. The optimization of the type of media to use during pattern deposition on the glass or plastic substrate is detailed next and resumed in the second part of Table 2.10. Once the carbon patterns were suspended in the piranha solution they were transferred into either an acetone or DI-water bath. The direct deposition of the carbon patterns from the piranha bath is not possible due to safety issues and to the attack of piranha to polymer substrates. The use of a water bath gave the best results since the deposited carbon could be dried off using a nitrogen gun and water did not attack the substrates used in this work. The use of acetone during deposition causes the carbon pattern to detach from the glass or polymer substrate upon blowing it dry. Acetone attacks polycarbonate and may only be used when depositing the pattern on selected substrates known to be resistant to acetone such as glass. The carbon pattern, deposited using water, was also dried by inserting the arrangement in a convection oven set at 120 °C. Blowing

the substrate dry was preferred since it led to a more rapid drying and to what qualitatively appears to be a better adhesion to the substrate.

**Table 2.10** Solutions used to detach a carbon film from a silicon or silicon/dioxide wafer and different media used to deposit such film on a glass or polymer substrate

Solutions used to induce detachment					
Name	T (°C)	Substrate	Detachment Speed (min)	Detachment uniformity	Remarks
Acetone	25	Si	60	poor	carbon film takes too long to detach, it detaches in separate pieces rather than as a whole pattern
Piranha 3:1 H <sub>2</sub> SO <sub>4</sub> :H <sub>2</sub> O <sub>2</sub>	25	SiO <sub>2</sub>	5-6	excellent	Detachment is obtained after immersion in DI water. Refer to text for details
	125	Si	2-3	excellent	Strong hydrodynamic forces due to solution bubbling break the suspended patterns
	125	SiO <sub>2</sub>	2-3	excellent	
DI-water	25	SiO <sub>2</sub>	-	-	NO DETACHMENT after 40 min
H <sub>2</sub> SO <sub>4</sub>	125	SiO <sub>2</sub>	-	-	NO DETACHMENT after 10 min
H <sub>2</sub> O <sub>2</sub>	125	SiO <sub>2</sub>	-	-	NO DETACHMENT after 10 min
Media used for pattern deposition					
name	Clean transfer	Remarks			
Acetone	YES	pattern flies off upon blowing it dry, evaporates at room temperature			
DI water	YES	pattern can be blown dry, requires convection oven to evaporate			
Piranha	NO	cannot be blown dry nor evaporated due to safety issues			

### 2.5.2 Metal connection leads

Ideally, the connection pads and leads of carbon-DEP devices should be made out of metal instead of carbon. Carbon is around 4 orders of magnitude less conductive than most metals and its use to fabricate the connection leads introduces a significant resistance in the electric circuit. The use of selected metals minimizes this resistance and prevents a voltage loss in the connection leads. The metal to be used must have a melting point well above the pyrolysis temperature and a CTE similar to that of the substrate to prevent the metal from detaching during pyrolysis. Furthermore, the CTE of the metal should be similar to that of carbon to maintain the carbon electrodes on top of the

connection leads through the pyrolysis process. Selected properties of several metals commonly used in microfabrication are shown in Table 2.11. The melting point is the first parameter to take into account to guarantee that the metal will not flow during pyrolysis. Since most of the metals (except for Ag and Al) shown have a melting point above 900 °C the next step is to consider a metal with a similar CTE than carbon and the substrate material. Here silicon is assumed to be the substrate material. The CTE of glass-like carbon ranges from 2 to  $3.7 \times 10^{-6} \cdot \text{K}^{-1}$  while that of silicon does in between 2.5 and  $4.442 \times 10^{-6} \cdot \text{K}^{-1}$ . Tungsten and chromium appear to be the best candidates in this case with tungsten being the first choice given its lower resistivity and higher melting point than chromium.

**Table 2.10** Selected properties of metals commonly used in microfabrication

Material	CTE ( $\times 10^{-6} \cdot \text{K}^{-1}$ )	Resistivity ( $\times 10^{-9} \cdot \Omega \cdot \text{m}$ )	Melting Point (°C)	Density ( $\text{g} \cdot \text{cm}^{-3}$ )
W – tungsten	4.5	52.7	3422	19.25
Cr – chromium	4.9	125	1907	7.15
Ti – titanium	8.6	420	1668	4.506
Pt – platinum	8.8	105	1768	21.45
Co – cobalt	13	62.4	1495	8.9
Ni – nickel	13.4	69.3	1455	8.908
Au – gold	14.2	22.13	1064	19.3
Cu – copper	16.5	16.78	1084	8.96
Ag – silver	18.9	15.87	961	10.49
Al – aluminum	23.1	26.5	660	2.6

**Note:** CTE = coefficient of thermal expansion

Chromium was tried in this work because it was already available and because the deposition parameters for chromium are well established. An electron-beam evaporator (Airco/Temesal CV-14) was used to deposit a 1500 Å-thick chromium layer on a

silicon/silicon dioxide 4" wafer. The deposition rate was  $1.5 \text{ \AA}\cdot\text{s}^{-1}$  for the first 500  $\text{\AA}$  and  $2.4 \text{ \AA}\cdot\text{s}^{-1}$  afterwards. The chromium layer was then patterned as connection pads and leads using a chrome etchant and an AZ photoresist layer as mask. The AZ layer was previously patterned using the positive-tone version of the mask used to pattern the first layer of SU-8 and which later became the carbon pads and connecting leads to the carbon electrodes. The AZ layer is stripped using acetone after patterning the chrome layer. SU-8 posts were then patterned on top of the chrome leads and the arrangement was pyrolyzed using the protocol detailed above. The initial results are shown in Fig. 2.27. The chrome layer does not detach from the substrate after pyrolysis. However, some degradation on the leads is present. Although the majority of the carbon posts remain it is hard to determine the degree of contact between the carbon and the chrome by only visual observation and further characterization is needed.

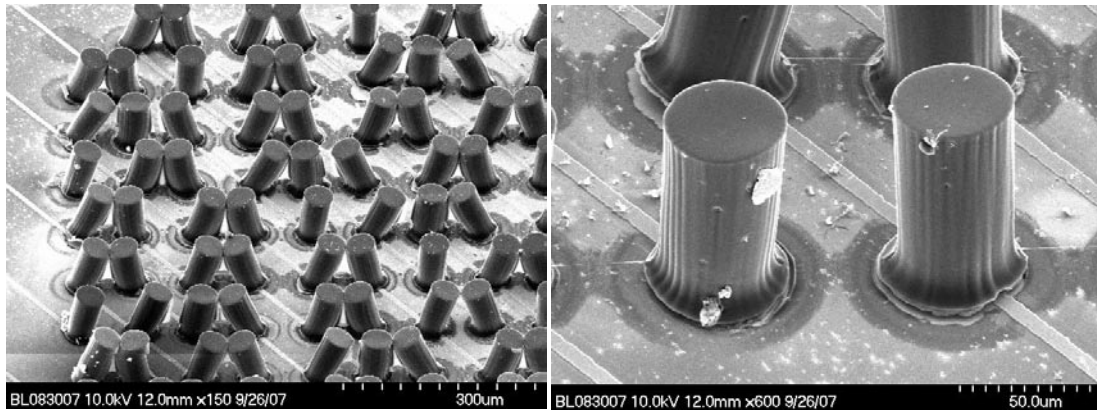


**Fig. 2.27** Preliminary results on the use of chromium to connect the pad and the base of the carbon electrodes

## **CHAPTER 3. Electromagnetic and Fluidodynamic characterization of a selected carbon-electrode DEP device**

The modeling of electric and flow velocity fields in a carbon-DEP device is presented in this chapter. The study presented here revolves around an electrode array geometry that is a replica of the physical device detailed as 2-stage in chapter 2, Table 2.7. The modeling methodology used here can be extrapolated to optimize device geometries and other experimental parameters to shorten development times of future carbon-DEP devices for different applications. Previous simulation work on the electric field that is created by a post electrode array includes that by Park et al <sup>204</sup>. These authors theoretically demonstrated the advantage of using 3D electrodes and the beneficial correlation of electromagnetic and flow velocity fields to improve the performance of a DEP filter. However, their results were obtained considering electrodes made out of a perfect conductor rather than carbon. The work presented in this chapter considers carbon electrodes. The material presented here is the result of a research collaboration with Javier Baylon-Cardiel and Sergio O. Martinez-Chapa from Tecnológico de Monterrey, Mexico (electromagnetic characterization) and Salvatore Cito at the time part of Universitat Rovira i Virgili, Spain (fluidodynamic characterization).

### **3.1 Electromagnetic characterization**

The effect of variations on electrode height, applied voltage and conductivity of the sample on the spatial distribution of the electric field gradient magnitude is quantified here. The DEP trapping force is directly proportional to the gradient of the magnitude square of the electric field and cells can only be trapped in those volumes with an electric

field magnitude higher than a certain value. The goal of this section is to calculate the volume of the regions with an electric field gradient magnitude that allows for cell trapping against a certain flow rate and to obtain the maximum trapping throughput of a carbon-DEP device. This maximum throughput depends on the electrode array dimensions and experimental parameters such as applied voltage and sample conductivity. The maximum throughput of a device can be used to limit the cell concentration in the sample and time of experiment to prevent the saturation of the array and a decrease in sorting efficiency. Materials and methods are detailed first followed by results and discussion.

### **3.1.1 Materials and Methods**

COMSOL Multi-physics 3.3a software (COMSOL, Sweden) running in a workstation featuring a SUN Blade 1500 with 1 GHz processor (SUN Microsystems, Inc. Santa Clara, CA now part of ORACLE), 4 GB of RAM and Solaris 9 (SUN Microsystems, Inc.) as operating system (OS) was used in this work. The geometry shown in Fig. 3.1a was used to obtain the spatial distribution of the electric field gradient magnitude ranges across a sample volume as electrode height, polarization voltage and sample conductivity changed. The 5 X 5 electrode array presented here is a simplification of the real experimental device.

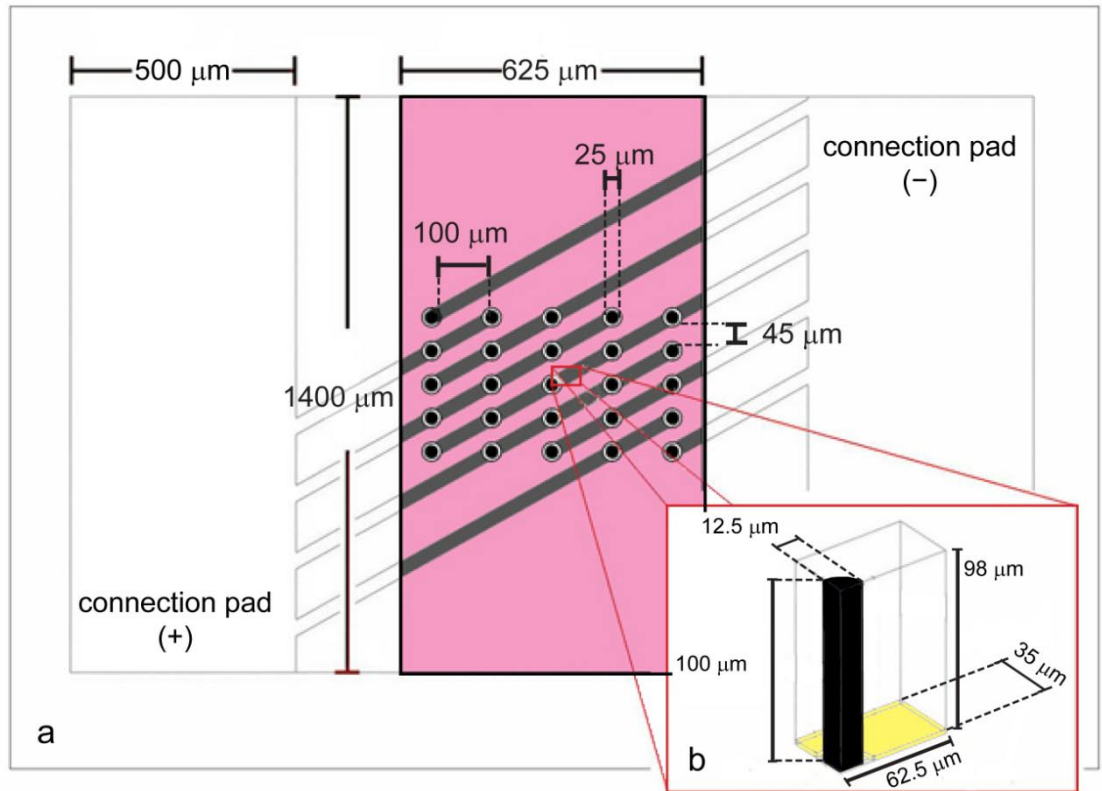


**Fig. 3.1** a) Geometry used to model the electric field in the sample volume (shaded area) and the ohmic losses in the connection pad and leads (un-shaded area). b) Dimension details on the polyhedron used as

The geometry contains two parts with different attributes. The first part is the shaded area which denotes a sample volume equal to  $8.575 \times 10^{-11} \text{ m}^3$  given by the product of a  $625 \times 1400 \text{ μm}^2$  surface and a channel height of  $98 \text{ μm}$  (the  $2 \text{ μm}$ -thick SU-8 layer is not included in the simulation). This volume represents a part of the flow through micro-channel fabricated in the real devices. All boundaries in this volume are considered electrically insulating except for the surface of the carbon electrodes (the dark circles in Fig. 3.1a). The conductivity of carbon is assumed to be  $1 \times 10^4 \text{ S} \cdot \text{m}^{-1}$  following the results detailed in chapter 2, section 2.1.1. The leads connecting the pads and the base of the electrodes ( $1.5 \text{ μm}$ -thick) are insulated from the sample by the SU-8 layer and are

considered to conduct only through the cross-section perpendicular to their length axis. The second part comprises the rest of the geometry shown in Fig. 3.1a and contains the connection pads and part of the connection leads. The thickness of these carbon structures is 1.5  $\mu\text{m}$ . All boundaries of the pads and leads are considered electrically insulating except for the cross-section of the connecting lead that is perpendicular to its length axis. This same cross-section permits the electrical coupling of the first and second parts (shaded and not-shaded) of the geometry shown in Fig. 3.1a. Separate simulations were done for each part to simplify the model and relax computational requirements. The results of the simulation to model the voltage drop on the connection pads and leads were coupled to the simulation to model the electric field in the sample volume using the *identity boundary condition* function available in COMSOL Multi-physics v3.3a (exploiting the shared boundary between the two parts of the geometry). This methodology allows for the consideration of ohmic losses in the connection leads as detailed in a section above (carbon electrical characterization). The polarizing voltages reported here are those applied in the connection pads.

The spatial distribution of different electric field magnitudes in the sample volume was calculated using a triangular mesh featuring 12 000 elements and 76 000 degrees of freedom. The Laplace equation

$$\nabla^2 V = 0 \tag{3.1}$$

is solved along the geometry using the *Lagrange method* available in the software used here. In this method the solution to Equation 3.1 is approximated by a low-order polynomial in every element of the mesh. The boundary conditions were already explained above. For the internal boundaries, a condition of continuity was considered.

The conductive pads, connecting leads and carbon posts were assumed to have a resistivity of  $1 \times 10^{-4} \Omega \cdot \text{m}$  based on the results obtained in chapter 2. SU-8 was assumed to have a resistivity of  $3 \times 10^4 \Omega \cdot \text{m}$ <sup>205</sup>. The height of the electrodes was varied from 5  $\mu\text{m}$  to 40, 70 and 100  $\mu\text{m}$ . The polarizing voltages used here were 5, 10, 20 and 40  $V_{\text{pp}}$  (peak-to-peak). The conductivity of the suspending medium was varied between 10, 100, 1000 and 5000  $\mu\text{S} \cdot \text{cm}^{-1}$ .

Although the ohmic loss along the length of the connecting leads causes each carbon post electrode to be polarized with a different voltage (details in sections “carbon electrical characterization” and SU-8 cover layer above) preliminary results showed that the magnitude of the electric field,  $\vec{E} = -\nabla V$ , around all posts remains constant. The voltage drop along the height of a carbon post is also observed to be negligible (around 0.001 V). This observation suggests that the magnitude of the electric field generated upon polarizing the carbon post electrodes does not vary in the z-axis. The electric field is expected to change only in the radial direction on the x-y plane.

### Method to calculate the volume of each electric field magnitude range

The method to calculate the sample volume subjected to a given electric field magnitude range is detailed in this section. Since the electric field created by a polarized carbon post electrode is symmetric in the x-y plane, calculations are simplified by only analyzing a quarter of the carbon electrode and the volume surrounding it as shown in Fig. 3.1b. The total sample volume is made of a finite number of such simplified geometries. These rectangular prisms feature a width of 62.5  $\mu\text{m}$ , depth of 35  $\mu\text{m}$  and a height equal to 98  $\mu\text{m}$  (the 2  $\mu\text{m}$ -thick SU-8 layer is not considered in the simulation). The results obtained

in this simplified volume are extrapolated to the other three quarters of the carbon post. Therefore, the total volume of a certain electric field magnitude range around a post electrode is the volume obtained in the calculation performed here times four.

A numerical method is used here to compute volume integrals from the value of the electric field at every point in the volume analyzed. The electric field values at each point were calculated using COMSOL Multi-physics 3.3a and the results exported into MATLAB 7.0 (The MathWorks, Natick, MA) where the numerical method was implemented. This method consists on a differential sweep through an  $x$ - $y$  plane to classify area elements into regions of different electric field magnitude. These regions are later multiplied by a height differential to obtain a volume. The process is repeated on a different  $x$ - $y$  plane until the whole height of the volume being analyzed has been swept. The differentials in the  $x$  and  $y$  directions were 0.20245 and 0.19492  $\mu\text{m}$  respectively. The height differential changed depending on the height of the electrodes. If the electrode height is not 100  $\mu\text{m}$  (but 5, 40 or 70  $\mu\text{m}$ ), the height differential was 5  $\mu\text{m}$ . This differential value was chosen because the number of points obtained from COMSOL Multi-physics 3.3a was limited by the memory of the equipment used here. However, it was found to be reasonably accurate to calculate the volumes in the 98  $\mu\text{m}$ -high rectangular prism. In the case of 100  $\mu\text{m}$ -high posts the height differential used was 98  $\mu\text{m}$ . This value was used because it was observed in the simulation results how the spatial distribution of the electric field created by electrodes as tall as the channel containing them does not change significantly in the  $z$ -axis (Fig. 3.3d). The numerical method was first validated by calculating the volume of a quarter of electrode given by an electric field equal to zero. A further validation is the fact that the sum of all volumes with an

electric field magnitude higher than zero equals the total volume of the rectangular prism minus the volume of the quarter of electrode.

### 3.1.2 Experimental validation

The simulation results obtained with COMSOL Multi-physics are experimentally validated in this section. Furthermore, the minimum electric field gradient magnitude required to trap cells flowing through the electrode array at a given rate is also specified. COMSOL multi-physics was used to calculate the electric field gradient created by the electrode array in the sample volume shown in Fig. 3.1a. The sample conductivity is  $10 \mu\text{S}\cdot\text{cm}^{-1}$  which is an approximate of the conductivity of DI water. The post electrodes feature a height of  $70 \mu\text{m}$  and are polarized by a  $20 \text{V}_{\text{pp}}$  signal. Experimental results were obtained by using a carbon-DEP chip similar to that described in the 2-stage column in Table 2.7. Two different experimental samples were used separately to demonstrate positive and negative DEP. The experimental sample to demonstrate positive DEP featured yeast cells (*S. cerevisiae*) in DI water. The sample is flowed through the carbon-DEP chip using a syringe pump to keep the flow rate constant at  $10 \mu\text{l}\cdot\text{min}^{-1}$ . A function generator was used to polarize the electrode array with a sinusoidal signal featuring magnitude of  $20 \text{V}_{\text{pp}}$  and frequency of  $100 \text{kHz}$ . At this frequency, viable and non viable yeast cells are attracted to those regions with a high electric field gradient (positive-DEP force). The experimental sample to demonstrate negative DEP featured  $8 \mu\text{m}$ -diameter latex particles (Duke Scientific, now part of Thermo Fisher Scientific) in DI water. In this case a drop of the sample is deposited on the electrode array which is open to the environment. No microfluidics are used in this approach. The electrode array is polarized

by a sinusoidal signal with magnitude  $20 V_{pp}$  and frequency 1 MHz. At this frequency the latex particles are clustered in those volumes with no electric field gradient (negative-DEP). Simulation and experimental results are shown in Fig. 3.2. The pictures of experimental results were taken 10 minutes after the experiment was started. The sample flow, when present, is from top to bottom.

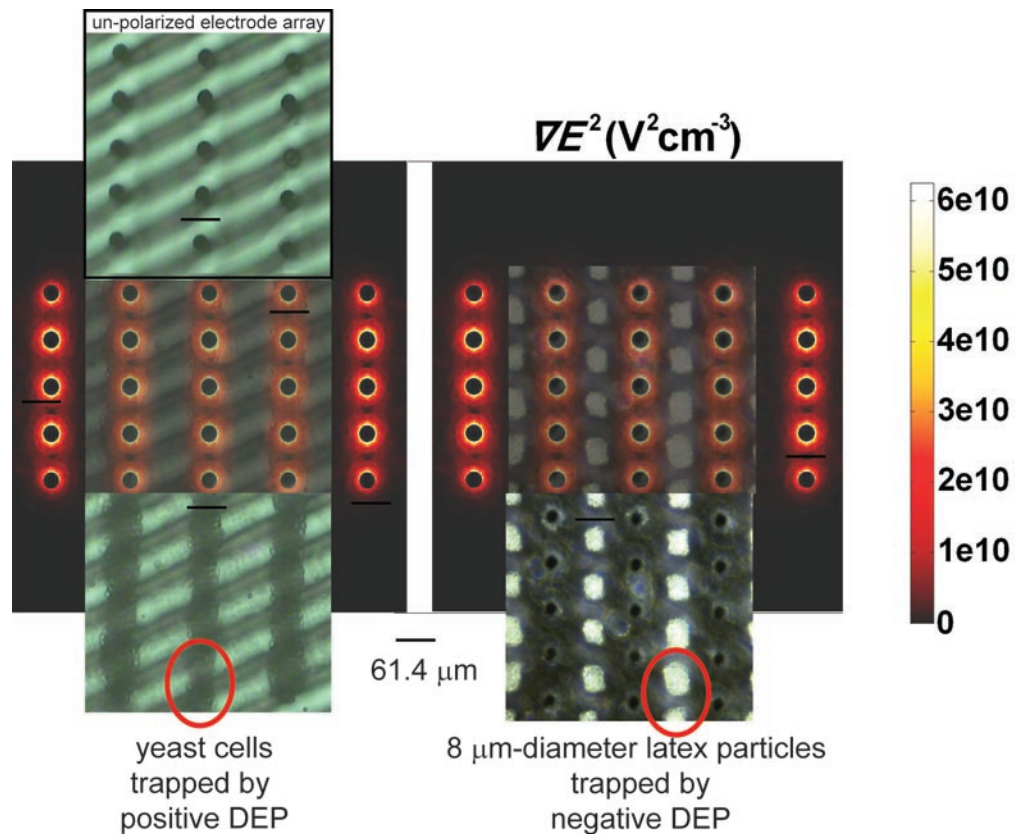


**Fig. 3.2** Experimental validation of the simulation results. Experimental results are positioned on top and overlapped with the simulation results (the figures with shades of red). Positive-DEP is demonstrated by trapping yeast cells (red ellipse on the left) against a flow rate of  $10 \mu\text{l min}^{-1}$ . Negative-DEP is demonstrated by clustering latex particles (red ellipse on the right) in stationary conditions. A picture of the un-polarized electrode array is shown in the top left

Positive-DEP is demonstrated on the left side of the figure by trapping yeast cells in the regions with strongest magnitude gradient. These volumes are those denoted by the brightest shades of red, yellows and whites in the simulation results and are located around the carbon electrodes in this case. Since the electrode array is asymmetric (the gap between electrodes in the y-axis is smaller than that in the x-axis) the strongest gradient is in the y-axis gaps between electrodes and is in these volumes where the yeast cells are mainly trapped. This gives rise to the characteristic columns which are collinear to the flow lines in the channel. A minimum electric field gradient magnitude of around  $0.75 \times 10^{10} \text{ V}^2 \cdot \text{cm}^{-3}$  is needed to trap yeast cells against a flow rate of  $10 \mu\text{l} \cdot \text{min}^{-1}$ . This value was determined based on the comparison between simulation and experimental results. The use of slower flow rates permits cell trapping in volumes with lower electric field gradient magnitude. A minimum electric field magnitude of  $0.3\text{-}0.5 \times 10^{10} \text{ V}^2 \cdot \text{cm}^{-3}$  is expected to be required to trap particles using positive-DEP in stationary conditions (no flow). Cells flowing at a faster rate than  $10 \mu\text{l} \cdot \text{min}^{-1}$ , for example at  $40 \mu\text{l} \cdot \text{min}^{-1}$ , only get trapped in regions with electric field magnitude higher than approximately  $3 \times 10^{10} \text{ V}^2 \cdot \text{cm}^{-3}$  as shown in Fig. 3.3. Negative-DEP is validated by the clustering of latex particles in the regions with the lowest magnitude of electric field gradient. Care must be taken to guarantee that the electric field magnitude used for DEP does not compromise the viability of the cell. More details on cell viability will be presented in the section Membrane breakdown in chapter 4.

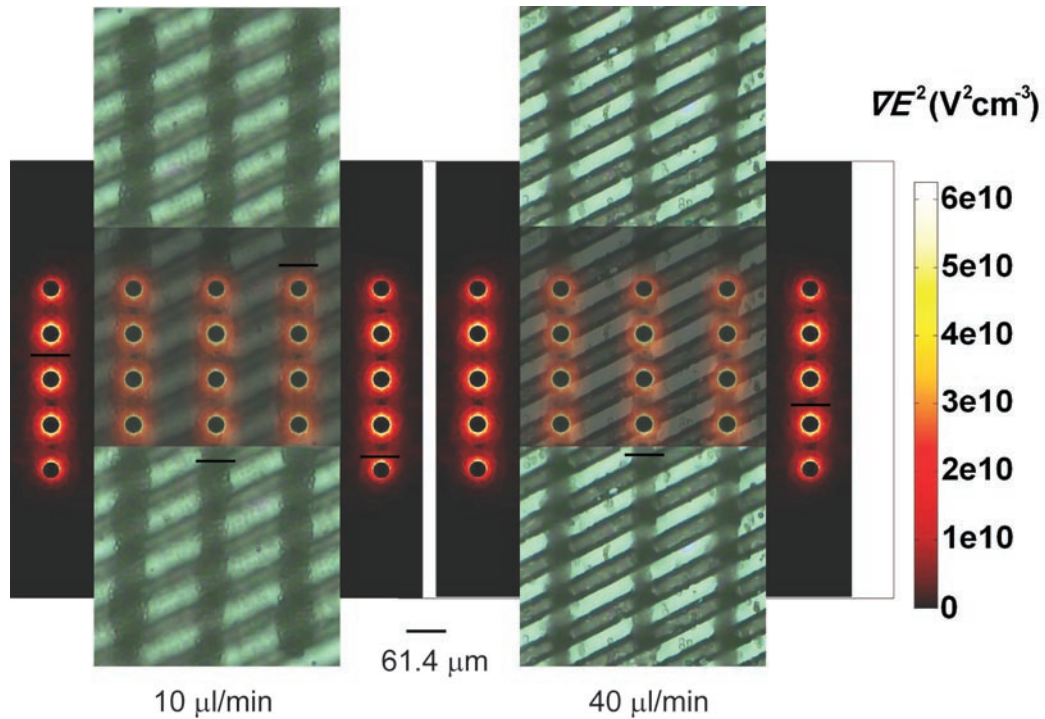


**Fig. 3.3** Yeast cells trapped using positive-DEP against a flow rate of 10 and 40  $\mu\text{l}\cdot\text{min}^{-1}$ . Note how the trapping efficiency is less in the case sample is flowed at 40  $\mu\text{l}\cdot\text{min}^{-1}$

### 3.1.3 Variations on electrode height

The variation of available volume for positive and negative-DEP depending on electrode height is detailed next. Four different electrode heights: 5, 40, 70 and 100  $\mu\text{m}$  are considered here and separate simulations are implemented for each value. The height of the electrode array is the only parameter changed in such set of simulations. All electrode arrays are contained in a 100  $\mu\text{m}$  channel. The sample conductivity and polarization voltage are kept constant at 100  $\mu\text{S}\cdot\text{cm}^{-1}$  and 20  $\text{V}_{\text{pp}}$  respectively. The electric field gradient around selected carbon post electrodes featuring different heights is shown in Fig. 3.4 as calculated using COMSOL multi-physics. The figures shown are x-z cross-sections of the correspondent electrode arrays. Fig. 3.4e shows the plot describing how the volumes of different electric field gradient magnitude intervals change depending on

the electrode height. This plot was obtained following the numerical method to calculate volumes detailed above. The sum of the volumes obtained for all electric field magnitudes for a given electrode height approximates the total volume of the rectangular prism minus the quarter of the carbon electrode presented in Fig. 3.1b.

The use of short electrodes offers the less total volume with a high electric field gradient magnitude. Based on the results obtained in the experimental validation section an electric field magnitude squared threshold of  $0.75 \times 10^{10} \text{ V}^2 \cdot \text{cm}^{-3}$  is assumed here to be necessary to trap yeast cells against a  $10 \mu\text{l} \cdot \text{min}^{-1}$  flow rate and a threshold of  $0.5 \times 10^{10} \text{ V}^2 \cdot \text{cm}^{-3}$  to trap cells in stationary conditions (no flow). The conditions to trap other cells can be determined using a similar methodology. Following the threshold electric field gradient magnitude obtained above, the use of  $5 \mu\text{m}$  electrodes offers a trapping volume of approximately  $6.51 \times 10^4 \mu\text{m}^3$  which is enough to hold 243 particles featuring a diameter of  $8 \mu\text{m}$  (the volume of such particle is  $268 \mu\text{m}^3$ ). As the height of the electrode increases the volume also increases to  $1.01 \times 10^5 \mu\text{m}^3$  ( $40 \mu\text{m}$ -high electrodes),  $1.15 \times 10^5 \mu\text{m}^3$  ( $70 \mu\text{m}$ -high electrodes) and  $2.05 \times 10^5 \mu\text{m}^3$  in the case of  $100 \mu\text{m}$ -high electrodes. This result validates the advantage of using 3D electrodes to fabricate high throughput DEP devices. Planar electrodes traditionally used in DEP offer even less trapping volume than the shortest electrodes presented here since their thickness is in the range of hundreds of nanometers.

The use of  $100 \mu\text{m}$ -high posts offers the most trapping volume given by the sum of all volumes with an electric field gradient magnitude squared higher than  $0.75 \times 10^{10} \text{ V}^2 \cdot \text{cm}^{-3}$ .

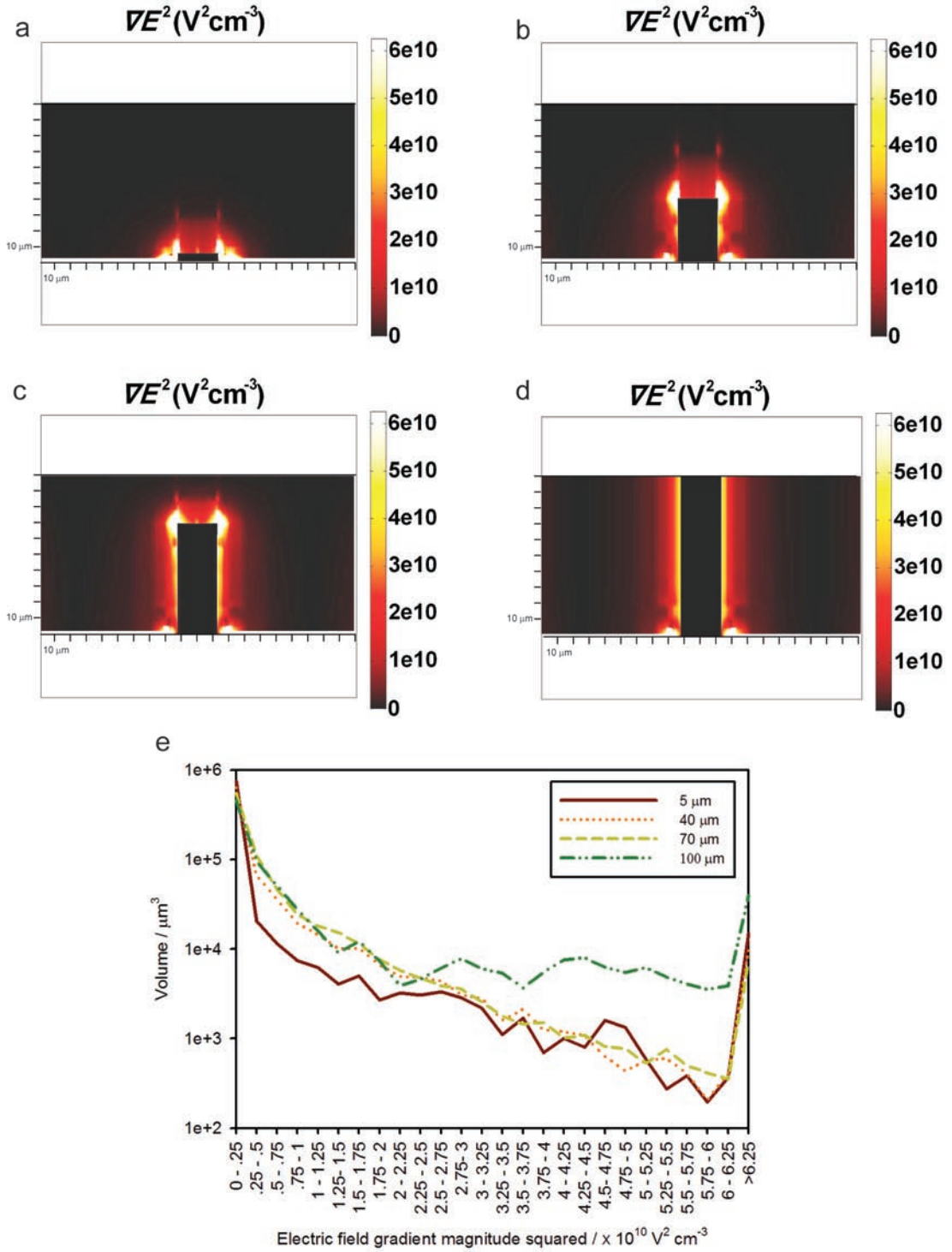


**Fig. 3.4** Spatial distribution of the electric field gradient magnitude squared around a carbon post electrode with a height of a) 5, b) 40, c) 70 and d) 100  $\mu m$ . e) Plot describing how the volumes of different electric field magnitude intervals change depending on the electrode height.

In general, the use of electrodes as tall as the channel containing them (as is the case of the 100  $\mu\text{m}$ -high posts presented here) offers a uniform distribution of the electric field along the height of the channel as shown in Figure 3.4d. In this case, the magnitude of the electric field mainly varies in the radial direction on the x-y plane and the degree of DEP manipulation on a given cell does not depend on its relative position to the total height of the channel. The benefit of using short electrodes to contain cells in negative-DEP regions is clearly demonstrated in Fig. 3.4e since such electrodes provide the most volume with no electric field gradient.

### **3.1.4 Variations on polarizing voltage**

The variation of positive and negative DEP volume depending on the voltage applied in the connection pads is detailed in this section. Individual simulations were implemented for applied voltages of 5, 10, 20 and 40  $V_{pp}$ . The height of the carbon post electrode and the sample conductivity are maintained constant at 100  $\mu\text{m}$  and 100  $\mu\text{S}\cdot\text{cm}^{-1}$  respectively. The distribution of the electric field throughout the sample volume for each applied voltage was calculated using COMSOL multi-physics. The volumes for different intervals of electric field magnitudes were calculated using MATLAB 7.0 following the numerical method detailed above. The results are shown in Fig. 3.5 and represent the spatial distribution of the electric field gradient magnitude squared around an exemplary carbon electrode. Fig. 3.5e plots the variation in the volume of different electric field gradient magnitude squared intervals depending on the polarization voltage.

The regions with highest magnitude of electric field are those immediately around the carbon post. Close inspection of Fig. 3.5 a) through d) show how the electric field

gradient is qualitatively the same regardless of the polarizing voltage. It is the magnitude in each region that increases as the polarizing voltage is increased. Therefore, the use of 40  $V_{pp}$  instead of 5  $V_{pp}$  as polarizing voltage provides more trapping volume and increases the throughput of a carbon-DEP device as shown in Fig. 3.5e. For example, polarizing the electrode array with 40  $V_{pp}$  creates a volume around each electrode capable to trap approximately 6 000 particles featuring an 8  $\mu\text{m}$ -diameter (considering an electric field gradient magnitude squared threshold of  $0.75 \times 10^{10} \text{ V}^2 \cdot \text{cm}^{-3}$ ). The use of a polarizing voltage equal to 5  $V_{pp}$  only creates a volume that is wide enough to trap 100 particles per electrode. Unfortunately the use of a 40  $V_{pp}$  polarizing voltage creates regions where the electric field magnitude is higher than  $7\,500 \text{ V} \cdot \text{cm}^{-1}$ . Such strong electric field may be detrimental to the cells. More details on cell viability are discussed in the section cell membrane breakdown in chapter 4.

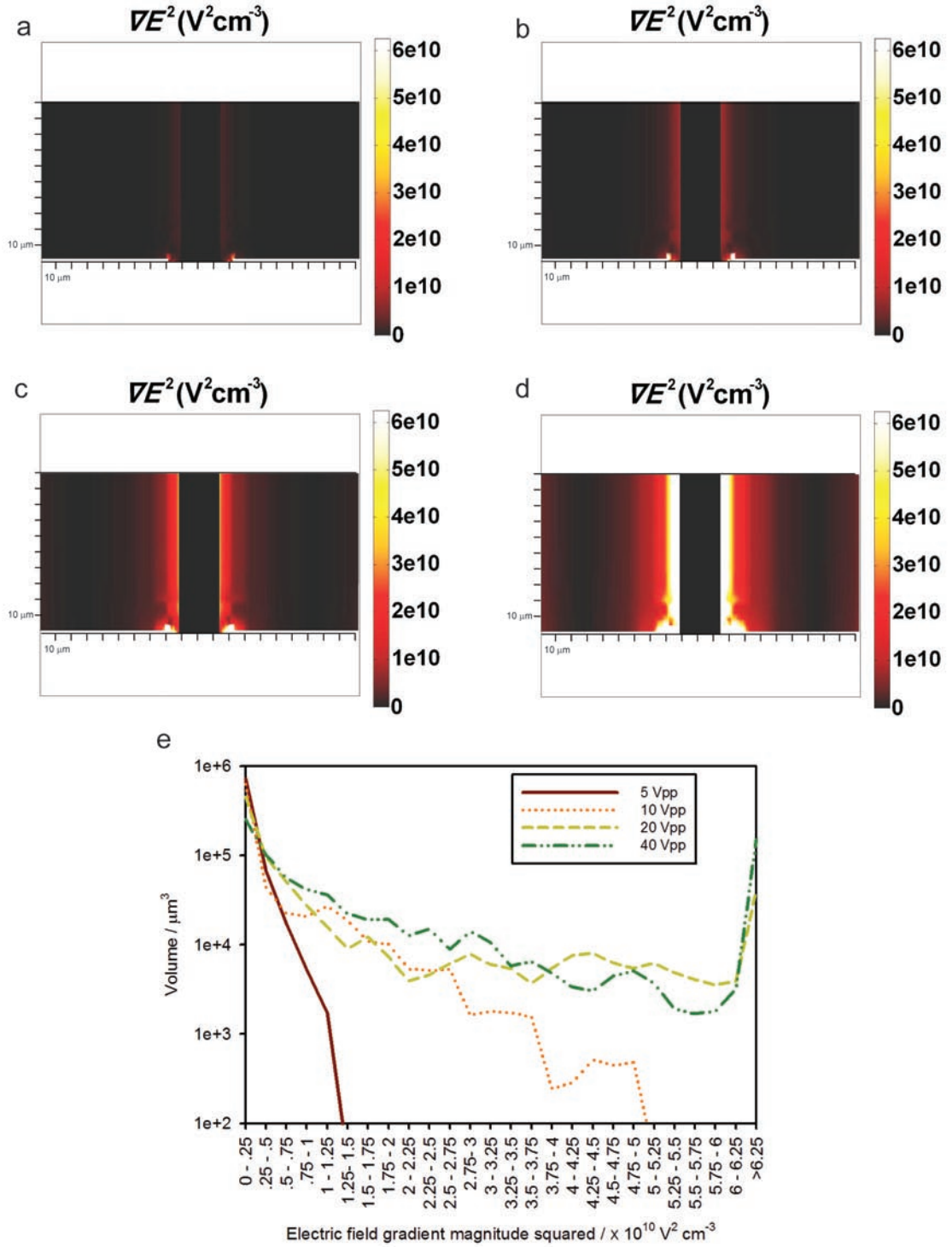


**Fig. 3.5** Spatial distribution of the electric field gradient magnitude squared around the carbon electrodes when polarized using different voltages: a) 5, b) 10, c) 20 and d) 40 Vpp. e) Plot describing how the volumes of different electric field gradient magnitude squared intervals change depending on the polarizing voltage

### 3.1.5 Variations on sample conductivity

The effect of sample conductivity on the trapping volume is presented in Fig. 3.6. Figures 3.6 a) through d) represent the results from individual simulations using conductivity values of 10, 100, 1000 and 5000  $\mu\text{S}\cdot\text{cm}^{-1}$  respectively. The figures represent the spatial distribution of the electric field gradient magnitude squared around selected carbon electrodes. The height of the carbon post electrode array and the polarization voltage are maintained constant at 100  $\mu\text{m}$  and 20  $V_{\text{pp}}$  respectively. Fig. 3.6e plots the variation in the volume of different electric field gradient magnitude squared intervals depending on the sample conductivity. Close inspection of Fig. 3.6 a) through d) show why a low conductive media is desired to maximize the trapping volume. The use of media with conductivity of 10  $\mu\text{S}\cdot\text{cm}^{-1}$  (DI water for example) creates a volume around each electrode capable to trap approximately 4 000 particles featuring an 8  $\mu\text{m}$ -diameter (considering an electric field magnitude threshold of  $0.75 \times 10^{10} \text{ V}^2\cdot\text{cm}^{-3}$ ). In contrast, the use of conductivity values equal to 5 000  $\mu\text{S}\cdot\text{cm}^{-1}$  (an approximate to the conductivity of blood which is around 6 000  $\mu\text{S}\cdot\text{cm}^{-1}$ ) only creates a volume that is wide enough to trap 1 300 particles per electrode. Fortunately, the difference on throughput obtained by varying the sample conductivity is not as big as that obtained when varying the electrode height or the polarizing voltage. The sample conductivity can then be varied across a wide range of values without paying a significant penalty on the throughput of the device. The conductivity of the media must be optimized first to prevent breakdown of the cell membrane and then to facilitate cell sorting using DEP as it will be detailed in chapter 4.

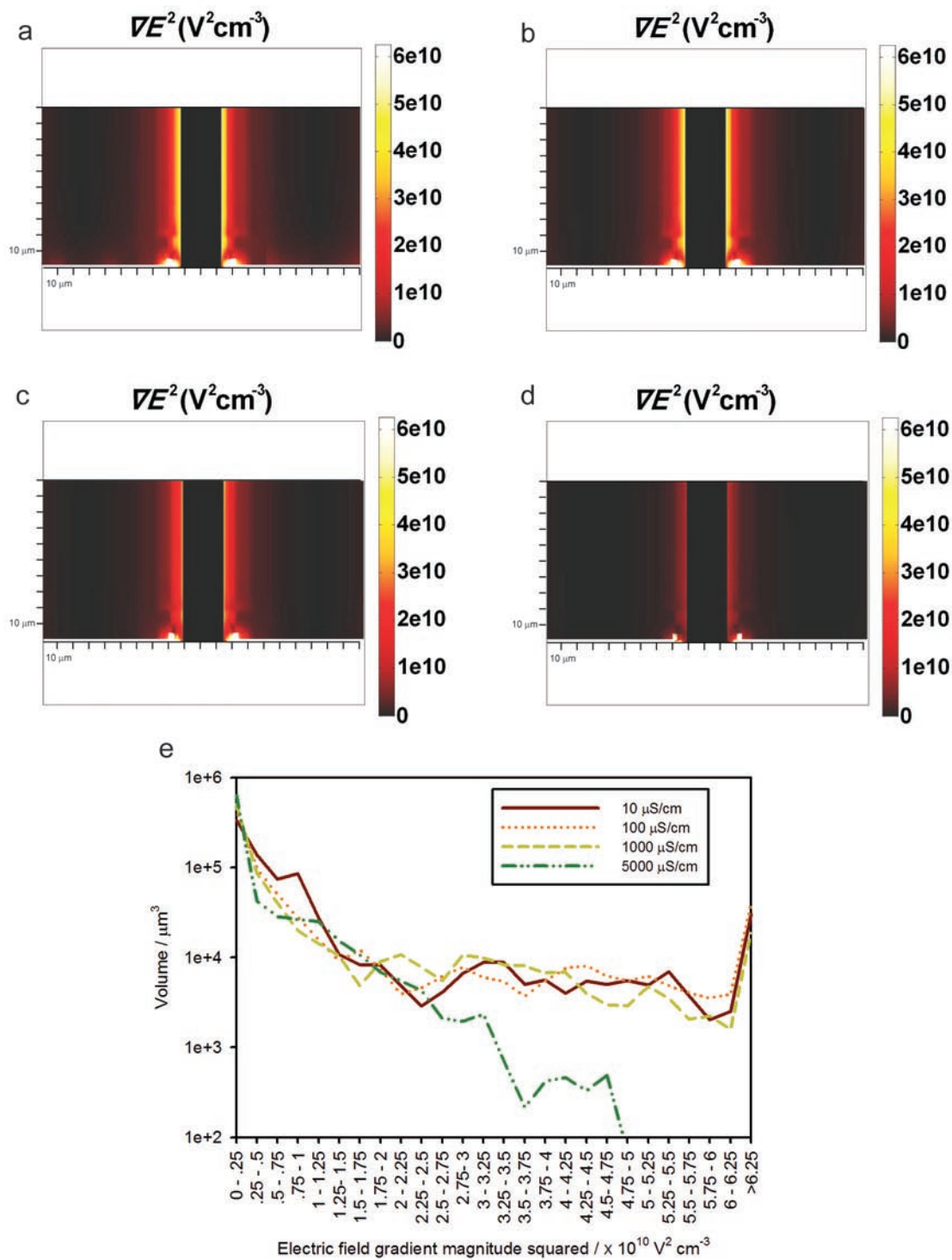


**Fig. 3.6** Spatial distribution of the electric field gradient magnitude squared around a polarized carbon electrode when surrounded by liquid with different conductivities: a) 10, b) 100, c) 1000 and d) 5000  $\mu S \cdot cm^{-1}$ . e) Plot describing how the volumes of different electric field gradient magnitude squared intervals change depending on the sample conductivity

### 3.2 Fluidodynamic characterization

Since the DEP trapping force must compete with the hydrodynamic drag force to retain the targeted cells around the electrodes the goal of this section is to estimate the hydrodynamic drag force by modeling the flow velocity field in a post electrode array. The hydrodynamic drag force  $F_{drag}$  of a spherical particle is related to the flow velocity by the Stokes equation

$$F_{drag} = -6\pi\eta r v \quad (3.2)$$

where  $\eta$  is the viscosity of the fluid,  $r$  is the radius of the particle and  $v$  is the flow velocity. Cells can be approximated as spherical particles. The same geometry used for the electromagnetic modeling (Fig. 3.1a) is used here but the electromagnetic and fluidodynamic simulations are independent from each other. The height of the post electrode array and the channel is 100  $\mu\text{m}$ . The channel floor is considered to be flat. Channel walls and electrode surfaces are assumed to be flat to simplify analysis even when experimental device does show minimal roughness on the mentioned surfaces.

Computational Fluid Dynamics (CFD) simulation was conducted using Fluent 6.3.26 (ANSYS, Inc.). Analysis was done numerically by solving the Navier-Stokes equation in a 3D structured grid using an absolute velocity formulation with a relaxation factor of 0.3 for the pressure, density body forces and momentum variables. The problem was solved in steady condition as a fully developed flow assuming a Newtonian flow with water as a fluid. No-slip boundary conditions are imposed on the channel walls and the surface of the carbon posts. A 3D pressure-based laminar approach was considered with a mass-flow channel inlet of  $1.66667 \times 10^{-7} \text{ kg}\cdot\text{s}^{-1}$  (equal to a water flow rate of  $10 \mu\text{l}\cdot\text{min}^{-1}$ ) and an outflow boundary condition at the outlet. Such condition assumes a zero normal

gradient for all flow variables except pressure and represents an idealized flow through channel. Velocity and pressure have been coupled using a standard model that uses a relationship between velocity and pressure corrections to enforce mass conservation and to obtain the pressure field. A second order upwind scheme was used for the numerical discretization of pressure and momentum.

### **3.2.1 Flow velocity field**

The 3D flow velocity field in the electrode array is shown in Fig. 3.7. The flow is parabolic in 3 dimensions as shown in figures c through f. The flow profile at the cross-section  $\alpha$  indicated in figure d) is shown in figure b). A maximum velocity of  $2.08 \times 10^{-2} \text{ m}\cdot\text{s}^{-1}$  is at the regions furthest away from the electrode and channel surfaces. A decreasing gradient on flow velocity magnitude is towards the electrode surfaces. The flow velocity is zero at the surface of the electrodes due to the no-slip boundary condition imposed in the simulation. The flow velocity in the plane perpendicular to the flow (y-z plane) is significantly stronger than that in the plane collinear with the flow (x-z plane) as determined by comparing figures e and f. This is a consequence of the asymmetry of the electrode array. The gap between posts in the axis collinear with the flow is half of that between posts in the axis perpendicular to the flow.

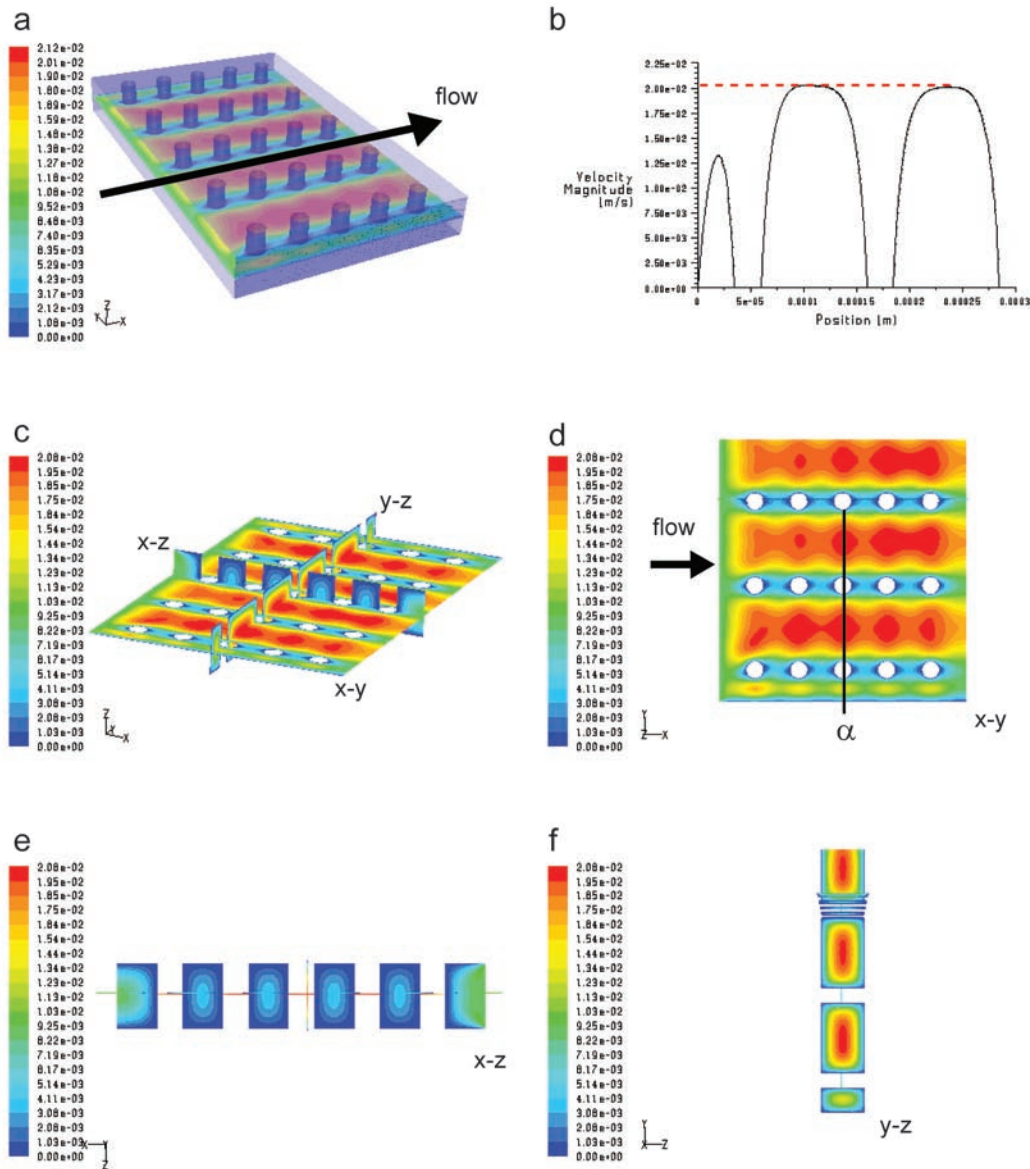


**Fig. 3.7** Different views of the flow velocity field established in an electrode array when flowing water at  $10 \mu\text{l} \cdot \text{min}^{-1}$ . a) Isometric view, b) flow profile at the cross-section  $\alpha$  indicated in d); c) 3D view showing the flow profile at the three planes: d) x-y, e) x-z and f) y-z

One advantage of using post electrodes in 3D carbon-DEP devices is the fact that this geometry does not disturb the laminar flow established in the micro-channel. The flow pathlines in the electrode array are shown in Fig. 3.8 and show how they remain

continuous throughout the whole array. Flow turbulence is not introduced in the channel to prevent physical forces other than the hydrodynamic drag force from competing against the DEP trapping force.

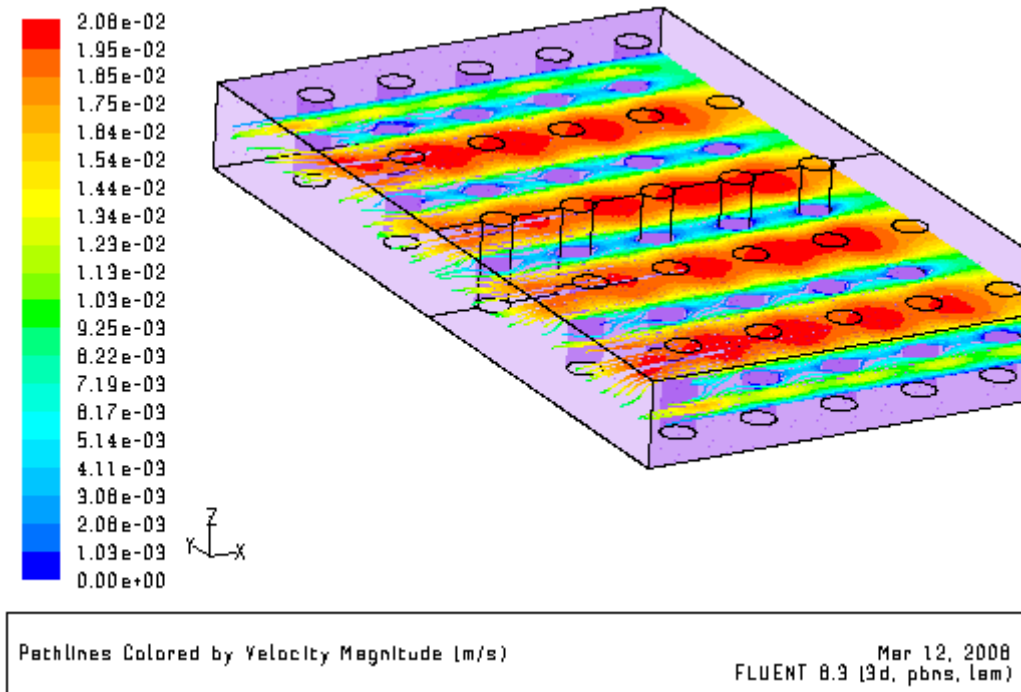


**Fig. 3.8** Flow pathlines through an electrode array

### 3.3 Discussion

The impact of electrode height, polarization voltage and sample conductivity on the volume distribution of different electric field gradient magnitude squared ranges is described by Figs. 3.9 a, b and c respectively. The maximum throughput of an individual electrode when trapping 8  $\mu\text{m}$  diameter particles, such as the yeast cells used in this work, can be calculated by adding the volume of all gradient magnitude ranges that lead to trapping, multiply the addition by 4 since the results shown here are for a quarter of

electrode and finally dividing the product by the volume of an individual 8  $\mu\text{m}$  particle. The ideal case when no air gaps exist in between the trapped particles is assumed here, the practical throughput may be slightly less than this result. For example the use of a 70  $\mu\text{m}$  tall electrode, a polarizing voltage of 20  $V_{pp}$  and a media conductivity of  $100 \mu\text{S}\cdot\text{cm}^{-1}$  yields an approximate maximum throughput of 1 720 yeast cells per electrode if a minimum gradient of  $0.75 \times 10^{10} \text{V}^2\cdot\text{cm}^{-3}$  is considered to induce trapping (Fig. 3.8a). A carbon-DEP device featuring a 5 X 160 70  $\mu\text{m}$ -high electrode array can thus trap up to  $1.36 \times 10^6$  yeast cells when using the experimental parameters just detailed. The use of tall electrodes, high polarization voltage and low sample conductivity is demonstrated to yield the widest volume to contain cells trapped by positive-DEP. In contrast, the use of short electrodes, low polarization voltage and high sample conductivities maximizes the volume for negative-DEP. Fig. 3.9 serves as a guide to optimize the electrode height, the polarization voltage and sample conductivity to maximize the trapping regions and increase throughput of carbon-DEP devices.

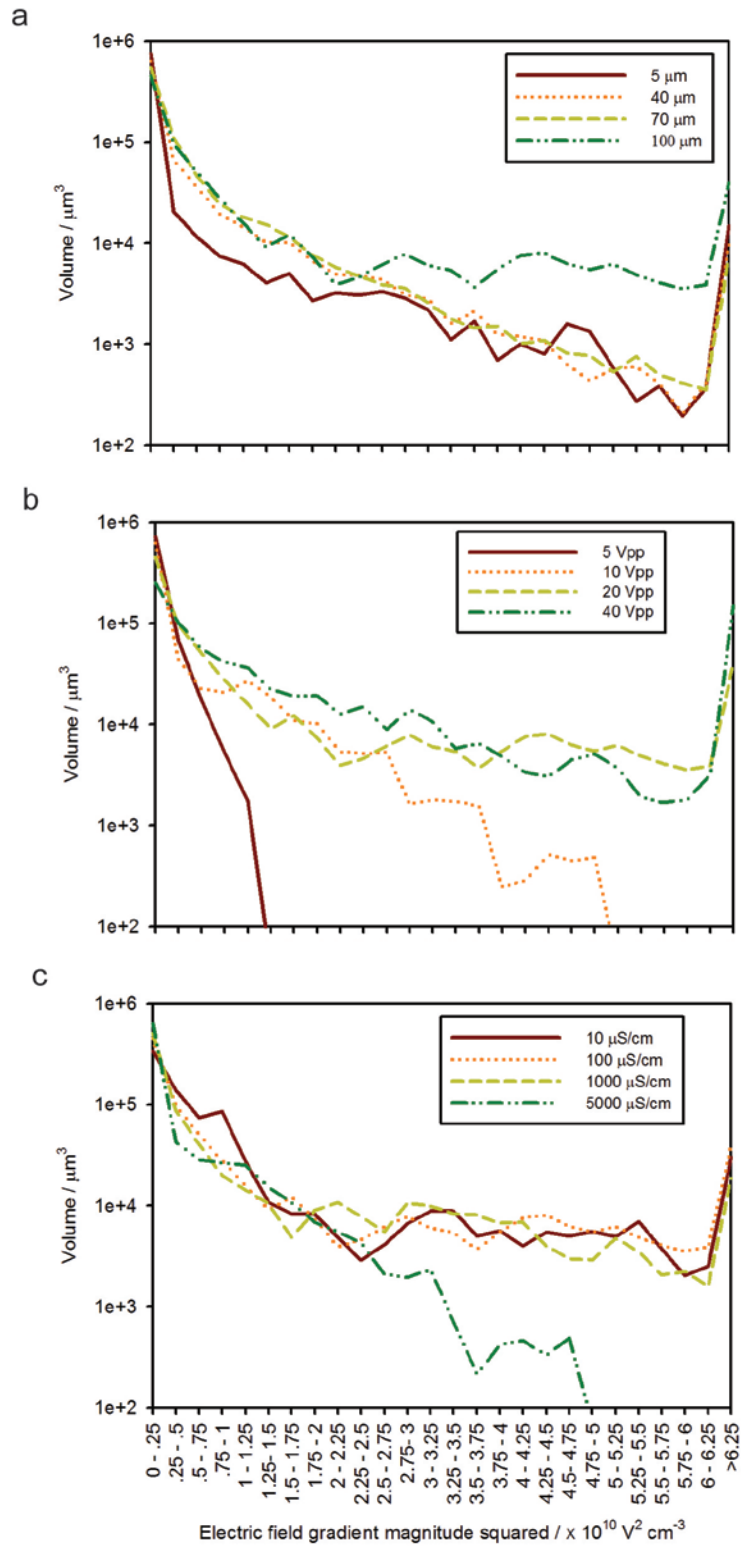


**Fig. 3.9** The impact of a) electrode height, b) polarization voltage and c) sample conductivity on the volume distribution of different electric field gradient magnitude squared ranges.

The hydrodynamic drag force on cells flowing through the electrode array can be calculated using equation 2.11 after extracting the flow velocity value at a desired point from Fig. 3.7. The DEP trapping force is directly proportional to the magnitude of the electric field gradient shown in Figs. 3.4 to 3.6 for the cases when the electrode height, polarization voltage and sample conductivity change. A cell will be trapped around the electrodes as long as the DEP force is stronger than the hydrodynamic drag force. Here the discussion is on the interaction of the flow velocity and electric fields in the electrode array. The discussion is based on the results shown in Fig. 3.10. The electric field gradient ( $\nabla E$ ) increases towards the surface of the electrodes while the flow velocity gradient ( $\nabla v$ ) decreases. Therefore, the regions with the strongest electric field gradient magnitude also feature the less flow velocity. This is extremely advantageous for cell trapping using positive DEP since the particles are trapped in the regions where the hydrodynamic drag force is minimal. DEP force requirements, *i.e.*, polarizing voltage and sample conductivity, could be relaxed in these regions and still achieve a desired throughput at a given flow rate. On the other hand, the particles repelled from the electrode surfaces using negative-DEP can be rapidly and efficiently eluted from the electrode array. This is because the particles are electrically repelled from the regions of highest electric field magnitude to those volumes with the strongest flow velocity. Thanks to the asymmetry of the electrode array presented here (electrode gap is shorter in one axis than in the other one) it is possible to restrict the cell trapping to regions parallel to the flow pathlines to minimally disturb the laminar flow.

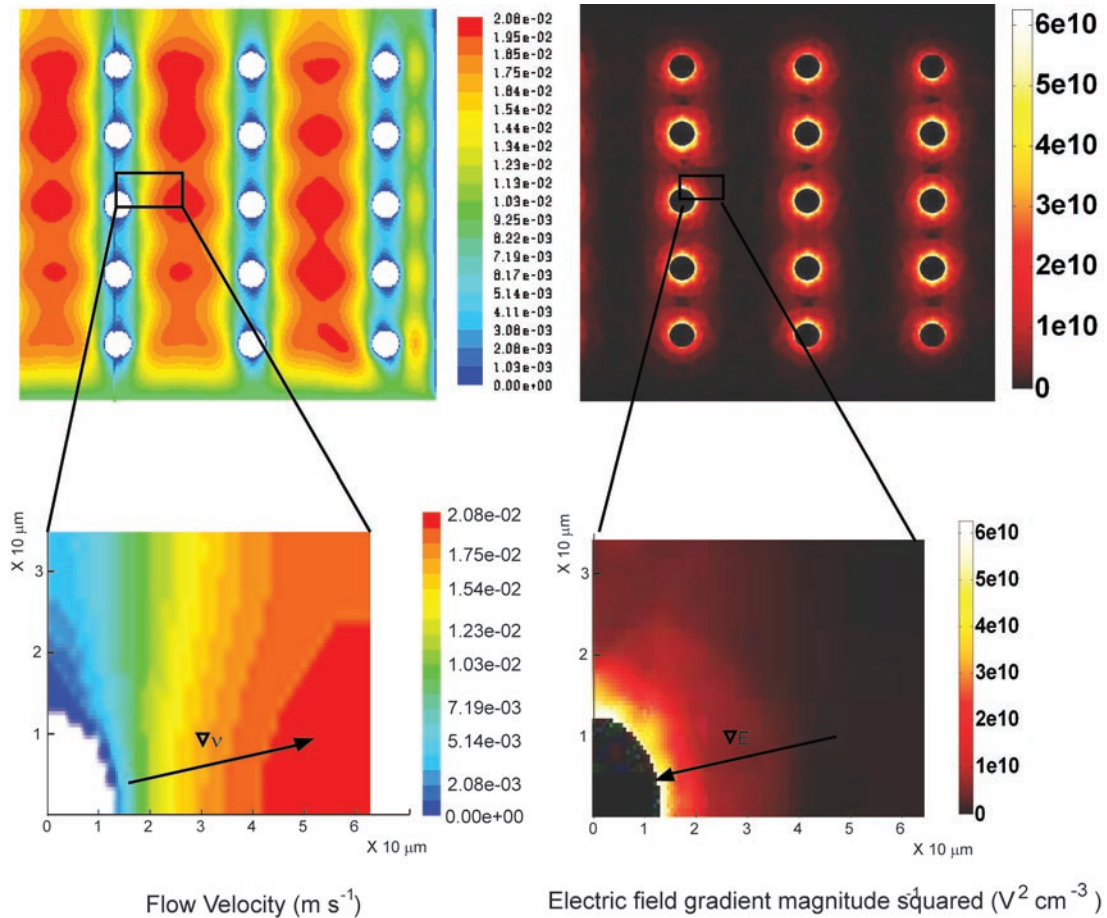


**Fig. 3.10** Comparison of the flow velocity and electric field gradient established in a polarized electrode array. The figures at the bottom are the detail of the areas contained in the rectangles indicated in the top figures. The quarter circle in the bottom left of the detailed views denotes quarter of a post electrode. The flow velocity and electric fields were solved independently from each other and any possible impact of AC electrokinetics on the fluid dynamics in the electrode array is not considered

The use of taller channels proves beneficial to increase the flow rate in the channel while keeping the flow velocity constant. The continuity equation establishes that the mass flow rate  $Q$  in a micro-channel equals the product of the flow velocity  $v$  and the cross-section area  $A$  of the channel ( $Q = v \cdot A$ ). The cross-section area of the channel can be increased by fabricating taller channels. Taller, rather than wider, channels are desired to maintain a small footprint of the DEP chips. The flow rate in the channel can then be increased to process a given sample volume in a shorter period of time but the flow velocity, and the

hydrodynamic drag force, is kept constant. This translates into more rapid cell sorting without sacrificing throughput.

## CHAPTER 4. Cell sorting using carbon-electrode DEP

The details on the experimental work performed to sort different kinds of cells using carbon-DEP devices are presented in this chapter. Previous experimental work on the use of carbon micro electrodes for DEP only includes a basic proof-of-concept by Park and Madou<sup>204</sup> where they clustered latex particles in between a 2 X 2 electrode array using negative-DEP. The manipulation of biological cells using carbon-electrode DEP is demonstrated here.

This chapter starts with general guidelines on how to optimize two important aspects that must be considered during experimentation: cell membrane breakdown and cell suspending media. Electrical loading of the cell causes a stress on the membrane which can compromise the viability of the cell if it is strong enough. The media must support cell viability for long periods of time and exhibit dielectric properties that represent an advantage in DEP, *i.e.*, low conductivity. Therefore, the media must be optimized in terms of its pH, osmolarity, conductivity and presence of nutrients. The different experimental samples used in this work are detailed in the second section of this chapter. The sample parameters detailed include type of particle, concentration of particle populations and the composition and conductivity of the suspending media. The DEP models of all the experimental samples are also presented. The third section details the experimental validation of cell manipulation using carbon-DEP. An experimental platform featuring a syringe pump is used in this chapter only to allow for the visualization of the behavior of different cells under DEP forces since the experimental platform featuring centrifugal microfluidics did not allow to do so. The syringe pump and a variety of fluidic interconnects are eliminated after the integration of DEP with

centrifugal microfluidics. Such integration is detailed in the next chapter. Different DEP functions are demonstrated in this chapter and include filtering and cell focusing using positive-DEP. The screening of other biologically relevant cells such as *E.coli* and *Drosophila melanogaster* is presented at the end of the chapter.

## **4.1 Experimental Considerations**

### **4.1.1 Cell membrane breakdown**

Every cell is enclosed by a plasma membrane. This lipid bi-layer structure is extremely thin (4-10 nm in thickness) and has a large collection of proteins embedded in it (Fig. 4.1). Transport of ions through the membrane is highly regulated by trans-membrane channel proteins, for example the sodium-potassium exchange pump, and under normal circumstances the membrane can be regarded as highly non-conducting. For example, the membrane conductivity of yeast cells has been calculated to be  $2.5 \times 10^{-7} \text{ S}\cdot\text{m}^{-1}$ <sup>4</sup>. The application of large direct current (DC) or low-frequency alternative current (AC) electric fields to a cell induces a large potential drop across the plasma membrane which can cause dielectric breakdown, membrane rupture and a significant increase on membrane conductivity. The length of the electric field pulse is also important; longer times lead to a more rapid cell death. Membrane breakdown may also be referred to as electroporation or electropermeabilization. Although the rupturing of the membrane can cause cell death it can also be optimized to introduce different agents such as DNA, enzymes and antibodies into the cell or to create new hybrids by electrofusion<sup>206</sup>. The goal of this section is to study the effect of media conductivity and electric field magnitude and

frequency on the membrane potential of yeast cells. It has previously been shown that breakdown occurs when the potential is above a threshold value which is specific to a kind of cell but usually is between 0.4 and 1 V<sup>16</sup>. For example, the maximum potential for neurons is only 0.4 V<sup>207</sup>. Therefore, the DEP experimental conditions must be optimized to prevent cell breakdown. Although the study is specific to yeast cells the methodology can be used for many other cell types.

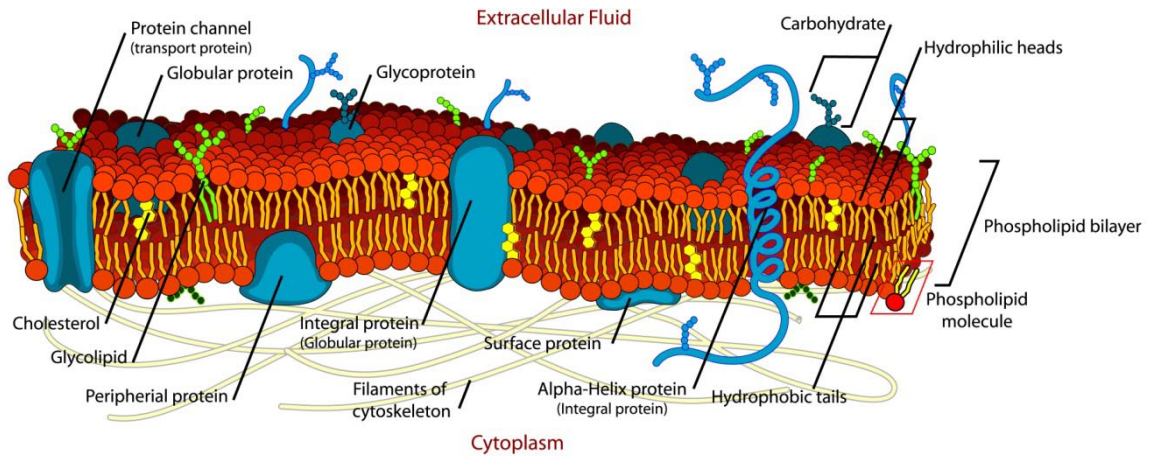


**Fig. 4.1** A cross-section of a cell membrane. This figure is shown here from Wikipedia.com under a public domain license. The original author is LadyofHats Mariana Ruiz

The membrane potential  $V_m$  of a spherical particle under an AC electric field can be calculated as<sup>16</sup>:

$$V_m = \frac{1.5Er\cos\alpha}{\sqrt{1+(2\pi f\tau)^2}} \quad (4.1)$$

where  $r$  is the radius of the particle,  $E$  and  $f$  are the magnitude and frequency of the electric field respectively and  $\alpha$  is the angle between the field line and a normal from the center of the particle to a point of interest on the membrane. In this work  $\alpha$  equals  $0^\circ$  to account for maximal trans-membrane potential. The time constant  $\tau$  of the membrane is given by

$$\tau = rC_{mem} \left( \frac{1}{\sigma_{cyto}} + \frac{1}{2\sigma_{media}} \right) \quad (4.2)$$

where  $C_{mem}$  is the capacitance of the membrane,  $\sigma_{cyto}$  is the conductivity of the cytoplasm and  $\sigma_{media}$  is the conductivity of the suspending media. Equation 4.1 assumes that the membrane conductivity can be neglected, the membrane thickness is much smaller than the cell radius and that the induced membrane potential is sufficiently high to neglect the resting membrane potential (the relatively static membrane potential of quiescent cells)<sup>207</sup>. The values of the different parameters used in this study are resumed in Table 4.1. The membrane potential as a function of electric field magnitude and frequency for three different conductivities is shown in Fig. 4.2 as obtained using equation 4.1.

**Table 4.1** Parameters used to calculate membrane potential on yeast cells

parameter	value	unit
$r$	4	$\mu\text{m}$
$C_{mem}$	0.011	$\text{F}\cdot\text{m}^{-2}$
$\sigma_{cyto}$	0.2	$\text{S}\cdot\text{m}^{-1}$
$\sigma_{media}$	0.001 – 0.1	$\text{S}\cdot\text{m}^{-1}$
$E$	$2.5 \times 10^3 - 2.5 \times 10^6$	$\text{V}\cdot\text{m}^{-1}$
$f$	$1 \times 10^4 - 1 \times 10^7$	Hz

The membrane potential is directly proportional to the conductivity of the media and the magnitude of the electric field but inversely proportional to the frequency of the field. In the case of yeast cells immersed in a media with conductivity less than  $0.001 \text{ S}\cdot\text{m}^{-1}$  (DI water) an electric field with magnitude as high as  $2 \times 10^5 \text{ V}\cdot\text{m}^{-1}$  and frequency down to 10 kHz can be applied without inducing membrane breakdown. However, the frequency of the field must be increased to 100 kHz if the electric field magnitude is more than  $1 \times 10^6 \text{ V}\cdot\text{m}^{-1}$  (Fig. 4.2a). If the conductivity of the media is increased to  $0.01 \text{ S}\cdot\text{m}^{-1}$  ( $100 \mu\text{S}\cdot\text{cm}^{-1}$ ) the maximum electric field magnitude that can be applied at 10 kHz decreases

to around  $6 \times 10^4 \text{ V}\cdot\text{m}^{-1}$ . A field magnitude higher than  $1 \times 10^6 \text{ V}\cdot\text{m}^{-1}$  may be used only if the frequency is higher than 1 MHz (Fig. 4.2b).

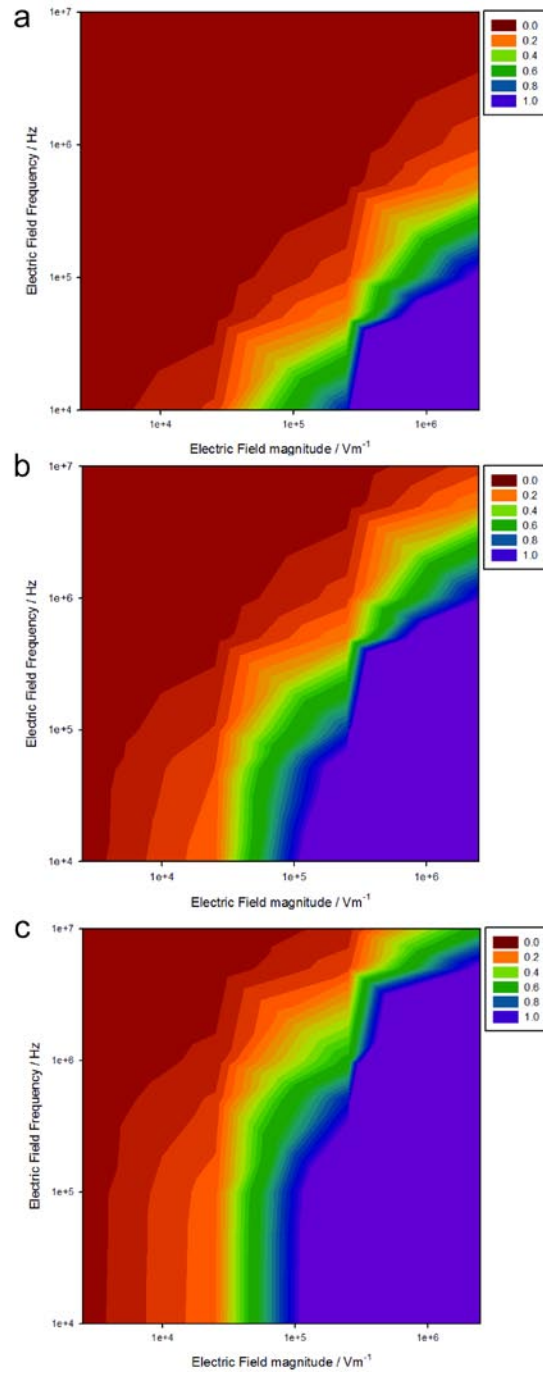


**Fig. 4.2** Membrane potential of a yeast cell as a function of electric field magnitude and frequency for medium conductivities of a)  $0.001 \text{ S}\cdot\text{m}^{-1}$ , b)  $0.01 \text{ S}\cdot\text{m}^{-1}$  and c)  $0.1 \text{ S}\cdot\text{m}^{-1}$

The use of a media with even higher conductivity, for example  $0.1 \text{ S}\cdot\text{m}^{-1}$ , makes it necessary to use fields with frequency as high as 10 MHz to prevent membrane breakdown when the magnitude of the field is around  $1 \times 10^6 \text{ V}\cdot\text{m}^{-1}$ . Field frequencies less than 10 kHz may only be used if the electric field magnitude is below  $6 \times 10^4 \text{ V}\cdot\text{m}^{-1}$  (Fig. 4.2c). In general, the use of a suspending media with low conductivity and an electric field featuring a low magnitude and high frequency is desired to prevent cell membrane breakdown.

The distribution of the electric field magnitude created in a sample volume using different polarizing voltages and sample conductivities was calculated using COMSOL Multi-physics following the methodology detailed in chapter 3, section 3.1. The change in volume of regions featuring an electric field value within specific ranges was calculated as electrode height, polarizing voltage and sample conductivity change following the methodology presented in section 3.1. The results are presented in Fig. 4.3. Figs. 4.2 and 4.3 must be used together to determine experimental parameters such as frequency of the electric field, the polarizing voltage and the sample conductivity to prevent membrane breakdown during DEP experiments. The volume of those regions with an electric field value capable to cause membrane breakdown must be minimized by optimizing sample parameters. Electroporation is not desired during DEP-assisted cell sorting because the viability of the processed cells must not be compromised.

The use of 70  $\mu\text{m}$  high electrodes may yield better results than 100  $\mu\text{m}$  ones if the cells to be manipulated are sensitive to electric field magnitudes higher than  $5\,000 \text{ V}\cdot\text{cm}^{-1}$  and the polarizing voltage and sample conductivity are maintained constant (see Fig. 4.3a). Electroporation studies may benefit from the use of 40  $\text{V}_{\text{pp}}$  polarizing voltages to

maximize the volume with electric field magnitude higher than  $7500 \text{ V}\cdot\text{cm}^{-1}$ . DEP applications may find this polarizing voltage too high to guarantee cell viability and polarizing voltages less than  $20 \text{ V}_{\text{pp}}$  may be required. Even though the use of low conductive media increases the volume for positive-DEP, it is often required to use conductive buffers during DEP experiments to maintain a balance in osmolarity between the cell interior and the suspending media (details on section 4.1.2).

An example on the utility of Figs. 4.2 and 4.3 follows. Figure 4.4 is used in this example and combines Figure 4.3b, which shows how the volume distribution of different ranges of electric field magnitude changes as the polarizing voltage is increased and the sample conductivity is  $0.01 \text{ S}\cdot\text{m}^{-1}$ . The change on membrane potential depending on sample conductivity and electric field frequency when the field magnitude equals  $7.5 \times 10^5 \text{ V}\cdot\text{m}^{-1}$  is shown in Fig. 4.4b. Here it is arbitrarily assumed that electric fields with magnitude higher than  $7.5 \times 10^5 \text{ V}\cdot\text{m}^{-1}$  are enough to electroporate a given cell. After inspection of Fig. 4.4a it is observed that the use of a polarizing voltage of  $40 \text{ V}_{\text{pp}}$  creates a volume around an electrode with electric field magnitude higher than  $7.5 \times 10^5 \text{ V}\cdot\text{m}^{-1}$  (gray square at the bottom right). This volume is wide enough to contain approximately 750 cells (if the cell features a  $8 \mu\text{m}$  diameter) which are at risk of membrane breakdown unless the field frequency is above a threshold value. Fig. 4.4b must then be used to determine such value. Frequencies higher than  $500\,000 \text{ kHz}$  are required if the sample conductivity is  $0.01 \text{ S}\cdot\text{m}^{-1}$  (dotted line).

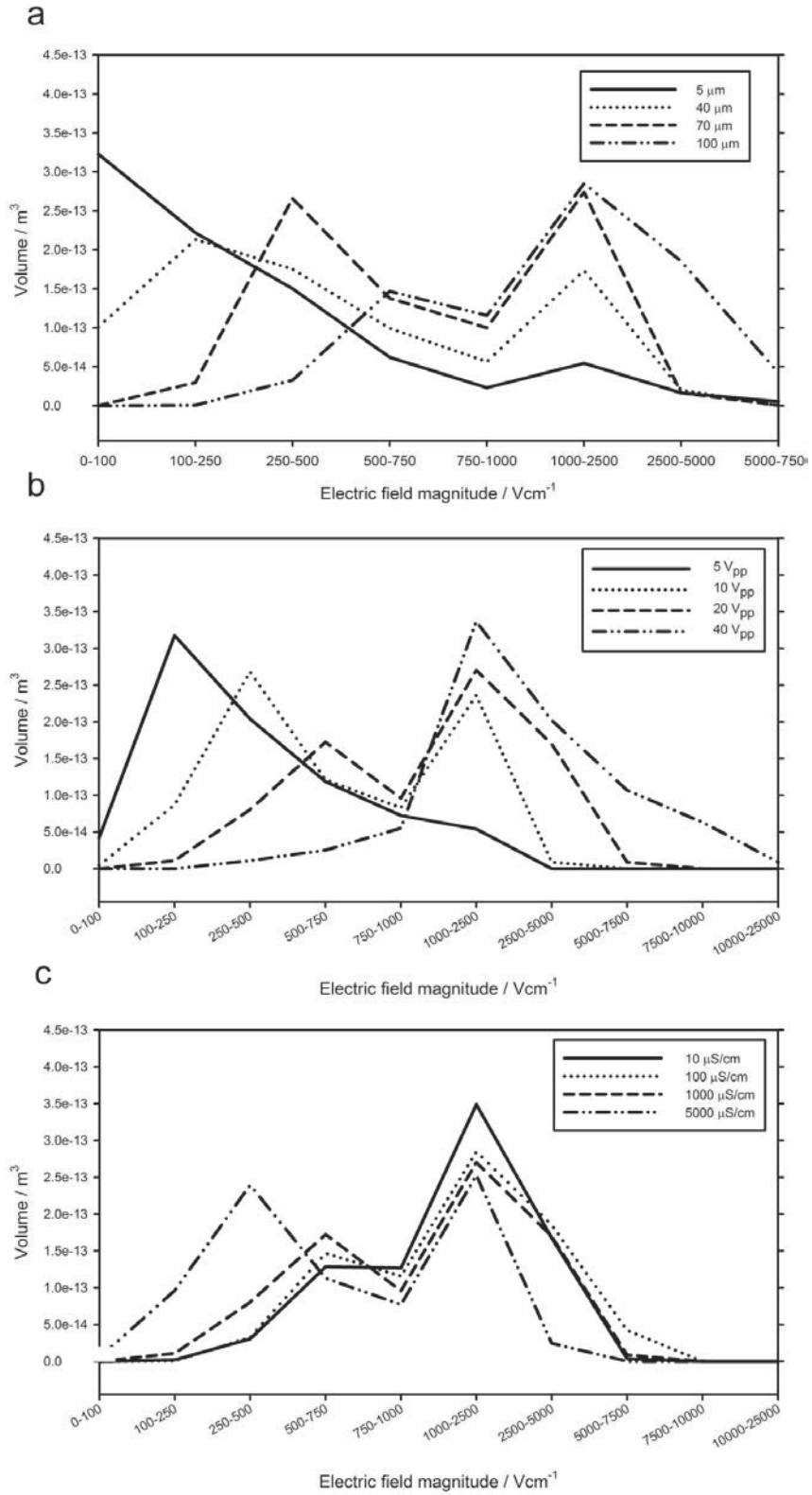


**Fig. 4.3** Volume distribution of specific electric field magnitude ranges created around a polarized electrode as the a) electrode height, b) polarizing voltage and c) sample conductivity change

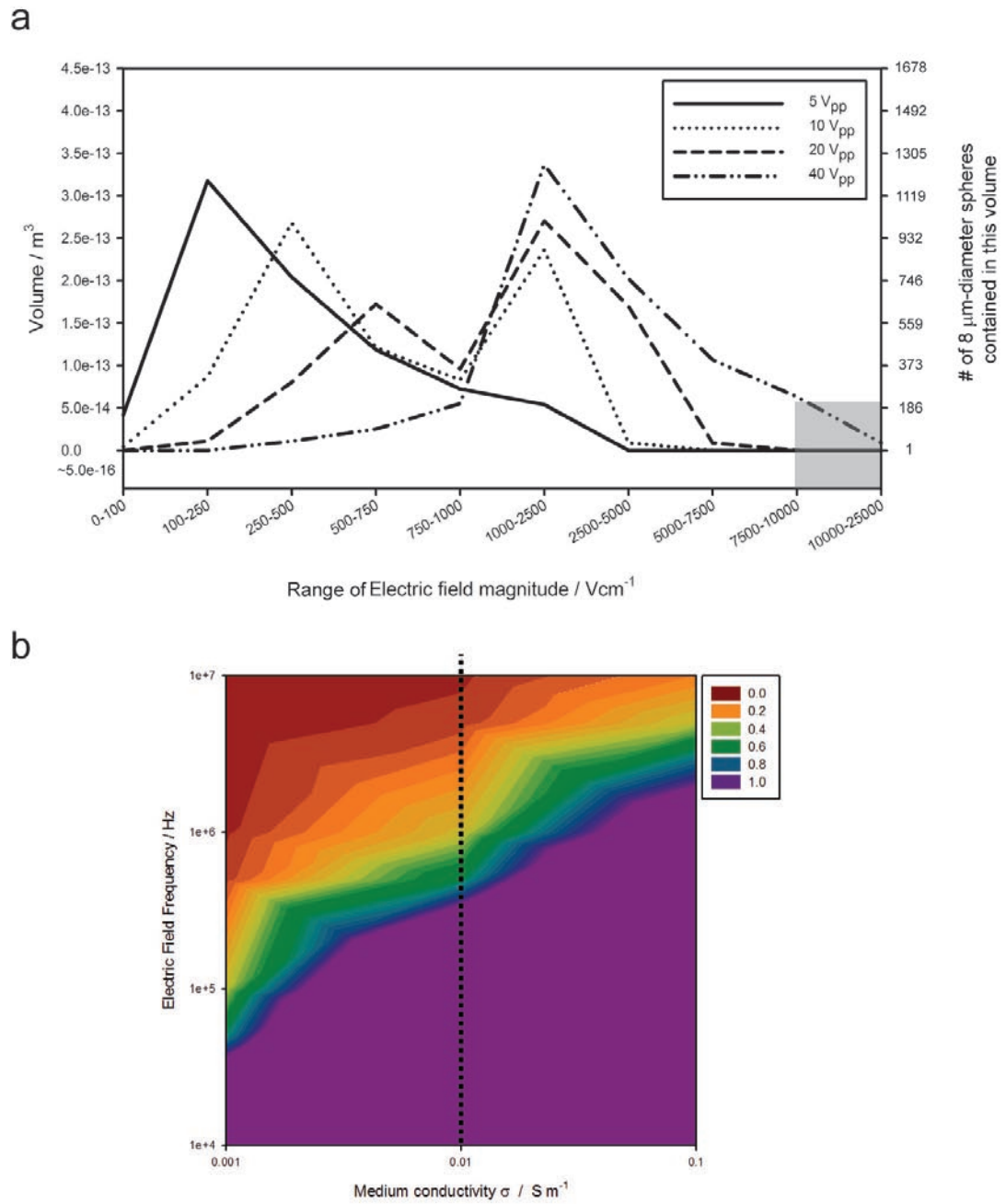


**Fig. 4.4** An example on how Fig. 4.2 and Fig. 4.3 must be used together to determine DEP experimental parameters to prevent cell membrane breakdown

### **4.1.2 The importance of the suspending media in DEP experiments**

The suspending media is perhaps the most important parameter to optimize in DEP applications involving cells. The use of low conductive media was just demonstrated to minimize the risk of membrane breakdown. Moreover, if the media is too conductive cell trapping using positive-DEP becomes impossible since negative-DEP will be induced in all cells contained in the sample. Low conductive media usually allows for both positive- and negative-DEP depending on the frequency of the field. This is because the complex permittivity of the cell can be higher or lower than that of the media (assuming a water-based media) which makes the Clausius-Mossotti factor (equation 1.2) positive or negative at a given field frequency. More details on the DEP behavior of yeast cells at different frequencies and different media conductivities are discussed below in section 4.2.1. Joule heating, also known as ohmic or resistive heating, also increases with media conductivity and can be detrimental to cell viability. The rise on temperature in the media is proportional to the electric current flowing through it which is directly proportional to the media conductivity. Up to this point the use of DI water as experimental media appears to be the ideal solution. However, other parameters such as osmolarity (or osmolality), pH and presence of nutrients must be taken into account to guarantee optimal cell support.

DI water lacks any nutrients and its solute and ion concentration is far below that of a cell cytoplasm. It also features a pH of approximately 4. For these reasons, a DEP experimental media features a buffer with nutrients dissolved at specific ratios. A buffer is an aqueous solution consisting of a mixture of a weak acid and its conjugate base or a weak base and its conjugated acid. Buffers are used to keep the pH at a nearly constant

value to guarantee survival of a given cell. Several buffers with a pH value between 6 and 8 exist since a pH within this range allows cells to thrive. Mammalian cells benefit from pH values between 7 and 7.5. Buffers used in DEP include Phosphate Buffered Saline or PBS (pH=7.4) and RPMI 1640 (pH=6.9-7.2). Some of Good's buffers<sup>10</sup> such as HEPES (pH=7.5) and BES (pH=7.15) have become staples in modern biology laboratories and are used in DEP as well. The use of a low conductive buffer is beneficial to achieve positive-DEP of a given cell. Unfortunately, the conductivity of some buffers prohibits their use in positive-DEP applications. Therefore, a DI water-based nutrient solution can be used to dilute a buffer to adjust pH and conductivity of the experimental sample. The conductivity of selected buffers is resumed in Table 4.2. Good's buffers, denoted with an asterisk in the table, typically feature very low conductivity values. The conductivity of the buffer depends on the concentration of the solute as illustrated in the case of peptone water solutions. A good review on the conductivity values of alternative buffers for DEP is that by Arnold<sup>209</sup>.

---

<sup>10</sup> Good's buffers are buffering agents selected and described by Norman E. Good and colleagues in 1966<sup>208</sup>. Good, N. E., Winget, G. D., Winter, W., Connolly, T. N., Izawa, S., and Singh, R. M. M., Hydrogen Ion Buffers for Biological Research, *Biochemistry* 5 (2), 467-477, 1966.. The buffers were selected in terms of 1) pH to support biological reactions (pH 6-8); 2) excellent solubility in water and low solubility in non polar solvents to ease handling and prevent the buffer from accumulating in cell membranes and other cell compartments; 3) membrane impermeability to prevent the buffer from passing through cell membranes; 4) minimal salt effect since highly ionic buffers may cause problems or complications in some biological systems; 5) well-behaved cation interactions to assure the complexes formed after the interaction of the buffer with cationic ligands remain soluble; 6) stability to resist enzymatic and non-enzymatic degradation; 7) optical absorbance to prevent the use of buffers that absorb visible or UV light which may interfere with spectrophotometric assay and 8) ease of preparation to reduce the costs related to the preparation and purification of the buffer. The buffers are currently (2010) known as: BES, BICINE, CAPS, EPPS, HEPES, MES, MOPS, PIPES, TAPS, TES and TRICINE.

**Table 4.2** Conductivity values of selected buffers

Media	$\sigma$ ( $\mu\text{S}\cdot\text{cm}^{-1}$ )
RPMI 1640	14590
Phosphate solution	13830
NaCl solution 9 g/l	11640
Ringer 1/4	3780
Sabouraud Broth 30 g/l	1369
Peptone water 10 g/l	1053
Peptone water 8 g/l	918
Peptone water 6 g/l	605
Peptone water 4 g/l	484
Peptone water 2 g/l	189
HEPES* 0.2 M pH 5	140
BES* 0.31 M	135.4
HEPES* 0.31 M	65.4
MOPS* 0.31 M	46

\*Denotes a Good's buffer

Nutrients are added to the buffer to mainly provide the cells with an energy source and growth factors. In the case of DEP the addition of growth factors is usually omitted and only sugars such as glucose, dextrose or sucrose are added as energy source. These solutes are added at a ratio to obtain optimal osmolality. The optimal osmolality for mammalian cells ranges between 260 and 350 mOsm/kg. Osmolality relates to osmolarity in that osmolality is the solute osmotic concentration per mass (Osm/kg) whereas osmolarity is per volume. Osmolarity is the measure of solute concentration, defined as the number of osmoles (Osm) of solute per liter of solution and is measured in Osm/L (read as “osmolar”). Osmolarity (and osmolality) relates to the more familiar term of molarity (M) in that osmolarity (and osmolality) measures moles of solute particles and molarity measures moles of solute. This distinction arises because some compounds dissociate in solution but others do not. For example, the readily dissociation of sodium chloride in  $\text{Na}^+$  and  $\text{Cl}^-$  ions yields 2 osmoles (Osm) of solute particles per mole of solute. Nonionic compounds such as sugars do not dissociate in solution and 1 mole of solute yields 1 osmole of solute. Selected examples of DEP experimental media and the

application they were used for are shown in Table 4.3. The use of DI water as suspending media is possible when working with microorganisms such as yeast and bacteria since they feature a cell wall that makes them more robust than mammalian cells. The use of a water-based solution featuring 8.3 wt% sucrose and 0.3 wt% dextrose yields an isoosmotic solution that has been used in the separation of several mammalian cells using DEP. The conductivity of the solution can then be adjusted by adding a specific amount of buffer such as RPMI 1640

**Table 4.3** Selected examples of DEP experimental media and their application

Media	$\sigma$ ( $S \cdot m^{-1}$ )	Cell type	Polarizing voltage and frequency	Electrode material and type of DEP trap	Ref.
250 mM sucrose. Adjust conductivity using 1640 RPMI	.12	neurons	8 Vpp, 4.7 MHz (pDEP) 300 kHz (nDEP)	platinum planar concentric	41
0.4 M phosphate buffer saline (PBS)	.607	Glial cells	2 Vpp 152 kHz (pDEP) 14.8 kHz (nDEP)		
300 mOsm sucrose, 1% calf serum (sucrose media)	not reported	Bovine pulmonary arterial endothelial cells	5 V 2 MHz (pDEP)	gold planar (fibronectin-covered)	210
		NIH/3T3 fibroblasts			
Cytocon II Buffer (Evotec Technologies GmbH, Germany)	.3	U-937 human lymphoma cells	0.8 Vrms 500 kHz (nDEP)	gold planar (deflection electrodes on top and bottom)	45
DI water	0.001	<i>E.coli</i>	10 Vpp 10 MHz (pDEP), 500 kHz (nDEP)	gold planar interdigitated castellated	211
8.5% sucrose, 3 mg/ml dextrose and 0.7 mM hemisodium EDTA	.01	HL-60	5 Vpp 200 kHz (pDEP)	gold planar interdigitated castellated	9
PBS+DI water, conductivity adjusted using NaOH	0.005	yeast	25 Vpp 20-100 kHz (pDEP)	doped silicon 3D serrated	44
8.5% sucrose, 0.3% dextrose and RPMI 1640 to adjust conductivity	0.02-0.055	Erythrocytes <sup>¶</sup>	5 Vpp 200 kHz (nDEP)	gold planar interdigitated castellated	212
		Erythrocytes (group "O")	5 Vpp 200 kHz (pDEP)		
320 mM sucrose, 2 mg/ml dextrose, NaCl solution to adjust conductivity	.002	DS19 <sup>§</sup>	3 Vrms 1 kHz (nDEP) 100 kHz (pDEP)	gold planar interdigitated castellated	213
DI water	0.00008	Micrococcus luteus	8 Vpp 1 MHz (pDEP)	gold planar interdigitated castellated	214
240 mM glycine, 460 mM mannitol in DI water	.00124	Festuca arundinacea			
8.5% sucrose, 0.3% glucose, 0.725% (v/v) RPMI	.015	Mouse fetal-derived NSPC <sup>Δ</sup>	8 V 1 MHz, (pDEP) <50 kHz (nDEP)	gold planar interdigitated	215
320 mM sucrose, 3 mg/ml glucose	0.001	CD34+	6 Vpp >50 kHz (pDEP) 5 kHz (nDEP)	gold planar interdigitated castellated	11

Notes: ¶ infected with drug resistant Plasmodium falciparum (malaria)

§ Friend murine erythroleukaemia

Δ Neural stem-precursor cell

## 4.2 Experimental samples

Most of the samples used in this work feature yeast cells (*S. cerevisiae*) and 8  $\mu\text{m}$  diameter latex particles (Duke Scientific, now part of Thermo Fisher Scientific). This is to accelerate the demonstration of the engineering behind the development of carbon-DEP devices and their integration in a centrifugal microfluidics platform. Yeast cells and latex particles have been widely used in DEP and their dielectric properties are well characterized<sup>4,216,217</sup>. The characteristics of all the experimental samples used in this work are detailed in Table 4.4. The application of carbon-DEP in the sorting of other biologically relevant cells is demonstrated when using the *E. coli* and *Drosophila* experimental samples. The pH of these samples was 7.08 and 6.485 respectively.

Yeast cells were obtained by dissolving 200 mg of Yeast (*S. cerevisiae*, Sigma-Aldrich) in 10 ml sterile YPD medium (MP Biomedicals) or 3 wt% Sabouraud broth and incubated aerobically at 30°C with 150-250 RPM rotation for 18 hours. This culture was then diluted into 100 ml of the equivalent media and incubated as before for a further 24 hours. *E. coli* 5K cells were grown overnight in 10 ml Luria-Bertani (LB) broth at 37 °C. *Drosophila melanogaster* S2 cells were grown overnight at room temperature and dark conditions in 10 ml of Schneider's media (Invitrogen, Carlsbad, CA) complemented with 10% fetal calf sera (FCS). Bacteriological Peptone Enzymatic Hydrolysate (peptone), Bovine Serum Albumin (BSA), dextrose and sucrose were obtained from Sigma-Aldrich. Experimental samples for DEP were obtained by pelleting the appropriate cell culture (*s. cerevisiae*, *e. coli* or *drosophila*) using centrifugation at 3000-5000 x g for 5-10 minutes and re-suspending the cells in experimental media. The sample was then diluted using experimental media until the desired cell concentration was reached. A similar procedure

was followed to obtain a solution of latex particles. This solution was later mixed at specific ratios with the cell dilution to obtain experimental samples 2-stage and spinDEP1. The ratio of viable to non viable cells varied in all samples since heat treatment was not used to render cells non viable. However, yeast cells were suspended in DI water in the 2-stage sample which rendered most of the cells non viable. The particle concentration in all experimental samples was set within  $10^5$  to  $10^7$  particles per milliliter. The use of this concentration was observed to prevent the saturation of the carbon electrode array. The conductivity of all media was kept at low levels to allow for the manipulation of cells using positive-DEP as will be illustrated in the next section. The use of BSA in the experimental media gives a significant advantage in that BSA prevents cell adhesion to the surfaces of the carbon-DEP device. This prevents a decrease in sorting efficiency due to non specific trapping.

**Table 4.4** Experimental samples used in this work. Different conductivity meters (Oakton CON510 Series or Corning 441) were used to obtain the conductivity of the samples. The cell concentration was determined by direct counting using an hemocytometer set featuring a Neubauer ruling (Hausser Scientific).

ID	Particles	Media	$\sigma$ ( $\mu\text{S}\cdot\text{cm}^{-1}$ )	Concentration and percentage composition
Proof of concept	Yeast cells ( <i>S. cerevisiae</i> )	1 part 3 wt% Sabouraud broth to 9 parts DI water	147.7	$8 \times 10^7$ cell per ml. Percentage composition not determined
Filter efficiency	Yeast cells ( <i>S. cerevisiae</i> )	0.6 wt% peptone water	510 <sup>#</sup>	$5.1 \times 10^7$ cells per ml. Percentage composition varied
2-stage filter	Yeast cells ( <i>S. cerevisiae</i> ) + 8 $\mu\text{m}$ -diameter latex particles	DI water	8	$2 \times 10^6$ particles <sup>¶</sup> per ml 91.3% yeast cells 8.7% latex particles
spinDEP1	Yeast cells ( <i>S. cerevisiae</i> ) + 8 $\mu\text{m}$ -diameter latex particles	0.1 wt% BSA <sup>§</sup> solution	31.2	$2.65 \times 10^5$ particles <sup>¶</sup> per ml 40% yeast cells 60% latex particles
spinDEP2	Yeast cells ( <i>S. cerevisiae</i> )	0.2 wt% peptone water	189.4	$4.2 \times 10^5$ cells per ml Percentage composition varied
E.coli	<i>Escherichia coli</i> 5K	0.6 wt% peptone water	900 <sup>#</sup>	$\sim 10^8$ cells per ml Cell viability not determined
Drosophila	<i>Drosophila S2</i>	0.1% BSA 8.6% sucrose 0.3% dextrose	60	$5 \times 10^5$ cells per ml Cell viability not determined

Notes: <sup>#</sup> The difference in conductivity between these two solutions of 0.6 wt% peptone is attributed to the use of different sources of DI water and human error during the weighting of peptone powder

<sup>¶</sup> the term particles in this case denotes yeast cells and latex particles

<sup>§</sup> BSA stands for Bovine Serum Albumin

### 4.2.1 DEP modeling of the experimental samples

The dielectric characterization of experimental samples containing yeast cells (and latex particles when applicable) is performed using Mathematica 5.2 for students (Wolfram Research Inc., Champaign, IL). The real part of the Clausius-Mossotti factor for different experimental media is shown in Fig. 4.5 as a function of the frequency of the applied electric field. Yeast cells, both viable and non viable, are modeled as two-shell particles using the dielectric parameters derived by Huang, et al <sup>4</sup> and following the approach described in the same reference. The one-shell model is used for the latex particles following the work by Morgan and colleagues <sup>218,219</sup> and accepting a surface conductance,  $K_s$ , of 1.3 nS based on the particle diameter of 8  $\mu\text{m}$  <sup>218</sup>.

The shell-model was detailed in chapter 1. Yeast cells, and most micro organisms and plant cells, are modeled as two-shell particles because they feature a cell wall around their membrane. A mammalian cell is often modeled as a one-shell particle because the inner sphere, the cytoplasm, is only surrounded by one shell, the membrane. The cytoplasm of all living cells can be approximated as a highly conductive salt solution with a large concentration of dissolved organic material (for example yeast cytoplasm conductivity is 0.2  $\text{S}\cdot\text{m}^{-1}$  <sup>220</sup>). Even when latex particles are homogeneous, they are modeled as a one-shell particle due to the electrical double layer forming at the interface of the latex particle and the suspending media.

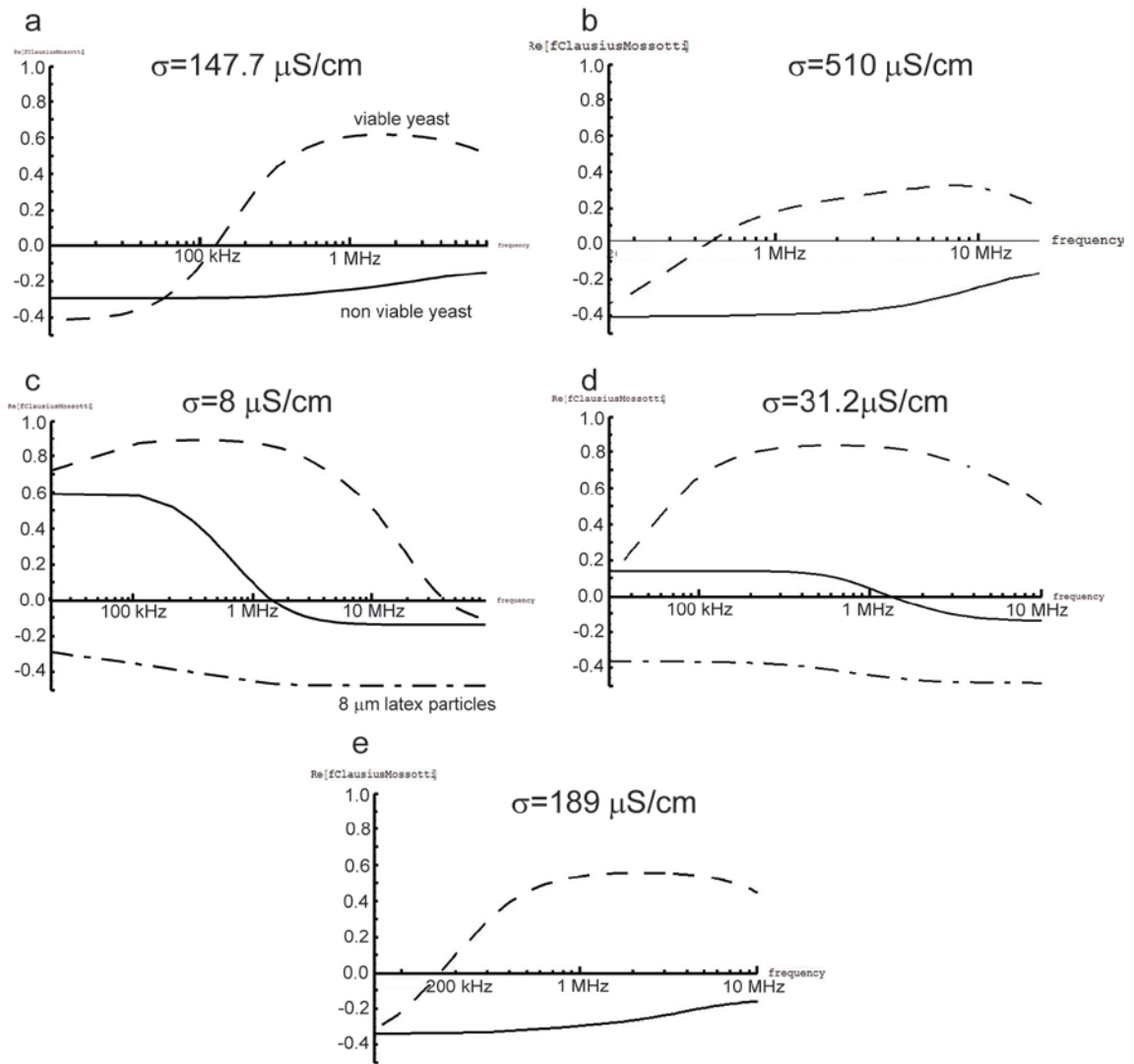


**Fig. 4.5** The real part of the Clausius-Mossotti factor depending on frequency for some of the experimental samples used in this work: a) Proof of concept, b) Filter efficiency, c) 2-stage, d) spinDEP1 and e) spinDEP2. The sample conductivities are a) 147.7, b) 510, c) 8, d) 31.2 and 189  $\mu\text{S}\cdot\text{cm}^{-1}$ . Further details on the experimental samples are shown in Table 4.5

The use of electric field frequencies within the range 1-10 MHz always leads to positive-DEP manipulation of viable yeast cells in all the experimental samples. This range can be expanded down to 100 kHz when the conductivity of the media is less than  $130 \mu\text{S}\cdot\text{cm}^{-1}$ . Non viable yeast can only be manipulated using positive-DEP at frequencies below 1 MHz and only when the conductivity of the media is less than around  $31.2 \mu\text{S}\cdot\text{cm}^{-1}$ . The magnitude of positive values of  $\text{Re}[f_{\text{CM}}]$  induced on a particle at a given frequency decreases as the media conductivity increases as illustrated in Fig. 4.6. At low conductivities both viable and non viable yeast can be manipulated using either positive- or negative-DEP. At very high conductivities ( $>1500 \mu\text{S}\cdot\text{cm}^{-1}$ ) or very high frequencies ( $>50$  MHz) both viable and non viable cells can only be manipulated using negative-DEP (Fig. 4.6a). The  $8 \mu\text{m}$  diameter latex particles used in this work are under a negative-DEP force across the whole frequency range and at all conductivity values. Positive-DEP of latex particles is only possible when the particle diameter is less than around  $5 \mu\text{m}$  and the media conductivity is less than around  $70 \mu\text{S}\cdot\text{cm}^{-1}$  as illustrated in Fig. 4.6b. In these cases the conductive double layer at the latex-media interface is bigger than the bulk of the particle and the particle can exhibit conductive properties<sup>221</sup>.

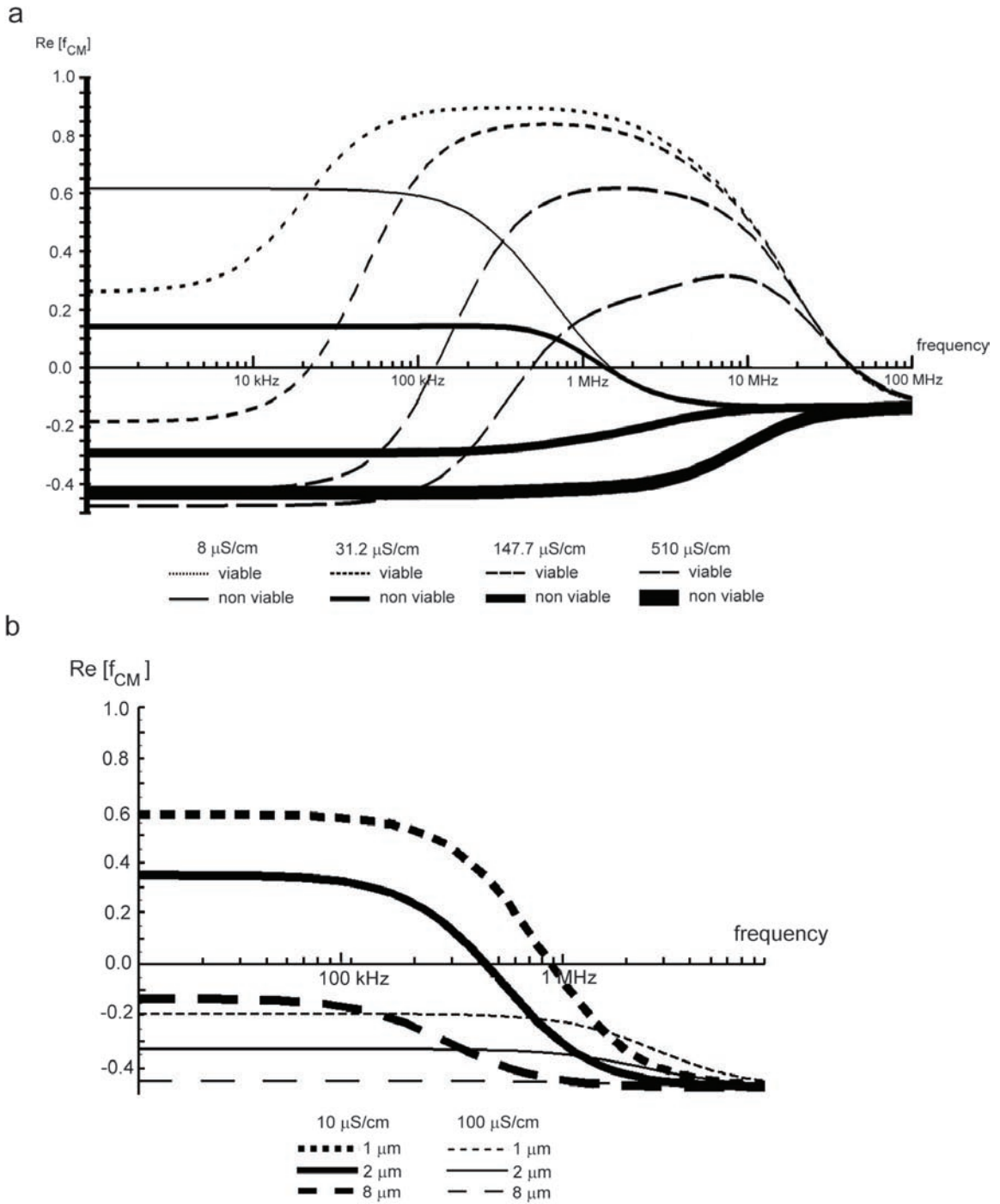


**Fig. 4.6** The real part of the Clausius Mossotti factor depending on field frequency and media conductivity for a) viable and non viable yeast cells and b) different sizes of latex particles

## **4.3 Experimental validation of carbon-DEP**

### **4.3.1 Test platform featuring a syringe pump**

The purpose of this work is to make a DEP experimental platform more portable and robust by replacing a syringe pump and fluidic interconnects with self-contained centrifugal microfluidics. However, an experimental platform featuring a syringe pump is first used here to visually characterize the DEP behavior of the particles contained in the different experimental samples and to validate different carbon-DEP designs. This characterization and validation could be done using a centrifugal platform by quantifying the change in concentration of targeted cells (those that were expected to be trapped) at the outlet of the channel as the frequency and voltage of the sinusoidal signal polarizing the electrode array varies. For example, the concentration of yeast cells at the outlet of the channel will be less when using a frequency of 20 MHz than when using a frequency of 100 kHz. At 20 MHz yeast cells experience negative-DEP while at 100 kHz they experience positive-DEP (Fig. 4.5a). However, visual validation using the syringe pump platform is significantly more rapid and less expensive than the process just described. This is because an experimental platform featuring a stationary syringe pump is easy to interface to a visualization module, *i.e.*, a microscope. The visualization of particles in a moving centrifugal platform is challenging due to the high spin speeds that are usually required to make a sample flow in the carbon-DEP chips. Expensive objective lenses with long working distance and ultra-fast image acquisition systems are likely to be required in this case. Therefore, the experimental samples and carbon-DEP designs are first characterized using a syringe pump platform and then used with the carbon-DEP modules integrated in the rotating platform to be detailed in chapter 5.

The first experimental setup used in this work is shown in Fig. 4.7. A syringe pump (KDS101, KD Scientific or PHD2000, Harvard Apparatus) is used to control the flow rate at which the experimental sample is injected into the carbon-DEP device. The sample is continuously stirred during the experiments thanks to the interaction between a tiny magnet contained in the syringe and an external magnet manipulated manually. The interface between the syringe and 1/16" OD (outside diameter) tubing is made using a female luer to 10-32 female connector and 10-32 fittings (Upchurch scientific P-629 and F-120 respectively) or a connector fabricated in-house which has been previously detailed by this author in. A combination of tubing, valves and Y-connectors (Upchurch Scientific parts 1522, P-782 and P-512 respectively) is used to route the sample and wash media into the chip. A function generator (Agilent 33250A or Stanford Research Systems DS345) is used to create the sinusoidal signal (with magnitude 10 V peak-to-peak and different frequencies detailed below) required to polarize the carbon electrode array. The carbon-DEP device is mounted on a microscope stage (Zeiss AXIO Imager A1m, Carl Zeiss, MOTIC PSM1000 or Nikon ECLIPSE LV100) and the electrode array and particles in the experimental sample are observed in a brightfield using a 5X, 10x or 20X objective lens. A 10X eyepiece was featured in all the microscopes used here. Images are recorded using a computer-controlled CCD camera (Photonfocus MV-D640C-3, Costar Imaging SI-C400N or RTKe Diagnostic Instruments SPOT #7.4Slider) attached to the microscope. The outlet of the carbon-DEP device is connected to different collecting tubes using FEP Teflon<sup>®</sup> tubing (Upchurch Scientific 1522). The fluidic system from the syringe outlets to the collecting tubes inlets expands an approximate volume of 240  $\mu$ l.

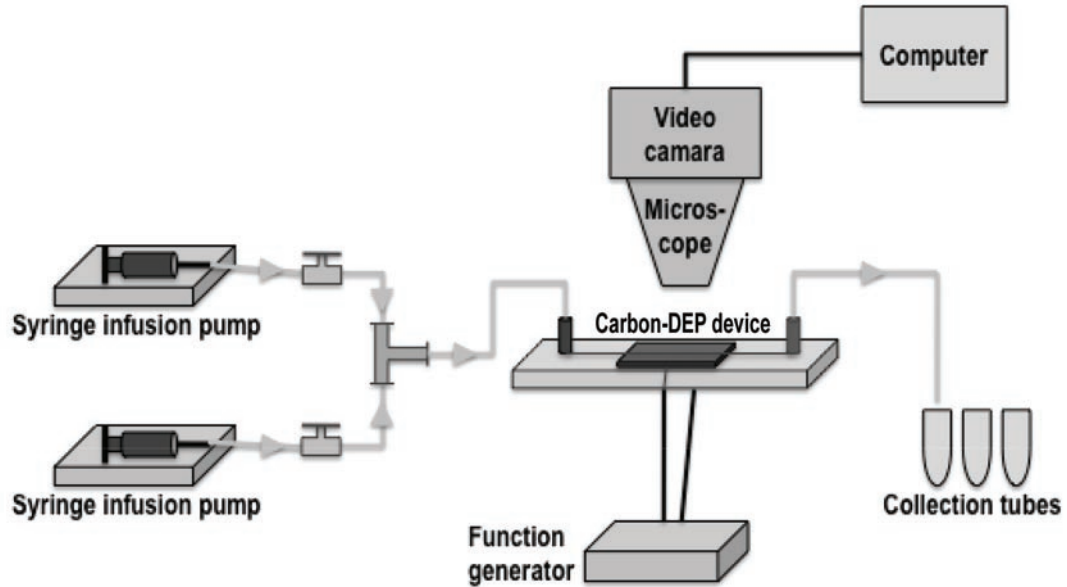


**Fig. 4.7** DEP experimental platform using a syringe pump

### 4.3.2 Proof of concept

The use of carbon electrodes for the dielectrophoretic manipulation of yeast cells was demonstrated using a single quadrupolar trap implemented with planar wedge electrodes. The DEP trap is shown in Fig. 4.8a. Fabrication details are given in Table 2.7 in Chapter 2. The experimental sample used is described in the row Proof of concept in Table 4.5. The DEP behavior of viable and non viable yeast when suspended in a media with conductivity of  $147.7 \mu\text{S}\cdot\text{cm}^{-1}$  is shown in Fig. 4.5a. A polarizing voltage of  $20 V_{pp}$  was used here. A frequency of 1 MHz was used to attract the viable yeast cells to the electrodes (positive-DEP) as shown in Fig. 4.8b. A frequency of 20 kHz was used to concentrate the yeast cells in between the electrodes (negative-DEP) as illustrated in Fig. 4.8c.

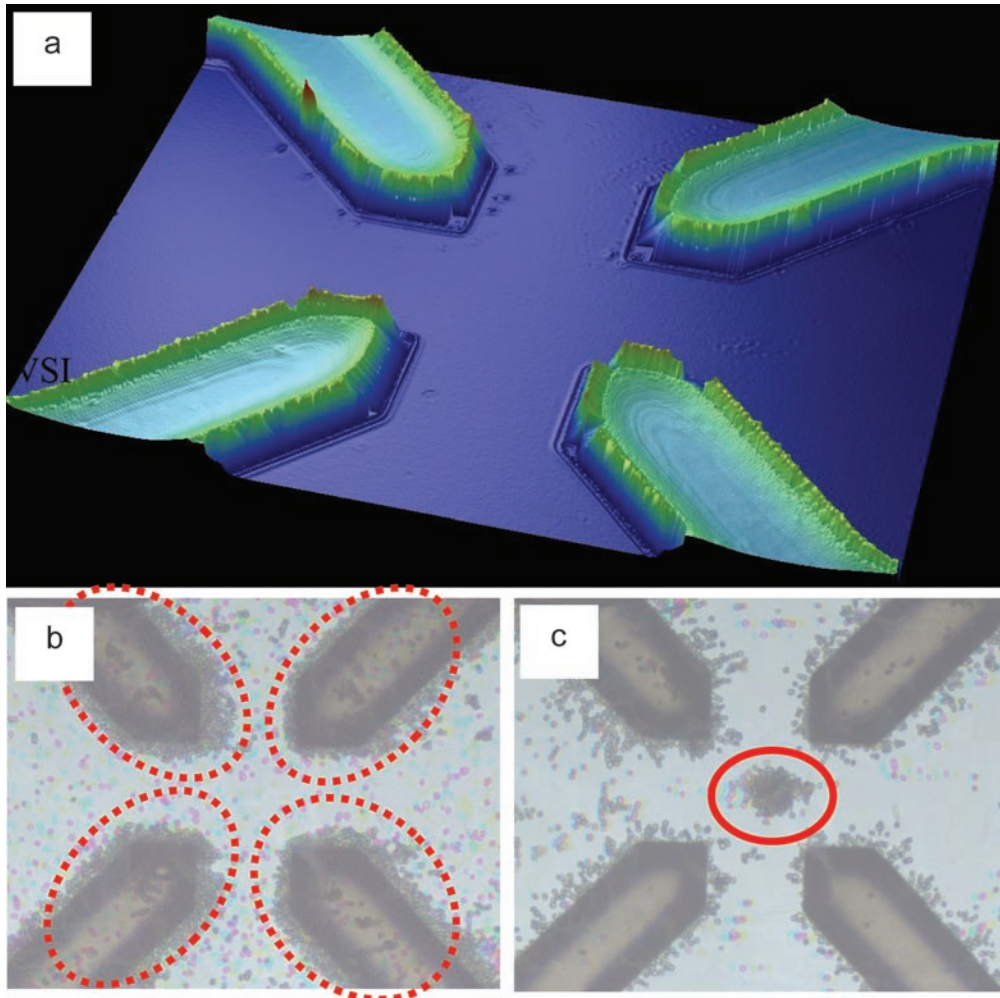


**Fig. 4.8** DEP manipulation of yeast cells using a a) quadrupolar trap implemented with planar carbon electrodes. b) yeast cells attracted to the edge of the electrodes by positive-DEP (dashed ellipses). c) yeast cells clustered in between electrodes by negative-DEP (solid oval)

### 4.3.3 Filter

This module was used to experimentally demonstrate how the use of 3D electrodes improves the throughput and efficiency of a DEP-assisted filter. Independent similar carbon-DEP devices but featuring 2D or 3D electrodes were used to filter viable cells out from a mix of viable and non viable yeast cells. The fabrication process of these experimental modules is detailed in columns 2D and 3D in Table 2.7. Briefly, 5.6 (2D) or 60 (3D)  $\mu\text{m}$ -high electrodes are contained in a 66  $\mu\text{m}$ -high channel (Fig. 4.9a). The

experimental sample is detailed in Table 4.5 under the ID Filter efficiency. Yeast cells are suspended in diluted 3 wt% Sabouraud broth to obtain a media conductivity of  $510 \mu\text{S}\cdot\text{cm}^{-1}$ . The DEP behavior of both viable and non viable yeast cells under this condition is shown in Fig. 4.5b. A sinusoidal signal of magnitude 10 Vpp and frequency 10 MHz is used to polarize both electrode arrays (2D and 3D). Viable yeast cells are expected to be trapped around the electrodes while non viable yeast cells are expected to flow through the electrode array. The retention efficiency of both 2D and 3D electrodes is shown in Fig. 4.9b as the sample flow rate is increased. The retention efficiency is calculated as the ratio of the quantity of the targeted particles (viable cells) retained by the filter to the quantity entering the filter. The number of viable and non viable cells present in the sample before and after the DEP experiment is determined by direct counting using a hemocytometer kit (Hausser scientific) featuring a Neubauer ruling to aid in the count. A trypan blue exclusion assay was used to determine cell viability. A filter efficiency of 1 denotes trapping of all targeted particles and is obtained here using the 3D electrodes as long as the sample is flowed at rates below  $3 \mu\text{l}\cdot\text{min}^{-1}$ . The filter efficiency is higher at all flow rates when using the 3D electrode array which allows for a greater enrichment of the non viable yeast cells at the channel outlet. In both cases, 2D and 3D, the retention efficiency decreases as the flow rate in the channel increases. However, the decrease in efficiency at any given flow rate when using the 3D electrode array is far less than that obtained when using 2D electrodes. The decrease in trapping efficiency as the flow rate in the channel increases is qualitatively demonstrated in Fig. 4.9c. A 3D electrode array is shown to trap a decreasing amount of yeast cells as the flow rate increases from 10 to  $20 \mu\text{l}\cdot\text{min}^{-1}$ .

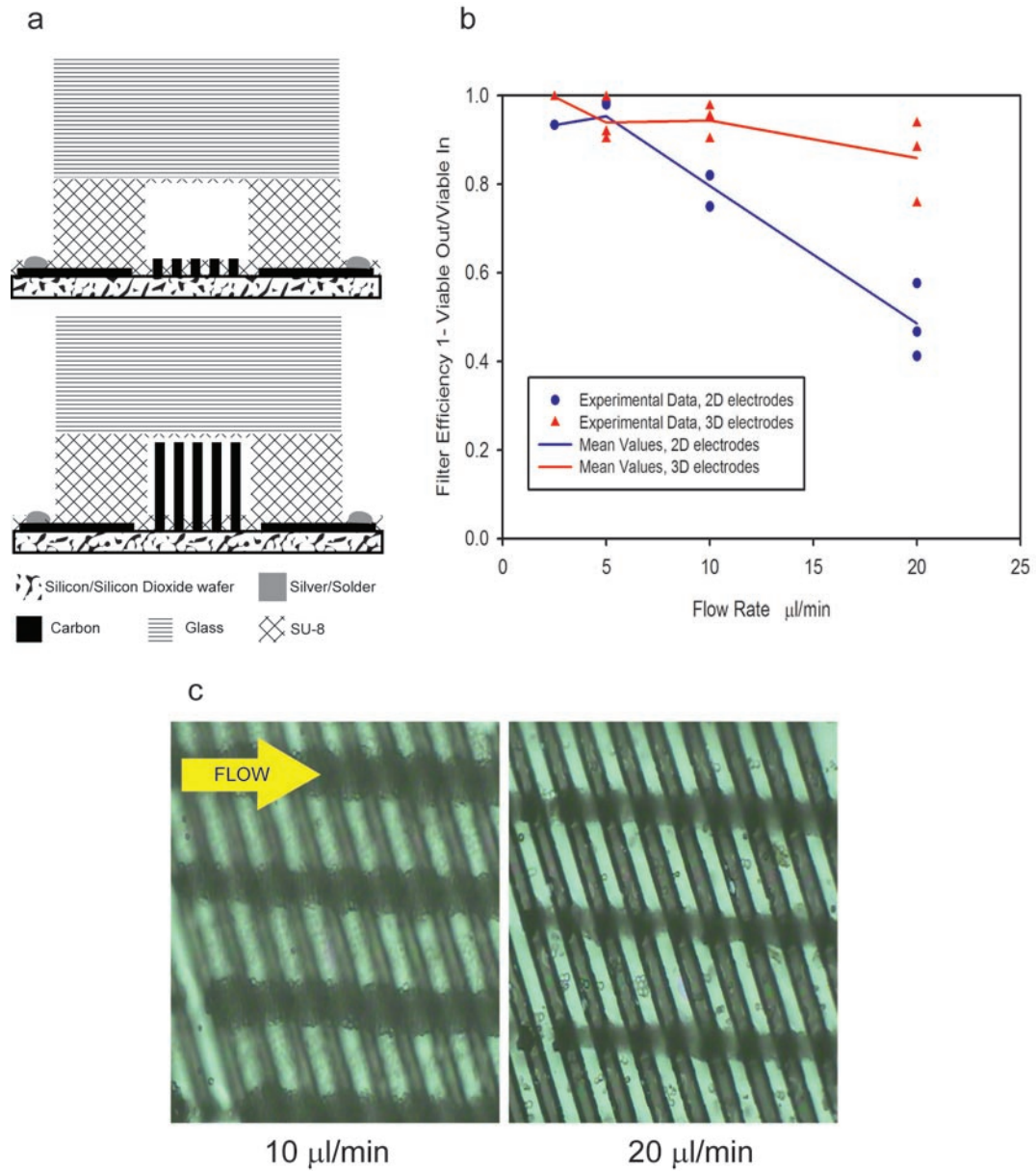


**Fig. 4.9** a) cross-sections of the 2D and 3D carbon-DEP experimental devices, b) filter efficiency depending on flow rate for both 2D and 3D filters and c) visual validation of the decrease in trapping efficiency as flow rate increases when using a 3D filter

### 4.3.4 Multi-stage filter

A general schematic of a multi-stage filter is presented in Fig. 4.10. Different electrode array geometries are positioned inside a micro channel. The array geometries can feature different electrode shapes, sizes and gaps in between them. Each array can be polarized with a different signal or more than one array can be polarized with the same signal. The goal of this system is to selectively trap different targeted particles in different arrays. The arrays can then be sequentially turned off to methodically release and collect one particle population at a time.

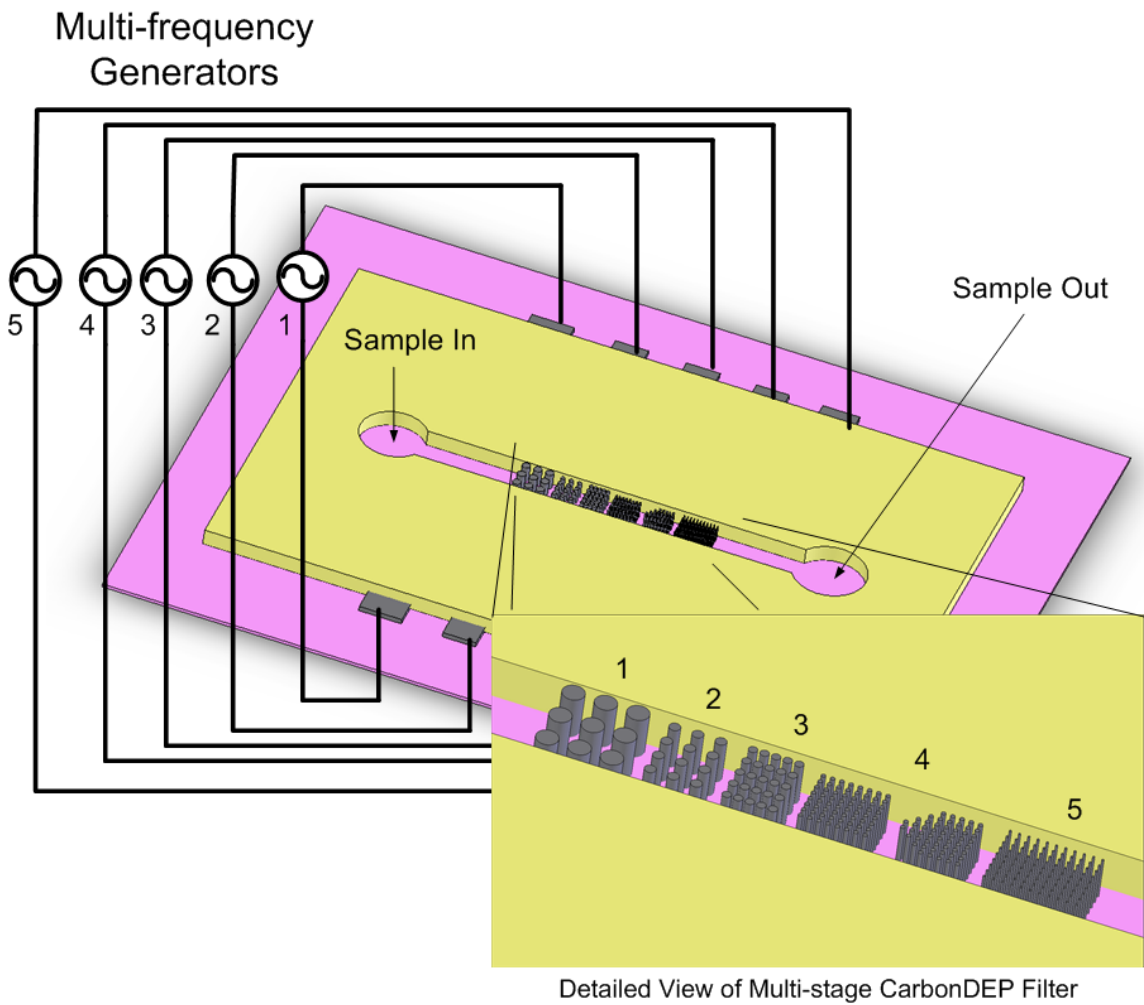


**Fig. 4.10** A general schematic of a multi-stage filter

A 2-stage filter is implemented here. The carbon-DEP device was fabricated as detailed in the column 2-stage in Table 2.7. The experimental sample is detailed in the row 2-stage in Table 4.4. Briefly, yeast cells and latex particles are suspended in DI water. Therefore, most of the yeast cells are rendered non viable. The dielectric characterization of the experimental sample is shown in Fig. 4.5c. Up to 3 ml of a 0.5 wt% Bovine Serum Albumin (BSA) solution were flowed through the carbon-DEP chip prior to all experiments. This was to block all surfaces and prevent yeast cells from adhering to them. All experiments began by flushing the channel clean using DI water. A sample volume of 45  $\mu\text{l}$  was then flowed in using a constant flow rate (10, 20 and 40  $\mu\text{l}\cdot\text{min}^{-1}$ ). The first electrode array in the path of the sample was polarized using a 5 MHz, 10  $V_{\text{pp}}$  sinusoidal signal to trap viable yeast cells. The second array was polarized by a 10  $V_{\text{pp}}$ , 500 kHz signal to trap both viable and non viable yeast. It is assumed that most of the viable cells are trapped in the first array. Latex particles are never trapped and are collected at the channel outlet. The results are shown in Fig. 4.11 when flowing the experimental sample over the electrode arrays at a rate of 10  $\mu\text{l}\cdot\text{min}^{-1}$ . Viable yeast cells are trapped in the array on the left while non viable cells are trapped in that on the right. The sharp difference on the number of cells trapped in each array is due to the fact that most yeast cells are rendered non viable upon suspension in DI water. The array on the right can be turned off first to release and collect non viable cells. The array on the left can be turned off last to release and collect viable cells. Three different populations: latex, non viable and viable yeast cells are then separated.

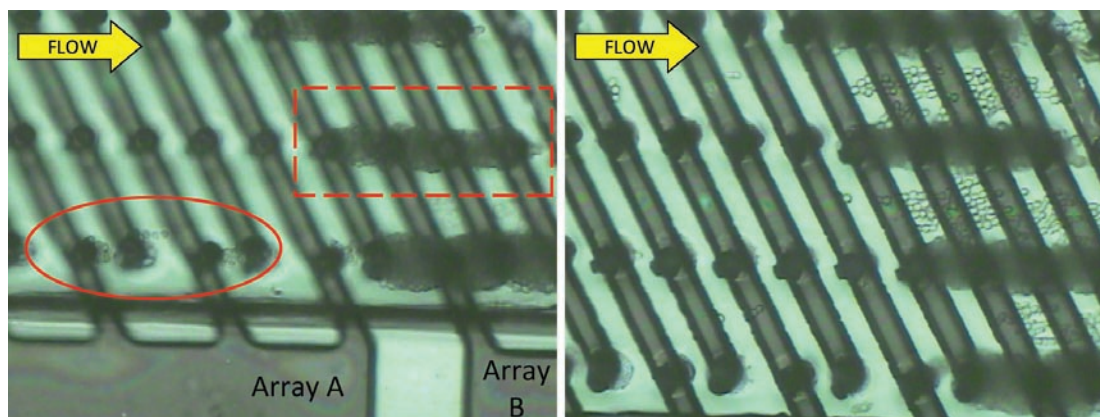


**Fig. 4.11** Trapping of viable (solid ellipse) and non viable yeast cells (dashed square) in different electrode arrays (A and B) using a 2-stage carbon-DEP filter

The capability of a 2-stage carbon-DEP filter to separate 3 different particle populations has been qualitatively demonstrated. However such separation can also be readily achieved by a single electrode array polarized at different frequencies at different times. The power of the proposed 2-stage filter becomes significant when separating a mix of particles featuring the DEP behavior shown in Fig. 4.12. The polarization of the first electrode array encountered by the incoming particle mix using a frequency A enables the trapping of Particle 1 and 3. The second array is polarized at a frequency B to trap Particle 1 and 2. Particle 4 is repelled from both electrode arrays regardless of the polarizing frequency. At this point Particle 3 is trapped in the first array, Particle 2 is trapped in the second array, Particle 1 is trapped in both arrays and Particle 4 is retrieved at the channel outlet. Changing the frequency applied to the second array from B to A results in the release of Particle 2 which can be collected at the channel outlet. The next step is to change the polarizing frequency of both arrays from A to B to release and collect Particle 3. The final step is to turn off all electrodes to release and collect Particle 1. A sample with these characteristics may be found when purifying biological cells or

micro organisms from ceramic and/or metallic particles and optimizing the conductivity of the suspending media.

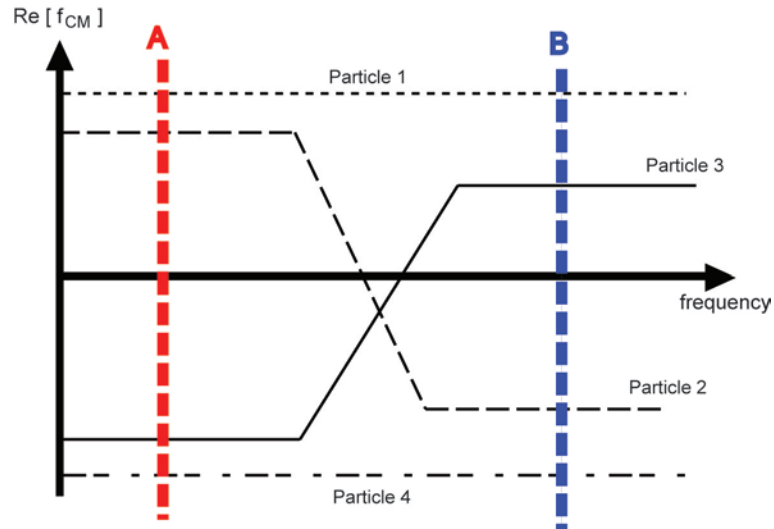


**Fig. 4.12** A theoretical particle mix to demonstrate the potential of a 2-stage filter

### 4.3.5 Cell focusing using positive-DEP

A similar device to that used in the Filter module above is used here to demonstrate cell focusing using positive-DEP. Few authors have demonstrated cell focusing using positive-DEP<sup>24</sup>. In contrast, cell focusing using negative-DEP is a common methodology for cell sorting where targeted particles are repelled to regions with the less electric field magnitude and aligned in characteristic lines (Renaud liquid electrodes, Wang Lee lateral flow electrodes). These characteristic lines remain through the length of a micro channel due to the laminar nature of the flow.

The experimental sample used in this work is described under ID Filter efficiency in Table 4.4. Its DEP characterization is shown in Fig. 4.5b. The electrode array is polarized

using a 10 V<sub>pp</sub>, 10 MHz sinusoidal signal to attract yeast cells to the surface of the electrodes. The sample flow rate is 5  $\mu\text{l}\cdot\text{min}^{-1}$ . Under these conditions yeast cells are attracted to the surface of the electrodes but are eluted in a direction co-linear with the positive-DEP regions in the electrode array. The principle works when the hydrodynamic force slightly overcomes the positive-DEP trapping force. The yeast cells flow away along those pathlines co-linear with the rows of polarized electrodes (positive-DEP regions) as shown in Fig. 4.13. This is because laminar flow is established in the channel and the flow pathlines are minimally disturbed by the post array geometry (details in chapter 3, section 3.2). Particles undergoing negative-DEP can also be focused into characteristic lines between the electrodes. Retrieval geometries such as a 3D funnel can be fabricated around each of these characteristic lines to retrieve sorted particles. The use of a 3D electrode array completely contained in the channel allows for the creation of several simultaneous streams of sorted cells. This compares advantageously to the use of 3D electrodes positioned only on the channel walls<sup>22</sup> where only one (using negative-DEP) or two (using positive-DEP) streams can be created.

The experimental module presented here allows for continuous cell sorting using simultaneous positive- and negative-DEP focusing. A high flow rate can be used during sorting since trapping is not required. This can significantly improve the throughput of current carbon-DEP devices.

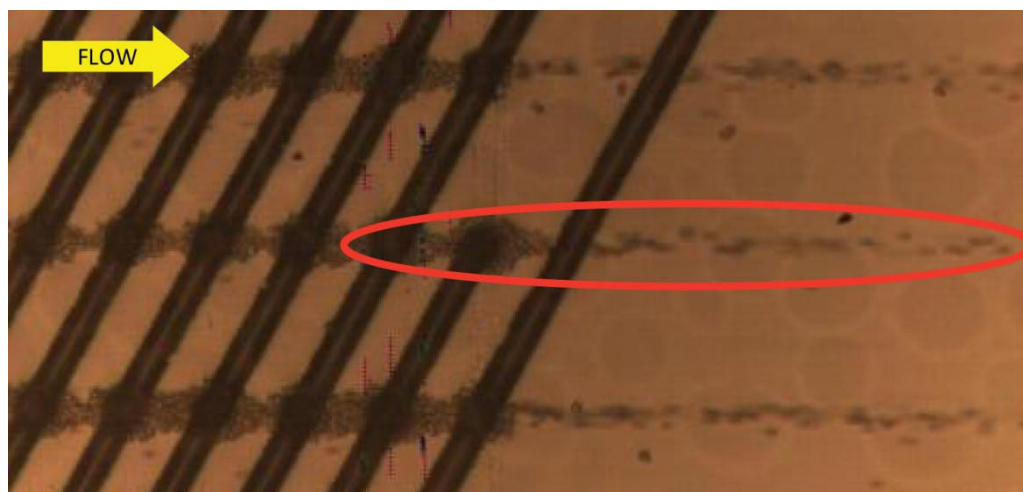


**Fig. 4.13** Yeast cells focused into characteristic lines using positive-DEP

### 4.3.6 Cell screening

#### *E.coli*

Previous studies with *E. coli* 5K strain and planar metal electrodes showed that the creation of an electric field gradient using sinusoidal signals with frequencies in the vicinity of 10 MHz result in positive-DEP whereas frequencies below 500 kHz resulted in negative DEP<sup>222</sup>. Part of this data is confirmed here using 3D carbon-DEP. An *E. coli* suspension (detailed as E.coli in Table 4.4) in peptone water ( $10^8$  cells·ml<sup>-1</sup>) was flowed over the electrode array at 1  $\mu\text{l}\cdot\text{min}^{-1}$  when the carbon electrodes were polarized by a sinusoidal signal of the specified frequency, ranging from 100 kHz to 30 MHz (Table 4.5). The experiment time at each frequency tested was 1 min, after which the electrodes were turned off and trapping was assessed visually under the microscope. Trapping could be confirmed because of the large number of cells appearing at the exit of the electrode array when electrodes were switched off. The relative degree of trapping at a given frequency was determined by qualitatively comparing the cell concentration at the exit of

the array in each case. Positive-DEP could not be determined by only assessing single cell trapping on the surface of the electrodes because of the small size of *E. coli* (~1  $\mu\text{m}$  diameter) and the fact that high magnification objectives (>10X) featured in the microscope used here (Zeiss AXIO Imager A1m) could not be properly interfaced to the carbon-DEP chip due to physical constraints. If trapping didn't occur, no significant changes could be discerned at the exit of the electrode array (data not shown). Negative-DEP is likely to be present at low frequencies as previously demonstrated [11]. However, the characterization of negative-DEP was not done here. Cell focusing by negative DEP could not be observed during experiments. Trapping of *E. coli* 5K was only observed when using frequencies in the range from 1 MHz to 10 MHz. The trapping DEP force was the strongest at frequencies around 10 MHz. No trapping was observed at frequencies below 1 MHz and above 10 MHz. The results obtained here are qualitatively but provide a frequency range where *E.coli* cells can be trapped.

**Table 4.5** Qualitative determination of the optimal frequency to trap *E. coli* using positive-DEP and carbon-DEP. The conductivity of the media is  $900 \mu\text{S}\cdot\text{cm}^{-1}$

Frequency	MHz						kHz		
	30	20	15	10	5	1	500	300	100
Degree of trapping	none			++	+++	+	none		

## ***Drosophila***

*Drosophila melanogaster* is a type of fruit fly extensively used as a model organism in genetics and developmental biology research <sup>223</sup>. The S2 cell line is derived from a primary culture of late stage (20-24 hours old) embryos. The qualitative characterization of the DEP behavior of *Drosophila* S2 cells is presented in this section. To the best

knowledge of the author this is the first written report on manipulation of this kind of cells using DEP. Cell cultures in Schneider's media (Invitrogen) were kindly provided by Lurette Forrest at Michael Cahalan's research group in UC Irvine. The experimental sample is detailed under the ID *Drosophila* in Table 4.4. Cells are re-suspended in a 0.1 wt% BSA solution complemented with sucrose and dextrose to yield an isotonic media featuring a conductivity of  $60 \mu\text{S}\cdot\text{cm}^{-1}$ . An experimental protocol similar to that followed in the characterization of *E. coli* is implemented here. The carbon electrode array was polarized using a sinusoidal signal of frequency ranging from 50 kHz to 15 MHz (Table 4.6) and magnitude  $10 V_{pp}$ . The experiment time was also 1 min during which trapping was assessed visually under the microscope. The use of a low magnification objective (10X) is enough to assess trapping because the cells are approximately  $15 \mu\text{m}$  in diameter. The trapping of *drosophila* cells is shown in Fig. 4.14. The relative degree of trapping was assessed by turning the electrodes off and qualitatively measuring the total concentration of cells at the exit of the array. A high cell concentration is expected if the DEP trapping force is strong. No significant changes at the exit of the electrode array are expected if trapping does not occur. Trapping of *drosophila* was observed at all frequencies within the range tested albeit in different degrees. The trapping DEP force appears to be the strongest at frequencies around 1 MHz. The characterization of negative DEP was not conducted here.

**Table 4.6** Qualitative determination of the optimal frequency to trap *drosophila* using positive-DEP and carbon-DEP. The conductivity of the media is  $60 \mu\text{S}\cdot\text{cm}^{-1}$

Frequency	MHz				kHz		
	15	10	5	1	500	100	50
Degree of trapping	+	+	++	+++	++	+	+

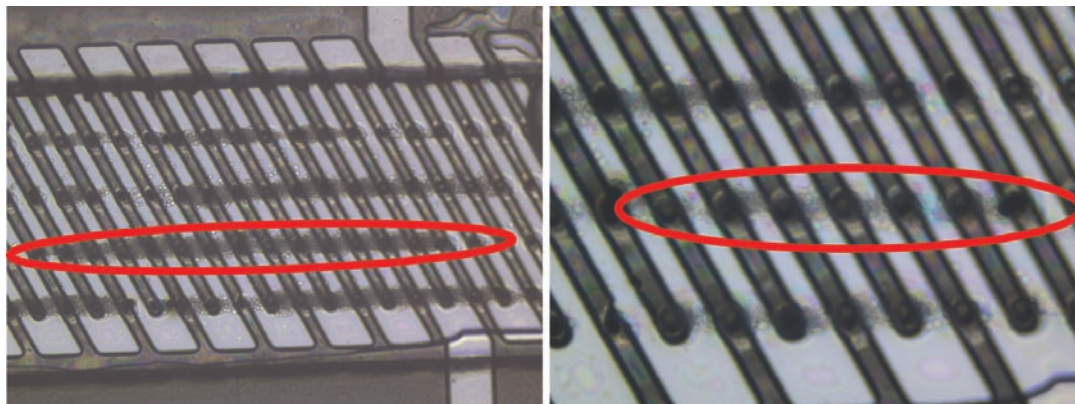


**Fig. 4.14** *Drosophila* S2 cells trapped in between arrays (red ellipses) using positive-DEP

## CHAPTER 5. The integration of DEP and centrifugal microfluidics

Traditional DEP platforms rely on a combination of syringes, piston pumps, tubing, valves, and fluidic ports for fluid manipulation that significantly increases their complexity and has prevented the implementation of DEP-based platforms in settings other than research. An experimental platform featuring a syringe pump was used in chapter 4 to demonstrate the sorting of different kind of cells using carbon-DEP. This chapter details the replacement of syringe piston pumping by centrifugal pumping on an electrically-interfaced compact disk (CD)-like microfluidics platform. The use of a CD platform significantly reduces the footprint and cost of a DEP system and makes it amenable for assay automation. The entire fluid network is contained in a single DEP chip to eliminate the use of syringes, external valves, tubing and any other supporting fluidic elements. This work differs from DEP platforms where electroosmosis is used as pumping force in that centrifugal pumping does not depend on the electric nor physicochemical properties of the sample.

The proposed combination of centrifugal and electric forces in a single platform has been reported before. Wang and colleagues demonstrated a dual-pumping CD-like electrophoresis-based separation system where the centrifugal and electrophoresis forces in the CD are balanced to obtain a better separation of the dyes rhodamine B and xylene cyanole<sup>224</sup>. This system differs from the one presented here in that only DC electrical signals were coupled to the rotating platform. An electrophoresis force is used to attract the most negatively charged dye towards the center of the CD while a centrifugal force pushes the heaviest dye (xylene cyanole) to the rim of the CD. Fuhr et al.<sup>225,226</sup> disclosed a swinging-rotor centrifugal system to conduct DEP with metal-electrodes using AC

electrical signals. In contrast to the CD-like rigid platform detailed below, the DEP devices in Fuhr et al's work are first aligned parallel to the center of rotation and gradually move to a position perpendicular to the rotation axis as the rotation speed increases (resembling a fairground carousel with swings). The use of a horizontal rigid platform such as the one demonstrated here yields a system with low height profile and, most importantly, eliminates moving parts (hinges for example) to add robustness to the platform. Another system somewhat similar to the one presented here is the one demonstrated by Boettcher et al<sup>45</sup>. In their approach a metal-electrode based DEP chip, a PCB-mounted signal generator and a couple of 9V batteries are positioned on a rotating platform. The Boettcher et al system differs from the one detailed here in two important respects: 1) it does not have the capability for remote control so that the signal generator's frequency and amplitude must be set before the experiments, and 2) the throughput, as it uses 2D metal electrodes, is low.

The chapter begins with a description of the individual components and their assembly to fabricate a SpinDEP platform. The use of the platform for DEP applications is then validated by filtering yeast cells from latex particles and viable from non viable yeast using carbon-DEP. Although carbon-DEP is used in this work, the SpinDEP platform may be used with other DEP chip designs, *i.e.*, those featuring metal electrodes or insulating structures (as in the case of insulator-based DEP, iDEP). However, the filter throughput and efficiency may decrease when using traditional 2D metal electrodes. A discussion on how particle sedimentation decreases performance of a DEP-assisted filter, and alternatives to prevent it, is presented towards the end of the chapter. The chapter ends detailing the advantages of replacing a syringe pump by centrifugal microfluidics in

DEP platforms and the broader impact of interfacing electrical signals to centrifugal microfluidics.

## **5.1 Platform components and fabrication**

The experimental setup consists of five parts: 1) a programmable motorized spin stand, 2) a function generator, 3) a specialized spin chuck and compact disk (CD) platform and 4) carbon-DEP chips. The assembly of the system is illustrated in Fig. 5.1. The CD platform is mechanically connected to the motor through a custom-made spin chuck that features a slip ring arrangement needed to electrically connect the function generator to the spinning platform. An electrical network is contained on the CD platform to interface the signal coming from the function generator to the carbon-DEP chips. The DEP chips are placed in the CD platform using designated slots. This modular arrangement makes for a user-friendly and rapid experimentation setup.

### **5.1.1 Motor spin stand**

The spin stand consists of a motor (Pacific Scientific Servo Motor) and its amplifier/controller (PAC SCI Programmable Servo Drive). The motor drive utilizes a graphical user interface program, ToolPAC, to easily configure and program the motor for varying spin profiles. An imaging system was utilized to examine fluid flow. The system is composed of a camera (Basler A301bc,  $640 \times 480$  pixels, 80 fps max., 10 $\times$  zoom lens mounted), a strobe light (PerkinElmer MVS-4200, 6  $\mu$ s duration), and a retro-reflective fiber-optic sensor (Banner D10 Expert Fiber-Optic Sensor). To trigger the camera, a reflective marker is placed on the surface of the CD and aligned with the fiber-

optic sensor. When the sensor detects the marker, a signal pulse is sent to the video capture board, triggering the camera and strobe light to acquire one image frame per CD revolution. This imaging system did not allow for the visualization of particles, averaging  $8\ \mu\text{m}$  in diameter, and was only used to analyze fluid flow and determine flow rates in the micro channel.

### **5.1.2 Function generator**

Sinusoidal voltage signals of different frequency and amplitude are generated by a Stanford Research Systems DS345 Function Generator. The specifications of this instrument include maximum working amplitude and frequency of  $20\ \text{V}_{\text{pp}}$  (peak-to-peak) and 20 MHz respectively.

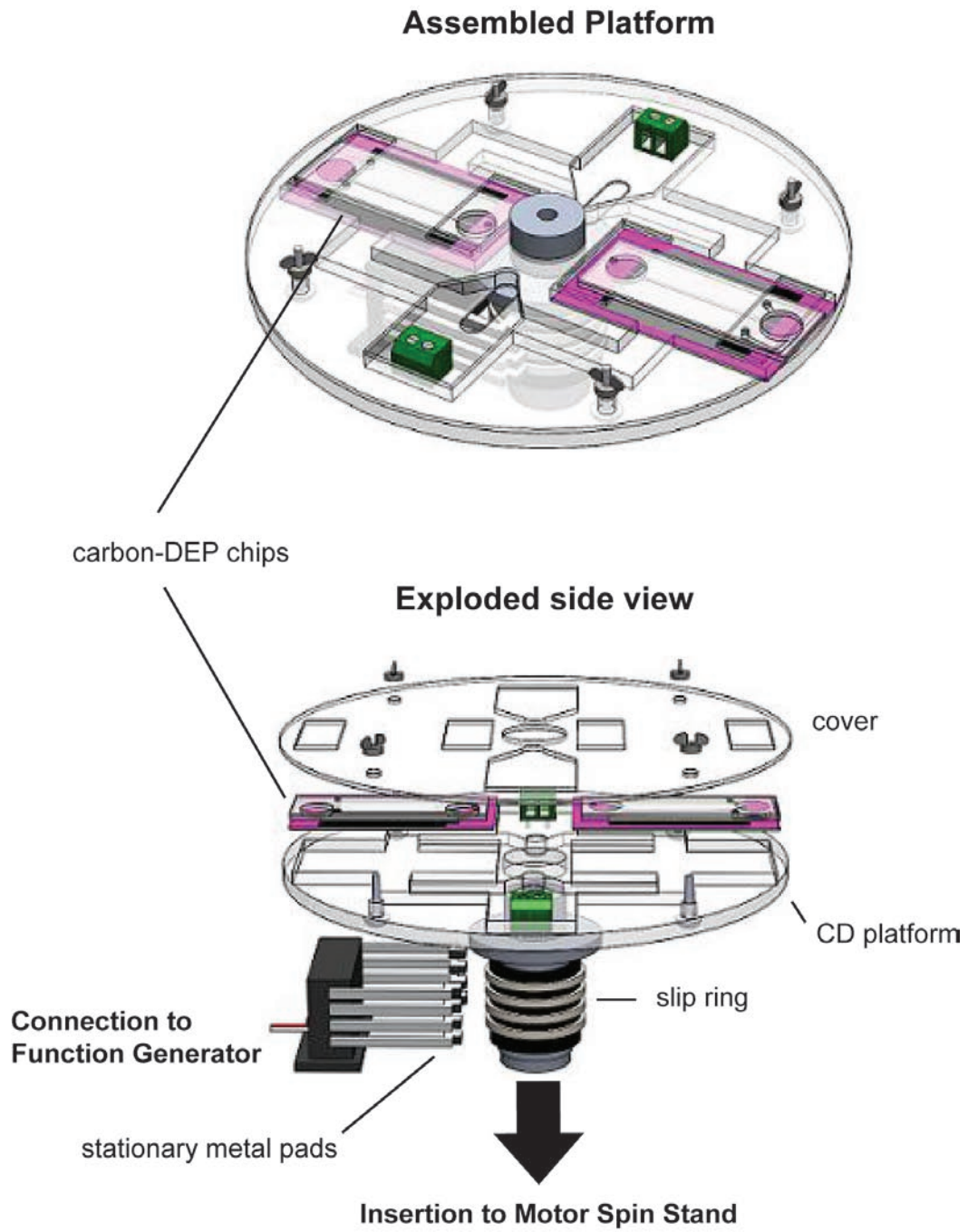


**Fig. 5.1** Assembly of a SpinDEP platform

### **5.1.3 Spin chuck and compact disk platform**

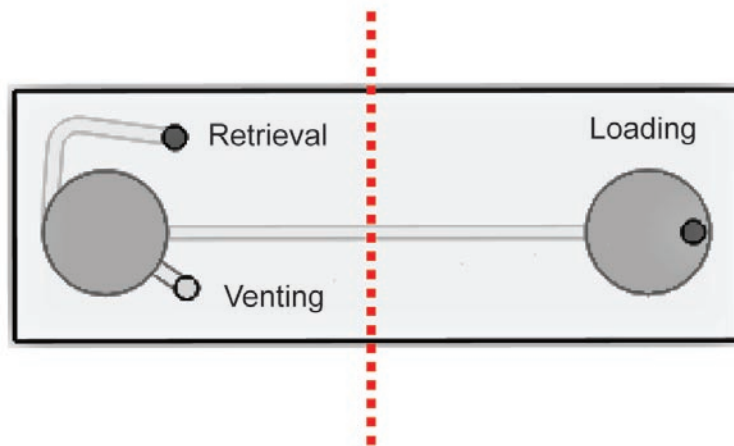
A custom-made aluminum spin chuck mechanically interfaces the compact disk platform to the motorized spin stand and enables an electrical connection between the spinning platform and the function generator using a slip ring. A slip ring is a hollow ceramic cylinder featuring metal (silver in this case) rings on its outer surface that once inserted around the spin chuck yields a permanent contact between the silver rings and a set of stationary brushes (silver graphite in our case) while spinning the chuck and the CD platform. The stationary brushes are wired to the function generator and the electric signal from the function generator is delivered via the slip ring to the spinning CD platform where is guided to the DEP chips using miniature screw-clamp terminal blocks and simple wiring. The compact disk platform allows for modular deployment of DEP chips and features a bottom substrate and a top cover. The bottom substrate (2.54 mm thick polycarbonate) contains the DEP chips in designated compartments while the top cover (1 mm thick polycarbonate) is used to prevent the DEP chips from detaching from the platform while spinning. Stainless steel nuts and bolts are used for the alignment of top cover to the bottom substrate and to secure the two polycarbonate pieces together. The platform used in this work can hold two carbon-DEP chips. The resulting platform, we call SpinDEP, features programmable centrifugal pumping and electrical forces.

### **5.1.4 3D carbon-DEP chips**

3D carbon-DEP chips are fabricated as stand-alone units, or modules, to allow for a rapid insertion and removal to and from the CD platform. Carbon-DEP chips feature carbon electrodes of different height which are fabricated following one of the procedures detailed in Table 2.3. Two different heights of carbon electrodes are used with centrifugal

microfluidics: 40 and 70  $\mu\text{m}$ . The fluid network around the electrode array is fabricated using polycarbonate (PC) and double-sided pressure-sensitive adhesive as detailed in section 2.1.2 and features two channels. The main flow channel is 600  $\mu\text{m}$  wide by 100  $\mu\text{m}$  high and holds the DEP carbon electrodes. The other channel is 1 mm wide and 100  $\mu\text{m}$  high and is used for sample retrieval. The top view and cross section of a carbon-DEP chip when containing 70  $\mu\text{m}$  high electrodes is illustrated in Fig. 5.2. The interface of the signal generator to the carbon-DEP chip was detailed above.

Top View



Cross section at dotted line

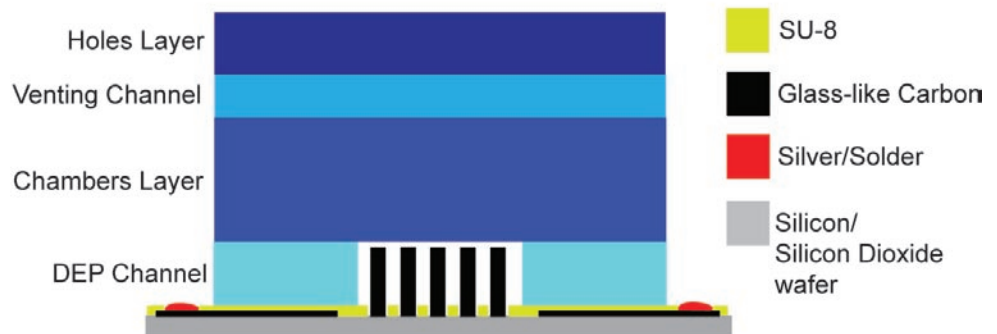


**Fig. 5.2** Top view and cross section of the carbon-DEP chip integrated with centrifugal microfluidics

## **5.2 Electrical and mechanical characterization of the SpinDEP platform**

Electrical tests demonstrate how 20 V<sub>pp</sub> sinusoidal signals with frequencies ranging from 1 kHz to 2 MHz are transmitted from the stationary function generator to a stationary measuring oscilloscope via the rotating CD platform without noticeable losses. Signal frequencies higher than 2 MHz cause impedance loading of the measurement circuit and lead to inappropriate readings. The platform is capable of spinning at frequencies up to 7000 rpm (116.6 Hz) without significant vibrations.

## **5.3 Flow characterization for SpinDEP experiments**

Filter efficiency in a DEP chip depends on the flow rate implemented in the channel: hydrodynamic forces compete with the DEP trapping force and too high a flow decreases the number of targeted particles than can be trapped. The flow rate induced in different carbon-DEP chips is characterized as a function of the rotation speed of the platform. The surface materials of the micro channels in carbon-DEP chips consist of double-sided pressure sensitive adhesive for the side walls, polycarbonate for the ceiling and SU-8 for the floor. Polycarbonate and SU-8 surfaces are expected to have a surface roughness on the order of hundreds of nanometers but side walls can present roughness on the order of micrometers as observed under the optical microscope (not shown). Such surface roughness has not been observed to be detrimental to the performance of the device. Negative effects such as flow turbulence or undesired cell trapping in wall crevices could not be discerned. The distribution of flow rates in both carbon-DEP chips (featuring either 40 μm high electrodes, as in CHIP 1, or 70 μm high electrodes, as in CHIP 2) when

flowing the experimental sample at spin rates ranging from 100 to 175 rpm is shown in Fig. 5.3.

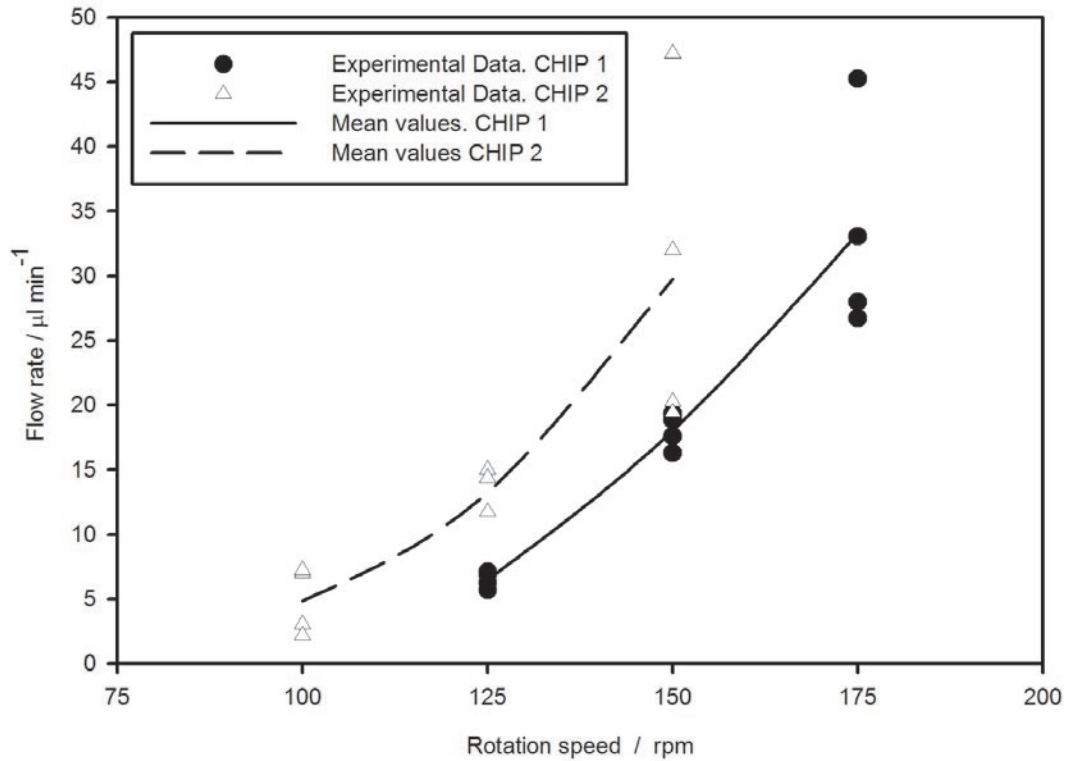


**Fig. 5.3** Flow rates established in two different carbon-DEP chips at different rotation speeds

Flow rate in the channel increases with spin speed. Spin rates between 100 and 175 rpm can induce flow rates as low as  $2 \mu\text{l min}^{-1}$  and as high as  $45 \mu\text{l min}^{-1}$  when using the channel geometry implemented here. However, spin speeds below 125 and 100 rpm for CHIP 1 and 2 respectively do not induce a flow in the micro channel observable using the imaging system specified above (so it is possible that flows of the order of  $\text{nl min}^{-1}$  do occur). Flow rates are relatively consistent at lower spin rates but exhibit a significant variation at 150 and 175 rpm for CHIP 1 and 2 respectively. It was previously suggested

<sup>176</sup> that the cause for the observed variability of the flow rate at a given rpm is due to the crude way of timing the flow (by eye) and this most likely is the case here as well. The variability in flow rates at high speeds (150-175 rpm) is higher than that at low spin speeds (100-125 rpm). For example at a flow rate of  $30 \mu\text{l min}^{-1}$ , timing errors of  $\pm 1$ ,  $\pm 2$  and  $\pm 3$  s represent a percentage change of 1, 2 and 3% respectively while this only represents a change of 0.1, 0.3 and 0.5% at a flow rate equal to  $5 \mu\text{l min}^{-1}$  (considering a sample volume of  $50 \mu\text{l}$  in both cases). To improve the flow rate reading one must consider incorporating a flow sensor in the channel. One option is the use of a flow sensor as introduced by Collins and Lee <sup>227</sup> who rely on the change of electric admittance on a set of parallel gold electrodes positioned at the channel bottom to measure flow rates up to  $35 \mu\text{l min}^{-1}$ . Another example, more suitable for the measurement of low flow rates, is described in the work by Wu and Sansen <sup>228</sup> who measured flow rates between 1 and  $15 \mu\text{l min}^{-1}$  using the electrochemical time-of-flight of oxygen which was quantified using micro fabricated amperometric sensors. The difference in induced flow rate between the channels of CHIP 1 and 2 at a given rpm observed in Fig. 5.3 is due to the unintended differences in alignment of each of the channels side-walls to a radial straight line between the center of rotation of the disk and its outer rim.

Using Equation 1.9 the induced flow rate in a channel that is perfectly aligned to the mentioned radial line with the flow rate in channels with different kinds of misalignments to that same radial line is compared. As shown in Figure 5.4a the misalignment is represented by variations in  $r_1$  and/or  $r_2$ . Here  $r_1$  and  $r_2$  are respectively the channel start point (or the point of the channel closest to the CD center of rotation), and the channel end point (or the point of the channel furthest away from the center of rotation). The

calculated values are shown in Fig. 5.4b as a function of spin speed and compared to the experimental curves previously shown in Fig. 5.3. The experimental results fall within the area delimited by misalignment errors of the channel. Furthermore, Fig. 5.4c shows how different kinds of misalignments impact the induced flow rate. Flow rate at a given spin speed decreases more rapidly when the channel end point is misaligned (case II in Fig. 5.4a) than when the channel start point is misaligned (case III in Fig. 5.4a). A misalignment of start and end points (case IV in Fig. 5.4a) leads to a linear decrease in flow rate that reaches zero faster than in both previous cases. The flow rate is zero when  $r_1$  and  $r_2$  are equal, *i. e.*, when the channel is parallel to the center of rotation, as predicted by Equation 1.9 ( $\Delta r = 0$ ). The use of a standardized fabrication process can minimize undesired misalignments of the channel to the center of rotation when positioning the DEP modules in the CD platform. A similar flow characterization was performed using different media and is detailed next.

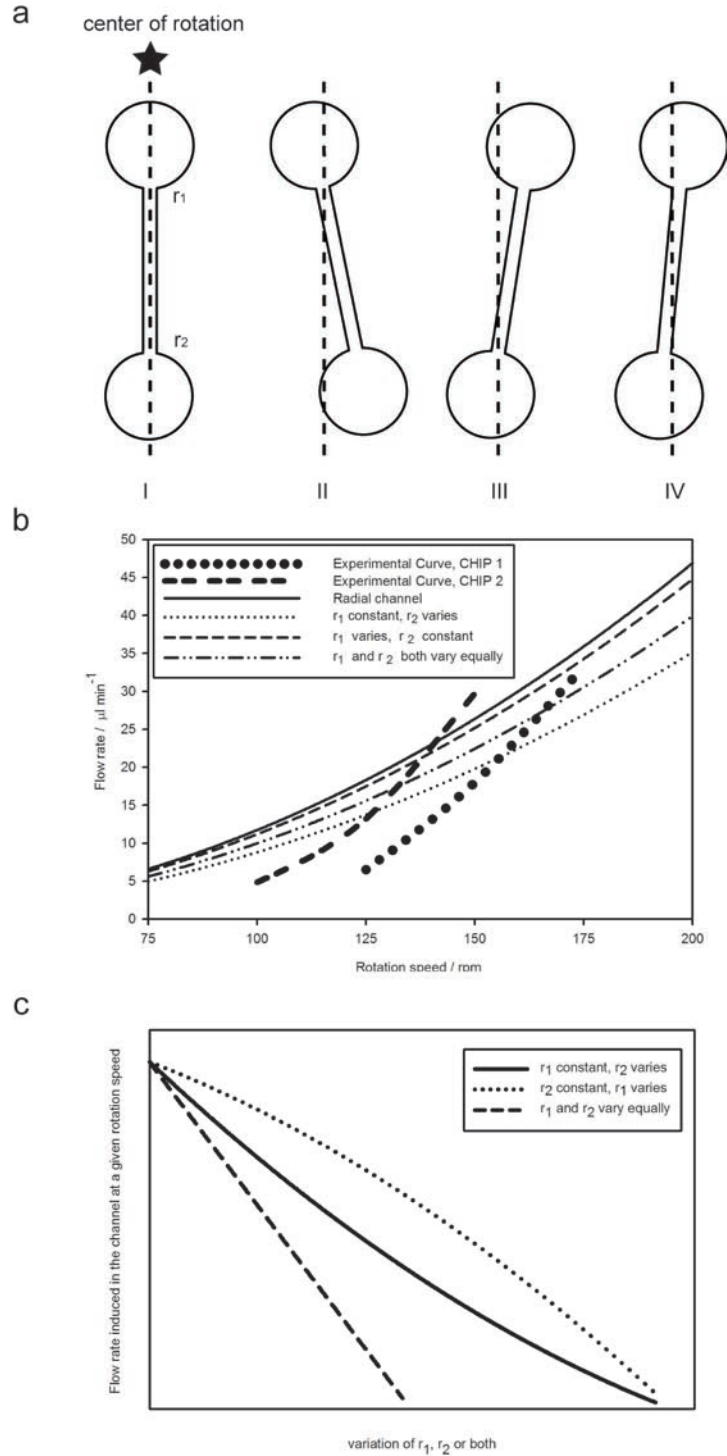


**Fig. 5.4** a) Different kinds of channel misalignment with respect to a radial line from the centre of rotation to the CD edge. b) Comparison between the flow rates established in the channel during experiments and those obtained theoretically considering different kinds of misalignments. c) Impact on the flow rate in the channel as the starting ( $r_1$ ) and end ( $r_2$ ) points of the channel vary

This characterization was conducted in a 600  $\mu\text{m}$  width, 100  $\mu\text{m}$  height channel fabricated completely in polycarbonate (PC). The channels are fabricated directly on a CD platform to eliminate any misalignments. These channels did not contain electrodes. The flow rate of different solutions: DI water, 0.6 wt% peptone, 0.1 wt% BSA and 0.2 wt% BSA was determined at different rotation speeds. Results are shown in Fig. 5.5. DI water behaves erratically. This is possibly due to the fact that water does not uniformly wet the PC surface due to the hydrophobic nature of the latter. The addition of BSA or peptone to DI water makes the flow behave more uniform. The addition of BSA leads to a solution that flows faster than that obtained when adding peptone. However, only the peptone solution flows at spin speeds below 175 rpm. The minimum spin speed at which DI water and BSA solutions flowed is 200 and 175 RPM respectively. It is suspected that the addition of peptone rather than BSA better improves wettability of the PC surface by water. The flow rate of a solution appears to be dependent on the solute concentration. For example, the flow rate of the 0.1 wt% BSA solution is slightly faster than that of the 0.2 wt% solution. This could be explained by the fact that the less concentrated solution is also less viscous.

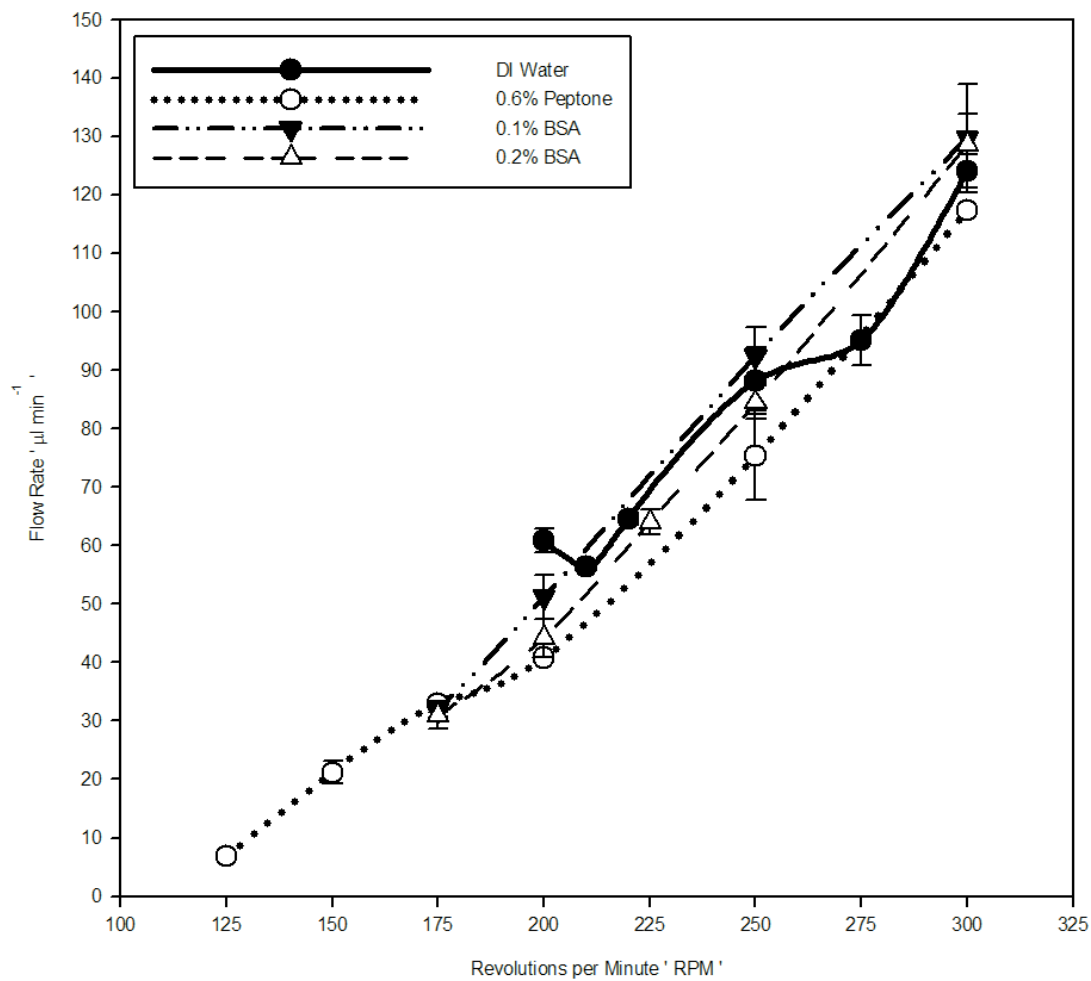


**Fig. 5.5** Flow rate characterization of different media as spin speed varies

## 5.4 Cell sorting using the SpinDEP platform

### 5.4.1 Experimental Protocol

Experiments are performed using either 40 or 70  $\mu\text{m}$  high carbon electrode posts. Two different experimental samples are used which are detailed in Table 4.4 as spinDEP1 and spinDEP2. The first sample, spinDEP1, is a mix of yeast cells and latex particles suspended in a 0.1 wt% BSA solution. The conductivity of the sample is  $31.2 \mu\text{S}\cdot\text{cm}^{-1}$ . A sinusoidal signal with frequency 200 kHz and amplitude of  $20 V_{\text{pp}}$  is used to selectively filter yeast cells, viable and non viable, from latex particles. In agreement with the DEP models shown in Fig. 4.4d, a working frequency of 200 kHz is optimal to induce the strongest positive DEP force on both non viable and viable yeast cells and attract them to the nearest electrode surface. At that same frequency, the latex particles are repelled from the nearest electrode surface by a negative DEP force and are eluted by the fluid flow. At working frequencies higher than 200 kHz, the force exerted on viable yeast increases but that on the non viable yeast cells diminishes. At frequencies lower than the optimal frequency of 200 kHz, the DEP force on non viable yeast cells remains the same as that at 200 kHz but the force acting on viable yeast cells decreases.

The second sample, spinDEP2, contains only yeast cells suspended in a 0.2 wt% peptone water. The conductivity of the sample is  $189 \mu\text{S}\cdot\text{cm}^{-1}$ . The polarizing signal in this case features a frequency of 1 MHz and magnitude  $20 V_{\text{pp}}$ . Following the DEP model shown in Fig. 4.4e, the use of this frequency causes the attraction of viable yeast cells to the nearest electrode surface. At this same frequency, non viable cells are repelled from the nearest electrode surface.

The experimental protocol detailed next is illustrated in Fig. 5.6. A volume of 50  $\mu\text{l}$  of the experimental sample, either spinDEP1 or spinDEP2, is first introduced into the inner chamber (the chamber closest to the CD center of rotation) where it is prevented from flowing into the channel containing the electrodes during loading by the hydrophobic valve in the inner chamber-channel interface <sup>229</sup>. Upon sample loading, the carbon electrodes are polarized using one of the sinusoidal signals detailed above. The channel containing the electrodes is then filled with the sample solution by rapid acceleration of the CD up to 800 rpm which causes the hydrophobic valve to burst <sup>229</sup>. Once the channel is filled, the platform is set to spin at a constant speed to induce a desired flow rate (which increases proportional to the spin speed). After the whole volume has passed through the channel the platform is stopped and the sample is retrieved from the outer chamber (the chamber closest to the CD outer edge) via the 1 mm wide channel. Electrodes are de-polarized after sample retrieval.

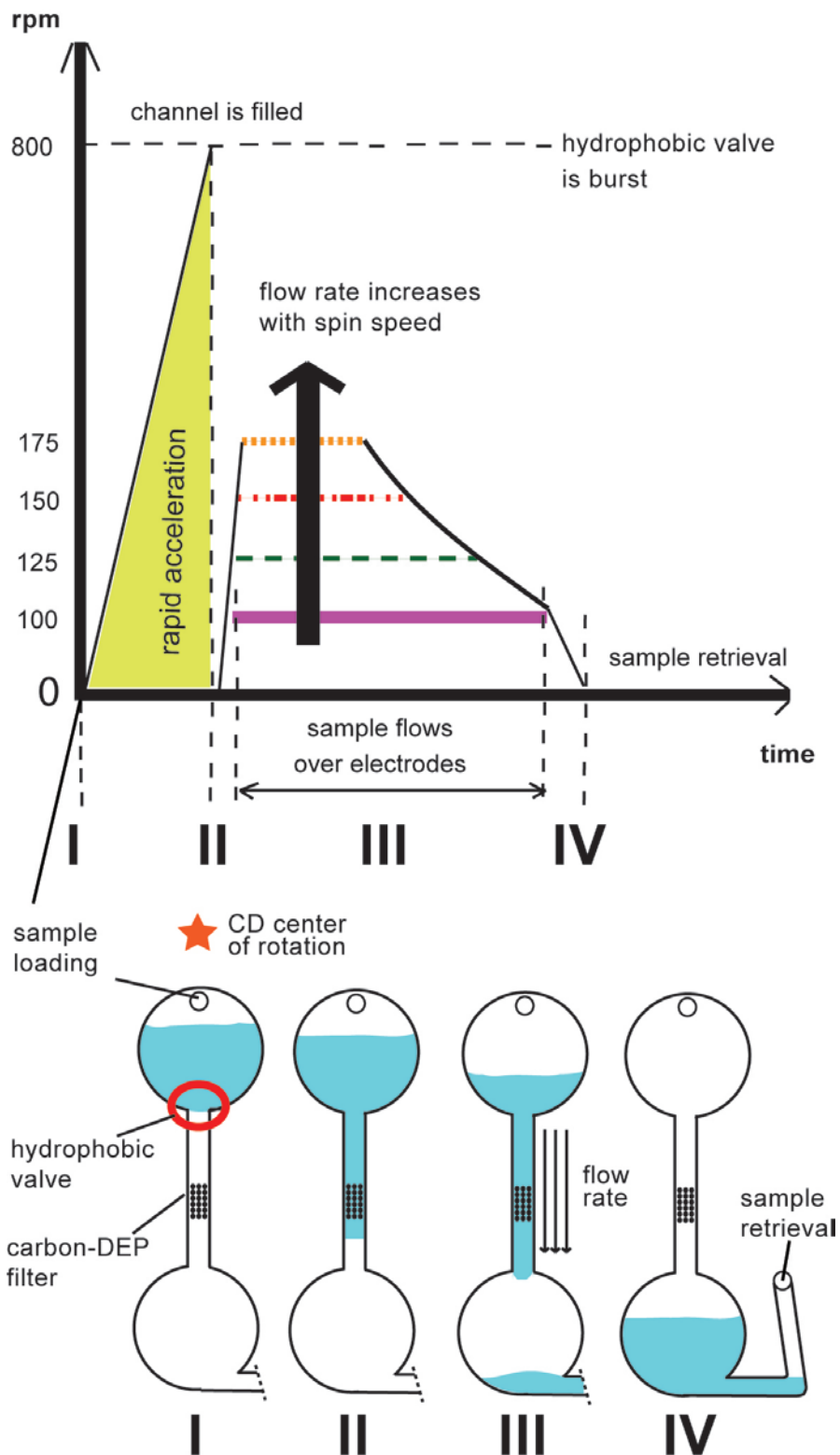


**Fig. 5.6** Experiment timeline (top) and corresponding processing steps (bottom): I. sample is loaded in the chamber; II. hydrophobic valve is burst and channel is filled; III. sample flows over carbon-DEP filter at a desired flow rate and IV. sample is retrieved

Sample flow rates are calculated by dividing the volume of the sample that flows from the inner to the outer chamber by the time it takes to do so. This time was assessed visually using the stroboscopic video microscopy system detailed above. Experimental times range from 1 to 16 min. Particle sedimentation becomes an issue with long experiment times (>5 min) and is further addressed below under Impact of particle sedimentation on filter efficiency.

Particle counts used in the quantification of filter efficiency (detailed in the next section) are carried out visually at a 200X magnification using a Nikon Eclipse LV100 Microscope. A hemacytometer set (Hausser Scientific) featuring an improved Neubauer ruling is used to aid in the count. The count values used for filter efficiency quantification (for example number of yeast cells in the sample after DEP-assisted filtration or the number of latex particles introduced in the DEP chip) are the average of four different counts performed for each sample. The standard deviation of the data set (each set has four counts) for a given sample was negligible and is not reported. Visual differentiation between latex particles and yeast cells is achieved without the use of any type of staining technique as their morphology is significantly different. Visual differentiation between viable and non viable cells is achieved using a trypan blue exclusion assay since their morphology is similar. The stain permeates through the cell membrane only in the case of non viable cells and stains the cell interior blue.

The targeted particles in this work are either yeast cells in general or viable yeast cells. The efficiency  $\eta$  when filtering a targeted particle from a mixture is defined in Equation 5.1 as the ratio of the number of targeted particles trapped in the filter over the total number of targeted particles upstream of the filter. The number of targeted particles

upstream of the filter is named  $PI$ . The number of targeted particles trapped in the DEP filter is given by the difference between  $PI$  and the number of targeted particles retrieved after the DEP filter which we name  $PO$ . Filter efficiency is then quantified as:

$$\eta = \frac{ParticlesTrapped}{ParticlesUpstream} = \frac{PI-PO}{PI} \quad (5.1)$$

To better illustrate the improvement on efficiency achieved with the use of carbon electrodes at different flow rates (details below under Impact of particle sedimentation on filter efficiency) the filter efficiency is normalized by dividing the number of targeted particles introduced in the DEP chip ( $PI$ ) by the total number of all particles present in the mixture introduced in the chip (denoted by  $TI$ ). In a similar way, the number of targeted particles retrieved from the chip ( $PO$ ) is divided by the total number of all particles contained in the sample retrieved from the DEP chip (given by  $TO$ ). The normalized equation is then:

$$\eta = \frac{\frac{PI}{TI} - \frac{PO}{TO}}{\frac{PI}{TI}} \quad (5.2)$$

As denoted in both Equations 5.1 and 5.2, a filter efficiency of one is achieved when targeted particles are absent in the sample retrieved from the DEP chip ( $PO = 0$ ) while a filter efficiency equal to zero is obtained when all targeted particles introduced in the DEP chip are retrieved from it after the experiment ( $PI = PO$ ).

### 5.4.2 Filtering of yeast cells from latex particles

The normalized filter efficiency when filtering yeast cells, from latex particles using either 40 or 70  $\mu\text{m}$ -high carbon electrodes as calculated from Equation 5.2 is shown in Fig. 5.7. The red dotted horizontal line denotes a base line given by the average of control values. Control values are obtained in the absence of a polarizing bias on the carbon electrodes. The use of 70  $\mu\text{m}$  high carbon electrodes yields a 100% filter efficiency at flow rates below  $5 \mu\text{l min}^{-1}$  and constitutes a better filter than the one based on 40  $\mu\text{m}$  high electrodes when considering flow rates below  $10 \mu\text{l min}^{-1}$ . At flow rates between 10 and  $35 \mu\text{l min}^{-1}$  the situation reverses and the use of 40  $\mu\text{m}$  high electrodes yields a better efficiency. Based on the simulation results shown in chapter 3, section 3.1 it is suspected that this result is due to experimental and statistical errors. The use of 70  $\mu\text{m}$ -high electrodes offers more trapping volume and a better coverage of the channel height than the use of 40  $\mu\text{m}$ -high ones at any given medium conductivity and polarizing voltage. The improvement of filter efficiency over the control base line approaches zero at flow rates above  $35 \mu\text{l min}^{-1}$ . Above this flow rate the hydrodynamic force overcomes the DEP trapping force. From Equation 5.2 the filter efficiency must obviously be zero when no particles are trapped by the filter, however in practice, undesirable experimental conditions such as particle sedimentation (see next section), adsorption to the channel surface, physical trapping of particles in crevices present in the micro channel, etc. explain this non-zero value of the control.

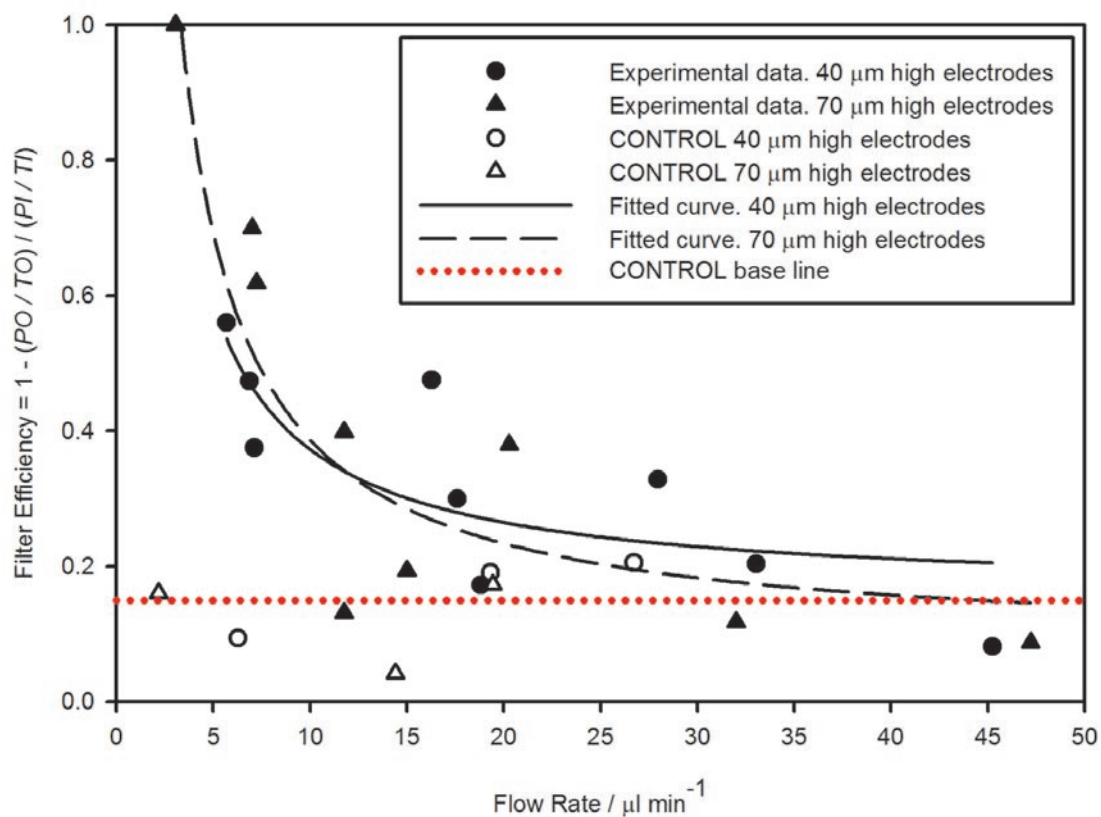


**Fig. 5.7** Filter efficiency vs. flow rate when filtering yeast cells from latex particles using 40 or 70- $\mu\text{m}$  high carbon electrodes

### 5.4.3 Cell viability assay

The normalized filter efficiency calculated using equation 5.2 when filtering viable yeast cells from non viable cells is shown in Fig. 5.8. Only the electrode array featuring 40  $\mu\text{m}$ -high carbon electrodes is used here. The red dotted horizontal line again denotes a base line given by the average of control values. Control values are obtained in the absence of a polarizing bias on the carbon electrodes. Flow rates below 10  $\mu\text{l}\cdot\text{min}^{-1}$  could not be achieved using this chip. The reason for this is suspected to be chip misalignment as detailed above. The use of 40  $\mu\text{m}$  high carbon electrodes yields a maximum efficiency

close 50% at flow rates around  $12 \mu\text{l}\cdot\text{min}^{-1}$ . The filter efficiency decreases proportional to the flow rate until it reaches the control base line at  $35 \mu\text{l}\cdot\text{min}^{-1}$ . Above this flow rate the hydrodynamic force overcomes the DEP trapping force. The control base line is given by the experimental results obtained when the electrodes are not turned on. Although the line should be at zero efficiency, experimental conditions including particle sedimentation and adsorption to the device surfaces are to blame for the non-zero value of the control.

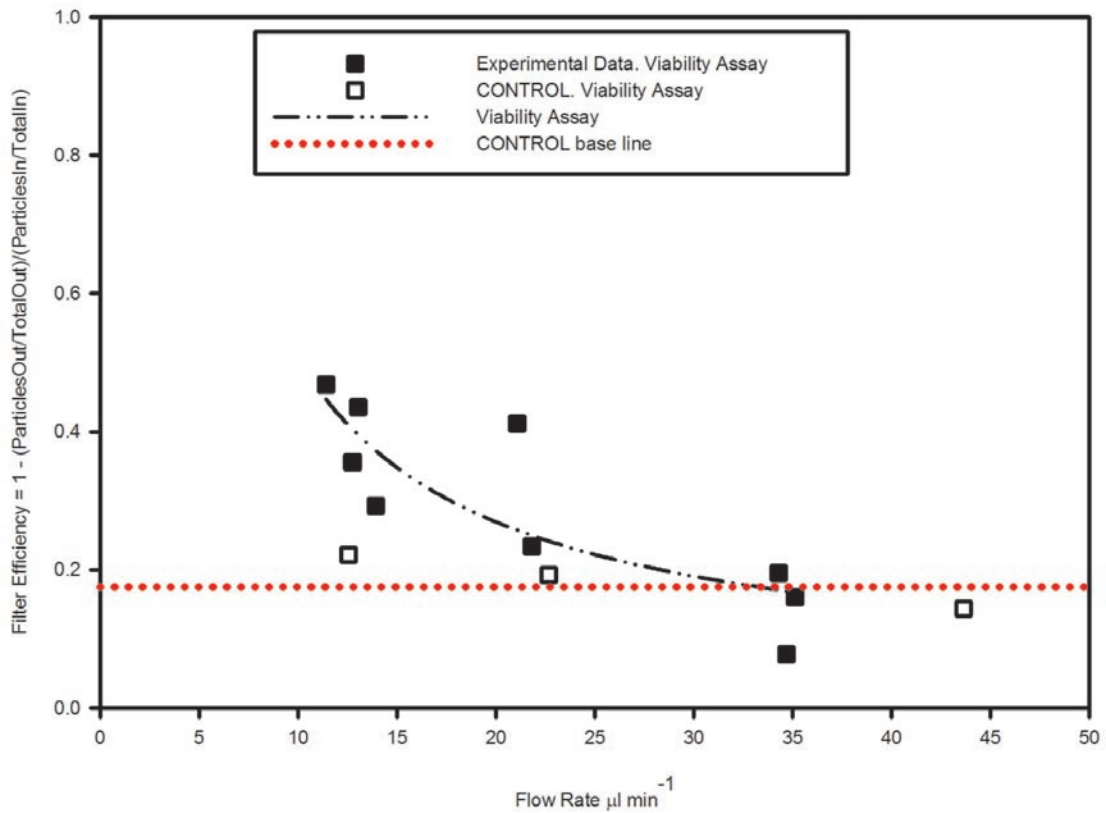


**Fig. 5.8** Filter efficiency vs. flow rate in a cell viability assay implemented with the SpinDEP platform

#### 5.4.4 Impact of particle sedimentation on filter efficiency

The filter efficiency as a function of the flow rate in the channel is again shown in Fig. 5.9a but now as calculated from Equation 5.1. Dashed and solid lines denote curves fitted to experimental data points (black curves) and control data points (red curves). The improvement of the filter efficiency over the control can be gleaned from Figure 5.9b. The comparison between Fig. 5.9a with Fig. 5.9b gives an insight about the impact of particle sedimentation on filter efficiency at different flow rates. At flow rates below  $10 \mu\text{l min}^{-1}$  the DEP trapping force overcomes the hydrodynamic force and filters most of the yeast cells. Even though the filter efficiency obtained with the use of either 40 and 70  $\mu\text{m}$  high electrodes is close to one at flow rates below  $10 \mu\text{l min}^{-1}$  the improvement over the control experiments carried on at similar flow rates is minimal. Low flow rates translate in slow flow velocities that allow for enough time for latex particles (and yeast cells that are not trapped in the filter) to sediment. Upon sedimentation, latex particles (and yeast cells) are likely to adsorb on the channel surfaces which results in low particle counts in the retrieved sample. At flow rates between 10 and  $25 \mu\text{l min}^{-1}$  the DEP trapping force is still stronger than the hydrodynamic force and filters a high percentage of the total population of yeast cells in the sample but now the flow velocity is fast enough to prevent sedimentation and effectively elutes the latex particles (and the yeast cells that could not be trapped) out of the channel. It is in this range where the highest improvement is achieved as illustrated in Fig. 5.9b. At high flow rates the hydrodynamic force completely overcomes the DEP trapping force exerted on the yeast cells by the electrode array and elutes all particles contained in the sample. In this case the improvement of filter efficiency over the control is minimal as illustrated at flow rates

above  $35 \mu\text{l min}^{-1}$  in Fig. 5.9b. A further experimental result to quantify sedimentation comes from the comparison between the number of total particles per unit volume that are retrieved from the chip and those initially introduced in it. At flow rates below  $10 \mu\text{l min}^{-1}$  the number of total particles retrieved from the chip is in average 58% of the total number of particles introduced in it and leads to an estimated 42% loss of particles due to sedimentation. No leaks were discerned in the experimental setup and the possibility of loss of particles from the fluid network is eliminated. Furthermore, at flow rates above  $10 \mu\text{l min}^{-1}$  the number of particles retrieved from the chip is close to the total count of particles introduced into it.

Future designs must account for the sedimentation effects described here. The sedimentation velocity  $U_s$  of a spherical particle in a given media can be derived by equating the Stokes drag force of the particle ( $D_s = 6\pi\mu r U_s$ ) with its weight minus bouyancy:

$$6\pi\mu r U_s = \frac{4}{3} \pi r^3 (\rho_{particle} - \rho_{fluid}) g \quad (5.3)$$

solving for  $U_s$  yields:

$$U_s = \frac{2r^2 (\rho_{particle} - \rho_{fluid}) g}{9\mu} \quad (5.4)$$

where  $\mu$  is the viscosity of the media,  $r$  is the particle radius,  $\rho_{fluid}$  is the density of the media,  $\rho_{particle}$  is the density of the particle and  $g$  is gravity (equal to  $9.81 \text{ m s}^{-2}$ ).  $U_s$  is also known as Stokes velocity and can be used to calculate the maximum time a particle can travel in a channel without sedimenting. Equation 5.4 describes the sedimentation velocity of an isolated particle immersed in an infinitely dilute solution and is used here as a basic model for particle sedimentation.

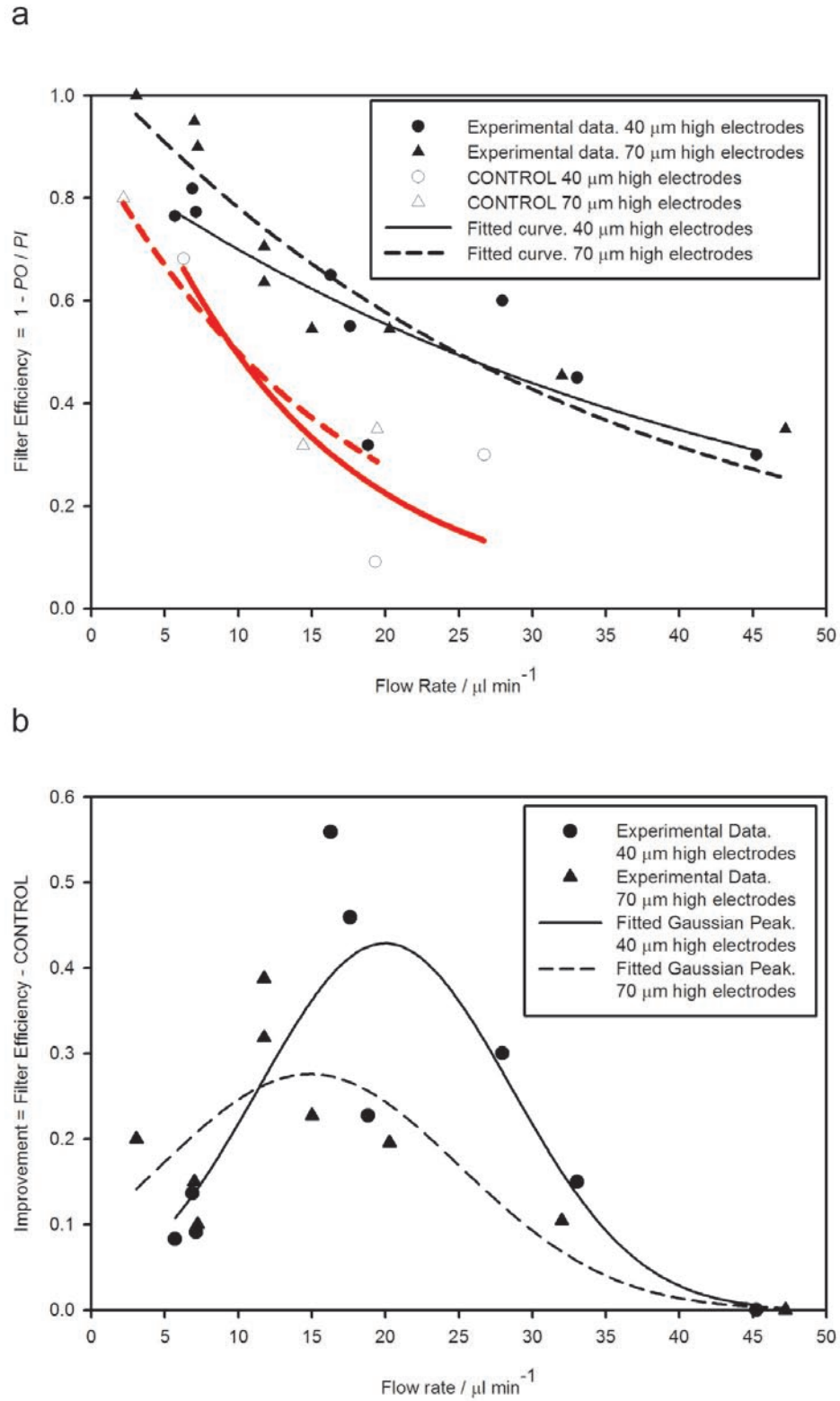


**Fig. 5.9** a) Filter efficiency at different flow rates when using 40 and 70  $\mu\text{m}$ -high electrodes and experimental sample spinDEP1 to filter yeast cells from latex particles. b) Improvement of filter efficiency over control experiments as flow rate increases

This idealized condition does not apply for a typical experimental sample where a particle is part of a large assembly of particles. However, modeling of particle settlement in a dense particle environment requires the use of computer simulation<sup>230</sup> and is beyond the scope of the current work. For instance, settling of particles in a dense solution creates velocity perturbations in the surrounding fluid that lead to long-range hydrodynamic interactions between the particles and causes a decrease in their settling velocity as compared to the idealized Stokes velocity.

To prevent particle sedimentation from negatively impacting the DEP filter efficiency a lower limit of the flow rate to be implemented in the channel must be calculated. For example, the analysis based on Fig. 5.9b identified that flow rates below  $10 \mu\text{l min}^{-1}$  are detrimental to filter efficiency.

A method to define an optimal range of flow rate values such that the particles that are not trapped by the filter are effectively eluted out of the channel is detailed next. The flow rate  $Q$  in the channel equals the product of flow velocity  $V$  times channel cross-section  $A$ ,

$$Q = VA \tag{5.5}$$

while the time  $t$  for a particle to travel a given channel length equals the ratio of channel length  $L$  to flow velocity  $V$ ,

$$t = \frac{L}{V} \tag{5.6}$$

Therefore the time required for a particle to travel a given length  $L$  of a channel with cross-section  $A$  can be calculated as a function of flow rate as:

$$t = \frac{LA}{Q} \tag{5.7}$$

by equating flow velocity in Equations 5.5 and 5.6. The channel used in this work features a length of 26.84 mm and a cross-section area of 600  $\mu\text{m}$  by 100  $\mu\text{m}$ . The relation between the time for a particle to travel the channel length and the flow rate, based on Equation 5.7, is illustrated in Fig. 5.10a. The sedimentation rates of yeast cells and latex particles are presented in this figure as well. The sedimentation rate of yeast cells (11.689  $\mu\text{m s}^{-1}$ ) and latex particles (8.2638  $\mu\text{m s}^{-1}$ ) is calculated from Equation 5.4 and is shown for the best case scenario of yeast cells and latex particles flowing close to the ceiling of the channel (100  $\mu\text{m}$  high). In this case, yeast cells may reach the bottom of the channel as fast as in 8.55 s while latex particles can do so in 12 s. The sedimentation rate of a given particle is constant regardless of the initial position of the particle in the channel and particles flowing closer to the channel bottom sediment faster. Fig. 5.10a helps in the establishment of an optimal flow rate that prevents particle sedimentation. For example, flow rates below 11  $\mu\text{l min}^{-1}$  are undesirable since they are too slow and allow for the sedimentation of all yeast cells (red dashed lines). However, the use of higher flow rates decreases the time a particle takes to travel the channel length. For instance, flow rates of around 24  $\mu\text{l min}^{-1}$  transport the particles across the channel length in 4 s and during that time only those particles initially at a height of 50  $\mu\text{m}$  or less from the channel bottom may sediment (red solid lines). The use of a design aid as represented in Fig. 5.10a must also take into account the fact that above certain flow rates the filter efficiency significantly drops as illustrated in Fig. 5.9b. If the flow rate desirable to avoid particle sedimentation yields a too low DEP filter efficiency for a given channel, the channel length and cross-section must be adapted to allow for slower flow rates, increased filter efficiency while also avoiding particle sediments. Channels with different

lengths and constant cross-section (600  $\mu\text{m}$  by 100  $\mu\text{m}$ ) and with different cross-sections and constant length (25 000  $\mu\text{m}$ ) respectively, are compared in Fig. 5.10b and e) in terms of the time it takes for a particle to travel the channel length given a fixed flow rate. The different curves are obtained using Equation 5.7. In contrast to the use of long channels, implementing shorter channels allows for slower flow rates in the channel and avoids particle sedimentation. For example, a horizontal line at 8.55 s (red dashed line) in Fig. 5.10b establishes the range of channel lengths (shorter than 15 000  $\mu\text{m}$ ) where flow rates below 10  $\mu\text{l min}^{-1}$  can be implemented without experiencing yeast sedimentation. However, the use of shorter channels limits the number of electrodes that can be contained in the channel and decreases the trapping volume available in the channel. The impact of increasing channel cross section on the time it takes for a given particle to travel a given channel length of 250 00  $\mu\text{m}$  as flow rate increases is shown in Fig. 5.10c. An increase of channel cross section requires the implementation of faster flow rates to avoid particle sedimentation. For instance, a channel cross section of 100  $\mu\text{m}$  high and 1 200  $\mu\text{m}$  wide ( $A = 120\,000\ \mu\text{m}^2$ ) requires the use of a flow rate as fast as 20  $\mu\text{l min}^{-1}$  to avoid sedimentation of a yeast cell flowing at the top of the channel (sedimentation time equals 8.55 s in this case and is denoted by the red dashed line). Unfortunately, at such high flow rate the DEP trapping force is completely voided by the hydrodynamic force and no yeast cells can be trapped. Plots like the ones in Figures 5.10a, b and c aid the process of reaching a compromise between trapping volume and channel dimensions to avoid particle sedimentation and improve the filter efficiency of a DEP device.

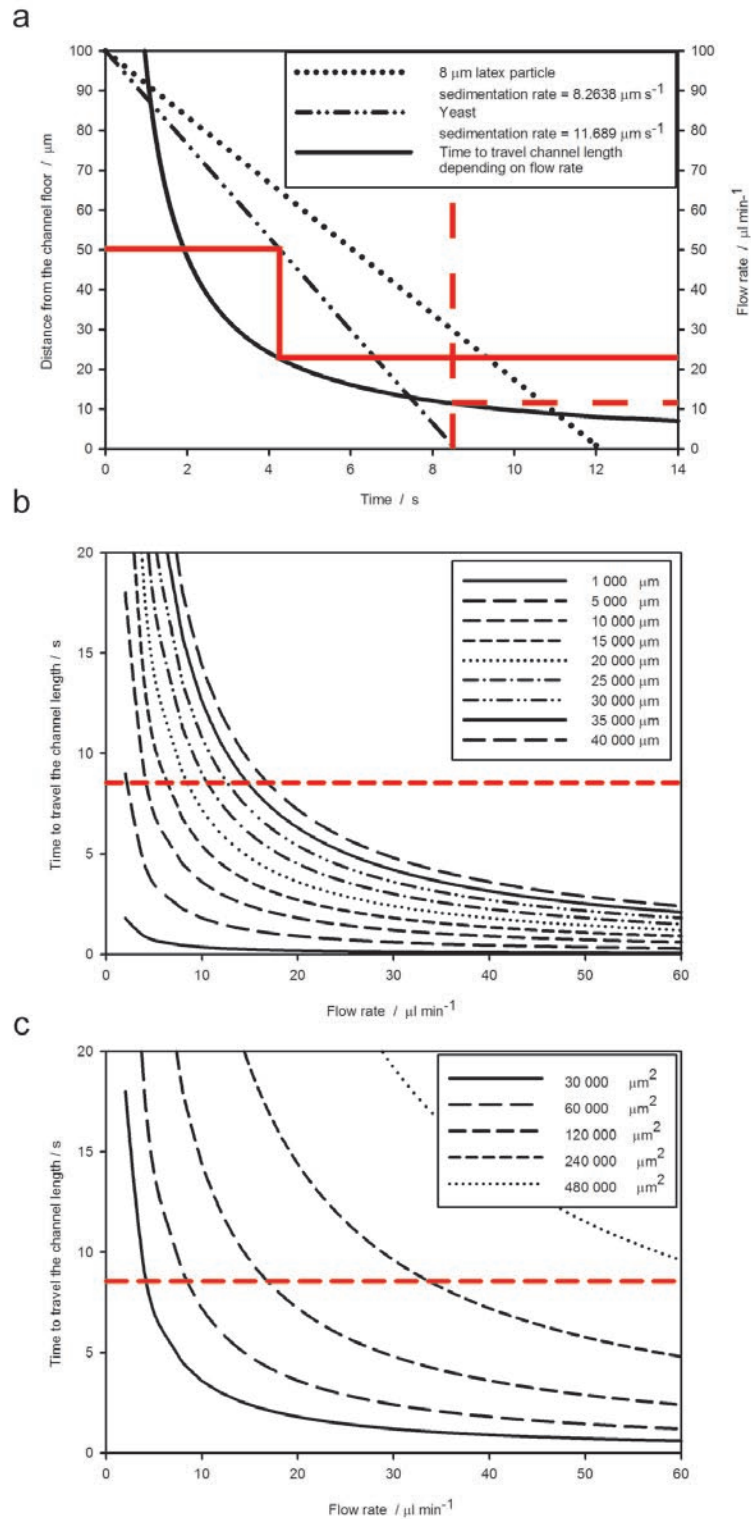


**Fig 5.10** a) Sedimentation rate of latex particles and yeast cells (black dotted and slashed lines) and time it takes for them to travel the channel length depending on the flow rate implemented in the channel (black solid curve). b) Time to travel the channel length vs. flow rate for channels with fixed cross section area ( $600 \mu\text{m}$  by  $100 \mu\text{m}$ ) but varying length. c) Time to travel the channel length vs. flow rate for channels with fixed length ( $25\,000 \mu\text{m}$ ) but varying cross section area

## 5.5 Advantages and broader impact of the SpinDEP platform

The CD-based DEP platform (SpinDEP) demonstrated here offers key advantages compared to more traditional DEP platforms with peristaltic or syringe pumps: 1) Footprint reduction; the current platform has the footprint of a data compact disc and a height less than 5 cm. 2) Cost reduction; external fluidic interconnects such as tubing, sample loading docks/ports, valves, splitters and/or syringe connectors are eliminated. Furthermore, because the flow rates induced in a channel by centrifugal forces (which can be as low as  $5 \text{ nl}\cdot\text{s}^{-1}$ <sup>176</sup>) depend mostly on the channel dimensions and its relative position and orientation to the center of rotation, high precision motors as those required in syringe pumps are not needed in centrifugal pumping. 3) Centrifugal pumping is “contact free” and does not require any mechanical interconnects to induce a pressure gradient for pumping. The virtual nature of the pumping force results in a vented system that is immune to the presence of air bubbles. 4) The demonstrated platform is a self-contained platform which minimizes the probability of sample leakage from the experimental setup. The complete fluidic network (and indeed the experiment or clinical test) can be contained in a single device (which can be disposable), be it a chip that can be embedded in a CD or the whole disk itself. 5) Centrifugal pumping does not depend on the physicochemical properties of the sample. 6) The demonstrated DEP platform is modular and amenable to integration with other sample preparation and detection architectures already demonstrated in CD-based platforms. It is important to clarify that the current platform does not operate at the point-of-care yet. Ongoing work is on the replacement of bulky and complex instrumentation, such as the described visualization system and the motor spins stand, for a miniaturized, less expensive stand-alone system.

The motor required for a SpinDEP unit at the point-of-care is expected to be similar to those used in conventional data CD units. The incorporation of flow rate sensors inside the fluid network (described above under Flow rate characterization of the carbon-DEP chip) eliminates the need for a visualization system like the one used in this work. The measurement of a desired variable, for example the concentration of a targeted cell population after enrichment, can be performed on the CD using fluorescence and absorption measurements or electrical methods such as dielectric spectroscopy.

This work also represents an important step towards integrating all types of electrokinetic phenomena (AC and DC) to other functions already demonstrated on CD platforms including valving, decanting, calibration, mixing, metering, sample splitting, and fluid separation. The addition of electrical forces to the CD platform affords a variety of functions previously not possible in CD fluidics: 1) Electrokinetic phenomena such as electrophoresis and dielectrophoresis allow for the bulk manipulation of cells, DNA and proteins with higher selectivity than hydrodynamics and centrifugation. It also allows for the selective manipulation and analysis of single entities, for example the isolation and electroporation of single cells to increase the efficiency in cell transfection for the genetic modification of stem cells<sup>231</sup>. 2) Electrodes in a centrifugal fluidic network enable novel mechanisms for analysis such as dielectric spectroscopy and electrochemical sensors. 3) Electric power on-CD permits the installation of different transducer modules on the CD and can enable the continuous interaction of forces such as optical, thermal and sonic with centripetal and electrical forces. Current CD platforms rely on external stationary transducer modules that only allow for intermittent interaction with a specific area of the CD (although the higher the spin rate the less intermittent the interaction is) and may

require the CD to become stationary to acquire data or manipulate a variable. While some applications may not require continuous interaction or even benefit from stationary conditions, real-time sensing of processes with fast kinetics and continuous manipulation of variables and objects of interest can prove beneficial in other applications. 4) The propulsion of fluids in current CD platforms is limited to centrifugal pumping from the center of a disk to its rim. Often this prevents the implementation of a whole diagnostic system in a single CD since cascading of all required functions (sample preparation, sorting, detection, etc.) cannot be fitted in the radius of a standard-sized CD. Electrokinetic phenomena can be used to drive a sample volume towards the CD center after centrifugation. For example, electroosmotic flow can return fluids to the CD center which gives the user the choice to drive the sample volume through the same processing network or to transfer to adjacent processing steps. 5) Electrical forces scale down favorably and can prove to have a stronger impact than centripetal forces in nanofluidics applications.

## CONCLUSION

The state-of-the-art in DEP and centrifugal microfluidics is advanced in this work. Carbon-electrode dielectrophoresis (carbon-DEP) has been demonstrated as a new alternative to current DEP technologies. Cell manipulation in the form of trapping and focusing has been achieved using carbon electrodes. Manipulated include *S. cerevisiae*, *E. coli* and *Drosophila melanogaster*. The use of volumetric (3D) electrodes has been demonstrated, both theoretically and experimentally, to yield higher trapping throughput and efficiency than 2D electrodes. The use of carbon electrodes affords several advantages over existing technologies: 1) a wider electrochemical stability window than gold and platinum which reduces the possibility to electrolyze the sample; 2) carbon is highly inert and biocompatible, and 3) the use of tens of volts to polarize a carbon-electrode array, instead of hundreds of volts as in the case of iDEP, is enough to induce a DEP force. Furthermore, 3D carbon electrodes are fabricated using a high-yield process that is relatively inexpensive.

The use of centrifugal forces for fluid pumping and fluid manipulation improves traditional DEP platforms in terms of footprint, cost, robustness and practicality. The integration of DEP with centrifugal microfluidics has been demonstrated with the extraction of a population of yeast cells from a background of latex particles and with a yeast-cell viability assay. The implemented modularity in the experimental platform allows for the use of interchangeable disposable chips depending on the type of assay or study to be conducted.

Centrifugal microfluidics is also advanced by the interfacing of programmable electrical signals to the rotating disk. The combination of electrical and centrifugal forces in a

single platform expands the number of applications where centrifugal microfluidics and electrokinetics are used by themselves. Electrokinetic phenomena does not scale up favorably since the magnitude of an electric field is inversely proportional to the separation between electrodes. Fluid manipulation using CD fluidics and centripetal forces does not scale down favorably since the fluidic resistance of a channel increases exponentially with a decrease in channel cross-section. In view of this, certain assays and fluidic functions may benefit better from electrokinetics than from CD fluidics and *vice versa*. An integrated system like the one demonstrated here is thus desired. This work is towards a CD-based point-of-care sample-to-answer system where sample preparation (mixing, conjugation, metering, splitting, lysis, etc.) is carried on using centripetal forces while selective fine manipulation is implemented with electrokinetics (electrophoresis, dielectrophoresis, electroporation, etc.).

## REFERENCES

- <sup>1</sup> Pohl, H. A., The Motion and Precipitation of Suspensoids in Divergent Electric Fields, *Journal of Applied Physics* 22 (7), 869-871, 1951.
- <sup>2</sup> Pohl, H. A., *Dielectrophoresis* Cambridge University Press, Cambridge, 1978.
- <sup>3</sup> Markx, G. H., Pethig, R., and Rousselet, J., The dielectrophoretic levitation of latex beads, with reference to field-flow fractionation, *Journal of Physics D: Applied Physics* 30 (17), 2470-2477, 1997.
- <sup>4</sup> Huang, Y., Holzel, R., Pethig, R., and Wang, X.-B., Differences in the AC electrodynamics of viable and non-viable yeast cells determined through combined dielectrophoresis and electrorotation studies, *Physics in Medicine and Biology* 37 (7), 1499-1517, 1992.
- <sup>5</sup> Markx, G. H., Talary, M. S., and Pethig, R., Separation of viable and nonviable yeast using dielectrophoresis, *Journal of Biotechnology* 32 (-), 29-37, 1994.
- <sup>6</sup> Markx, G. H., Huang, Y., Zhou, X. F., and Pethig, R., Dielectrophoretic characterization and separation of microorganisms, *Microbiology-UK* 140TY - JOUR Copyright 2003 SciSearch Plus , 585-591, 1994.
- <sup>7</sup> Hodgson, C. E. and Pethig, R., Determination of the viability of Escherichia coli at the single organism level by electrorotation, *Clinical chemistry* 44 (9), 2049-2051, 1998.
- <sup>8</sup> Hughes, M. P., Morgan, H., Rixon, F. J., Burt, J. P. H., and Pethig, R., Manipulation of herpes simplex virus type 1 by dielectrophoresis, *Biochimica et Biophysica Acta-General Subjects* 1425 (-), 119-126, 1998.
- <sup>9</sup> Becker, F. F., Wang, X. B., Huang, Y., Pethig, R., Vykoukal, J., and Gascoyne, P. R. C., The removal of human leukaemia cells from blood using interdigitated microelectrodes, *Journal of Applied Physics* 27 , 2659-2662, 1994.
- <sup>10</sup> Becker, F. F., Wang, X. B., Huang, Y., Pethig, R., Vykoukal, J., and Gascoyne, P. R. C., Separation of human breast cancer cells from blood by differential dielectric affinity, *Proceedings of the National Academy of Sciences of the United States of America* 92 , 860-864, 1995.
- <sup>11</sup> Talary, M. S., Mills, K. I., Hoy, T., Burnett, A. K., and Pethig, R., Dielectrophoretic separation and enrichment of CD34+ cell subpopulation from bone marrow and peripheral blood stem cells, *Medical and Biological Engineering and Computing* 33 (2), 235-237, 1995.
- <sup>12</sup> Stephens, M., Talary, M. S., Pethig, R., Burnett, A. K., and Mills, K. I., The dielectrophoresis enrichment of CD34+ cells from peripheral blood stem cells harvests, *Bone Marrow Transplantation* 18 (4), 777-782, 1996.
- <sup>13</sup> Morgan, H. and Green, N. G., *AC Electrokinetics: Colloids and Nanoparticles* Research Studies Press LTD, Hertfordshire, England, 2003.
- <sup>14</sup> Fuhr, G., Glasser, H., Muller, T., and Schnelle, T., Cell manipulation and cultivation under ac electric-field influence in highly conductive culture media, *Biochimica et Biophysica Acta-General Subjects* 1201 (-), 353-360, 1994.
- <sup>15</sup> Müller, T., Fiedler, S., Schnelle, T., Ludwig, K., Jung, H., and Fuhr, G., High frequency electric fields for trapping of viruses, *Biotechnology Techniques* 10 (-), 221-226, 1996.
- <sup>16</sup> Zimmermann, U. and Neil, G. A., *Electromanipulation of Cells* CRC Press, Boca Raton, FL, 1996.

17. Jones, T. B., *Electromechanics of Particles* Cambridge University Press, USA, 1995.
18. Grom, F., Kentsch, J., Müller, T., Schnelle, T., and Stelzle, M., Accumulation and trapping of hepatitis A virus particles by electrohydrodynamic flow and dielectrophoresis, *Electrophoresis* 27 (7), 1386-1393, 2006.
19. Washizu, M., Bio-nanotechnology of DNA, in *2nd Annual International IEEE-EMB Special Topic Conference on Microtechnologies in Medicine & Biology*, Madison, WI, USA, pp. 1-3-6.
20. Gascoyne, P. R. C. and Vykoukal, J. V., Dielectrophoresis-based sample handling in general-purpose programmable diagnostic instruments, *Proceedings of the IEEE* 92 (1), 22-42, 2004.
21. Voldman, J., Gray, M., Toner, M., and Schmidt, M., A Microfabrication-based Dynamic Array Cytometer, *Analytical Chemistry* 74 , 3984-3990, 2002.
22. Wang, L., Flanagan, L., and Lee, A. P., Side-Wall Vertical Electrodes for Lateral Field Microfluidic Applications, *Journal of Microelectromechanical Systems* 16 (2), 454-461, 2007.
23. Cummings, E. B. and Singh, A. K., Dielectrophoresis in Microchips Containing Arrays of Insulating Posts: Theoretical and Experimental Results, *Analytical Chemistry* 75 (18), 4724-4731, 2003.
24. Cummings, E. B., Streaming dielectrophoresis for continuous-flow microfluidic devices, *IEEE Engineering in Medicine and Biology Magazine* 22 (-), 75-84, 2003.
25. Demierre, N., Braschler, T., Muller, R., and Renaud, P., Focusing and continuous separation of cells in a microfluidic device using lateral dielectrophoresis, *Sensors and Actuators, B: Chemical* 132 (2), 388-396, 2008.
26. Iliescu, C., Xu, G. L., Samper, V., and Tay, F. E. H., Fabrication of a dielectrophoretic chip with 3D silicon electrodes, 2005.
27. Hughes, M. P., *Nanoelectromechanics in Engineering and Biology* CRC Press, Boca Raton, FL, 2002.
28. Hagedorn, R., Fuhr, G., Muller, T., and Gimsa, J., Traveling-Wave Dielectrophoresis of Microparticles, *Electrophoresis* 13 (1-2), 49-54, 1992.
29. Gascoyne, P. R. C., Huang, Y., Pethig, R., Vykoukal, J., and Becker, F. F., Dielectrophoretic Separation of Mammalian-Cells Studied by Computerized Image-Analysis, *Measurement Science & Technology* 3 (5), 439-445, 1992.
30. Becker, F. F., The removal of human leukaemia cells from blood using interdigitated microelectrodes, *Journal of physics. D, Applied physics* 27 (12), 2659, 1994.
31. Talary, M. S., Mills, K. I., Hoy, T., Burnett, A. K., and Pethig, R., Dielectrophoretic Separation and Enrichment of Cd34+ Cell Subpopulation from Bone-Marrow and Peripheral-Blood Stem-Cells, *Medical & Biological Engineering & Computing* 33 (2), 235-237, 1995.
32. Markx, G. H. and Pethig, R., Dielectrophoretic Separation of Cells - Continuous Separation, *Biotechnology and Bioengineering* 45 (4), 337-343, 1995.
33. Gascoyne, P. R. C., Wang, X. B., Huang, Y., and Becker, F. F., Dielectrophoretic separation of cancer cells from blood, *Ieee Transactions on Industry Applications* 33 (3), 670-678, 1997.
34. Suehiro, J. and Pethig, R., The dielectrophoretic movement and positioning of a biological cell using a three-dimensional grid electrode system, *Journal of Physics D: Applied Physics* 31 (-), 3298-3305, 1998.

- <sup>35</sup> Hughes, M. P. and Morgan, H., Dielectrophoretic characterization and separation of antibody-coated submicrometer latex spheres, *Analytical Chemistry* 71 , 3441-3445, 1999.
- <sup>36</sup> Chan, K. L., Morgan, H., Morgan, E., Cameron, I. T., and Thomas, M. R., Measurements of the dielectric properties of peripheral blood mononuclear cells and trophoblast cells using AC electrokinetic techniques, *Biochimica Et Biophysica Acta-Molecular Basis of Disease* 1500 (3), 313-322, 2000.
- <sup>37</sup> Heida, T., Rutten, W. L. C., and Marani, E., Dielectrophoretic trapping of dissociated fetal cortical rat neurons, *IEEE Transactions on Biomedical Engineering* 48 (8), 921-930, 2001.
- <sup>38</sup> Pethig, R., Bressler, V., Carswell-Crumpton, C., Chen, Y., Foster-Haje, L., Garcia-Ojeda, M. E., Lee, R. S., Lock, G. M., Talary, M. S., and Tate, K. M., Dielectrophoretic studies of the activation of human T lymphocytes using a newly developed cell profiling system, *Electrophoresis* 23 (13), 2057-2063, 2002.
- <sup>39</sup> Suehiro, J., Hamada, R., Noutomi, D., Shutou, M., and Hara, M., Selective detection of viable bacteria using dielectrophoretic impedance measurement method, *Journal of Electrostatics* 57 (6-10), 157-168, 2003.
- <sup>40</sup> Gray, D. S., Tan, J. L., Voldman, J., and Chen, C. S., Dielectrophoretic registration of living cells to a microelectrode array, *Biosensors & Bioelectronics* 19 (7), 771-780, 2004.
- <sup>41</sup> Prasad, S., Zhang, X., Yang, M., Ni, Y., Parpura, V., Ozkan, C. S., and Ozkan, M., Separation of individual neurons using dielectrophoretic alternative current fields, *Journal of Neuroscience Methods* 135 (1-2), 79-88, 2004.
- <sup>42</sup> Gascoyne, P., Satayavivad, J., and Ruchirawat, M., Microfluidic approaches to malaria detection, *Acta Tropica* 89 (-), 357-369, 2004.
- <sup>43</sup> Das, C. M., Becker, F., Vernon, S., Noshari, J., Joyce, C., and Gascoyne, P. R. C., Dielectrophoretic segregation of different human cell types on microscope slides, *Analytical Chemistry* 77 (9), 2708-2719, 2005.
- <sup>44</sup> Iliescu, C., Xu, G. L., Samper, V., and Tay, F. E. H., Fabrication of a dielectrophoretic chip with 3D silicon electrodes, *Journal of Micromechanics and Microengineering* 15 (3), 494-500, 2005.
- <sup>45</sup> Boettcher, M., Jaeger, M., Riegger, L., Ducrée, J., Zengerle, R., and Duschl, C., Lab-on-chip-based cell separation by combining dielectrophoresis and centrifugation, *Biophysical Reviews and Letters* 1 (4), 443-451, 2006.
- <sup>46</sup> Wang, L. S., Marchenko, S., Huang, J. T., Jeon, N. L., Monuk, E., Flanagan, L. A., and Lee, A. P., Design and fabrication of vertical electrodes in microchannels for particles/cells sorting by dielectrophoresis, *2006 International Conference on Microtechnologies in Medicine and Biology*, 147-150 305, 2006.
- <sup>47</sup> Flanagan, L. A., Lu, J., Wang, L., Marchenko, S. A., Jeon, N. L., Lee, A. P., and Monuki, E. S., Unique dielectric properties distinguish stem cells and their differentiated progeny, *Stem Cells* 26 (3), 656-665, 2008.
- <sup>48</sup> Pethig, R., Menachery, A., Heart, E., Sanger, R. H., and Smith, P. J. S., Dielectrophoretic assembly of insulinoma cells and fluorescent nanosensors into three-dimensional pseudo-islet constructs, *Iet Nanobiotechnology* 2 (2), 31-38, 2008.

- <sup>49</sup>. Menachery, A., Chappell, S., Errington, R. J., Morris, D., Smith, P. J., Wiltshire, M., Furon, E., and Burt, J., Dielectrophoretic characterization and separation of metastatic variants of small cell lung cancer cells, *NSTI-Nanotech* 3, 4, 2008.
- <sup>50</sup>. An, J., Lee, J., Lee, S. H., Park, J., and Kim, B., Separation of malignant human breast cancer epithelial cells from healthy epithelial cells using an advanced dielectrophoresis-activated cell sorter (DACS), *Analytical and Bioanalytical Chemistry* 394 (3), 801-809, 2009.
- <sup>51</sup>. Hashimoto, M., Kaji, H., and Nishizawa, M., Selective capture of a specific cell type from mixed leucocytes in an electrode-integrated microfluidic device, *Biosensors & Bioelectronics* 24 (9), 2892-2897, 2009.
- <sup>52</sup>. Gascoyne, P. R. C., Noshari, J., Anderson, T. J., and Becker, F. F., Isolation of rare cells from cell mixtures by dielectrophoresis, *Electrophoresis* 30 (8), 1388-1398, 2009.
- <sup>53</sup>. Cheng, I. F., Froude, V. E., Zhu, Y. X., Chang, H. C., and Chang, H. C., A continuous high-throughput bioparticle sorter based on 3D traveling-wave dielectrophoresis, *Lab on a Chip* 9 (22), 3193-3201, 2009.
- <sup>54</sup>. Gascoyne, P. R. C., Dielectrophoretic-Field Flow Fractionation Analysis of Dielectric, Density, and Deformability Characteristics of Cells and Particles, *Analytical Chemistry* 81 (21), 8878-8885, 2009.
- <sup>55</sup>. Hirota, Y., Hakoda, M., and Wakizaka, Y., Separation characteristics of animal cells using a dielectrophoretic filter, *Bioprocess and Biosystems Engineering* 33 (5), 607-612, 2010.
- <sup>56</sup>. Ng, S. Y., Reboud, J., Wang, K. Y. P., Tang, K. C., Zhang, L., Wong, P., Moe, K. T., Shim, W., and Chen, Y., Label-free impedance detection of low levels of circulating endothelial progenitor cells for point-of-care diagnosis, *Biosensors & Bioelectronics* 25 (5), 1095-1101, 2010.
- <sup>57</sup>. Yang, F., Yang, X. M., Jiang, H., Bulkhaults, P., Wood, P., Hrushesky, W., and Wang, G. R., Dielectrophoretic separation of colorectal cancer cells, *Biomicrofluidics* 4 (1), -, 2010.
- <sup>58</sup>. Lee, H. J., Lee, S. H., Yasukawa, T., Ramon-Azcon, J., Mizutani, F., Ino, K., Shiku, H., and Matsue, T., Rapid and simple immunosensing system for simultaneous detection of tumor markers based on negative-dielectrophoretic manipulation of microparticles, *Talanta* 81 (1-2), 657-663, 2010.
- <sup>59</sup>. Villemejeane, J., *Nanomanipulation of Living Cells on a Chip Using Electric Field: General Concepts and Microdevices* 2010 *Fifth IEEE International Symposium on Electronic Design Test & Applications*, 2010.
- <sup>60</sup>. Shafiee, H., Caldwell, J. L., and Davalos, R. V., A Microfluidic System for Biological Particle Enrichment Using Contactless Dielectrophoresis, *Journal of the Association for Laboratory Automation* 15 (3), 224-232, 2010.
- <sup>61</sup>. Dinh, N.-D. and Liu, C.-H., A Lab-on-Chip for Separating and Focusing Bioparticles via Dielectrophoresis, *IFMBE Proceedings* 27, 2010.
- <sup>62</sup>. Feldman, Y., Ermolina, I., and Hayashi, Y., Time Domain Dielectric Spectroscopy Study of Biological Systems, *IEEE Transactions on Dielectrics and Electrical Insulation* 10 (5), 728-753, 2003.

- <sup>63.</sup> Gascoyne, P. and Vykoukal, J., Dielectrophoresis-Based Sample Handling in General-Purpose Programmable Diagnostic Instruments, *Proceedings of the IEEE* 92 (1), 22-42, 2004.
- <sup>64.</sup> Wang, L., Flanagan, L. A., Jeon, N. L., Monuki, E., and Lee, A. P., Dielectrophoresis switching with vertical sidewall electrodes for microfluidic flow cytometry, *Lab on a Chip* 7 , 1114-1120, 2007.
- <sup>65.</sup> Lapizco-Encinas, B. H., Simmons, B. A., Cummings, E. B., and Fintschenko, Y., Dielectrophoretic Concentration and Separation of Live and Dead Bacteria in an Array of Insulators, *Analytical Chemistry* 76 (6), 1571-1579, 2004.
- <sup>66.</sup> Davalos, R. V., McGraw, G. J., Wallow, T. I., Morales, A. M., Krafcik, K. L., Cummings, E. B., and Simmons, B. A., Performance impact of dynamic surface coatings on polymeric insulator-based dielectrophoretic particle separators, *Analytical and Bioanalytical Chemistry* 390 (3), 847-855, 2008.
- <sup>67.</sup> Simmons, B. A., McGraw, G. J., Davalos, R. V., Fiechtner, G. J., Fintschenko, Y., and Cummings, E. B., The Development of Polymeric Devices as Dielectrophoretic Separators and Concentrators, *MRS Bulletin* 31 , 120-124, 2006.
- <sup>68.</sup> Ilescu, C., Yu, L., Xu, G., and Tay, F. E. H., A Dielectrophoretic Chip with a 3-D Electric Field Gradient, *Journal of Microelectromechanical Systems* 15 (6), 1506-1513, 2006.
- <sup>69.</sup> Yu, L., Ilescu, C., Xu, G., and Tay, F. E. H., Sequential field-flow cell separation method in a dielectrophoretic chip with 3-D electrodes, *Journal of Microelectromechanical Systems* 16 (5), 1120-1129, 2007.
- <sup>70.</sup> Lapizco-Encinas, B. H., Simmons, B. A., Cummings, E. B., and Fintschenko, Y., Insulator-Based Dielectrophoresis for the Selective Concentration and Separation of Live Bacteria in Water, *Electrophoresis* 25 , 1695-1704, 2004.
- <sup>71.</sup> Lapizco-Encinas, B. H., Davalos, R., Simmons, B. A., Cummings, E. B., and Fintschenko, Y., An Insulator-Based (Electrodeless) Dielectrophoretic Concentrator for Microbes in Water, *Journal of microbiological methods* 62 , 317-326, 2005.
- <sup>72.</sup> Martinez-Duarte, R., Turon Teixidor, G., Mukherjee, P. P., Kang, Q., and Madou, M. J., Perspectives of Micro and Nanofabrication of Carbon for Electrochemical and Microfluidic Applications, in *Microfluidics and Microfabrication*, Chakraborty, S. Springer, 2009, pp. 181-263.
- <sup>73.</sup> Fitzer, E., Kochling, K. H., Boehm, H. P., and Marsh, H., Recommended Terminology for the Description of Carbon as a Solid, *Pure and applied chemistry* 67 (3), 473-506, 1995.
- <sup>74.</sup> Wang, C., Jia, G., Taherabadi, L. H., and Madou, M. J., A Novel Method for the Fabrication of High-Aspect Ratio C-MEMS Structures, *Journal of Microelectromechanical Systems* 14 (2), 348-358, 2005.
- <sup>75.</sup> Cowlard, F. C. and Lewis, J. C., Vitreous Carbon - A New Form of Carbon, *Journal of Materials Science* 2 , 507-512, 1967.
- <sup>76.</sup> Jenkins, G. M., Kawamura, K., and Ban, L. L., Formation and Structure of Polymeric Carbons, *Proceedings of the Royal Society of London. Series A, Mathematical and Physical Sciences* 327 (1571), 501-517, 1972.
- <sup>77.</sup> Stanitski, C. L. and Mooney, V., Osseous attachment to vitreous carbons, *Journal of Biomedical Materials Research* 7 (3), 97-108, 1973.

- <sup>78</sup>. Benson, J., Elemental Carbon as a Biomaterial, *Journal of Biomedical Materials Research* 5 (6), 41-47, 1971.
- <sup>79</sup>. Benson, J., Carbon offers advantages as implant material in human body, *NASA Technical Brief* , 1969.
- <sup>80</sup>. Turon Teixidor, G., Gorkin Iii, R. A., Tripathi, P. P., Bisht, G. S., Kulkarni, M., Maiti, T. K., Battacharyya, T. K., Subramaniam, J. R., Sharma, A., Park, B. Y., and Madou, M., Carbon microelectromechanical systems as a substratum for cell growth, *Biomedical Materials* 3 , 034116, 2008.
- <sup>81</sup>. Pesin, L. A., Structure and Properties of glass-like carbon, *Journal of Materials Science* 37 , 1-28, 2002.
- <sup>82</sup>. Jenkins, G. M. and Kawamura, K., Structure of Glassy Carbon, *Nature* 231 , 175-176, 1971.
- <sup>83</sup>. Bragg, R. H. and Hammond, M. L., X-ray study of pyrolytic graphites and glassy carbons, *Carbon* 3 (3), 340-340, 1965.
- <sup>84</sup>. McFeely, S. P., Kowalczyk, S. P., Ley, L., Cavell, R. G., Pollak, R. A., and Shirley, D. A., X-ray photoemission studies of diamond, graphite, and glassy carbon valence bands, *Physical Reviews B* 9 (12), 5268-5278, 1974.
- <sup>85</sup>. Weintraub, E. and Miller, L. B., 1156509, 1915, Microphone.
- <sup>86</sup>. Redfern, B. and Greens, N., US 3109712, 1963, Bodies and Shapes of Carbonaceous Materials and Processes for their Production.
- <sup>87</sup>. Yamada, S. and Sato, H., Some Physical Properties of Glassy Carbon, *Nature* 193 , 261-262, 1962.
- <sup>88</sup>. Lewis, J. C., Redfern, B., and Cowlard, F. C., Vitreous carbon as a crucible material for semiconductors, *Solid-State Electronics* 6 (3), 251-254, 1963.
- <sup>89</sup>. Hucce, E. E., Fuys, R. A., and Craig, R. G., Glassy Carbon: a potential Dental Implant Material, 7 (3), 263-274, 1973.
- <sup>90</sup>. Hobkirk, J. A., Tissue reactions to implanted vitreous carbon and high purity sintered alumina, *Journal of Oral Rehabilitation* 4 (4), 355-368, 1976.
- <sup>91</sup>. Maropis, P. S., Molinari, J. A., Appel, B. N., and Baumhammers, A., Comparative study of vitreous carbon, pyrolytic carbon, pyrolytic graphite/silicon-carbide, and titanium implants in rabbit mandibles, *Oral surgery, oral medicine and oral pathology* 43 (4), 506-512, 1977.
- <sup>92</sup>. Schueller, O. J. A., Brittain, S. T., and Whitesides, G. M., Fabrication of glassy carbon microstructures by pyrolysis of microfabricated polymeric precursors, *Advanced Materials* 9 (6), 477-&, 1997.
- <sup>93</sup>. Schueller, O. J. A., Brittain, S. T., and Whitesides, G. M., Fabrication of glassy carbon microstructures by soft lithography, *Sensors and Actuators A: Physical* 72 (2), 125-139, 1999.
- <sup>94</sup>. Schueller, O. J. A., Brittain, S. T., and Whitesides, G. M., Fabrication of Glassy Carbon Microstructures by Pyrolysis of Microfabricated Polymeric Precursors, *Advanced Materials* 9 (6), 477-480, 1997.
- <sup>95</sup>. Schueller, O. J. A., Brittain, S. T., Marzolin, C., and Whitesides, G. M., Fabrication and Characterization of Glassy Carbon MEMS, *Chemistry of Materials* 9 (6), 1399-1406, 1997.

- <sup>96.</sup> Kim, J., Song, X., Kinoshita, K., Madou, M., and White, R., Electrochemical Studies of Carbon Films from Pyrolyzed Photoresist, *Journal of the Electrochemical Society* 145 (7), 2314-2319, 1998.
- <sup>97.</sup> Ranganathan, S., McCreery, R., Majji, S. M., and Madou, M., Photoresist-derived carbon for microelectromechanical systems and electrochemical applications, *Journal of the Electrochemical Society* 147 (1), 277-282, 2000.
- <sup>98.</sup> Kostecki, R., Song, X., and Kinoshita, K., Influence of Geometry on the Electrochemical Response of Carbon Interdigitated Microelectrodes, *Journal of the Electrochemical Society* 147 (5), 1878-1881, 2000.
- <sup>99.</sup> Ranganathan, S. and McCreery, R. L., Electroanalytical Performance of Carbon Films with Near-Atomic Flatness, *Analytical Chemistry* 73 , 893-900, 2001.
- <sup>100.</sup> Singh, A., Jayaram, J., Madou, M., and Akbar, S., Pyrolysis of negative photoresists to fabricate carbon structures for microelectromechanical systems and electrochemical applications, *Journal of the Electrochemical Society* 149 (3), E78-E83, 2002.
- <sup>101.</sup> Lorenz, H., Despont, M., Fahrni, M., LaBianca, N., Vettiger, P., and Renaud, P., SU-8: a low-cost negative resist for MEMS, *Journal of Micromechanics and Microengineering* 7 , 121, 1997.
- <sup>102.</sup> Min, H.-S., Park, B. Y., Taherabadi, L., Wang, C., Yeh, Y., Zaouk, R., Madou, M. J., and Dunn, B., Fabrication and properties of a carbon/polypyrrole three-dimensional microbattery, *Selected Papers Presented at the 3rd INTERNATIONAL CONFERENCE ON POLYMER BATTERIES FUEL CELLS(PBFC 2007) on the occasion of Professor Bruno Scrosati's 70th birthday - PBFC 2007* 178 (2), 795-800, 2008.
- <sup>103.</sup> Galobardes, F., Wang, C., and Madou, M., Investigation on the solid electrolyte interface formed on pyrolyzed photoresist carbon anodes for C-MEMS lithium-ion batteries, *Proceedings of the joint 11th International Conference on New Diamond Science and Technology and the 9th Applied Diamond Conference 2006 - ICNDST-ADC 2006* 15 (11-12), 1930-1934, 2006.
- <sup>104.</sup> Teixidor, G. T., Zaouk, R. B., Park, B. Y., and Madou, M. J., Fabrication and characterization of three-dimensional carbon electrodes for lithium-ion batteries, *Journal of Power Sources* 183 (2), 730-740, 2008.
- <sup>105.</sup> Lin, P.-C., Park, B. Y., and Madou, M. J., Development and characterization of a miniature PEM fuel cell stack with carbon bipolar plates, *Journal of Power Sources* 176 (1), 207-214, 2008.
- <sup>106.</sup> Park, B. Y. and Madou, M. J., Design, fabrication, and initial testing of a miniature PEM fuel cell with micro-scale pyrolyzed carbon fluidic plates, *Journal of Power Sources* 162 , 369-379, 2006.
- <sup>107.</sup> Xu, H., Malladi, K., Wang, C., Kulinsky, L., Song, M., and Madou, M., Carbon post-microarrays for glucose sensors, *Biosensors and Bioelectronics* 23 (11), 1637-1644, 2008.
- <sup>108.</sup> Martinez-Duarte, R., Andrade-Roman, J., Martinez, S. O., and Madou, M. J., A High Throughput Multi-stage, Multi-frequency Filter and Separation Device based on Carbon Dielectrophoresis, in *The 11th Annual NSTI Nanotechnology Conference and Trade Show*, pp. 316-319.
- <sup>109.</sup> Martinez-Duarte, R., Gorkin, R. A., Abi-Samra, K., and Madou, M. J., The integration of 3D carbon-electrode dielectrophoresis on a CD-like centrifugal microfluidic platform, *Lab on a Chip* 10 (8), 1030-1043, 2010.

- <sup>110</sup>. Martinez-Duarte, R., Cito, S., Collado-Arredondo, E., Martinez, S. O., and Madou, M. J., Fluidodynamic and Electromagnetic Characterization of 3D Carbon Dielectrophoresis with Finite Element Analysis, *Sensors and Transducers Journal* 3 (Special Issue), 25-36, 2008.
- <sup>111</sup>. Martinez-Duarte, R., Madou, M. J., Kumar, G., and Schroers, J., A Novel Method for Amorphous Metal Micromolding using Carbon MEMS, in *15th International Conference on Solid-State Sensors, Actuators & Microsystems, Transducers 2009*, pp. 188-191.
- <sup>112</sup>. Martinez-Duarte, R., *Fabrication of Carbon Micro Molds*, University of California, Irvine, 2009.
- <sup>113</sup>. Sharma, C. S., Kulkarni, M. M., Sharma, A., and Madou, M., Synthesis of carbon xerogel particles and fractal-like structures, *Chemical Engineering Science* 64 (7), 1536-1543, 2009.
- <sup>114</sup>. Park, B. Y., Zaouk, R., Wang, C., and Madou, M. J., A Case for Fractal Electrodes in Electrochemical Applications, *Journal of the Electrochemical Society* 154 (2), P1-P5, 2007.
- <sup>115</sup>. Jeong, O. C. and Konishi, S., Three-dimensionally combined carbonized polymer sensor and heater, *Sensors and Actuators A* 143 , 97-105, 2008.
- <sup>116</sup>. Nishikawa, K., Fukuyama, K., and Nishizawa, T., Structure Change of Glass-like Carbon with Heat Treatment, Studied by Small Angle X-Ray Scattering: I. Glass-like Carbon Prepared from Phenolic Resin, *Japan Journal of Applied Physics* 37 , 6486-6491, 1998.
- <sup>117</sup>. Jenkins, G. M. and Kawamura, K., *Polymeric Carbon - Carbon Fibre, Glass and Char* Cambridge University Press, London, New York, 1976.
- <sup>118</sup>. Aggarwal, R. K., Bhatia, G., Bahl, O. P., and Malik, M., Development of Glass-Like Carbon from Phenol Formaldehyde Resins Employing Monohydric and Dihydric Phenols, *Journal of Materials Science* 23 (5), 1677-1684, 1988.
- <sup>119</sup>. Neenan, T. X., Callstrom, M. R., Bachman, B. J., McCreery, R. L., and Alsmeyer, D. C., Doped Glassy Carbon Materials (DGC): Their Synthesis from Polymeric Precursors and Investigation of Their Properties, *British Polymer Journal* 23 , 171-177, 1990.
- <sup>120</sup>. Hishiyama, Y., Igarashi, K., Kanaoka, I., Fujii, H., Kaneda, T., Koidesawa, T., Shimazawa, Y., and Yoshida, A., Graphitization behavior of Kapton-derived carbon film related to structure, microtexture and transport properties, *Carbon* 35 (5), 657-668, 1997.
- <sup>121</sup>. Fitzer, E., Schaefer, W., and Yamada, S., The formation of glasslike carbon by pyrolysis of polyfurfuryl alcohol and phenolic resin, *Carbon* 7 (6), 643, 1969.
- <sup>122</sup>. Fitzer, E. and Schäfer, W., The Effect of Crosslinking on the Formation of Glasslike Carbons from Thermosetting Resins, *Carbon* 8 , 353-364, 1970.
- <sup>123</sup>. Malladi, K., Wang, C., and Madou, M., Fabrication of suspended carbon microstructures by e-beam writer and pyrolysis, *Carbon* 44 , 2602-2607, 2006.
- <sup>124</sup>. Lee, L.-H., Mechanisms of Thermal Degradation of Phenolic Condensation Polymers. II. Thermal Stability and Degradation Schemes of Epoxy Resins, *Journal of Polymer Science Part A: Polymer Chemistry* 3 , 859-882, 1965.
- <sup>125</sup>. Gac, N. A., Spokes, G. N., and Benson, S. W., Thermal Degradation of Nadic Methyl Anhydride-Cured Epoxy Novolac, *Journal of Polymer Science: Part A-1* 8 , 593-608, 1970.

- <sup>126.</sup> Fitzer, E., Mueller, K., and Schaefer, W., The Chemistry of the Pyrolytic Conversion of Organic Compounds to Carbon, in *Chemistry and Physics of Carbon*, Walker Jr, P. L. Marcel Dekker, Inc., New York, 1971, pp. 238-383.
- <sup>127.</sup> Lyons, A. M., Wilkins, C. W., and Robbins, M., Thin Pinhole-free Carbon Films, *Thin Solid Films* 103 , 333-341, 1983.
- <sup>128.</sup> Nakagawa, H. and Tsuge, S., Studies on Thermal Degradation of Epoxy Resins by High-Resolution Pyrolysis-Gas Chromatography, *Journal of Analytic and Applied Pyrolysis* 12 , 97-113, 1987.
- <sup>129.</sup> Chen, K. S. and Yeh, R. Z., Pyrolysis kinetics of epoxy resin in a nitrogen atmosphere, *Journal of Hazardous Materials* 49 , 105-113, 1996.
- <sup>130.</sup> Ma, C. C. M., Chen, C. Y., Kuan, H. C., and Chang, W. C., Processability, Thermal, Mechanical, and Morphological Properties of Novolac Type-Epoxy Resin-Based Carbon-Carbon Composite, *Journal of Composite Materials* 38 , 311-322, 2004.
- <sup>131.</sup> Mehrotra, B. N., Bragg, R. H., and Rao, A. S., Effect of heat treatment temperature (HTT) on density, weight and volume of glass-like carbon (GC), *Journal of Materials Science* 18 , 2671-2678, 1983.
- <sup>132.</sup> Ito, H., Chemical Amplification Resists: history and Development within IBM, *IBM Journal of Research and Development* 41 , 69-80, 1996.
- <sup>133.</sup> Abgrall, P., Conedera, V., Camon, H., Gue, A.-M., and Nguyen, N.-T., SU-8 as a structural material for labs-on-chips and microelectromechanical systems, *Electrophoresis* 28 , 4539-4551, 2007.
- <sup>134.</sup> Crivello, J. V. and Lam, J. H. W., Diaryliodonium Salts. A New Class of Photoinitiators for Cationic Polymerization, *Macromolecules* 10 (6), 1307-1315, 1977.
- <sup>135.</sup> Crivello, J. V. and Lam, J. H. W., Photoinitiated Cationic Polymerization with Triarylsulfonium Salts, *Journal of Polymer Science* 17 , 977-999, 1979.
- <sup>136.</sup> Crivello, J. V. and Lam, J. H. W., Complex Triarylsulfonium Salt Photoinitiators. I. The Identification, Characterization, and Syntheses of a New Class of Tryarylsulfonium Salt Photoinitiators, *Journal of Polymer Science Part A: Polymer Chemistry* 18 , 2677-2695, 1980.
- <sup>137.</sup> Gelorme, J. D., Cox, R. J., and Gutierrez, S. A. R., 4882245, 1989, Photoresist Composition and Printed Circuit Boards and Packages made therewith.
- <sup>138.</sup> Angelo, R., Gelorme, J., Kucynski, J., Lawrence, W., Pappas, S., and Simpson, L., US 5102772, 1992, Photocurable epoxy composition with sulfonium salt photoinitiator.
- <sup>139.</sup> Chollet, F., 2009.
- <sup>140.</sup> Guerin, L. J., 2005.
- <sup>141.</sup> Bertsch, A., Lorenz, H., and Renaud, P., 3D Microfabrication by Combining Microstereolithography and Thick Resist UV Lithography, *Sensors and Actuators A* 73 , 14-23, 1999.
- <sup>142.</sup> Yang, R. and Wang, W., A Numerical and Experimental Study on Gap Compensation and Wavelength Selection in UV-Lithography of Ultra-High Aspect Ratio SU-8 Microstructures, *Sensors and Actuators B: Chemical* 110 (2), 279-288, 2005.
- <sup>143.</sup> Williams, J. D. and Wang, W., Study on the postbaking process and the effects on UV lithography of high aspect ratio SU-8 microstructures, *Journal of Microlithography, Microfabrication and Microsystems* 3 , 563-568, 2004.

- <sup>144.</sup> Ling, Z. G., Lian, K., and Jian, L., Improved patterning quality of SU-8 microstructures by optimizing the exposure parameters, in *Advances in Resist Technology and Processing XVIII*, pp. 1019-1027.
- <sup>145.</sup> Lorentz, H., Despont, M., Fahrni, N., Brugger, J., Vettiger, P., and Renaud, P., High-aspect-ratio, ultrathick, negative-tone near-UV photoresist and its applications for MEMS, *Sensor Actuat A - Phys* 64 , 33-39, 1998.
- <sup>146.</sup> Madou, M. J., *Manufacturing Techniques for Microfabrication and Nanotechnology* CRC Press, Boca Raton, FL, 2009.
- <sup>147.</sup> del Campo, A. and Greiner, C., SU:8 a photoresist for high-aspect-ratio and 3D submicron lithography, *Journal of Micromechanics and Microengineering* 17 , R81-R95, 2007.
- <sup>148.</sup> Anderson, N. G., Analytical techniques for cell fractions : XII. A multiple-cuvet rotor for a new microanalytical system, *Analytical Biochemistry* 28, 545-562, 1969.
- <sup>149.</sup> Madou, M. and Kellog, G. J., LabCD: a centrifuge-based microfluidic platform for diagnostics, *Proceedings of SPIE* 3259 , 80-93, 1998.
- <sup>150.</sup> Michelle, S., Shari, O., Lance, G., Theresa, T., Howard, H., Noa, S., Hitesh, J., Greg, K., and Bruce, C., ADMET Assays on Tecan's LabCD-ADMET System, 8 (2), 74-77, 2003.
- <sup>151.</sup> Kido, H., Maquieira, A., and Hammock, B. D., Disc-based immunoassay microarrays, *Analytica Chimica Acta* 411 (1-2), 1-11, 2000.
- <sup>152.</sup> Gyros, A. B.
- <sup>153.</sup> Barathur, R., Bookout, J., Sreevatsan, S., Gordon, J., Werner, M., Thor, G., and Worthington, M., New disc-based technologies for diagnostic and research applications, *Psychiatric Genetics* 12 (4), 2002.
- <sup>154.</sup> Alexandre, I., Houbion, Y., Collet, J., Hamels, S., Demartean, J., Gala, J., and Remacle, J., Compact disc with both numeric and genomic information as DNA microarray platform, *Biotechniques* 33 (2), 435-6, 438-9, 2002.
- <sup>155.</sup> Abaxis, I., 2009.
- <sup>156.</sup> Steigert, J., Grumann, M., Brenner, T., Riegger, L., Harter, J., Zengerle, R., and Ducree, J., Fully integrated whole blood testing by real-time absorption measurement on a centrifugal platform, *Lab on a Chip* 6 (8), 1040-1044, 2006.
- <sup>157.</sup> Schembri, C. T., Burd, T. L., Kopf-Sill, A. R., Shea, L. R., and Braynin, B., Centrifugation and capillarity integrated into a multiple analyte whole blood analyser, *Journal of Automatic Chemistry* 17 (3), 99-104, 1995.
- <sup>158.</sup> Lee, B. S., Lee, J.-N., Park, J.-M., Lee, J.-G., Kim, S., Cho, Y.-K., and Ko, C., A fully automated immunoassay from whole blood on a disc, *Lab on a Chip* 9 (11), 1548-1555, 2009.
- <sup>159.</sup> Kido, H., Micic, M., Smith, D., Zoval, J., Norton, J., and Madou, M., A novel, compact disk-like centrifugal microfluidics system for cell lysis and sample homogenization, *Supramolecular Chemistry Applied to Interfaces, Selected papers presented at the 2006 Florida Annual Meeting and Exhibition of the American Chemical Society, and at the Western Regional Meeting of the American Chemical Society* 58 (1), 44-51, 2007.
- <sup>160.</sup> Kellogg, G. J., Arnold, T. E., Carvalho, B. L., Duffy, D. C., and Sheppard, N. F., Microfluidics in a rotating CD, van den Berg, A., Olthius, W., and Bergveld, P., pp. 239-242.

- <sup>161.</sup> Martensson, G., Skote, M., Malmqvist, M., Falk, M., Asp, A., Svanvik, N., and Johansson, A., Rapid PCR amplification of DNA utilizing Coriolis effects, *European Biophysics Journal* 35 (6), 453-458, 2006.
- <sup>162.</sup> Honda, N., Lindberg, U., Andersson, P., Hoffmann, S., and Takei, H., Simultaneous Multiple Immunoassays in a Compact Disc-Shaped Microfluidic Device Based on Centrifugal Force, *Clinical chemistry* 51 (10), 1955-1961, 2005.
- <sup>163.</sup> Peytavi, R., Raymond, F. R., Gagne, D., Picard, F. J., Jia, G., Zoval, J., Madou, M., Boissinot, K., Boissinot, M., Bissonnette, L., Ouellette, M., and Bergeron, M. G., Microfluidic Device for Rapid (<15 min) Automated Microarray Hybridization; 10.1373/clinchem.2005.052845, *Clin Chem* 51 (10), 1836-1844, 2005.
- <sup>164.</sup> Jia, G., Ma, K.-S., Kim, J., Zoval, J. V., Peytavi, R., Bergeron, M. G., and Madou, M. J., Dynamic automated DNA hybridization on a CD (compact disc) fluidic platform, *Sensors and Actuators B: Chemical* 114 (1), 173-181, 2006.
- <sup>165.</sup> Chen, H., Wang, L., and Li, P. C. H., Nucleic acid microarrays created in the double-spiral format on a circular microfluidic disk, *Lab on a Chip* 8 (5), 826-829, 2008.
- <sup>166.</sup> Boettcher, M., Jaeger, M., Riegger, L., Ducrée, J., Zengerle, R., and Duschl, C., Lab-On-Chip-Based Cell Separation by Combining Dielectrophoresis and Centrifugation, *Biophysical Reviews and Letters* 1, 9, 2006.
- <sup>167.</sup> Thomas, N., Ocklind, A., Blikstad, I., Griffiths, M., Kenrick, K., Derand, H., Ekstrand, G., Ellström, C., Larsson, A., and Andersson, P., Integrated cell based assays in microfabricated disposable CD devices, in *Proc of MicroTAS*, pp. 249-252.
- <sup>168.</sup> Kim, N., Dempsey, C. M., Zoval, J. V., Sze, J.-Y., and Madou, M. J., Automated microfluidic compact disc (CD) cultivation system of *Caenorhabditis elegans*, *Sensors and Actuators B: Chemical* 122 (2), 511-518, 2007.
- <sup>169.</sup> Kim, N., Dempsey, C. M., Kuan, C.-J., Zoval, J. V., O'Rourke, E., Ruvkun, G., Madou, M. J., and Sze, J. Y., Gravity Force Transduced by the MEC-4/MEC-10 DEG/ENaC Channel Modulates DAF-16/FoxO Activity in *Caenorhabditis elegans*; 10.1534/genetics.107.076901, *Genetics* 177 (2), 835-845, 2007.
- <sup>170.</sup> Manz, A., Graber, N., and Widmer, H. M., Miniaturized Total Chemical Analysis Systems: a Novel Concept for Chemical Sensing, *Sensors and Actuators B1* , 244-248, 1990.
- <sup>171.</sup> Zoval, J. V. and Madou, M. J., Centrifuge Based Fluidic Platforms, *Proceedings of IEEE* 92 , 140-153, 2004.
- <sup>172.</sup> Madou, M., Zoval, J., Jia, G. Y., Kido, H., Kim, J., and Kim, N., Lab on a CD, *Annual Review of Biomedical Engineering* 8, 601-628, 2006.
- <sup>173.</sup> Beebe, D. J., Mensing, G. A., and Walker, G. M., Physics and Applications of Microfluidics in Biology, *Annual Review of Biomedical Engineering* 4 , 261-286, 2002.
- <sup>174.</sup> Duffy, D. C., McDonald, J. C., Schueller, O. J. A., and Whitesides, G. M., Rapid Prototyping of Microfluidic Systems in Poly(dimethylsiloxane), *Analytical Chemistry* 70 (23), 4974-4984, 1998.
- <sup>175.</sup> Jens, D. and et al., The centrifugal microfluidic Bio-Disk platform, *Journal of Micromechanics and Microengineering* 17 (7), S103, 2007.
- <sup>176.</sup> Duffy, D. C., Gillis, H. L., Lin, J., Sheppard Jr, N. F., and Kellogg, G. J., Microfabricated Centrifugal Microfluidic Systems: Characterization and Multiple Enzymatic Assays, *Analytical Chemistry* 71 (20), 4669-4678, 1999.

- <sup>177.</sup> Duffy, D. C., Gillis, H. L., Lin, J., Sheppard, N. F., and Kellogg, G. J., Microfabricated centrifugal microfluidic systems: Characterization and multiple enzymatic assays, *Analytical Chemistry* 71 (20), 4669-4678, 1999.
- <sup>178.</sup> Lai, S., Wang, S., Luo, J., Lee, L. J., Yang, S.-T., and Madou, M. J., Design of a Compact Disk-like Microfluidic Platform for Enzyme-Linked Immunosorbent Assay, *Analytical Chemistry* 76 (7), 1832-1837, 2004.
- <sup>179.</sup> Johnson, R. D., Badr, I. H. A., Barrett, G., Lai, S., Lu, Y., Madou, M. J., and Bachas, L. G., Development of a Fully Integrated Analysis System for Ions Based on Ion-Selective Optodes and Centrifugal Microfluidics, *Analytical Chemistry* 73 (16), 3940-3946, 2001.
- <sup>180.</sup> Badr, I. H. A., Johnson, R. D., Madou, M. J., and Bachas, L. G., Fluorescent Ion-Selective Optode Membranes Incorporated onto a Centrifugal Microfluidics Platform, *Analytical Chemistry* 74 (21), 5569-5575, 2002.
- <sup>181.</sup> Park, J. M., Cho, Y. K., Lee, B. S., Lee, J. G., and Ko, C., Multifunctional microvalves control by optical illumination on nanoheaters and its application in centrifugal microfluidic devices, *Lab on a Chip* 7 (5), 557-564, 2007.
- <sup>182.</sup> Grumman, M., Geipel, A., Riegger, L., Zengerle, R., and Ducree, J., Batch-mode mixing on centrifugal microfluidics platform, *Lab chip* 5, 560-565, 2005.
- <sup>183.</sup> Ducrée, J., Haeberle, S., Brenner, T., Glatzel, T., and Zengerle, R., Patterning of flow and mixing in rotating radial microchannels, *Microfluidics and Nanofluidics* 2 (2), 97-105, 2006.
- <sup>184.</sup> Li, B., Liu, M., and Chen, Q., Low-stress ultra-thick SU-8 UV photolithography process for MEMS, *Journal of Microlithography, Microfabrication and Microsystems* 4 (4), 043008-1-043008-6, 2005.
- <sup>185.</sup> Williams, J. D. and Wang, W., Using megasonic development of SU-8 to yield ultra-high aspect ratio microstructures with UV lithography, *Microsystem Technologies* 10 , 694-698, 2004.
- <sup>186.</sup> Shirtcliffe, N. J., Aqil, S., Evans, C., McHale, G., Newton, M. I., Perry, C. C., and Roach, P., The use of high aspect ratio photoresist (SU-8) for super-hydrophobic pattern prototyping, *Journal of Micromechanics and Microengineering* 14, 1384-1389, 2004.
- <sup>187.</sup> Vora, K. D., Shew, B. Y., Harvey, E. C., Hayes, J. P., and Peele, A. G., Specification of mechanical support structures to prevent SU-8 stiction in high aspect ratio structures, *Journal of Micromechanics and Microengineering* 15 , 978-983, 2005.
- <sup>188.</sup> Tanaka, T., Morigami, M., and Atoda, N., Mechanism of Resist Pattern Collapse during Development Process, *Japan Journal of Applied Physics* 32, 6059-6064, 1993.
- <sup>189.</sup> Hwang, S.-F., Yu, J.-H., Lai, B.-J., and Liu, H.-K., Young's modulus and interlaminar fracture toughness of SU-8 film on silicon wafer, *Mechanics of Materials* 40 (8), 658-664, 2008.
- <sup>190.</sup> Al-Halhouli, A. T., Kampen, I., Krah, T., and Büttgenbach, S., Nanoindentation testing of SU-8 photoresist mechanical properties, *Microelectronic Engineering* 85 (5-6), 942-944, 2007.
- <sup>191.</sup> Chemical, H., Glass like carbon.
- <sup>192.</sup> Symonds, J., Sadegh, A. M., Hawkins, H. V., Dodge, D. D., Cloud, G. L., Hyer, M. W., and Case, S. W., Chapter 5: Strength of Materials, in *Mark's Standard Handbook for Mechanical Engineers*, 11th ed., Avallone, E. A., Baumeister, T., and Sadegh, A. M. McGraw-Hill Professional, New York, 2007, pp. 1792.

- <sup>193.</sup> Yamashita, Y., Sub-0.1  $\mu\text{m}$  Patterning with High Aspect Ratio of 5 Achieved by Preventing Pattern Collapse, *Japan Journal of Applied Physics* 35, 2385-2386, 1996.
- <sup>194.</sup> Vrentas, J. S. and Duda, J. L., Diffusion in polymer-solvent systems. I. Reexamination of the free-volume theory, *Journal of Polymer Science Part B: Polymer Physics* 15, 403-416, 1977.
- <sup>195.</sup> Vrentas, J. S. and Duda, J. L., Diffusion in Polymer-Solvent Systems. II. A Predictive Theory for the Dependence of Diffusion Coefficients on Temperature, Concentration, and Molecular Weight, *Journal of Polymer Science Part B: Polymer Physics* 15, 417-439, 1977.
- <sup>196.</sup> Shaw, M., Nawrocki, D., Hurditch, R., and Johnson, D., Improving the process capability of SU-8, *Microsystem Technologies* 10 , 1-6, 2003.
- <sup>197.</sup> Lee, K. Y., LaBianca, N., Rishton, S. A., Zolgharnain, S., Gelorme, J. D., Shaw, J., and Chang, T. H. P., Micromachining applications of a high resolution ultrathick photoresist, *J Vac Sci Technol B* 13 , 3012-3016, 1995.
- <sup>198.</sup> Reznikova, E. F., Mohr, J., and Hein, H., Deep Photo-Lithography Characterization of SU-8 Resist Layers, *Microsystem Technologies* 11, 282-291, 2005.
- <sup>199.</sup> Tanaka, T., Mitsuaki, M., Hiroaki, O., and Taro, O., Freeze-Drying Process to Avoid Resist Pattern Collapse, *Japan Journal of Applied Physics* 32 (12R), 5813-5814, 1993.
- <sup>200.</sup> Namatsu, H., Yamazaki, K., and Kurihara, K., Supercritical resist dryer, *Journal of Vacuum Science and Technology B* 18 (2), 780-784, 2000.
- <sup>201.</sup> Jincao, Y. and Matthews, M. A., Prevention of Photoresist Pattern Collapse by Using Liquid Carbon Dioxide, *Industrial & Engineering Chemistry Research* 40 (24), 5858-5860, 2001.
- <sup>202.</sup> Park, B. Y., Taherabadi, L., Wang, C., Zoval, J., and Madou, M. J., Electrical Properties and Shrinkage of Carbonized Photoresist Films and the Implications for Carbon Microelectromechanical Systems Devices in Conductive Media, *Journal of the Electrochemical Society* 152 (12), J136-J143, 2005.
- <sup>203.</sup> Kim, K., Park, D. S., Lu, H. M., Che, W., Lee, J. B., and Ahn, C. H., A tapered hollow metallic microneedle array using backside exposure of SU-8, *Journal of Micromechanics and Microengineering* 14, 597-603, 2004.
- <sup>204.</sup> Park, B. Y. and Madou, M. J., 3-D electrode designs for flow-through dielectrophoretic systems, *Electrophoresis* 26 , 3745-3757, 2005.
- <sup>205.</sup> Buss, B. G., Evans, D. N., Liu, H., Shang, T., Oliphant, T. E., Schultz, S. M., and Hawkins, A. R., Quantifying resistivity using scanning impedance imaging, *Sensors and Actuators A: Physical* 137 (2), 338-344, 2007.
- <sup>206.</sup> Neumann, E., Sowers, A. E., and Jordan, C. A., *Electroporation and Electrofusion in Cell Biology* Plenum Publishing Corporation, New York, 1989.
- <sup>207.</sup> Heida, T., Wagenaar, J. B. M., Rutten, W. L. C., and Marani, E., Investigating Membrane Breakdown of Neuronal Cells Exposed to Nonuniform Electric Fields by Finite-Element Modeling and Experiments, *IEEE T Bio-Med Eng* 49 (10), 1195-1203, 2002.
- <sup>208.</sup> Good, N. E., Winget, G. D., Winter, W., Connolly, T. N., Izawa, S., and Singh, R. M. M., Hydrogen Ion Buffers for Biological Research, *Biochemistry* 5 (2), 467-477, 1966.
- <sup>209.</sup> Arnold, W. M., Positioning and Levitation Media for the Separation of Biological Cells, *IEEE Transactions on Industry Applications* 37 (5), 1468-1475, 2001.

- <sup>210</sup>. Gray, D. S., Tan, J. L., Voldman, J., and Chen, C. S., Dielectrophoretic registration of living cells to a microelectrode array, *Biosensors and Bioelectronics* 19 (12), 1765-1774, 2004.
- <sup>211</sup>. Castellarnau, M., Zine, N., Bausells, J., Madrid, C., Juarez, A., Samitier, J., and Errachid, A., Integrated cell positioning and cell-based ISFET biosensors, *Sensors and Actuators B: Chemical* 120 (2), 615-620, 2007.
- <sup>212</sup>. Gascoyne, P., Mahidol, C., Ruchirawat, M., Satayavivad, J., Watcharasit, P., and Becker, F. F., Microsample preparation by dielectrophoresis: Isolation of malaria, *Lab on a Chip - Miniaturisation for Chemistry and Biology* 2 (2), 70-75, 2002.
- <sup>213</sup>. Gascoyne, P. R. C., Huang, Y., Pethig, R., Vykoukal, J., and Becker, F. F., Dielectrophoretic separation of mammalian cells studied by computerized image analysis, *Measurement Science and Technology* 3 (5), 439-445, 1992.
- <sup>214</sup>. Markx, G. H. and Pethig, R., Dielectrophoretic separation of cells - continuous separation, *Biotechnology and bioengineering* 45 (-), 337-343, 1995.
- <sup>215</sup>. Flanagan, L. A., Lu, J., Wang, L., Marchenko, S., Jeon, N. L., Lee, A. P., and Monuki, E., Unique Dielectric Properties Distinguishing Stem Cells and Their Differentiated Progeny, *Stem cells* 26 (3), 656-665, 2008.
- <sup>216</sup>. Ermolina, I. and Morgan, H., The electrokinetic properties of latex particles: comparison of electrophoresis and dielectrophoresis, *Journal of colloid and interface science* 285 , 419-428, 2005.
- <sup>217</sup>. Hughes, M. P., Dielectrophoretic behavior of latex nanospheres: Low-frequency dispersion, *Journal of colloid and interface science* 250 (-), 291-294, 2002.
- <sup>218</sup>. Green, N. G. and Morgan, H., Dielectrophoresis of submicrometer latex spheres. 1. Experimental results, *Journal of Physical Chemistry B* 103 (-), 41-50, 1999.
- <sup>219</sup>. Ermolina, I. and Morgan, H., The electrokinetic properties of latex particles: comparison of electrophoresis and dielectrophoresis, *Journal of Colloid and Interface Science* 285 , 419-428, 2005.
- <sup>220</sup>. Crane, J. S. and Pohl, H. A., A study of living and dead yeast cells using dielectrophoresis, *Journal of the Electrochemical Society* 115 (-), 584-586, 1968.
- <sup>221</sup>. Green, N. G. and Morgan, H., Dielectrophoretic investigations of sub-micrometre latex spheres, *Journal of Physics D: Applied Physics* 30 (-), 2626-2633, 1997.
- <sup>222</sup>. Castellarnau, M., Errachid, A., Madrid, C., Juarez, A., and Samitier, J., Dielectrophoresis as a tool to characterize and differentiate isogenic mutants of *Escherichia coli*, *Biophysical journal* 91 (10), 3937-3945, 2006.
- <sup>223</sup>. Adams, M. D., Celniker, S. E., Holt, R. A., Evans, C. A., Gocayne, J. D., Amanatides, P. G., Scherer, S. E., Li, P. W., Hoskins, R. A., Galle, R. F., George, R. A., Lewis, S. E., Richards, S., Ashburner, M., Henderson, S. N., Sutton, G. G., Wortman, J. R., Yandell, M. D., Zhang, Q., Chen, L. X., Brandon, R. C., Rogers, Y.-H. C., Blazej, R. G., Champe, M., Pfeiffer, B. D., Wan, K. H., Doyle, C., Baxter, E. G., Helt, G., Nelson, C. R., Gabor Miklos, G. L., Abril, J. F., Agbayani, A., An, H.-J., Andrews-Pfannkoch, C., Baldwin, D., Ballew, R. M., Basu, A., Baxendale, J., Bayraktaroglu, L., Beasley, E. M., Beeson, K. Y., Benos, P. V., Berman, B. P., Bhandari, D., Bolshakov, S., Borkova, D., Botchan, M. R., Bouck, J., Brokstein, P., Brottier, P., Burtis, K. C., Busam, D. A., Butler, H., Cadieu, E., Center, A., Chandra, I., Cherry, J. M., Cawley, S., Dahlke, C., Davenport, L. B., Davies, P., Pablos, B. d., Delcher, A., Deng, Z., Mays, A. D., Dew, I., Dietz, S. M., Dodson, K., Doup, L. E., Downes, M., Dugan-Rocha, S., Dunkov, B. C., Dunn, P., Durbin, K. J.,

- Evangelista, C. C., Ferraz, C., Ferriera, S., Fleischmann, W., Fosler, C., Gabrielian, A. E., Garg, N. S., Gelbart, W. M., Glasser, K., Glodek, A., Gong, F., Gorrell, J. H., Gu, Z., Guan, P., Harris, M., Harris, N. L., Harvey, D., Heiman, T. J., Hernandez, J. R., Houck, J., Hostin, D., Houston, K. A., Howland, T. J., Wei, M.-H., Ibegwam, C. *et al.*, The Genome Sequence of *Drosophila melanogaster*, *Science* 287 (5461), 2185-2195, 2000.
- <sup>224</sup>. Wang, G. J., Hsu, W. H., Chang, Y. Z., and Yang, H., Centrifugal and Electric Field Forces Dual-Pumping CD-like Microfluidic Platform for Biomedical Separation, *Biomedical Microdevices* 6 (1), 47-53, 2004.
- <sup>225</sup>. Fuhr, G., Schnelle, T., Hagedorn, R., and Miller, T., 6749736, 2004, Electrode arrangement for the dielectrophoretic diversion of particles.
- <sup>226</sup>. Fuhr, G. and Hagedorn, R., 6465225, 2002, Method and device for manipulating particles in microsystems.
- <sup>227</sup>. Collins, J. and Lee, A. P., Microfluidic flow transducer based on the measurement of electric admittance, *Lab on a Chip* 4, 7-10, 2004.
- <sup>228</sup>. Wu, J. and Sansen, W., Electrochemical time of flight flow sensor, *Sensors and Actuators A: Physical* 97-98, 68-74, 2002.
- <sup>229</sup>. Madou, M., Zoval, J., Jia, G., Kim, J., and Kim, N., Lab on a CD, *Annual Review of Biomedical Engineering* 8, 601-628, 2006.
- <sup>230</sup>. Guazzelli, E., Sedimentation of small particles: how can such a simple problem be so difficult?, *Comptes Rendus Mecanique* 334, 539-544, 2006.
- <sup>231</sup>. Valero, A., Post, J. N., van Nieuwkastele, J. W., ter Braak, P. M., Kruijer, W., and van den Berg, A., Gene transfer and protein dynamics in stem cells using single cell electroporation in a microfluidics device, *Lab on a chip* 8, 62-67, 2008.